

**A HIGH PRECISION MEASUREMENT OF CHARGE SYMMETRY  
BREAKING IN np ELASTIC SCATTERING AT 347 MeV**

By

**JIANGUO ZHAO**

A THESIS

SUBMITTED TO THE FACULTY OF GRADUATE STUDIES IN PARTIAL  
FULFILLMENT OF THE REQUIREMENTS  
FOR THE DEGREE OF

**DOCTOR OF PHILOSOPHY**

IN

**PARTICLE/NUCLEAR PHYSICS**

DEPARTMENT OF PHYSICS  
**THE UNIVERSITY OF MANITOBA**  
WINNIPEG, MANITOBA  
CANADA

© JANUARY, 1995



National Library  
of Canada

Acquisitions and  
Bibliographic Services Branch

395 Wellington Street  
Ottawa, Ontario  
K1A 0N4

Bibliothèque nationale  
du Canada

Direction des acquisitions et  
des services bibliographiques

395, rue Wellington  
Ottawa (Ontario)  
K1A 0N4

*Your file* *Votre référence*

*Our file* *Notre référence*

**The author has granted an irrevocable non-exclusive licence allowing the National Library of Canada to reproduce, loan, distribute or sell copies of his/her thesis by any means and in any form or format, making this thesis available to interested persons.**

**L'auteur a accordé une licence irrévocable et non exclusive permettant à la Bibliothèque nationale du Canada de reproduire, prêter, distribuer ou vendre des copies de sa thèse de quelque manière et sous quelque forme que ce soit pour mettre des exemplaires de cette thèse à la disposition des personnes intéressées.**

**The author retains ownership of the copyright in his/her thesis. Neither the thesis nor substantial extracts from it may be printed or otherwise reproduced without his/her permission.**

**L'auteur conserve la propriété du droit d'auteur qui protège sa thèse. Ni la thèse ni des extraits substantiels de celle-ci ne doivent être imprimés ou autrement reproduits sans son autorisation.**

ISBN 0-612-13594-2

**Canada**

Name \_\_\_\_\_

Dissertation Abstracts International is arranged by broad, general subject categories. Please select the one subject which most nearly describes the content of your dissertation. Enter the corresponding four-digit code in the spaces provided.

Nuclear/Particle Physics.

0610

U·M·I

SUBJECT TERM

SUBJECT CODE

Subject Categories

THE HUMANITIES AND SOCIAL SCIENCES

COMMUNICATIONS AND THE ARTS

Architecture ..... 0729  
 Art History ..... 0377  
 Cinema ..... 0900  
 Dance ..... 0378  
 Fine Arts ..... 0357  
 Information Science ..... 0723  
 Journalism ..... 0391  
 Library Science ..... 0399  
 Mass Communications ..... 0708  
 Music ..... 0413  
 Speech Communication ..... 0459  
 Theater ..... 0465

EDUCATION

General ..... 0515  
 Administration ..... 0514  
 Adult and Continuing ..... 0516  
 Agricultural ..... 0517  
 Art ..... 0273  
 Bilingual and Multicultural ..... 0282  
 Business ..... 0688  
 Community College ..... 0275  
 Curriculum and Instruction ..... 0727  
 Early Childhood ..... 0518  
 Elementary ..... 0524  
 Finance ..... 0277  
 Guidance and Counseling ..... 0519  
 Health ..... 0680  
 Higher ..... 0745  
 History of ..... 0520  
 Home Economics ..... 0278  
 Industrial ..... 0521  
 Language and Literature ..... 0279  
 Mathematics ..... 0280  
 Music ..... 0522  
 Philosophy of ..... 0998  
 Physical ..... 0523

Psychology ..... 0525  
 Reading ..... 0535  
 Religious ..... 0527  
 Sciences ..... 0714  
 Secondary ..... 0533  
 Social Sciences ..... 0534  
 Sociology of ..... 0340  
 Special ..... 0529  
 Teacher Training ..... 0530  
 Technology ..... 0710  
 Tests and Measurements ..... 0288  
 Vocational ..... 0747

LANGUAGE, LITERATURE AND LINGUISTICS

Language  
 General ..... 0679  
 Ancient ..... 0289  
 Linguistics ..... 0290  
 Modern ..... 0291  
 Literature  
 General ..... 0401  
 Classical ..... 0294  
 Comparative ..... 0295  
 Medieval ..... 0297  
 Modern ..... 0298  
 African ..... 0316  
 American ..... 0591  
 Asian ..... 0305  
 Canadian (English) ..... 0352  
 Canadian (French) ..... 0355  
 English ..... 0593  
 Germanic ..... 0311  
 Latin American ..... 0312  
 Middle Eastern ..... 0315  
 Romance ..... 0313  
 Slavic and East European ..... 0314

PHILOSOPHY, RELIGION AND THEOLOGY

Philosophy ..... 0422  
 Religion  
 General ..... 0318  
 Biblical Studies ..... 0321  
 Clergy ..... 0319  
 History of ..... 0320  
 Philosophy of ..... 0322  
 Theology ..... 0469

SOCIAL SCIENCES

American Studies ..... 0323  
 Anthropology  
 Archaeology ..... 0324  
 Cultural ..... 0326  
 Physical ..... 0327  
 Business Administration  
 General ..... 0310  
 Accounting ..... 0272  
 Banking ..... 0770  
 Management ..... 0454  
 Marketing ..... 0338  
 Canadian Studies ..... 0385  
 Economics  
 General ..... 0501  
 Agricultural ..... 0503  
 Commerce-Business ..... 0505  
 Finance ..... 0508  
 History ..... 0509  
 Labor ..... 0510  
 Theory ..... 0511  
 Folklore ..... 0358  
 Geography ..... 0366  
 Gerontology ..... 0351  
 History  
 General ..... 0578

Ancient ..... 0579  
 Medieval ..... 0581  
 Modern ..... 0582  
 Black ..... 0328  
 African ..... 0331  
 Asia, Australia and Oceania ..... 0332  
 Canadian ..... 0334  
 European ..... 0335  
 Latin American ..... 0336  
 Middle Eastern ..... 0333  
 United States ..... 0337  
 History of Science ..... 0585  
 Law ..... 0398  
 Political Science  
 General ..... 0615  
 International Law and  
 Relations ..... 0616  
 Public Administration ..... 0617  
 Recreation ..... 0814  
 Social Work ..... 0452  
 Sociology  
 General ..... 0626  
 Criminology and Penology ..... 0627  
 Demography ..... 0938  
 Ethnic and Racial Studies ..... 0631  
 Individual and Family  
 Studies ..... 0628  
 Industrial and Labor  
 Relations ..... 0629  
 Public and Social Welfare ..... 0630  
 Social Structure and  
 Development ..... 0700  
 Theory and Methods ..... 0344  
 Transportation ..... 0709  
 Urban and Regional Planning ..... 0999  
 Women's Studies ..... 0453

THE SCIENCES AND ENGINEERING

BIOLOGICAL SCIENCES

Agriculture  
 General ..... 0473  
 Agronomy ..... 0285  
 Animal Culture and  
 Nutrition ..... 0475  
 Animal Pathology ..... 0476  
 Food Science and  
 Technology ..... 0359  
 Forestry and Wildlife ..... 0478  
 Plant Culture ..... 0479  
 Plant Pathology ..... 0480  
 Plant Physiology ..... 0817  
 Range Management ..... 0777  
 Wood Technology ..... 0746  
 Biology  
 General ..... 0306  
 Anatomy ..... 0287  
 Biostatistics ..... 0308  
 Botany ..... 0309  
 Cell ..... 0379  
 Ecology ..... 0329  
 Entomology ..... 0353  
 Genetics ..... 0369  
 Limnology ..... 0793  
 Microbiology ..... 0410  
 Molecular ..... 0307  
 Neuroscience ..... 0317  
 Oceanography ..... 0416  
 Physiology ..... 0433  
 Radiation ..... 0821  
 Veterinary Science ..... 0778  
 Zoology ..... 0472  
 Biophysics  
 General ..... 0786  
 Medical ..... 0760

Geodesy ..... 0370  
 Geology ..... 0372  
 Geophysics ..... 0373  
 Hydrology ..... 0388  
 Mineralogy ..... 0411  
 Paleobotany ..... 0345  
 Paleocology ..... 0426  
 Paleontology ..... 0418  
 Paleozoology ..... 0985  
 Palynology ..... 0427  
 Physical Geography ..... 0368  
 Physical Oceanography ..... 0415

HEALTH AND ENVIRONMENTAL SCIENCES

Environmental Sciences ..... 0768  
 Health Sciences  
 General ..... 0566  
 Audiology ..... 0300  
 Chemotherapy ..... 0992  
 Dentistry ..... 0567  
 Education ..... 0350  
 Hospital Management ..... 0769  
 Human Development ..... 0758  
 Immunology ..... 0982  
 Medicine and Surgery ..... 0564  
 Mental Health ..... 0347  
 Nursing ..... 0569  
 Nutrition ..... 0570  
 Obstetrics and Gynecology ..... 0380  
 Occupational Health and  
 Therapy ..... 0354  
 Ophthalmology ..... 0381  
 Pathology ..... 0571  
 Pharmacology ..... 0419  
 Pharmacy ..... 0572  
 Physical Therapy ..... 0382  
 Public Health ..... 0573  
 Radiology ..... 0574  
 Recreation ..... 0575

Speech Pathology ..... 0460  
 Toxicology ..... 0383  
 Home Economics ..... 0386

PHYSICAL SCIENCES

Pure Sciences  
 Chemistry  
 General ..... 0485  
 Agricultural ..... 0749  
 Analytical ..... 0486  
 Biochemistry ..... 0487  
 Inorganic ..... 0488  
 Nuclear ..... 0738  
 Organic ..... 0490  
 Pharmaceutical ..... 0491  
 Physical ..... 0494  
 Polymer ..... 0495  
 Radiation ..... 0754  
 Mathematics ..... 0405  
 Physics  
 General ..... 0605  
 Acoustics ..... 0986  
 Astronomy and  
 Astrophysics ..... 0606  
 Atmospheric Science ..... 0608  
 Atomic ..... 0748  
 Electronics and Electricity ..... 0607  
 Elementary Particles and  
 High Energy ..... 0798  
 Fluid and Plasma ..... 0759  
 Molecular ..... 0609  
 Nuclear ..... 0610  
 Optics ..... 0752  
 Radiation ..... 0756  
 Solid State ..... 0611  
 Statistics ..... 0463  
 Applied Sciences  
 Applied Mechanics ..... 0346  
 Computer Science ..... 0984

Engineering  
 General ..... 0537  
 Aerospace ..... 0538  
 Agricultural ..... 0539  
 Automotive ..... 0540  
 Biomedical ..... 0541  
 Chemical ..... 0542  
 Civil ..... 0543  
 Electronics and Electrical ..... 0544  
 Heat and Thermodynamics ..... 0348  
 Hydraulic ..... 0545  
 Industrial ..... 0546  
 Marine ..... 0547  
 Materials Science ..... 0794  
 Mechanical ..... 0548  
 Metallurgy ..... 0743  
 Mining ..... 0551  
 Nuclear ..... 0552  
 Packaging ..... 0549  
 Petroleum ..... 0765  
 Sanitary and Municipal ..... 0554  
 System Science ..... 0790  
 Geotechnology ..... 0428  
 Operations Research ..... 0796  
 Plastics Technology ..... 0795  
 Textile Technology ..... 0994

PSYCHOLOGY

General ..... 0621  
 Behavioral ..... 0384  
 Clinical ..... 0622  
 Developmental ..... 0620  
 Experimental ..... 0623  
 Industrial ..... 0624  
 Personality ..... 0625  
 Physiological ..... 0989  
 Psychobiology ..... 0349  
 Psychometrics ..... 0632  
 Social ..... 0451

EARTH SCIENCES

Biogeochemistry ..... 0425  
 Geochemistry ..... 0996



**A HIGH PRECISION MEASUREMENT OF CHARGE SYMMETRY BREAKING  
IN NP ELASTIC SCATTERING AT 347 MEV**

**BY**

**JIANGUO ZHAO**

**A Thesis submitted to the Faculty of Graduate Studies of the University of Manitoba  
in partial fulfillment of the requirements of the degree of**

**DOCTOR OF PHILOSOPHY**

**© 1995**

**Permission has been granted to the LIBRARY OF THE UNIVERSITY OF MANITOBA  
to lend or sell copies of this thesis, to the NATIONAL LIBRARY OF CANADA to  
microfilm this thesis and to lend or sell copies of the film, and LIBRARY  
MICROFILMS to publish an abstract of this thesis.**

**The author reserves other publication rights, and neither the thesis nor extensive  
extracts from it may be printed or other-wise reproduced without the author's written  
permission.**

## Abstract

Studying the nucleon-nucleon (NN) interaction, particularly its short range behavior, is of fundamental interest in nuclear and particle physics. In the present experiment (TRIUMF Experiment 369), the breaking of charge symmetry in the NN interaction was measured via a non-zero difference of the neutron-proton elastic scattering analyzing powers,  $\Delta A \equiv A_n - A_p$ , where the subscripts denote polarized nucleons. Scattering asymmetries were measured with a 347 MeV neutron beam (produced through the  $D(\vec{p}, \vec{n})2p$  reaction) incident on a frozen spin type proton target. The beam and the target were alternately polarized. Scattered neutrons and recoil protons were detected in coincidence in the center-of-mass angle range from  $50^\circ$  to  $90^\circ$  with a mirror symmetric (with respect to the neutron beam axis) detection system. The  $A_n$  and  $A_p$  measurements were interleaved and conducted with the same detection system, the same beam and target properties (except polarization) and frequent reversal of the spin polarization directions. At the zero-crossing angle, where the analyzing powers vanish, all systematic errors except those correlated with spin reversal and background correction were eliminated to at least second order. The experiment determined the difference of the zero-crossing angles to be  $\Delta\theta \equiv \theta_n - \theta_p = 0.438^\circ \pm 0.054^\circ(\text{stat.}) \pm 0.051^\circ(\text{syst.})$  (*c.m.*) based on fits of the measured asymmetry curves over the angular range  $53.4^\circ \leq \theta_{cm} \leq 86.9^\circ$ . Using the experimentally determined slope of the analyzing power  $dA/d\theta = (-1.35 \pm 0.05) \times 10^{-2} \text{ deg}^{-1}$ , the difference of the analyzing powers at the zero-crossing angle is  $\Delta A = [59 \pm 7(\text{stat.}) \pm 7(\text{syst.}) \pm 2(\text{syst.})] \times 10^{-4}$ . The shape of the angular distribution of  $\Delta A$  in the angular range of the experiment was also extracted. The experimental results, the difference of the analyzing powers and the shape of  $\Delta A(\theta)$ , agree well with various theoretical predictions based on meson exchange theory pointing to its success as parameterization of the NN interaction.

# Acknowledgements

First of all, I would like to thank my supervisor Prof. W.T.H. van Oers for introducing me to this field and for his guidance and support throughout the years of my study in the group. His leadership role and thorough knowledge on the subject and on all aspects of the experiment in particular were critical to the success of the experiment and were very beneficial to me.

The success of such a large scale experiment would not have been possible without the effort of the collaborators as a whole. I would like to thank everyone in the collaboration for the successful completion of this challenging experiment, and therefore the realization of this thesis. The collaborators were:

R. Abegg, A.R. Berdoz, J. Birchall, J.R. Campbell, C.A. Davis, P.P.J. Delheij, L. Gan, P.W. Green, L.G. Greeniaus, D.C. Healey, R. Helmer, N. Kolb, E. Korkmaz, L. Lee, C.D.P. Levy, J. Li, C.A. Miller, A.K. Opper, S.A. Page, H. Postma, W.D. Ramsay, J. Soukup, G.M. Stinson, W.T.H. van Oers, A.N. Zelenski, J. Zhao.

In this thesis, as a document of complete description of the experiment, I have “borrowed” other collaborators’ efforts freely even without giving references (most of them were numerous internal reports). The experiment was an effort spanning over about 10 years and consisted lots of detailed aspects. Many people have contributed a lot to some especially challenging aspects of the experiment beside the general responsibilities which every collaborator shared. I would like to mention the following contributions in particular (though it should be understood that this is not a complete list): John Campbell for Monte Carlo simulations; Jim Birchall for systematic error calculations; Paul Delheij, Dennis Healey and the TRIUMF target group for the FST; Phil Levy, Anatoly Zelenski and the TRIUMF ion source group for the optically pumped polarized ion source; Peter Green for on-line and off-line computing packages; Chuck Davis and Andy Miller for electronics setup;

and Liping Gan for Monte Carlo simulations of the neutron beam.

Some members of University of Manitoba Group, namely, Drs. Jim Birchall, Alain Berdoz, Larry Lee, John Campbell, Chuck Davis, Shelley Page and Des Ramsay deserve special thanks. Over the years, I have learnt from them a lot on a daily basis. They have helped me in different ways since I first came to Canada from a country where people speak chinese and have a different culture. Finally without them and Dr. W.T.H. van Oers, the thesis would read much worse than it does now.

Dr. Gordon Greeniaus (the co-spokesperson of the experiment with Dr. W.T.H. van Oers) first introduced me to the data analysis of this rather complicated experiment and gave me advice in the course of data analysis. I have benefitted from his expertise of analyzing physics problems as well as technical issues. Jin Li shared lots of knowledge regarding the experiment with me and contributed a lot to the experiment up to the point when he switched his career. Drs. Andy Miller, Paul Delheij and Rudy Abegg gave me various help at different stages of the experiment.

Various committees (advisory and examination) have kept me more or less on track in the course of my graduate study . I would like to thank them for their service over the years.

Finally, I would like to thank fellow graduate students in the Manitoba Nuclear and Particle Physics group over last six year who shared physics and beyond with me.

# Contents

<b>Abstract</b>	<b>iv</b>
<b>Acknowledgements</b>	<b>v</b>
<b>List of Figures</b>	<b>xi</b>
<b>List of Tables</b>	<b>xvii</b>
<b>1 Introduction</b>	<b>1</b>
<b>2 Overview</b>	<b>10</b>
2.1 Early Evidence of Isospin Symmetry Violation and Current Status	11
2.1.1 The low energy nucleon-nucleon $^1S_0$ scattering length and effective range . . . . .	11
2.1.2 Binding Energy Differences of Mirror Nuclei - Okamoto-Nolen-Schiffer Anomaly . . . . .	13
2.2 Charge Symmetry Breaking in $np$ Elastic Scattering . . . . .	14
2.2.1 Experimental Aspects . . . . .	14
2.2.2 Theoretical Aspects . . . . .	17
2.3 Other Isospin Symmetry Studies . . . . .	26
<b>3 Experimental Details</b>	<b>30</b>
3.1 General Description . . . . .	30
3.2 Proton Beam Production and Transport System . . . . .	32

3.3	Neutron Beam Production and Collimation . . . . .	39
3.4	Proton Polarimeter and Beam Energy Monitor . . . . .	42
3.5	Secondary Emission Monitors . . . . .	48
3.6	Phase Lock System . . . . .	51
3.7	Neutron Polarimeter and Profile Monitor . . . . .	52
3.8	Spin Precession . . . . .	54
3.9	Frozen Spin Target . . . . .	59
3.10	Proton Detection System . . . . .	65
3.11	Neutron Detection System . . . . .	71
3.12	Electronics and Data Acquisition . . . . .	75
3.13	Run Procedure . . . . .	80
<b>4</b>	<b>Monte Carlo Simulations</b>	<b>83</b>
4.1	Neutron Beam Properties . . . . .	83
4.2	np Coincidence Events . . . . .	87
<b>5</b>	<b>Data Analysis</b>	<b>99</b>
5.1	General Description . . . . .	99
5.2	System Parameter Analysis . . . . .	100
5.2.1	Proton Beam Energy . . . . .	101
5.2.2	Proton Polarization . . . . .	102
5.2.3	$LD_2$ Target . . . . .	106
5.2.4	Neutron Beam Polarization . . . . .	109
5.2.5	Neutron Beam Profile . . . . .	110
5.2.6	SEM Asymmetry and Beam Position Stability . . . . .	113
5.2.7	FST Holding Field, Polarization and Position . . . . .	116
5.2.8	Neutron Detector Position and Gain Calibration . . . . .	118

5.3	Selection of Elastic Scattering $np$ Events . . . . .	121
5.3.1	Proton Track Reconstruction . . . . .	121
5.3.2	Proton Time-Of-Flight and Kinetic Energy . . . . .	131
5.3.3	Neutron Position and Angle . . . . .	135
5.3.4	Neutron Time-of-Flight (TOF) and Kinetic Energy . . . . .	140
5.3.5	Neutron Bar Gain Renormalization . . . . .	140
5.3.6	Kinematical Observables and Data Constraints . . . . .	142
5.4	Asymmetries and Zero-Crossing angles . . . . .	145
5.5	Neutron Beam Energy . . . . .	149
5.6	Background and Other Corrections . . . . .	152
5.6.1	Background Correction . . . . .	152
5.6.2	Neutron Beam Energy Difference Correction . . . . .	156
5.7	Slope of the Analyzing Powers . . . . .	158
5.8	Shape of " $\Delta A(\theta)$ " . . . . .	160
<b>6</b>	<b>Systematic Errors</b>	<b>161</b>
6.1	Introduction . . . . .	161
6.2	Sources of Systematic Errors . . . . .	166
6.2.1	Proton Beam Energy, Position and Direction at the $LD_2$ Target . . . . .	166
6.2.2	Neutron Beam Energy Stability . . . . .	172
6.2.3	FST Parameters . . . . .	172
6.2.4	Beam or Target Polarization . . . . .	182
6.2.5	Misalignment of Apparatus . . . . .	189
6.2.6	Multiple Scattering . . . . .	190
6.2.7	Neutron Detection Efficiency Stability . . . . .	192
6.2.8	Background . . . . .	194

6.3	Tests of Systematic Errors in the Data Analysis . . . . .	198
6.3.1	Different $\chi^2$ Tests . . . . .	198
6.3.2	Different Neutron Bar Software Thresholds . . . . .	201
6.3.3	Different Angular Range Fits . . . . .	202
6.3.4	Background . . . . .	202
6.3.5	Average Neutron Beam Energy Difference . . . . .	203
<b>7</b>	<b>Results and Discussions</b>	<b>205</b>
	<b>Bibliography</b>	<b>213</b>
	<b>Appendices</b>	<b>220</b>
<b>A</b>	<b>Delay Line Multiwire Chamber Calibrations</b>	<b>220</b>
<b>B</b>	<b>Spin Precession Magnets Calibration</b>	<b>223</b>
<b>C</b>	<b>Analyzing Power Angular Distributions and Zero-crossing Angles</b>	<b>228</b>
<b>D</b>	<b>Event Structure</b>	<b>231</b>

# List of Figures

1.1	<i>Symmetry operations for <math>np</math> elastic scattering with either neutron or proton polarized, and the relation between charge symmetry and the equality of the differential cross-sections (when <math>P_n = P_p</math>) . . .</i>	5
1.2	<i>An illustration of the method employed to extract <math>\Delta A \equiv A_n - A_p</math> from the difference in the <math>A_n</math> and <math>A_p</math> zero-crossing angles, <math>\Delta\theta</math>, for <math>np</math> elastic scattering . . . . .</i>	8
2.1	<i>Charge symmetry breaking mechanisms in <math>np</math> elastic scattering . .</i>	24
2.2	<i>(a) Various predictions for <math>\Delta A</math> at 347 MeV are compared; (b) the different contributions to <math>\Delta A</math> as predicted by Iqbal and Niskanen .</i>	25
2.3	<i>Feynman diagram of a particle-antiparticle loop for the <math>\rho^0 - \omega</math> mixing amplitude . . . . .</i>	27
2.4	<i>Charge symmetric sketches of <math>np \rightarrow d\pi^0</math> in the center-of-mass frame</i>	28
2.5	<i>(a) <math>\eta - \pi^0</math> mixing in the transition potential; (b) <math>\eta - \pi^0</math> mixing in the production vertex . . . . .</i>	29
3.1	<i>Layout of the beam transport system and schematic view of the experimental apparatus . . . . .</i>	31
3.2	<i>Definition of the coordinates and conventions . . . . .</i>	33
3.3	<i>A block diagram of the TRIUMF optically pumped polarized ion source based on the proposal of L.W. Anderson . . . . .</i>	36

3.4	<i>A schematic diagram of the TRIUMF optically-pumped polarized <math>H^-</math> ion source . . . . .</i>	37
3.5	<i>Beam timing resolution (a) and neutron beam energy (b) spectra with the phase restricted time tune of the cyclotron as measured by the R.F. phase stabilized timing signals . . . . .</i>	38
3.6	<i>A schematic diagram of the geometric shape and the size of the neutron collimator aperture . . . . .</i>	41
3.7	<i>A schematic representation of the proton polarimeter/proton beam energy monitor . . . . .</i>	44
3.8	<i>A schematic diagram showing the rotation of the solid angle defining counter in relation to the beam offsets . . . . .</i>	45
3.9	<i>Some details of the right arm of the proton polarimeter/proton beam energy monitor . . . . .</i>	47
3.10	<i>IBP trigger . . . . .</i>	49
3.11	<i>Schematic diagram of the SEM assembly . . . . .</i>	50
3.12	<i>Schematic drawing of the neutron profile monitor and polarimeter . . . . .</i>	53
3.13	<i>Schematic diagram of spin precession along the beam line . . . . .</i>	56
3.14	<i>Energy levels of the electron-proton system in presence of a strong magnetic field and re-population of the states by microwave irradiation . . . . .</i>	60
3.15	<i>Schematic diagram of the FST . . . . .</i>	62
3.16	<i>FST holding field strength around the target from the field mapping . . . . .</i>	66
3.17	<i>A detailed view of the detection system . . . . .</i>	68
3.18	<i>The main neutron detection scintillation array . . . . .</i>	74
3.19	<i>Simplified electronics diagram of the proton detection system . . . . .</i>	77
3.20	<i>Simplified electronics diagram of the neutron detection system . . . . .</i>	78
3.21	<i>Simplified electronics diagram of the np coincidence . . . . .</i>	79

4.1	<i>Simulated distributions of the horizontal neutron beam profiles . . .</i>	88
4.2	<i>(a) simulated neutron beam energy distribution; and (b) the correlation of the neutron beam energy and polarization . . . . .</i>	89
4.3	<i>(a) a simulated distribution of the variation of the neutron beam energy profile at the FST location; and (b) a simulated distribution of the variation of the neutron beam polarization profile at the FST location . . . . .</i>	90
4.4	<i>(a) cross-section view of the FST; and (b) recoil proton tracking . .</i>	93
4.5	<i>(a) holding field deflection; (b) energy loss; (c) multiple scattering of recoil protons . . . . .</i>	95
4.6	<i>Simulated kinematical variable distributions (connected) and a comparison to the distributions of data (discrete) . . . . .</i>	96
4.7	<i>The scattering angles at the vertices versus the measured proton momenta and angles . . . . .</i>	98
5.1	<i>Proton beam energy distributions . . . . .</i>	103
5.2	<i>Proton polarization as measured by the CSB polarimeter and the IBP and consistency of the two measurements . . . . .</i>	107
5.3	<i>LD<sub>2</sub> target density fluctuation and the influence on the beam energy and the zero-crossing angle . . . . .</i>	108
5.4	<i>Stability and consistency of the neutron polarimeters . . . . .</i>	111
5.5	<i>Neutron beam profile distributions with a plastic cross or a steel I-beam in the beam . . . . .</i>	114
5.6	<i>Neutron beam profile at the profile monitor location compared to a Monte Carlo simulation . . . . .</i>	115
5.7	<i>SEM asymmetry distributions . . . . .</i>	117
5.8	<i>Hall probe readings showing the stability of the FST holding field .</i>	119

5.9	<i>The difference of the measured horizontal positions of the button events in the front and rear banks of the neutron bars . . . . .</i>	121
5.10	<i>Typical scaled pulse height distributions . . . . .</i>	122
5.11	<i>(a) time difference spectrum of the pulser events in the DLCs; and (b) relative positions of the pulser peaks and the picket fence structure which gave the pulser locations and separations better than the design note specifications . . . . .</i>	124
5.12	<i>Proton track residual distributions . . . . .</i>	128
5.13	<i>Schematic diagram of the proton track deflection in the holding field and the reconstructed proton track and vertices from the measured coordinates . . . . .</i>	129
5.14	<i>Distributions of the reconstructed proton vertices . . . . .</i>	130
5.15	<i>(a) proton polar angle <math>\theta_p</math> distribution and (b) azimuthal angle <math>\phi_p</math> distribution . . . . .</i>	132
5.16	<i>Schematic diagram showing the division of the E-counters into five areas for timing calculations . . . . .</i>	134
5.17	<i>(a) a distribution of the corrected proton kinetic energy and (b) a distribution of the difference between the measured proton kinetic energy and the kinematically expected proton energy from the measured proton angle . . . . .</i>	136
5.18	<i>Time difference spectra of (a) the neutron singles (b) button events and (c) veto overlap events . . . . .</i>	137
5.19	<i>Distributions of polar (a) and azimuthal (b) angles of the scattered neutrons . . . . .</i>	139

5.20	<i>(a) the measured neutron kinetic energy and (b) a distribution of the difference of the measured neutron kinetic energy and the kinematically expected neutron kinetic energy at the measured neutron angle . . . . .</i>	141
5.21	<i>A distribution of the neutron scintillator bar pulse height after pedestal subtraction and renormalization . . . . .</i>	142
5.22	<i>Determination of proton momentum weighted sigmas . . . . .</i>	146
5.23	<i><math>\chi^2_{sum}</math> and <math>\chi^2_i</math> distributions. Arrows indicate the cuts applied . . . .</i>	147
5.24	<i>Distributions of kinematic variables before and after cuts . . . . .</i>	148
5.25	<i>A sample asymmetry distribution of polarized FST data . . . . .</i>	151
5.26	<i>Neutron beam energy distributions (a) a comparison of the measured to the simulated neutron beam energy (b) the correlation of the two neutron beam energy measurements . . . . .</i>	153
5.27	<i>Opening angle (a) and coplanarity angle (b) distributions of the background data . . . . .</i>	157
5.28	<i>Opening angle distribution of the carbon data (bottom) and the FST data (top) for normalizing the tails and estimating the carbon contribution . . . . .</i>	158
6.1	<i>Angular distributions of spin correlation parameters for np elastic scattering at 347 MeV . . . . .</i>	185
7.1	<i>Shape of <math>\Delta A</math> and comparison to the Iqbal and Niskanen's prediction</i>	207
7.2	<i>Summary of current experimental results on CSB in np elastic scattering compared to the theoretical predictions by Iqbal and Niskanen, and Holzenkamp, Holinde and Thomas . . . . .</i>	210
A.1	<i>DLCs in calibration mode . . . . .</i>	221

B.1	<i>Schematic diagram of the rotations and directions of the polarization at various locations . . . . .</i>	226
B.2	<i>Precession curves of the precession magnets . . . . .</i>	227

# List of Tables

3.1	<i>Geometric details of the CSB polarimeter . . . . .</i>	43
3.2	<i>A sample list of the targets on the polarimeter target ladders . . . . .</i>	46
3.3	<i>IBP geometry . . . . .</i>	48
3.4	<i>Spin precession magnet settings . . . . .</i>	59
3.5	<i>FST material in the particle's paths . . . . .</i>	63
3.6	<i>Typical operating parameters of the FST . . . . .</i>	65
3.7	<i>Geometric positions of the proton detection system . . . . .</i>	67
3.8	<i>Dimensions of the proton detectors . . . . .</i>	68
3.9	<i>Geometric positions of the neutron detection system . . . . .</i>	72
3.10	<i>Typical four day cycle run scheme . . . . .</i>	81
5.1	<i>FST position offsets . . . . .</i>	120
5.2	<i>Horizontal pulser positions as determined from the DLC calibrations</i>	125
5.3	<i>Zero-crossing angles of <math>A_n</math> and <math>A_p</math> before the corrections . . . . .</i>	150
5.4	<i>Difference of the zero-crossing angles before the corrections . . . . .</i>	150
5.5	<i>Ratios and analyzing powers of the background contribution . . . . .</i>	155
6.1	<i>Summary of the estimates of the systematic errors in the difference of the analyzing powers from the system parameters . . . . .</i>	197
6.2	<i>Zero-crossing angles of <math>A_n</math> and <math>A_p</math> after the corrections . . . . .</i>	199
6.3	<i>Difference of the zero-crossing angles after the corrections . . . . .</i>	199

6.4	<i>Dependence of the difference in the zero-crossing angles on the neutron bar software threshold . . . . .</i>	201
6.5	<i>Difference of the zero-crossing angles for different angle ranges . .</i>	202
6.6	<i>Summary of the systematic errors in the difference of the zero-crossing angles . . . . .</i>	204
C.1	<i>The analyzing powers, <math>A_p</math> and <math>A_n</math>, at 347 MeV . . . . .</i>	230
D.1	<i>DCR bit map . . . . .</i>	232

# Chapter 1

## Introduction

Symmetries are often used to help reveal the fundamental aspects of nature. Understanding the symmetries or the violation of the symmetries of a system can be a valuable guide to the construction of a theory and the simplifications necessary to make it tractable. In the study of particle and nuclear physics, symmetries are of great importance and are routinely invoked. Some symmetries are well known from classical physics; others are quantum mechanical concepts. In addition, some symmetries appear to hold absolutely, while others are obeyed under certain conditions or “approximately”. Energy, linear momentum, angular momentum and electric charge conservation fall in the former category. Those which hold only “approximately” include parity, charge conjugation and isospin symmetries. Detailed studies of these latter symmetries and their violation can give deep insight into the details of the fundamental interactions at short distances. This may be particularly true in exploring the nucleon-nucleon (NN) interaction and forming the bridge between quantum chromo dynamics (QCD) and the effective NN interaction represented by meson exchange theories.

Compelling evidence of an inter-nucleon force followed Chadwick’s discovery

of the neutron in 1932. It was believed that the “fundamental building blocks” of matter were protons and neutrons. The postulation of a non-Coulombic strong force was required to bind nuclei. Since then, the nucleon-nucleon (NN) force has been extensively studied.

Following the postulation of a nucleon force, it was suggested by Heisenberg that, due to the similarities between protons and neutrons (mass and spin), the forces between protons and protons, neutrons and neutrons, and neutrons and protons should be the same after subtracting the Coulomb force [1,2]. By analogy with spin in ordinary space, the nucleons were suggested to have isotopic spin (or isospin),  $\mathbf{I}$ , oriented up or down in isotopic space (or isospace). The third component of isospin is related to the electric charge. Conventionally it is defined as:

$$\text{proton} \quad \mathbf{I} = 1/2, \quad I_3 = +1/2 \quad (1.1)$$

$$\text{neutron} \quad \mathbf{I} = 1/2, \quad I_3 = -1/2. \quad (1.2)$$

Charge independence (or isospin independence) of the strong interaction states that the  $nn$ ,  $pp$  and  $np$  forces are the same in the same quantum mechanical state except for the electromagnetic interaction; or that the Hamiltonian of the interaction between nucleons commutes with isospin  $\mathbf{I}$ ,

$$[H, \mathbf{I}] = 0, \quad (1.3)$$

where,  $\mathbf{I}=\mathbf{I}(1)+\mathbf{I}(2)$  is the total isospin of a system.

Charge symmetry is a less strict symmetry. It states that, apart from electromagnetic effects, a system of mesons and nucleons behaves exactly as its “charge counterpart”, provided that the particles are in the same space-spin states. In the

nucleon-nucleon system, charge symmetry implies the equality of the  $nn$  and  $pp$  interactions, but this equality is not a sufficient condition for charge symmetry. Charge symmetry also has implications for the  $np$  system [2,3]. Formally, this is an operation of an  $180^\circ$  rotation in isospace about the second axis (or  $y$  axis). The charge symmetry operator of a system can be written as:

$$P_{CS} = e^{i\pi I_2}. \quad (1.4)$$

The interaction of a system which conserves charge symmetry obeys the commutation rule:

$$[H, P_{CS}] = 0. \quad (1.5)$$

The study of isospin symmetry has been pursued both experimentally and theoretically for a long time. Much evidence has been accumulated over the years that charge symmetry holds in general to the order of one percent. It has been extensively studied in several review papers [2,4,5,6] and will be discussed briefly in Chapter 2. Quantum Chromo Dynamics (QCD, the underlying theory of the strong interaction) indicates that each and every violation of isospin symmetry has its origin in the mass difference of the up and down quarks and in the electromagnetic interactions among quarks. Isospin symmetry was the first “internal symmetry” (independent of space and time) that was postulated and examined in elementary particle physics. It is an approximate symmetry because the electromagnetic interaction clearly violates the symmetry. The postulated symmetry is also a prominent example of the existence and usefulness of approximate or “broken” symmetries in physics. It has been generalized to other hadronic systems of mesons and baryons and has been found to hold approximately. This is also the prime example of a symmetry that is peculiar to the strong or hadronic interaction. It is broken by the electromagnetic and weak interactions. In view of its practical and principal importance, it is highly desirable to perform detailed and

accurate tests of the implications of isospin invariance. Such tests should establish not only the degree to which isospin is conserved, but also the behaviour of the symmetry breaking amplitude as a function of kinematical variables.

This thesis reports on a high precision measurement of charge symmetry breaking in  $np$  elastic scattering at 347 MeV [7]. In the  $np$  system, the charge symmetry operation interchanges neutrons and protons, which is equivalent to an exchange of the up-down quarks in the quark description of the NN interaction. It is a two-body system without the Coulomb interaction. The study of charge symmetry breaking in the  $np$  system belongs to a distinct class of isospin symmetry studies (than comparing the  $nn$  and  $pp$  systems). Any indication of CSB in such a system stems from the NN strong interaction and the electromagnetic spin-orbit interaction. Extensive studies of CSB in the  $np$  system will help to clarify details of the NN interaction, in particular its short and intermediate range behaviour, and will also supply demanding benchmarks for meson exchange theories of the NN interaction. It is also possible that some underlying quark effects will be revealed since it is believed that charge symmetry breaking fundamentally arises from the electromagnetic interaction among the quarks and from the up-down quark mass difference [5,6].

In the  $np$  system, charge symmetry leads to the equality of the differential cross-sections for polarized neutrons scattering from unpolarized protons and vice versa. Figure. 1.1 illustrates the physical principle of the experiment, with either the neutron beam or the proton target being polarized, and the relation between charge symmetry and the equality of the differential cross-sections (when  $P_n = P_p$ ) and analyzing powers. Analyzing powers, cross-sections and the yields are related

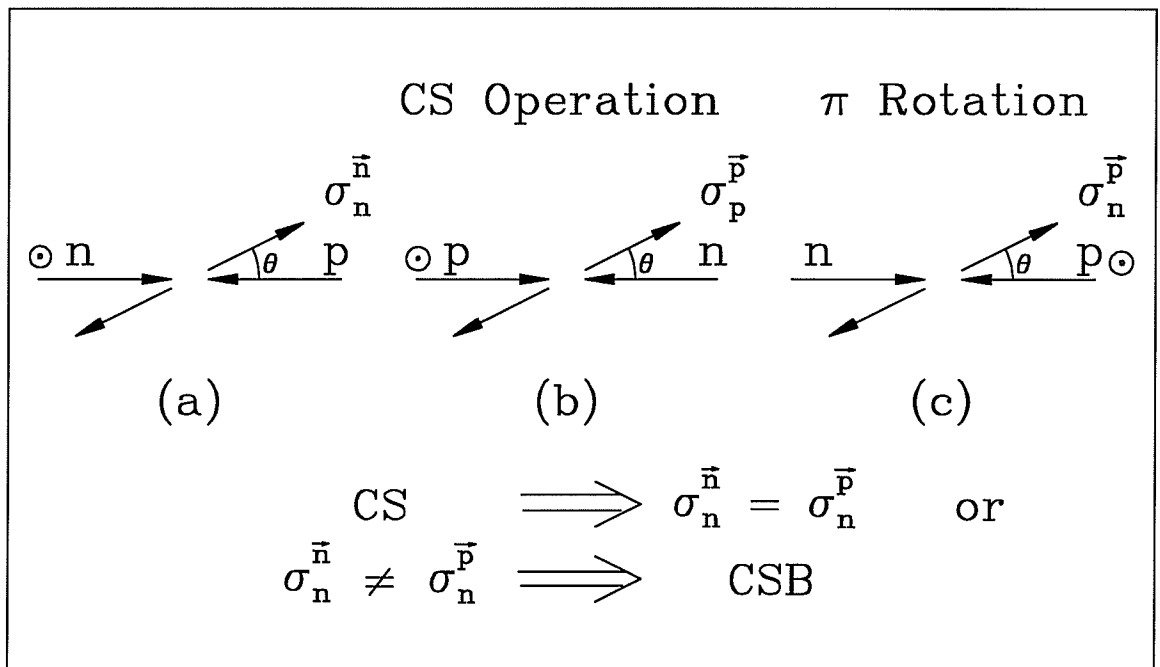


Figure 1.1: *Symmetry operations for np elastic scattering with either neutron or proton polarized, and the relation between charge symmetry and the equality of the differential cross-sections (when  $P_n = P_p$ ).*

as follows:

$$A = \frac{\sigma^+ - \sigma^-}{\sigma^+ + \sigma^-}, \quad (P = 1), \quad (1.6)$$

$$\sigma^\pm = \sigma_o(1 \pm PA), \quad (1.7)$$

$$N^\pm \propto I \cdot \sigma^\pm \cdot d\Omega, \quad (1.8)$$

where superscripts “ $\pm$ ” denote the spin polarization direction (up/down),  $\sigma_o$  is the differential cross-section involving unpolarized nucleons,  $P$  is polarization,  $I$  is the intensity of a beam,  $N$  is the number of observed scattering events, and  $d\Omega$  is the solid angle within which particles are detected. In the experiment, particles were detected on both the left and right sides of the beam. Left-right asymmetries and analyzing powers can be obtained from:

$$\epsilon = \frac{N_L^+ - N_R^+}{N_L^+ + N_R^+}, \quad (1.9)$$

$$A = \frac{1}{P} \cdot \epsilon, \quad (1.10)$$

and similarly for the other spin direction. Any difference in the analyzing powers,

$$\Delta A \equiv A_n - A_p, \quad (1.11)$$

will signify the breaking of charge symmetry. The magnitude of  $\Delta A$  is expected to be small, on the order of a percent. Therefore, control of systematic errors is critical to such a measurement. Designed as a null experiment to control systematic errors, the difference of the analyzing powers was measured at the zero-crossing angle, the angle at which the average of the analyzing powers vanishes. This can be understood with the following expressions:

$$\epsilon_n = P_n \cdot A_n = P_n \cdot (\langle A \rangle + \frac{1}{2}\Delta A), \quad (1.12)$$

$$\epsilon_p = P_p \cdot A_p = P_p \cdot (\langle A \rangle - \frac{1}{2}\Delta A), \quad (1.13)$$

$$\Delta\epsilon \equiv \epsilon_n - \epsilon_p = \Delta P \cdot \langle A \rangle + \langle P \rangle \cdot \Delta A, \quad (1.14)$$

$$\langle A \rangle \equiv \frac{1}{2}(A_n + A_p), \quad (1.15)$$

$$\langle P \rangle \equiv \frac{1}{2}(P_n + P_p), \quad (1.16)$$

$$\Delta P \equiv P_n - P_p, \quad (1.17)$$

where  $\epsilon$  is scattering asymmetry, subscripts denote polarized nucleons,  $\Delta\epsilon$  is the difference of the scattering asymmetries with either neutron or proton polarized,  $\langle A \rangle$  and  $\Delta A$  are the average and difference of the analyzing powers,  $\langle P \rangle$  and  $\Delta P$  are the average and the difference of the polarizations. To measure  $\Delta A$  to the accuracy of  $10^{-4}$ , the polarization needs to be known to the same level, which is unattainable at present. However, at the zero-crossing angle, where  $\langle A \rangle = 0$ , the difference of the asymmetries and the difference of the analyzing power has the following simple relation:

$$\Delta\epsilon = \langle P \rangle \cdot \Delta A. \quad (1.18)$$

Rather than measuring  $\Delta A$  directly at the zero-crossing angle, the difference of the zero-crossing angles, where the respective analyzing powers cross zero,

$$\Delta\theta_o \equiv \theta(A_n = 0) - \theta(A_p = 0), \quad (1.19)$$

is measured. The two measurements, with either the neutron beam polarized or the proton target polarized, were interleaved and performed with the same detector systems and identical beam and target properties (except polarization). The difference of the zero-crossing angles,  $\Delta\theta_o$ , is related to the difference of  $\Delta A$  by

$$\Delta A = -(dA/d\theta) \cdot \Delta\theta_o. \quad (1.20)$$

Figure. 1.2 illustrates the method of deducing  $\Delta A$  from the measured difference of the zero-crossing angles of the analyzing powers.

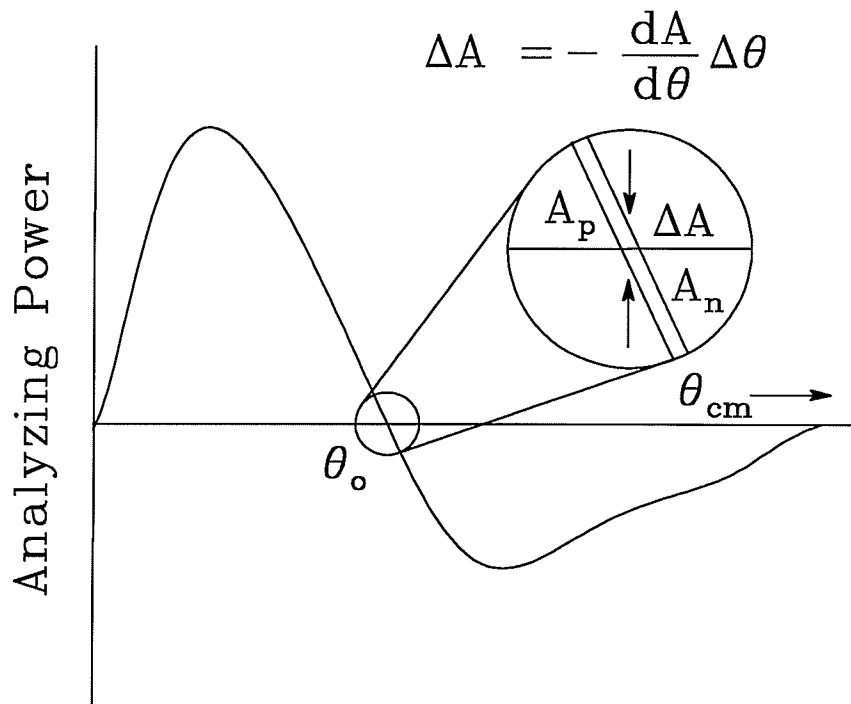


Figure 1.2: An illustration of the method employed to extract  $\Delta A \equiv A_n - A_p$  from the difference,  $\Delta\theta_o$ , in the  $A_n$  and  $A_p$  zero-crossing angles for  $np$  elastic scattering.  $dA/d\theta$  is from phase-shift analyses or determined experimentally;  $\Delta\theta_o$  is measured in the experiment.

The experiment was designed to measure the difference of the analyzing powers,  $\Delta A$ , in  $np$  elastic scattering at an incident neutron beam energy of 347 MeV. The experimental goal [7] was to achieve a statistical accuracy in  $\Delta A$  of  $8 \times 10^{-4}$  and a systematic uncertainty similar to or better than obtained in the previous experiment at 477 MeV [8], which gave a result of  $\Delta A = (47 \pm 22 \pm 8) \times 10^{-4}$ . After the original proposal was submitted, the optically pumped polarized ion source (OPPIS) was developed. In line with the prediction of the OPPIS performance, more ambitious experimental goals were set of measuring  $\Delta A$  to an accuracy of  $5 \times 10^{-4}$  and of extracting the shape of the angular distribution of  $\Delta A$  [9]. Theoretical predictions based on meson exchange theory (which will be discussed in detail in Chapter 2) give a typical value of the difference in the analyzing powers at the zero-crossing angle at 347 MeV of  $5 \times 10^{-3}$ .

The notation of  $\Delta A$ ,  $\langle A \rangle$ ,  $\Delta P$ ,  $\langle P \rangle$  and  $\Delta\theta_o$  as defined here will be used throughout.

This thesis is organized as follows: Chapter 2 will give a theoretical and experimental overview of the study of isospin symmetry; Chapter 3 will discuss the experimental apparatus and electronics used for this experiment; Chapter 4 will describe Monte Carlo simulations of various aspects of the experiment; Chapter 5 will describe details of the data analysis; estimates of the systematic errors and various tests of the systematic errors will be presented in Chapter 6; and the results of the experiment, along with a discussion of these findings will be presented in Chapter 7. A discussion of the calibration of the delay line chambers and the spin precession magnets used in this experiment, and a summary of the online event structure will be found in the appendices.

# Chapter 2

## Overview

Careful tests of the validity of isospin symmetry have been made starting in the 1950s and have been carried on since then. Much evidence has been accumulated in favor of the violation of charge symmetry and charge independence on the order of a percent. Experimental investigations have been extended from the early observations of the low energy nucleon-nucleon singlet scattering length differences and the binding energy differences of mirror nuclei, to studies of spin observables in medium energy  $np$  elastic scattering and other subatomic systems (i.e., systems involving pions and other mesons, hypernuclei, or involving photon and deuteron beams). The amount and quality of data accumulated from charge symmetry breaking studies over the last 25 years is very impressive. Theoretical interpretations and predictions of the observed isospin symmetry breaking effects have been progressing as the experimental evidence accumulates. However, it was not until recently that the understanding of the fundamental cause of this symmetry breaking in terms of quantum chromo dynamics (QCD) and meson exchange theories of the nucleon-nucleon (NN) interaction was achieved. Some selected experimental and theoretical studies are briefly discussed in the following sections, focusing on  $np$  elastic scattering experiments and theoretical interpretations.

## 2.1 Early Evidence of Isospin Symmetry Violation and Current Status

### 2.1.1 The low energy nucleon-nucleon $^1S_0$ scattering length and effective range

Early evidence of charge independence breaking and charge symmetry breaking in the nucleon-nucleon (NN) interaction, after subtracting electromagnetic contributions, is seen in the difference of the low energy NN scattering lengths,  $a_{pp}$ ,  $a_{nn}$  and  $a_{np}$ , and the effective ranges,  $r_{pp}$ ,  $r_{nn}$  and  $r_{np}$ . Over the years, experimental accuracy has been improved and the uncertainties in these scattering parameters have decreased [5,6,10]:

$$a_{nn}^N = -18.8 \pm 0.3 \text{ fm}, \quad r_{nn}^N = 2.75 \pm 0.11 \text{ fm}, \quad (2.1)$$

$$a_{pp}^N = -17.3 \pm 0.4 \text{ fm}, \quad r_{pp}^N = 2.85 \pm 0.04 \text{ fm}, \quad (2.2)$$

$$a_{np}^N = -23.748 \pm 0.009 \text{ fm}, \quad r_{np}^N = 2.75 \pm 0.05 \text{ fm}. \quad (2.3)$$

Here, the superscript ‘N’ denotes that the electromagnetic effect has been subtracted. Comparing the nuclear strong interaction part of the  $^1S_0$  scattering lengths  $a_{nn}^N$ ,  $a_{pp}^N$  and  $a_{np}^N$ , a charge dependence occurs in the difference,

$$\frac{1}{2}(a_{nn}^N + a_{pp}^N) - a_{np}^N = 5.7 \pm 0.3 \text{ fm}. \quad (2.4)$$

This difference can be explained as arising mainly from one-pion exchange, namely due to the mass difference of the neutral and charged pions. If  $a_{nn}^N$  and  $a_{pp}^N$  are compared, charge symmetry breaking can be realized from the fact that the  $nn$  interaction appears to be slightly more attractive than the  $pp$  interaction. However, this difference ( $-1.5 \pm 0.5$  fm, the CSB effect) is much smaller than the charge

independence breaking effect. It has been shown [11,12], with meson-exchange-based theory, that  $\rho^0 - \omega$  mixing plays a dominant role in this difference. However, the corrections for the electromagnetic effects have non-negligible theoretical uncertainties, with off-shell ambiguities in the Coulomb corrections being the worst problem. Here, the main concern of CSB is the strong interaction part of the NN interaction. In removing the direct electromagnetic effect from the  $pp$  interaction, model dependence has to be introduced, since the NN interaction at small separations and the  $pp$  off-energy-shell interaction are not adequately known. Because of the lack of neutron targets, accurate knowledge of the  $nn$  scattering parameters ( $a_{nn}$  and  $r_{nn}$ ) is obtained from the  $D(\pi^-, \gamma)2n$  reaction, a three-body reaction with only two strongly interacting particles (two neutrons) in the final state. The NN scattering parameters can also be determined with the deuteron breakup reactions  $nd \rightarrow nnp$  and  $pd \rightarrow ppn$ . The various nucleon-nucleon final state interactions, three-body nuclear forces and the Coulomb interaction (in the case of  $pd \rightarrow ppn$ ), dominate the uncertainties of the scattering parameters extracted from nucleon-induced deuteron breakup.

A new measurement of the  $nn$  scattering parameters is currently underway at TRIUMF [13]. This experiment uses the  $D(\pi^-, \gamma)2n$  reaction in triple-coincidence mode and aims to achieve an accuracy of 0.2 - 0.3 fm in the scattering length,  $a_{nn}$ . The parameter  $r_{nn}$  will also be determined from the experiment. Detailed studies of CSB in the scattering length difference will provide information on the interesting  $\rho^0 - \omega$  mixing contribution.

## 2.1.2 Binding Energy Differences of Mirror Nuclei - Okamoto-Nolen-Schiffer Anomaly

Charge symmetry breaking has been observed in the binding energy differences of mirror nuclei, the well-known Okamoto-Nolen-Schiffer effect [14,15]. The observed  ${}^3H - {}^3He$  (the lightest mirror nuclei) binding energy difference is 764 keV. After correcting for direct electromagnetic contributions,  $71 \pm 19 \pm 5$  keV of this effect remains [11]. The first error is due to the error envelope of the measured form factors and the second is an estimate of the shortcomings of the model-independent procedure applied. This residue in binding energy difference can only be explained by CSB nuclear forces. It is also consistent with the strong interaction part of the  $nn$  interaction being slightly more attractive than the  $pp$  interaction. It has been demonstrated that the same origin as in the scattering lengths difference, i.e.,  $\rho^0 - \omega$  mixing, dominates [11,12]. For heavier nuclei, the  $\rho^0 - \omega$  mixing accounts for more than 70% of the binding energy differences of mirror nuclei [12,6], after correcting for electromagnetic effects. Other contributions including the effects of the medium modifications of the nucleon masses [16] are responsible for the rest of the differences. However, the complications of the nuclear many-body problem lead to non-negligible uncertainties and make it very difficult to interpret the Okamoto-Nolen-Schiffer effect in terms of CSB components of the NN interaction (with the exception of  ${}^3H - {}^3He$ ).

Various models with quark degrees of freedom have been tried in the study of charge symmetry breaking effects. So far, most calculations are model dependent and are sometimes in contradiction with each other. It is believed that the quark mass difference is responsible for the nuclear interaction part of the charge symmetry breaking effects in the binding energy differences and the scattering length

difference. This is consistent with the dominance of the  $\rho^0 - \omega$  mixing in these CSB effects, since the  $\rho^0 - \omega$  mixing has its origin in the up-down quark mass difference [5,6,17].

## 2.2 Charge Symmetry Breaking in $np$ Elastic Scattering

### 2.2.1 Experimental Aspects

The use of spin observables in  $np$  elastic scattering to examine CSB was suggested long ago. Wolfenstein [18] remarked that isospin conservation implies the equality of the polarization of protons scattered at an angle  $\theta$  with that of neutrons scattered at an angle of  $\pi - \theta$  in the center-of-mass (c.m.) when unpolarized protons are scattered from unpolarized neutrons. This equality can be understood from the equivalence of neutrons and protons under the strong interaction, if charge symmetry holds. Accurate measurements of the polarization are very difficult since measuring the polarization of the scattered neutrons and recoil protons requires second scatterings, so a precise comparison is not feasible. However, the analyzing powers of polarized neutrons  $A_n$  and that of polarized protons  $A_p$  have been compared (as will be discussed in detail later in the text). It is to be noted that the effects are expected to be small, of the order of the fine structure constant. This makes such a class of experiments extremely difficult. Large data sets are required to achieve good statistical accuracy, and very good systematic error control is needed.

Experimental investigations of charge symmetry breaking in the  $np$  system

became possible in the 1980s when both intense polarized neutron beams and polarized proton targets with a large hydrogen content became available. Measurements of many spin parameters requiring both polarized neutron beams and polarized proton targets could then be executed at the same time in order to control systematic errors.

The first of this type of experiments, searching for charge symmetry breaking in  $np$  elastic scattering, was carried out at TRIUMF at 477 MeV [19,8]. Proton and neutron analyzing powers ( $A_p$  and  $A_n$ , respectively) were compared at the zero-crossing angle where the average of  $A_n$  and  $A_p$  goes through zero. Any non-zero difference of  $\Delta A \equiv A_n - A_p$  would indicate violation of charge symmetry. The experiment yielded a result of  $\Delta A = [47 \pm 22 \pm 8] \times 10^{-4}$  over an angular range of  $59^\circ - 80^\circ$  in the center-of-mass system. The result is a little over two standard deviations from zero. This demonstrated a CSB effect caused by non-electromagnetic terms of the class IV force (see the Section 2.2.2). In particular, the CSB term corresponding to the  $np$  mass difference affecting the one-pion-exchange was clearly observed.

A similar experiment was carried out at the Indiana University Cyclotron Facility (IUCF) in  $np$  elastic scattering at 183 MeV [20,21]. Data were taken with beam and target polarized simultaneously, and spin observables were extracted. The result reported is  $\Delta A \equiv A_n - A_p = [34.8 \pm 6.2 \pm 4.1] \times 10^{-4}$  [22] averaged over an angular range in the center-of-mass system from  $82.2^\circ$  to  $116.1^\circ$ , over which the average of the analyzing powers,  $\langle A \rangle$ , averages to zero. This latter result differs from zero by 4.5 standard deviations and differs from the value expected from the electromagnetic spin-orbit interaction alone by 3.4 standard deviations.

It represented the strongest experimental evidence of charge symmetry breaking in  $np$  elastic scattering and the most clearcut observation of a class IV CSB strong interaction term. At the IUCF energy of 183 MeV, the  $\rho^0 - \omega$  mixing contribution to  $\Delta A$  was clearly observed (an approximately two standard deviation effect).

The extraction of the angular distribution of  $\Delta A$  is very difficult. This can be seen from the following expression:

$$\epsilon_n - \epsilon_p = \langle A(\theta) \rangle \Delta P + \Delta A(\theta) \langle P \rangle. \quad (2.5)$$

To obtain  $\Delta A(\theta)$  at the  $10^{-4}$  level, the polarizations would need to be known to a level not attainable at present. The best one can determine is

$$“\Delta A(\theta)_{expt}” = \Delta A(\theta)_{true} + c \cdot A(\theta). \quad (2.6)$$

Here  $c$  is directly related to the uncertainty of  $\Delta P / \langle P \rangle$ . The IUCF experiment extracted the component of  $\Delta A(\theta)$  which is “uncorrelated” with  $A(\theta)$  by adjusting  $c$  until the variance ( $\langle “\Delta A”^2 \rangle - \langle “\Delta A” \rangle^2$ ) of the “ $\Delta A(\theta)$ ” data set reached a minimum. A 12-point angular distribution of “ $\Delta A$ ” was obtained from the experiment within limitations imposed by uncertainties in the measured beam and target polarizations. At the TRIUMF experimental energies (477 MeV and 347 MeV), the angular distribution of  $\Delta A(\theta)$  near the zero-crossing angle of the analyzing powers has a shape similar to the analyzing power,  $A(\theta)$ , itself. Therefore, the minimum variance method used by the IUCF experiment can not be applied. In principle, if the theoretical prediction of the zero-crossing angle of  $\Delta A$  were very accurate and if the asymmetries at that angle could be measured very accurately, then  $\Delta P / \langle P \rangle$  could be determined and the angular distribution of  $\Delta A$  could be extracted. Alternatively, a comparison of the shape of  $\Delta A$  with theoretical predictions can be made by adjusting the constant  $c$  until the chi-square between

the measurement and the calculation is minimized (this will be discussed in detail in Chapter 5).

The earlier experimental results are in excellent agreement with theoretical predictions [23,24,25,26,27,28] (details are discussed in the next section) which included contributions from: (1) the neutron magnetic moment interacting with the proton current in one photon exchange; (2) the neutron and proton mass difference affecting one pion exchange; (3) the interesting  $\rho^0 - \omega$  mixing calculated with on-shell mixing amplitudes; and (4) other smaller contributions from two-pion exchange, the  $np$  mass difference affecting  $\rho$  exchange and indirect quark effects. Using complex phase shift amplitudes, it has been shown that inelasticity changes  $\Delta A$  by 10% at 800 MeV, but becomes vanishingly small at lower energies (i.e., 477 MeV or below) [29]. These results show that the meson-exchange NN potential models are effective and should provide satisfactory predictions. It has been noted that on-shell mixing amplitudes are needed to evaluate  $\rho^0 - \omega$  mixing in order to achieve agreement between the theoretical predictions and the IUCF experimental results ( see the next section for details).

## 2.2.2 Theoretical Aspects

Although it has been argued that charge symmetry breaking fundamentally arises from quark degrees of freedom (the up and down quark mass difference and the electromagnetic interactions among quarks), it has also been shown that the meson-exchange theory is an effective theory of the NN interaction in practical studies. Most quantitative calculations of the NN interaction to date are based on the meson exchange theory. This is not contradictory to the argument that quark degrees of freedom are the underlying source of charge symmetry break-

ing, because applications of Quantum Chromo Dynamics (QCD) in the low energy, non-perturbative regime relevant to nuclear physics are expected to yield the meson-exchange picture [30]. The meson-exchange-based theory gives satisfactory predictions of the experimental observations of CSB in  $np$  elastic scattering. However, there are serious questions regarding the use of on-mass-shell mixing amplitudes to evaluate virtual meson mixing processes. Some important issues concerning off-mass-shell behaviour have been raised [31]. Furthermore, recent evaluations of the  $\rho^0 - \omega$  mixing parameter from QCD have raised some fundamental questions about the conventional calculations using on-shell mixing amplitudes, and the earlier excellent agreement between theoretical predictions and experimental measurements needs re-examination. This will be further discussed below.

NN potentials have been classified by Henley and Miller [4] into four classes according to their transformation properties under isospin symmetry operations.

Class (I) are isoscalar potentials, symmetric under isospin operations. They are charge independent and can be written in the form:

$$V_I = a + b\vec{I}(i) \cdot \vec{I}(j). \quad (2.7)$$

These are the dominant parts of the NN interaction and provide isospin symmetry.

Class (II) are isotensor potentials which maintain charge symmetry but break charge independence. Such potentials can be written as:

$$V_{II} = c[I_3(i)I_3(j) - \frac{1}{3}\vec{I}(i) \cdot \vec{I}(j)]. \quad (2.8)$$

Class (III) are those potentials which break both charge independence and charge symmetry, but which are symmetric under the interchange of particles ( $1 \leftrightarrow 2$ ) in isospin space.

$$V_{III} = d[I_3(i) + I_3(j)]. \quad (2.9)$$

A class (III) potential differentiates between the  $nn$  and  $pp$  system. However, it does not give rise to isospin mixing in a two-body system, since it conserves the total isospin:

$$[V_{III}, I^2] \propto [I_3, I^2] = 0. \quad (2.10)$$

Therefore, it has no effect on the  $np$  system.

Class (IV) potentials also break both charge symmetry and charge independence, but they cause mixing of isospin. These potentials are proportional to

$$V_{IV} = e[I_3(i) - I_3(j)] + f[\vec{I}(i) \times \vec{I}(j)]_3. \quad (2.11)$$

In a two-body system, these potentials cause the mixing of  $^1L_j$  and  $^3L_j$  states (e.g.,  $^1P_1$ - $^3P_1$ ,  $^1D_2$ - $^3D_2$ ,  $^1F_3$ - $^3F_3$  ...). They will only affect the  $np$  system and have no effect on the  $pp$  or  $nn$  systems.

Here, the variables  $a$ ,  $b$ ,  $c$ ,  $d$ ,  $e$  and  $f$  are space and spin scalar operators and  $i$ ,  $j$  are the labels of the two nucleons. Both class (III) and class (IV) are isovector potentials.

The experiment reported on in this thesis is sensitive to class (IV) potentials. The CSB effect causing the scattering length difference is due to class III potentials. Therefore these two types of CSB experiments test different aspects of the NN interaction and complement each other. However, CSB studies in the  $np$  system

are considered to be superior since it is a two-body system without the Coulomb interaction. After taking consideration of the time reversal invariance of the class IV potentials expressed above, the potentials can be written in the form:

$$V_{IV} = [I_3(1) - I_3(2)][\vec{\sigma}(1) - \vec{\sigma}(2)] \cdot \vec{L}v(r) + [\vec{I}(1) \times \vec{I}(2)]_3[\vec{\sigma}(1) \times \vec{\sigma}(2)] \cdot \vec{L}w(r). \quad (2.12)$$

Here  $\sigma$  denotes the Pauli spin matrices for nucleons,  $\vec{L}$  is angular momentum,  $w(r)$  and  $v(r)$  are scalar operators independent of spin and isospin.

Lorentz invariance, parity conservation, time reversal symmetry and charge independence reduce the 16 possible nucleon-nucleon scattering amplitudes to 5 linearly independent ones for each value of the isospin. Furthermore, the generalized Pauli principle, i.e., the requirement that the two-nucleon wave function be antisymmetric with respect to the interchange of the two nucleons, imposes the condition:

$$(-1)^{L+S+I} = -1, \quad (2.13)$$

where  $L$  is the total angular momentum,  $S$  is the total spin, and  $I$  is the total isospin. If the parity and isospin quantum numbers are conserved, then the generalized Pauli principle leads to the consequence that total spin is also conserved, and spin singlet-triplet transitions are forbidden. For systems of identical particles, in the state of  $I = 1$ , total spin is always conserved. If parity is conserved and isospin is violated, the Pauli principle requires that the total spin of the  $np$  system not be conserved and accordingly, that spin singlet-triplet transitions are allowed. The number of linearly independent scattering amplitudes for the  $np$  system will then increase from 5 to 6. The scattering matrix can be written as [32,33]:

$$M(\vec{k}_i, \vec{k}_f) = \frac{1}{2}[(a+b) + (a-b)(\vec{\sigma}_1 \cdot \hat{n})(\vec{\sigma}_2 \cdot \hat{n}) + (c-d)(\vec{\sigma}_1 \cdot \hat{l})(\vec{\sigma}_2 \cdot \hat{l}) + (c+d)(\vec{\sigma}_1 \cdot \hat{m})(\vec{\sigma}_2 \cdot \hat{m}) + e(\vec{\sigma}_1 + \vec{\sigma}_2) \cdot \hat{n} + f(\vec{\sigma}_1 - \vec{\sigma}_2) \cdot \hat{n}] \quad (2.14)$$

where  $a, b, c, d, e$  and  $f$  are complex amplitudes which are energy and angle dependent, the unit vectors  $\hat{l}, \hat{m}$  and  $\hat{n}$  are:

$$\hat{l} = \frac{\vec{k}_f + \vec{k}_i}{|\vec{k}_f + \vec{k}_i|}, \quad \hat{m} = \frac{\vec{k}_f - \vec{k}_i}{|\vec{k}_f - \vec{k}_i|}, \quad \hat{n} = \frac{\vec{k}_i \times \vec{k}_f}{|\vec{k}_i \times \vec{k}_f|}, \quad (2.15)$$

$\vec{k}_i$  and  $\vec{k}_f$  are momentum vectors of the incident and scattered neutron, and  $\vec{\sigma}_1$  and  $\vec{\sigma}_2$  are Pauli spin matrices of the neutron and proton. The sixth amplitude,  $f$ , which is responsible for CSB can be expressed as [34]:

$$f(\theta) = -\frac{i}{2k} \sum_{j=1}^{\infty} (2J+1) \sin 2\bar{\gamma}_J \exp(i\bar{\delta}_J + i\bar{\delta}_{JJ}) d_{10}^J(\theta), \quad (2.16)$$

where  $\bar{\gamma}_J$  is the mixing angle corresponding to spin singlet-triplet transitions,  $\bar{\delta}_J$  and  $\bar{\delta}_{JJ}$  are the singlet and uncoupled triplet bar phase shifts, respectively, and  $d_{10}^J$  are Wigner functions. The mixing angle,  $\bar{\gamma}_J$  can be expressed as:

$$\bar{\gamma}_J = -2E_T k \sqrt{J(J+1)} \int_0^{\infty} dr r^2 R_J(r) g(r) R_{JJ}(r), \quad (2.17)$$

where  $E_T$  is the total c.m. energy and  $g(r)$  is  $v(r)$  or  $(-1)^J w(r)$  of Eq. (2.12).  $R_J(r)$  and  $R_{JJ}(r)$  are distorted (by strong interaction) wave functions and can be normalized asymptotically:

$$R(r) \xrightarrow{r \rightarrow \infty} \sin(kr - \frac{1}{2}J\pi + \bar{\delta})/kr \quad (2.18)$$

where  $\bar{\delta}$  is  $\bar{\delta}_J$  or  $\bar{\delta}_{JJ}$  for  $R_J(r)$  and  $R_{JJ}(r)$ , respectively. Since the short range part of the strong interaction is not well-known, different potential models have to be used to calculate the distorted wave functions.

There are two experimentally accessible observables to measure charge symmetry breaking effects (for a complete list of charge symmetry breaking parameters, see Ref. [33]). The difference between the analyzing powers  $A_n$  and  $A_p$  for  $np$  elastic scattering is proportional to the isospin mixing amplitude  $f(\theta)$  and can be expressed as:

$$\Delta A(\theta) \equiv A_n(\theta) - A_p(\theta) = \frac{2}{\sigma_0} \text{Re}(b^* f) \quad (2.19)$$

The other possibility is to measure the difference in the spin correlation parameters  $C_{xz}$  and  $C_{zx}$ . This difference can be written as:

$$\Delta C(\theta) \equiv C_{xz}(\theta) - C_{zx}(\theta) = \frac{2}{\sigma_0} \text{Im}(c^* f). \quad (2.20)$$

The TRIUMF and IUCF experiments measured the difference of the analyzing powers. Due to the intrinsic difficulties of excluding unwanted polarization components in both the incident beam and the target, a measurement of the difference in  $C_{zx}$  and  $C_{xz}$  has not yet been attempted.

There are many sources of CSB contributions to  $\Delta A$ . It is argued that at the quark level, all CSB contributions are due to the up and down quark mass difference and to the electromagnetic interactions among the quarks. In recent years, various attempts have been made to use quark degrees of freedom, as described by the fundamental theory of the strong interaction (QCD), to evaluate the CSB effects. These calculations are still qualitative and very model dependent. At low and intermediate energies, meson exchange NN potential models are applied and more reliable predictions are provided. Calculations show that the primary contributions are due to:

(a) One-photon exchange (Fig. 2.1 (a)). The electromagnetic interaction between the proton charge current and the neutron magnetic moment generates a class IV

force of type  $v(r)$  (Eq. 2.12).

(b) One-pion exchange (Fig. 2.1 (b)). The  $np$  mass difference in charged one  $\pi$ -exchange generates a class IV potential of type  $w(r)$  (Eq. 2.12). This term has major contributions to the result of the TRIUMF experiments.

(c) Meson mixing. A class IV force of type  $v(r)$  arises from the electromagnetic mixing of the neutral vector mesons  $\rho^0 - \omega$  (having similar masses:  $m_{\rho} = 768.1$  MeV and  $m_{\omega} = 781.95$  MeV) during their propagation (Fig. 2.1 (c)). This contribution is interesting because of its short range nature. It is believed that the up-down quark mass difference has crucial contributions to  $\rho^0 - \omega$  mixing [5,17]. This term usually gives little contribution to  $\Delta A$  near the zero-crossing angle of  $\langle A(\theta) \rangle$  except at the IUCF experimental energy, where it accounts for about 40% of  $\Delta A$  at the zero-crossing angle.  $\pi - \eta$  mixing generates a class III interaction and therefore does not contribute to  $\Delta A$  [35], assuming one boson exchange.

(d) Other smaller effects. Like the pion exchange, the  $np$  mass difference affecting charged  $\rho$  exchange gives rise to a class IV force of type  $w(r)$ , but its effect is much smaller than one-pion-exchange effects. Other processes including  $2\pi$ -exchange,  $\sigma$  meson exchange and small indirect quark effects have been calculated and shown to be small. Contributions due to the  $\gamma - \pi$  mixing have not been calculated, but are assumed to be small [5].

In Fig. 2.2(a), various predictions based on meson exchange NN potential models for  $\Delta A$  at 347 MeV, by Iqbal and Niskanen (IN [23,24]), Williams, Thomas and Miller (WTM [25,26]), Holzenkamp, Holinde and Thomas (HHT [27]) and Ge

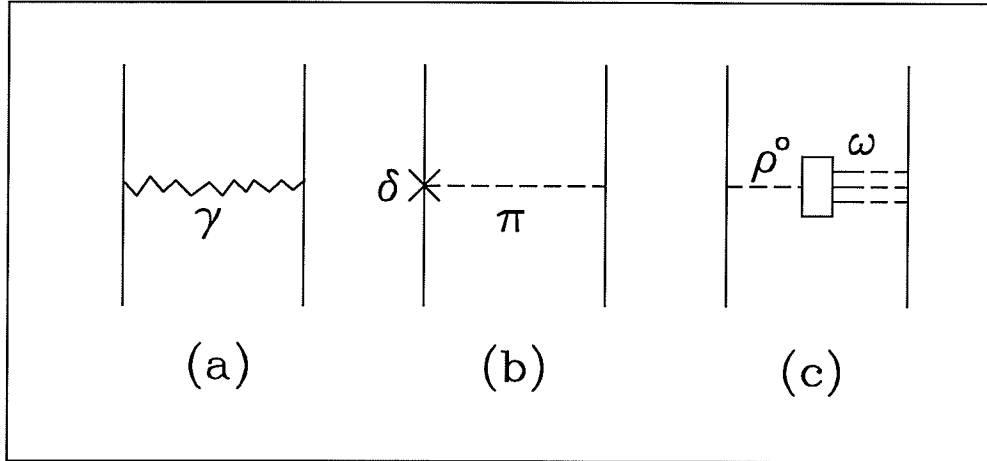


Figure 2.1: *Charge symmetry breaking mechanism in np elastic scattering.*

and Svenne (GS [28]), are compared. Figure 2.2(b) shows the different meson exchange contributions to  $\Delta A$  as calculated by Iqbal and Niskanen [24]. The electromagnetic term accounts for much of the WTM - GS difference. The WTM-HHT difference is due to the treatment of the  $\rho$  and  $\rho^0 - \omega$  terms. CSB experiments sensitive to the region away from the zero-crossing angle can possibly distinguish these latter terms, but even measurements at the zero-crossing angle provide useful tests of the meson exchange picture of the NN interaction at short distances. A relativistic treatment was employed in the IN calculation. The one-boson-exchange model has provided quantitatively satisfactory calculations of CSB in the NN interaction. These calculations, in general, gave very good agreement with the previous CSB experiments. In particular, the interesting  $\rho^0 - \omega$  mixing has to be included in the calculation to interpret the IUCF experimental result (approximately a two standard deviation effect).

However, the theoretical argument is far from settled. Concerns [31] have been raised regarding the application of the on-shell meson mixing amplitude to the off-shell virtual process such as the  $\rho^0 - \omega$  mixing. The exchanged vector

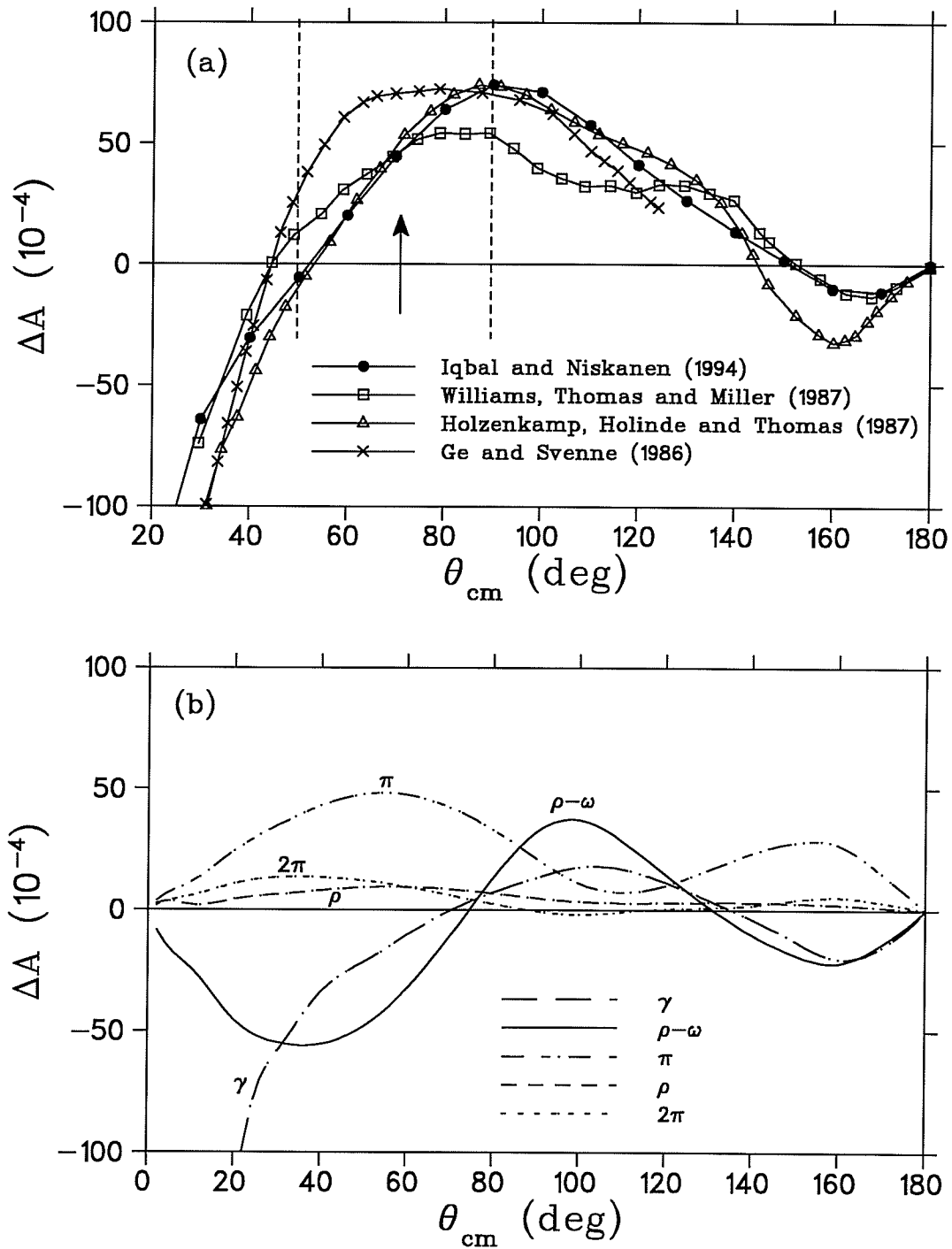


Figure 2.2: (a) Various predictions for  $\Delta A$  at 347 MeV are compared; the dash lines show the angular range covered by this experiment and the arrow shows where the zero-crossing angle is; (b) the different contributions to  $\Delta A$  as predicted by Iqbal and Niskanen.

meson has a space-like momentum, far from the on-shell point. In all the previous calculations, it was customary to assume that the  $\rho^0 - \omega$  mixing amplitude was a constant over this range of four-momentum. The on-mass-shell vector meson  $\rho^0 - \omega$  mixing was observed in the cross-section measurement of the reaction  $e^+e^- \rightarrow \pi^+\pi^-$  [36]. The strong interaction contribution to the mixing amplitude is  $\langle \rho^0 | H_{str} | \omega \rangle = -(5130 \pm 600) \text{ MeV}^2$  (on-mass-shell) [37]. It has been shown with a simple model (Fig. 2.3) that the mixing amplitude had a node near  $q^2 = 0$  so that neither the sign nor the magnitude in the space-like region was determined by the on-shell value [31]. Recently, some calculations [37,38,39,40,41,42,43] have been published which revealed a node at or near  $q^2 = 0$ , with a consequent change in the sign of the mixing amplitude. This off-shell effect will cause the  $\rho^0 - \omega$  mixing contribution to the CSB effect to vanish or at least to become significantly smaller than what was obtained from calculations using the on-shell mixing amplitude. These results have a serious impact on previous theoretical predictions of CSB with on-shell mixing amplitudes, and question the validity of the good agreement with the experimental data. On the other hand, it has been argued [6] that current experimental results support the previous calculations with on-shell mixing amplitudes and that various calculations of off-shell effects have imperfections and need support from experimental results. There is still much controversy and more theoretical as well as experimental investigations are required to settle the issue.

## 2.3 Other Isospin Symmetry Studies

Charge symmetry requires that the  $np \rightarrow d\pi^0$  cross-section be symmetric about  $90^\circ$  in the center-of-mass (Fig. 2.4). Theoretical calculations have shown that a non-zero (up to -0.7% at  $0^\circ$ ) forward-backward asymmetry could arise from

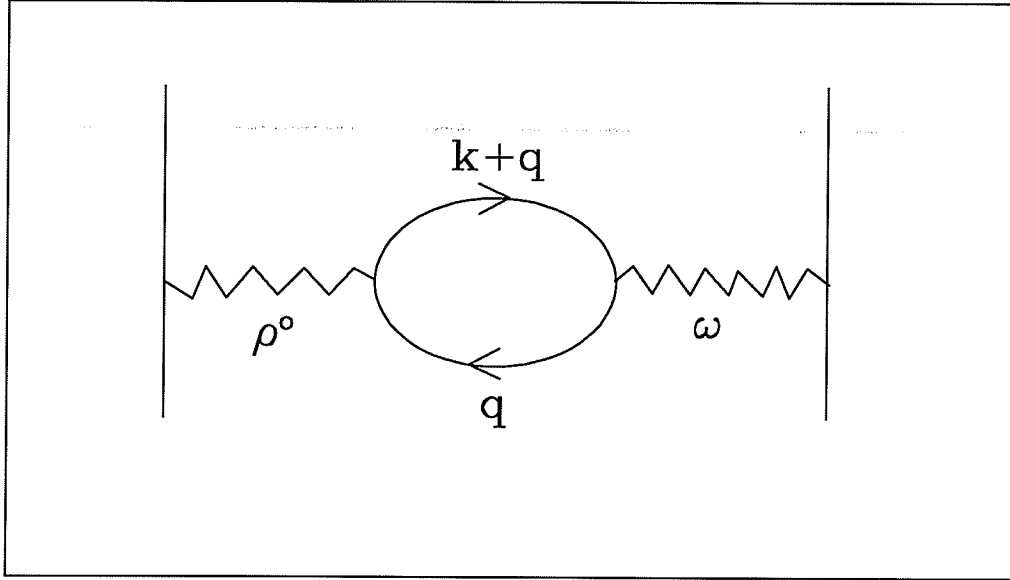


Figure 2.3: *Feynman diagram of a particle-antiparticle (e.g., quark-antiquark) loop for the  $\rho^0 - \omega$  mixing amplitude, the external meson momentum  $\mathbf{k}$  and the loop momentum  $\mathbf{q}$ .*

charge symmetry breaking [35,44]. In the c.m. system, the asymmetry is defined as:

$$A_{fb} \equiv \frac{\sigma(\theta) - \sigma(\pi - \theta)}{\frac{1}{2}[\sigma(\theta) + \sigma(\pi - \theta)]}, \quad (2.21)$$

where  $\theta$  is the angle between the incident  $n$  and the outgoing  $d$ . The mixing of  $\pi$  and  $\eta$  mesons (which generates a class III force in  $np$  elastic scattering, and therefore does not contribute to the difference of the analyzing powers) generates a class IV interaction and has a significant contribution to the CSB effect in this reaction (figs. 2.5 (a) and (b)). The latest calculation [44] shows that the  $\pi - \eta$  and  $\pi - \eta'$  contributions are almost an order of magnitude larger than other effects such as the  $np$  mass difference,  $\gamma$ -exchange and  $\rho^0 - \omega$  mixing. Earlier measurements did not yield statistically conclusive results on this CSB effect [45,46]. A new measurement of this forward-backward asymmetry at 281 MeV has been proposed and is in a preparatory stage at TRIUMF [47]. To reduce the systematic errors,

the experiment uses a broad range magnetic spectrometer set at zero degree and measures the full angular distribution of the recoil deuteron in a single momentum setting. Furthermore, a comparison to the charge symmetric reaction  $pp \rightarrow d\pi^+$  will be made to study the response of deuterons. The experiment is expected to yield a statistical accuracy of  $\pm 7 \times 10^{-4}$ . The latest prediction for the  $A_{fb}$  is  $-50 \times 10^{-4}$  [44]. Since the calculations also used on-shell mixing amplitudes to evaluate the  $\pi - \eta$  mixing, and off-shell considerations of the  $\pi - \eta$  mixing show similar effects to the off-shell  $\rho^0 - \omega$  mixing [48,49,50], the experimental result may provide information on the off-shell effect of meson mixing.

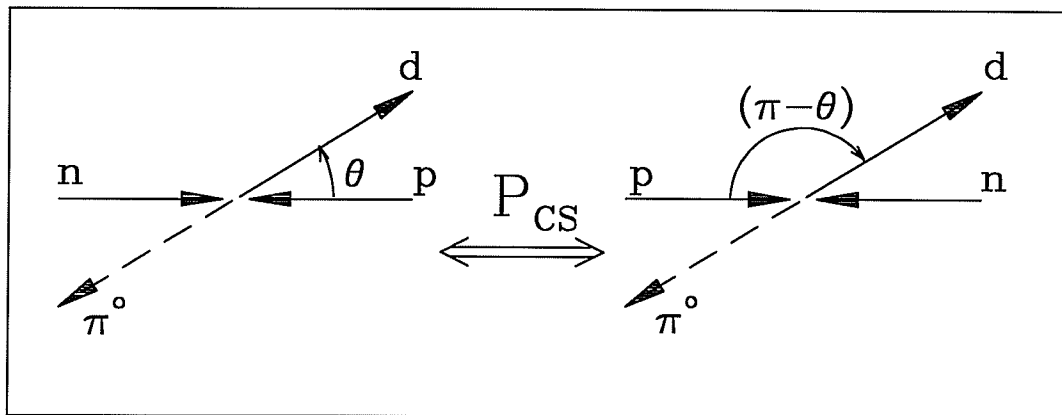


Figure 2.4: *Charge symmetric sketches of  $np \rightarrow d\pi^0$  in the center-of-mass frame.*

Isospin symmetry studies have been extended into many other systems involving pions (i.e., comparison of the  $\pi^\pm$  differential cross-section for elastic scattering from  $d$  or  ${}^4\text{He}$  targets [51,52]), deuterons (searching for the charge symmetry forbidden reaction  $dd \rightarrow {}^4\text{He} \pi^0$  [53] or comparison of the spin observables of  $dd$  breakup reactions  ${}^2\text{H}(\vec{d}, dp)n$ ,  ${}^2\text{H}(\vec{d}, dn)p$  and  ${}^2\text{H}(\vec{d}, np)d$  [54]), photons [55] and hypernuclei [56]. These studies have been extensively reviewed in two recent review articles [5,6].

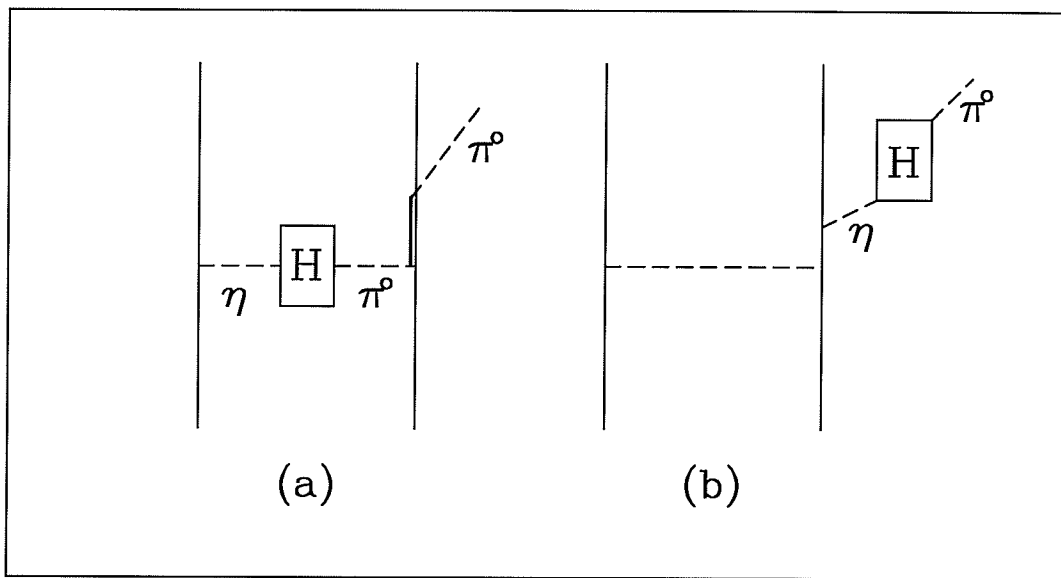


Figure 2.5: (a)  $\eta - \pi^0$  mixing in the transition potential; (b)  $\eta - \pi^0$  mixing in the production vertex.

# Chapter 3

## Experimental Details

### 3.1 General Description

The experiment was conducted with a 347 MeV neutron beam scattering off a frozen spin proton target (FST). The neutron beam and the proton target were alternately polarized for the measurements of  $A_n$  and  $A_p$ , respectively, where subscripts denote the polarized nucleons. Identical beam properties and target composition (except polarization) and the same detection system were used for the interleaved measurements. Scattered neutrons and recoil protons were detected in coincidence by a mirror symmetric detection system to cancel geometric systematic errors. Frequent flip of the neutron beam or proton target spin directions cancelled systematic errors not correlated with spin directions. At the zero-crossing angle, all systematic errors, except those due to background corrections, were eliminated to second order in an expansion in the error contributions. The protons were detected by a time-of-flight (TOF)/range telescope and the neutrons were detected by a scintillation detector array. Figure 3.1 shows schematically the beam line and the detection system.

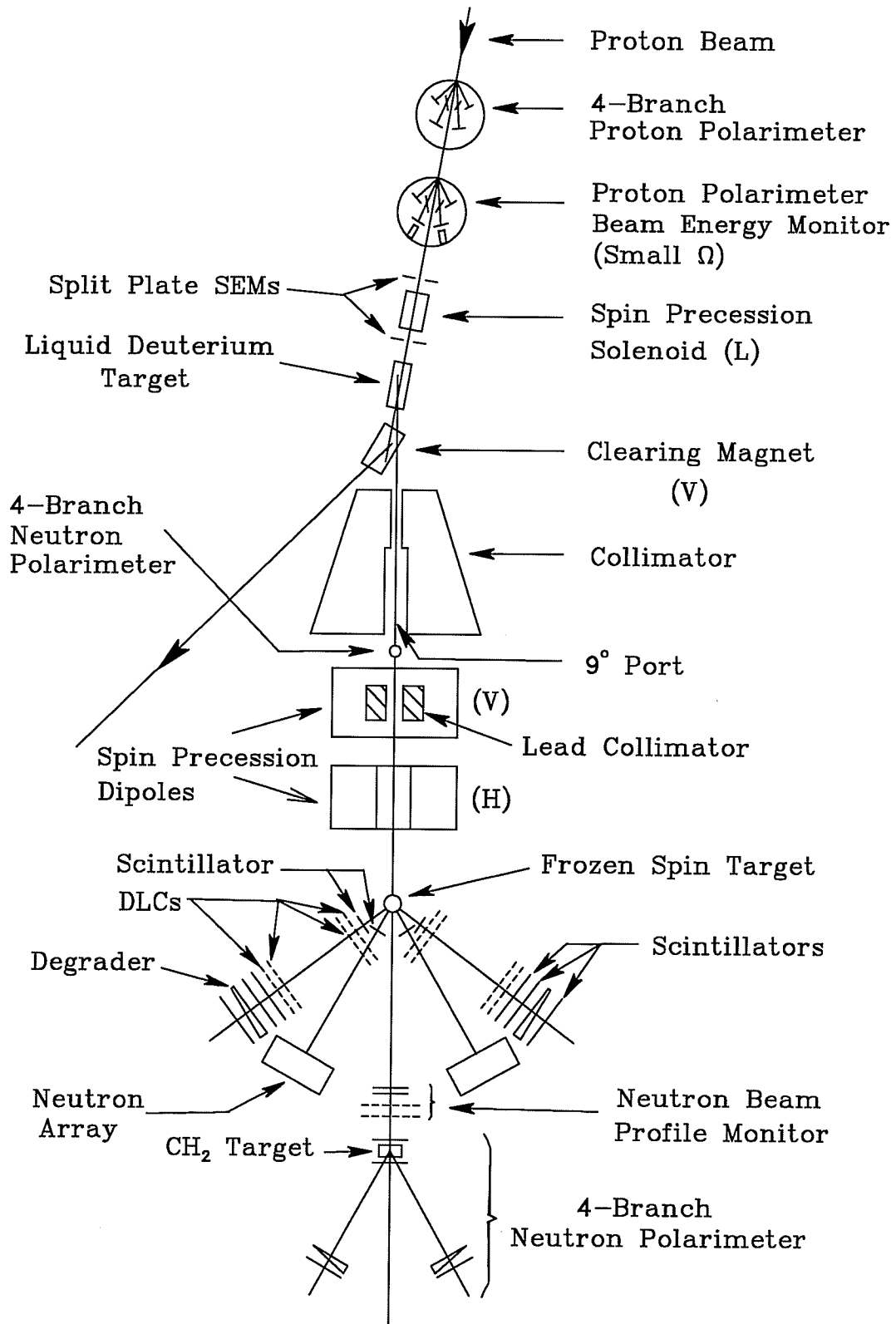


Figure 3.1: *Layout of the beam transport system and schematic view of the experimental apparatus.*

For future reference, the neutron beam coordinates are defined as follows (Fig. 3.2): the  $z$ -axis is chosen to be along the neutron beam direction with the positive direction pointing downstream; the  $y$ -axis is chosen to be the vertical direction pointing up; and the  $x$ -axis is chosen to be from right to left looking downstream (the Madison convention [57] ); “physical” left and right sides are defined by the physical locations of the detectors with respect to the neutron beam axis, again looking downstream. Left and right events are defined according to the primary scattered particles, the neutrons; left events are those with neutrons detected by the neutron array on the physical left side and protons detected on the physical right side, and right events are those with neutrons detected by the neutron array on the physical right side and protons detected on the physical left side. Other local coordinates are also used which relate to the beam coordinates by a rotation about the  $y$  axis by angles corresponding to the detector positions or the proton beam direction. The following sections will describe in detail the beam production and transport system, beam monitors, experimental detectors and the run procedure (see also Refs. [58,59]).

## 3.2 Proton Beam Production and Transport System

Polarized  $H^-$  ions were obtained from the TRIUMF optically pumped polarized ion source (OPPIS) [60]. The nuclear polarized  $H^-$  source was based on L.W. Anderson’s proposal [61] as shown in Fig. 3.3. A hydrogen plasma was created within an electron-cyclotron resonance (ECR) cavity by 28 GHz microwave ionization of hydrogen gas in a high magnetic field. The absorbed power was

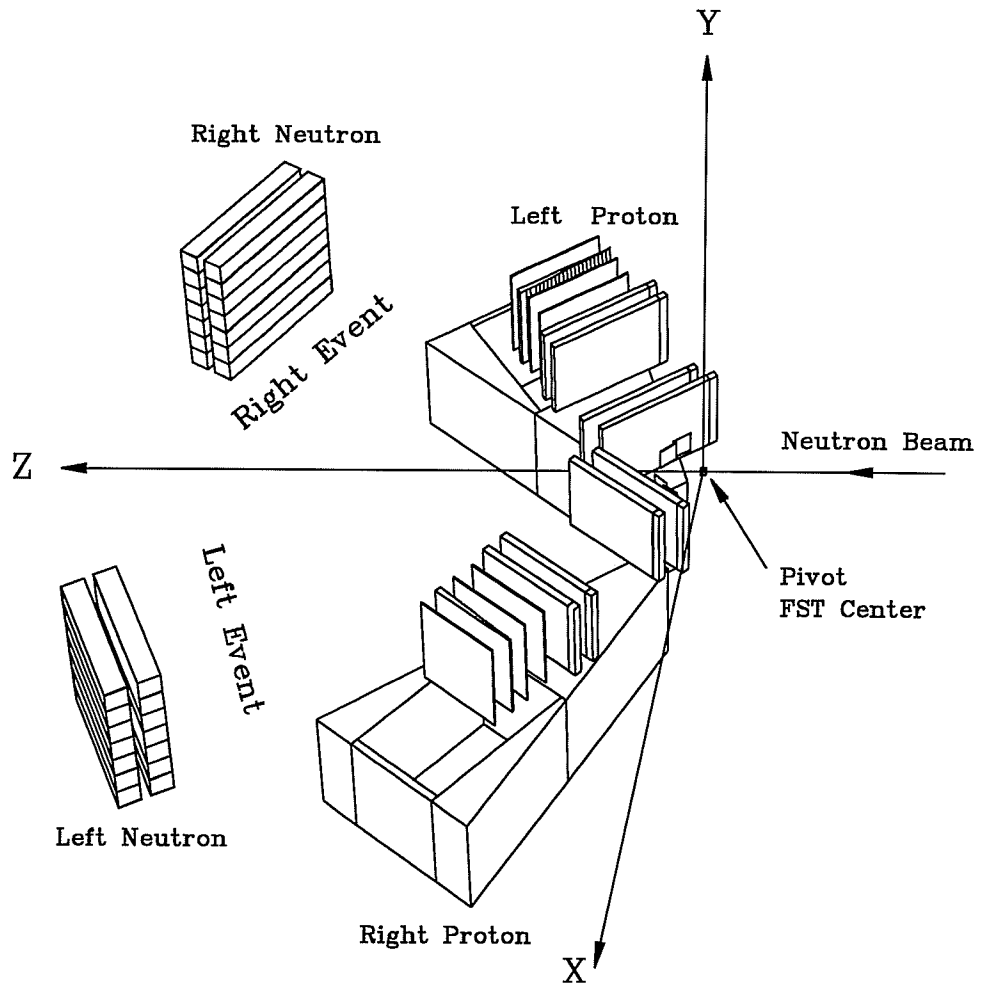


Figure 3.2: *Definition of the coordinates and conventions.*

typically 850 W. A proton beam was extracted from the ECR cavity plasma by an electrode system which accelerated the beam to an energy of several keV. The proton beam entered a polarized Rb vapor cell where a fraction of the protons picked up polarized electrons by charge transfer from Rb and were thus neutralized. The polarization was induced by optical pumping of the Rb vapor with circularly polarized laser light tuned to the  $D_1$  transition of Rb at 795 nm. Most of the neutralized hydrogen atoms were created in the excited  $n=2$  states (2s or 2p). For that reason it was necessary that charge exchange occurred within a high magnetic field ( $\sim 2$  T) which preserved the hydrogen polarization as the atoms decayed to the ground state. An electrostatic deflector immediately downstream of the neutralizer removed all charged species from the beam which had passed through the Rb cell. The magnetic field reversed direction in the region between the neutralizer and (negative) ionizer cells, and as the neutral hydrogen beam traversed this region, the polarization was transferred to the nucleus by means of a Sona transition [62]. The nuclear polarized hydrogen atoms picked up electrons in a sodium (Na) vapor ionizer cell. The unpolarized sodium vapor in the ionizer cell was thick, so that multiple charge exchange collisions produced an  $H^-$  beam with a conversion factor of roughly 7-10%. Figure 3.4 shows schematically the TRIUMF OPPIS. The  $H^-$  beam was accelerated to 300 keV and injected into the TRIUMF cyclotron for further acceleration. A beam intensity of  $15\mu A$  with a normalized emittance of about  $0.04 \pi \cdot \text{mm} \cdot \text{mrad}$  and polarization of as high as 80%, as measured by a low energy polarimeter based on the  ${}^6\text{Li}(p, {}^3\text{He})\alpha$  reaction, was achieved at the source. Approximately one quarter of the beam was accelerated by the cyclotron, which has a relatively low acceptance. To minimize the possible correlation of spin direction reversal and beam position change, proton spin direction reversal was achieved at the ion source by changing the frequency

and polarization of the optical pumping laser.

A 369 MeV proton beam was extracted from the TRIUMF cyclotron by stripping the electrons from the  $H^-$  ions with a carbon stripping foil. The beam had a negligible loss in current, but lost some polarization (about a few percent) at several cyclotron depolarization resonances. A phase restricted tune was used [63] to keep the beam burst time width within 1 ns FWHM (beam burst separation was 43 ns), which improved the resolution of the neutron beam energy measurement from its time-of-flight (TOF) (Fig. 3.5). This beam tune caused a decrease in the beam current by about a factor of 2 because slits were put in to restrict the phase acceptance. At the neutron production liquid-deuterium ( $LD_2$ ) target, the proton beam had a polarization of about 75% at up to 2.5  $\mu A$  current. The time structure of the beam was measured with a timing signal from one of the proton polarimeters, IBP, relative to the phase stabilized R.F. timing signals. The beam was tuned at the beginning of each 12-hour shift when the  $A_n$  and  $A_p$  measurements were interchanged.

Since the zero-crossing angles of the analyzing powers change significantly with the beam energy compared to the magnitude of the signal and the accuracy of this measurement ( $d\theta_o/dE_{nbeam} \simeq 0.048^\circ/\text{MeV}$ ), the proton beam energy was monitored by a beam energy monitor (BEM) and kept stable within  $\pm 0.05$  MeV by small adjustments of the R.F. or slight changes of the stripping foil position. The absolute knowledge of the proton beam energy was not critical and only needed to be known to a few MeV as long as it was much smaller than the neutron beam energy spread (about 11 MeV FWHM), since only the difference of the analyzing powers was a concern to the experiment. The absolute proton beam energy was

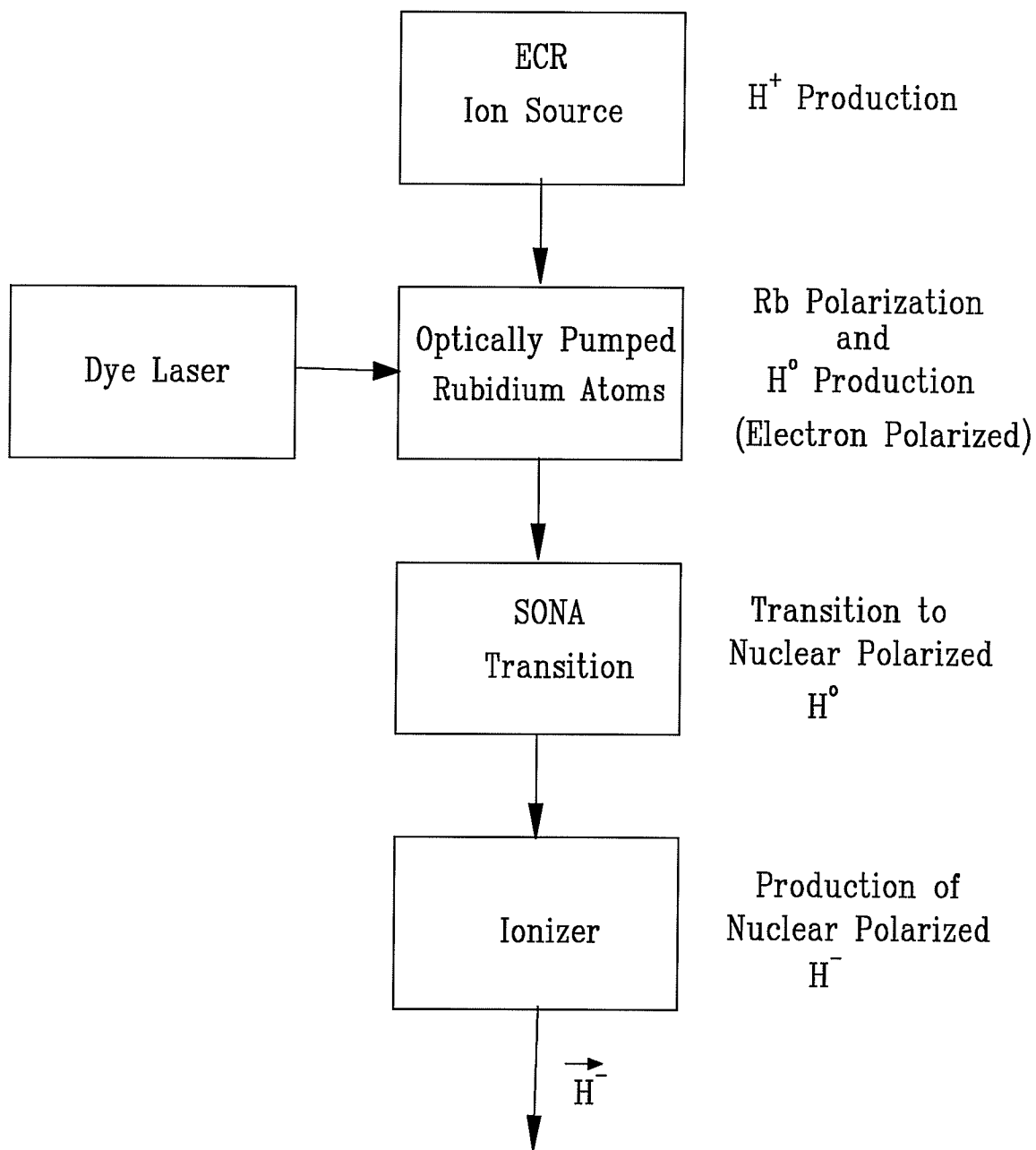
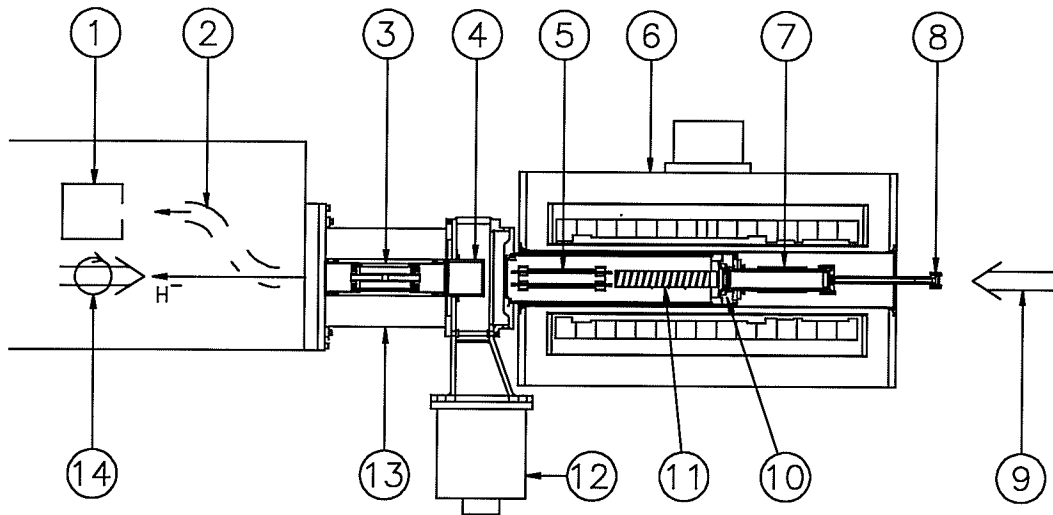


Figure 3.3: A block diagram of the TRIUMF optically pumped polarized ion source based on the proposal of L.W. Anderson.



- |                           |                             |
|---------------------------|-----------------------------|
| 1) Faraday Cup            | 8) Window for Probe Laser   |
| 2) Bender                 | 9) Probe Laser Light        |
| 3) Ionizer Na Cell        | 10) Extraction Lens         |
| 4) Sona Transition Region | 11) Rb Charge Exchange Cell |
| 5) Deflection Plates      | 12) Cryopump                |
| 6) S.C. Solenoid          | 13) Ionizer Solenoid        |
| 7) ECR Plasma Chamber     | 14) Pump Laser Light        |

Figure 3.4: A schematic diagram of the TRIUMF optically-pumped polarized  $H^-$  ion source. The  $H^-$  beam goes towards the left for acceleration and injection to the cyclotron.

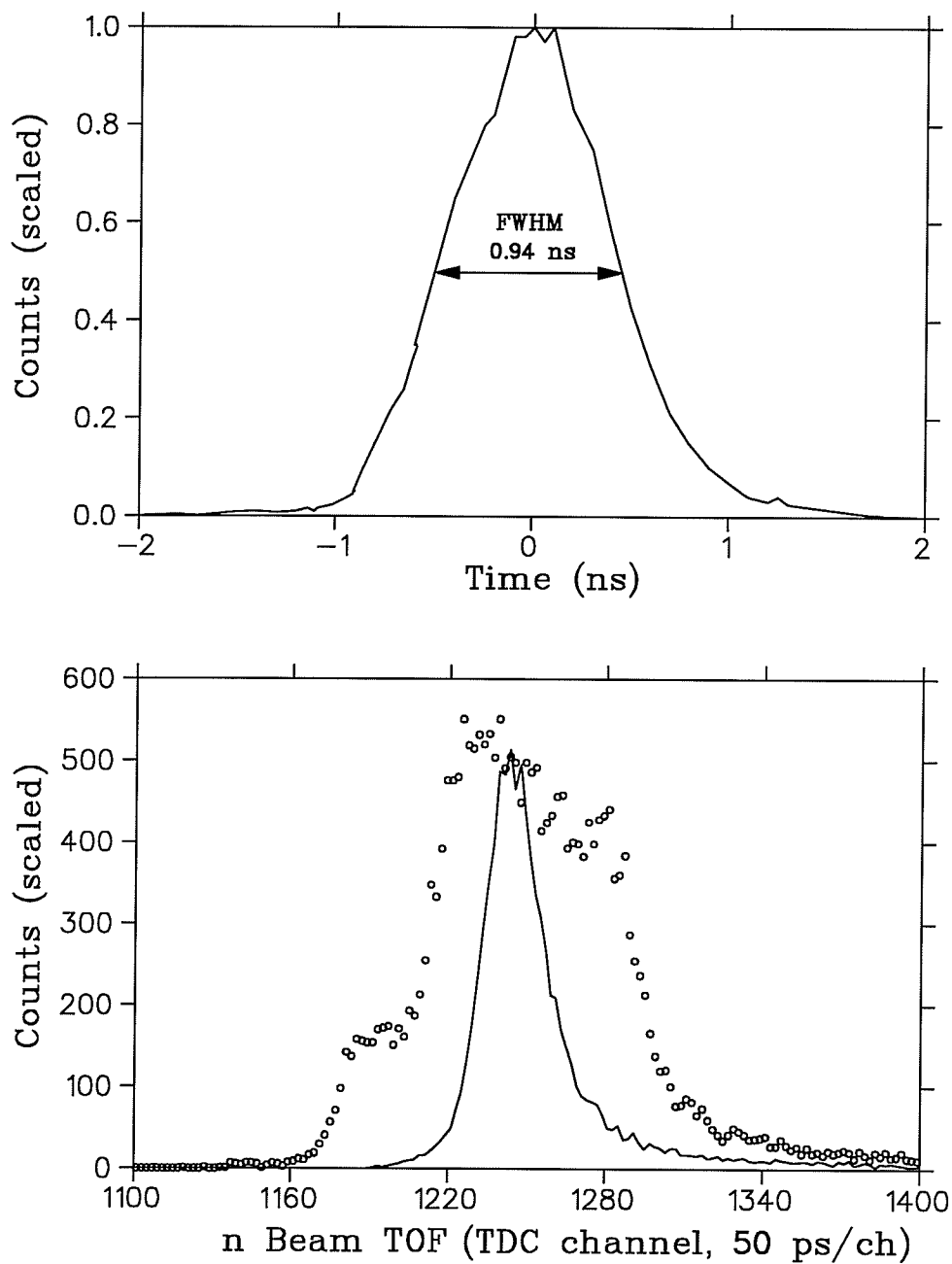


Figure 3.5: (a) Beam timing resolution, as measured by the time difference of the In-Beam-Polarimeter and the R.F. phase stabilized timing signals; (b) the neutron beam time width as measured by the R.F. timing signal before (discrete) and after (connected) applying the phase restricted time tune.

$368.3 \pm 1.0$  MeV obtained from the cyclotron beam-extraction stripping-foil radius and its calibration. In principle, the values of beam polarization were not required for the measurement of zero-crossing angle difference, but they were measured as accurately as possible for systematic error studies. The proton beam polarization was measured by two polarimeters, the In-Beam-Polarimeter (IBP) and the Charge Symmetry Breaking Polarimeter (CSB polarimeter).

The proton beam profile was monitored during the beam tuning by several retractable horizontal and vertical wire chambers placed at critical points along the beam line. The most critical wire chamber, placed approximately 0.65 m in front of the  $LD_2$  target during the beam tuning, had a wire spacing of 1 mm. For the CSB experiment, stability of the position of the proton beam at the  $LD_2$  target was essential. A shift in the beam centroid, especially when correlated with the reversal of the proton beam polarization direction, could produce unacceptable systematic errors. Proton beam spin reversal was achieved at the ion source to minimize such effects, but centroid shifts upon reversal could still arise. Two split plate secondary electron emission monitors (SEMs) were installed in the proton beam line to stabilize the proton beam position on the  $LD_2$  target. Details of these monitors along the beam line will be described in the following sections.

### 3.3 Neutron Beam Production and Collimation

A polarized neutron beam with an average energy of 347 MeV and FWHM of about 11 MeV was produced by the proton beam incident upon a liquid-deuterium ( $LD_2$ ) target through the reaction  $D(\vec{p}, \vec{n})2p$ . The  $LD_2$  target had a cylindrical geometry with a length of  $0.217 \pm 0.004$  m and a diameter of 0.051 m. The target

was operated at a temperature of approximately 22.5 K, a pressure of 17.5 psi and a density of about  $0.162 \text{ g/cm}^3$ . The end windows of the target cell were made of 0.051 mm thick stainless steel and the target wall was 0.254 mm thick stainless steel. The target was separated from the cyclotron vacuum by a 0.13 mm stainless steel window. The density of the target was kept stable (to  $\pm 0.0005 \text{ g/cm}^3$ ) since density changes would affect the average neutron beam energy and therefore the zero-crossing angles. A neutron beam intensity of about  $10^5 / (\mu\text{A} \cdot \text{cm}^2 \cdot \text{s})$  at the FST was achieved. The portion of the incident proton beam that did not interact in the  $LD_2$  target was swept by a dipole magnet, 4AB2, and transported into the external 4A beam dump. To take advantage of the large sideways to sideways spin transfer coefficient ( $r_t$ ) of the  $D(\vec{p}, \vec{n})2p$  reaction, the proton spin polarization was rotated from the normal direction (vertical transverse) into the scattering plane (horizontal transverse direction) by a superconducting solenoid (JANIS). This transfer coefficient is largest at  $9^\circ$  where the neutron beam was extracted [64].

The distances from the center of the  $LD_2$  target to the entrance and exit of the collimator were 2.93 m and 6.28 m, respectively. The collimator, 3.35 m long, was made of steel pipes welded to a steel frame filled with lead and had extraction ports at angles ranging from  $0^\circ$  to  $27^\circ$  in  $3^\circ$  steps. The pipes were built in two sections. The downstream section was 1.50 m long and 128 mm in diameter while the upstream section measured 102 mm in diameter. The unused ports were shut with removable steel plugs. In the  $9^\circ$  port, rectangular apertures were cut into steel collimator inserts which defined the geometric size of the neutron beam at the FST. To minimize the background contribution from the materials surrounding the FST, it was desired that the neutron beam fully illuminate the FST, but

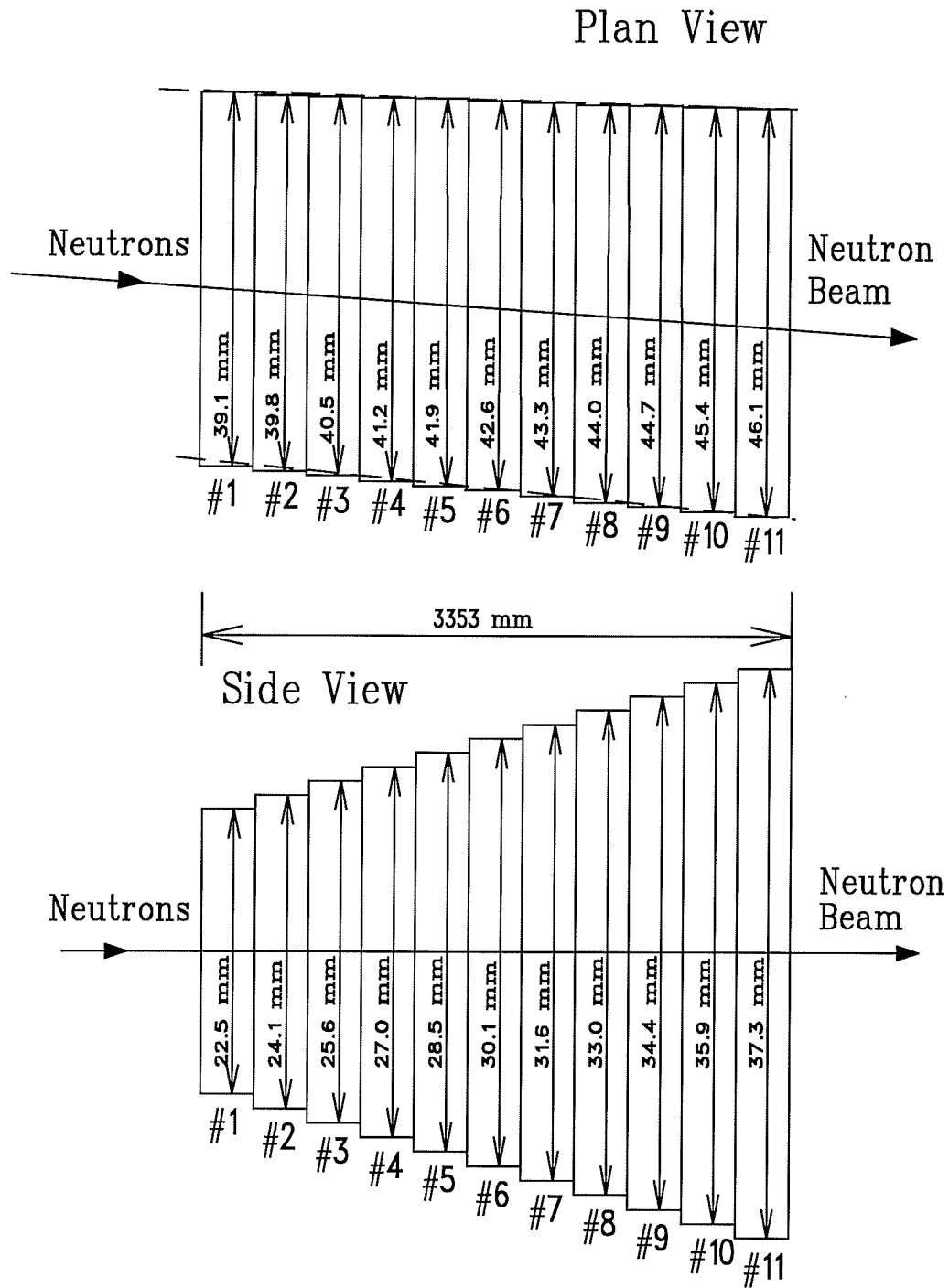


Figure 3.6: A schematic diagram of the geometric shape and the size of the neutron collimator aperture.

minimize the illumination of the surrounding material. The aperture used for the experiment ranged in size from a 39.1 mm horizontal  $\times$  22.5 mm vertical aperture to 46.1 mm  $\times$  37.3 mm, to approximate a tapered shape (Fig. 3.6). The neutron beam profile, neutron beam energy and polarization were monitored during the data taking and also simulated with Monte Carlo calculations [66]. Discussion of the Monte Carlo simulations and the comparison to the experimental measurements will be presented in Chapter 4 and Chapter 5.

## 3.4 Proton Polarimeter and Beam Energy

### Monitor

The proton polarization was measured by two polarimeters, the In-Beam Polarimeter (IBP) and the Charge Symmetry Breaking polarimeter (CSB polarimeter) [67,68]. The CSB polarimeter was a two-branch system which included a beam energy monitor (BEM) assembly and was used to monitor the proton beam transverse vertical polarization and the beam energy. It was composed of two detector assemblies viewing a hydrogen-containing (kapton) foil located 6.32 m upstream of the  $LD_2$  target in a 1.52 m diameter scattering chamber. The assemblies observed  $pp$  scattering events from a kapton target at  $\pm 17^\circ$  with respect to the incident beam axis. The layout of the polarimeter and the BEM combination is shown in Fig. 3.7. The forward arm of each assembly was composed of two scintillators (polarimeter) followed by a large Cu degrader (85 mm) and a six scintillator stack interspersed with 1 mm Cu sheets. Two additional detectors were located within the scattering chamber to complete each assembly by acting as recoil counters for the  $pp$  scattering. The polarimeter was designed to be insensitive to minor shifts

( $\pm 2$  mm) in the beam centroid. This was achieved by rotating the solid angle defining counter (A) by an angle  $\beta$  (Fig. 3.8). Both solid angle and  $pp$  differential cross-section variations due to beam shifts could be compensated for by choosing a proper angle  $\beta$ . It was determined that a rotation of  $68^\circ$  was optimal at 500 MeV [68]. Polarimeter geometric details are given in table 3.1.

Table 3.1: *Geometric details of the CSB polarimeter.*

Defining counter	vertical dimension	10 mm
	horizontal dimension	25 mm
	distance to target	774.7 mm
	solid angle	0.16 msr
	theta range	$\pm 0.37^\circ$
	azimuthal range	$\pm 1.26^\circ$
	central angle	$17^\circ$
	rotation angle	$68^\circ$
Recoil counter	vertical dimension	20 mm
	horizontal dimension	10 mm
	distance to target	203.2 mm
	solid angle	4.84 msr
	theta range	$\pm 1.41^\circ$
	azimuthal range	$\pm 3.0^\circ$
	central angle	$68.9^\circ$

The proton polarization in the normal direction could be calculated from the measured left-right asymmetry and the  $pp$  analyzing power ( $A_p$ ). Because of the

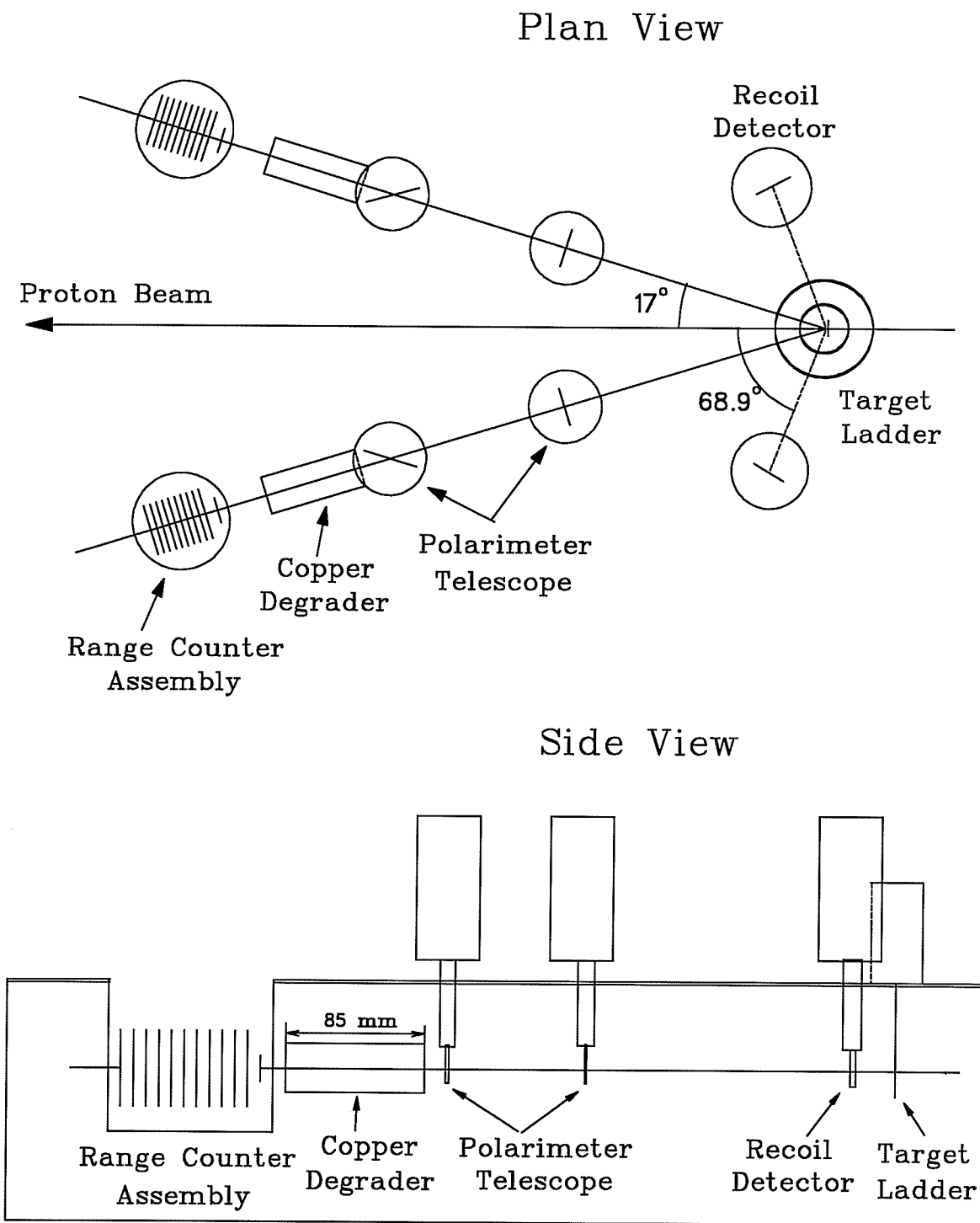


Figure 3.7: A schematic representation of the proton polarimeter/proton beam energy monitor.

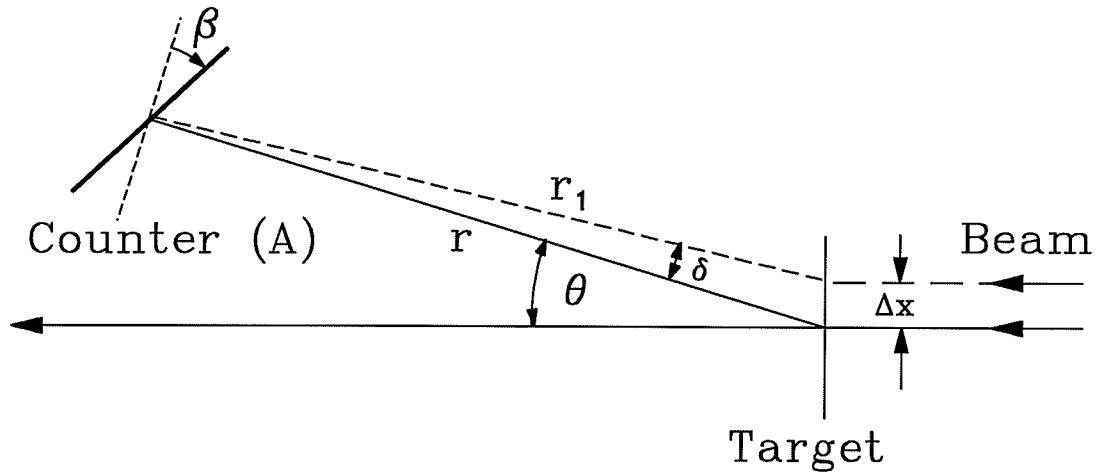


Figure 3.8: A schematic diagram showing the rotation of the solid angle defining counter in relation to the beam offsets [68].

carbon content in the polarimeter target material, an effective analyzing power,

$$A_{eff} = \alpha \cdot A_p \quad (3.1)$$

was required to account for the contribution of the quasi-elastic scattering  $C(p, pp)$  to the measured asymmetry, where  $\alpha$  is a correction factor obtained from polarimeter calibrations with a graphite target. To calibrate the polarimeter, different targets with differing hydrogen-carbon ratios were used, i.e.,  $CH_2$ , kapton ( $C_{22}H_{10}N_2O_5$ ) foils of different thicknesses, and pyrolytic-graphite (C) targets. The different polarimeter targets were mounted on a target ladder with an appropriate offset along the beam line to account for the change in opening angle ( $\theta_{scattered} + \theta_{recoil}$ ) with energy. The vertical position of the target ladder was controlled by a remote control motor system and the different targets could be selected remotely during the polarimeter calibrations. The polarimeters were calibrated several times during each data taking period since some small changes in the effective analyzing power were possible due to radiation damage of the target material in the beam. Table 3.2 shows a sample list of the targets mounted on the polarimeter target ladders.  $CH_2$  is a preferred target because it has a ratio

of free protons to bound protons of 1/3 and corrections for carbon content are easily made. But, due to their better resistance to radiation damage by integrated beam flux, kapton foils were used during the data taking. Instrumental asymmetries of the polarimeters were monitored and corrected by data collection using the unpolarized state of the beam. A typical spin polarization cycle was polarized:unpolarized:polarized = (1 min):(1/4 min):(1 min); every polarization “on” state (spin up or down chosen randomly at OPPIS) was followed by a polarization “off” state (unpolarized).

Table 3.2: A sample list of the targets on the polarimeter target ladders.

Position	CSB polarimeter		IBP	
	Target	Thickness	Target	Thickness
# 6	Carbon	4.9 $mg/cm^2$	N/A	
# 5	$CH_2$	1.404 $mg/cm^2$	ZnS	
# 4	Kapton	1.251 $mg/cm^2$	Carbon	3 $mg/cm^2$
# 3	Kapton	1.209 $mg/cm^2$	$CH_2$	1.43 $mg/cm^2$
# 2	ZnS		Parylene	200 $\mu g/cm^2$
# 1	Blank		Blank	

The proton beam energy was measured by the BEM based on a range determination. Figure 3.9 shows a schematic diagram of the proton BEM counter configuration. The differential range assembly was made up of six 10 mm thick plastic scintillators separated by 1 mm thick plates of Cu. The mean proton energy was calculated from:

$$E_{ave} = \Sigma N_i E_i / \Sigma N_i, \quad (3.2)$$

where  $N_i$  is the number of particles stopping in the scintillator  $B_i$  or the Cu after it and  $E_i$  is the average energy of the particles whose last counter triggered is  $B_i$ .  $E_i$ 's were calculated with the TRIUMF energy loss program LOSSPROG [83] based on the Bethe-Bloch equation. A resolution of  $\sigma = 35$  keV in the relative mean proton beam energy, given 16,000 counts (over  $\sim 15$  minutes of beam time at  $1.5 \mu\text{A}$  beam current) in each BEM arm was achieved. With the design of the BEM, the observed beam energy from the individual arm of the BEM was sensitive to the beam position, but the average value of both arms was independent of small beam position shifts. For beam motion from  $-10$  mm to  $+10$  mm about the nominal position, the average calculated beam energy varied by 140 keV (during the course of the experiment, the shift in beam centroid at the polarimeter was less than 1 mm).

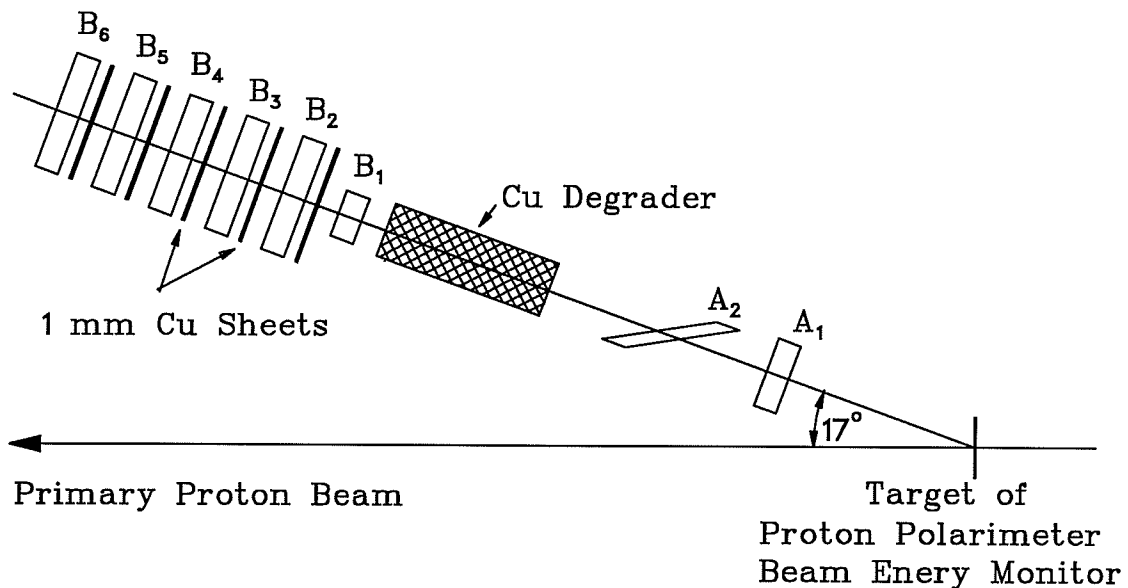


Figure 3.9: Some details of the right arm of the proton polarimeter/proton beam energy monitor.  $A_1$ ,  $A_2$  and  $B_1$  through  $B_6$  are scintillation counters. The recoil counter is not shown. The total length of the copper degrader in front of the  $B_1$  counter is 85 mm.

The IBP was a four-branch polarimeter and measured both left-right and bottom-top asymmetries. Its design principle was similar to the CSB polarimeter's described above, but it had larger solid angle coverage (table 3.3). Therefore at high beam currents, i.e.,  $2 \mu A$ , the accidental coincidence rate 3.10 would be unacceptably high if a normal thickness kapton or  $CH_2$  target was used. To make use of the IBP, a thin parylene target ( $(CH)_x$ ,  $\sim 200 \mu g/cm^2$ ) was employed during the data taking which made the polarimeter function consistently with the CSB polarimeter (see Chapter 5). Figure 3.10 shows schematically the triggering of the IBP. The accidental coincidence rate was estimated by delaying the recoil counter signals by 43 ns (which corresponds to the beam burst separation) and requiring the coincidence with the scattering counter signals.

Table 3.3: *Detector geometry (3.10) of the IBP (in mm).*

Detector	Distance	Angle wrt beam	Size
L1	762	$17^\circ$	$58.6 \times 50.8 \times 6.4$
L2	508	$17^\circ$	$50.8 \times 50.8 \times 6.4$
L3	203	$70^\circ$	$152.4 \times 50.8 \times 12.7$

### 3.5 Secondary Emission Monitors

The proton beam position, both horizontal and vertical, at the  $LD_2$  target were stabilized and monitored by a set of secondary electron emission monitors (SEMs) and a feedback system, which included a computer control system and a set of steering magnets. Each SEM contained five parallel, electrically separated (by 3.2 mm gaps along the beam line) aluminum foils. The foils were  $8 \mu m$  thick

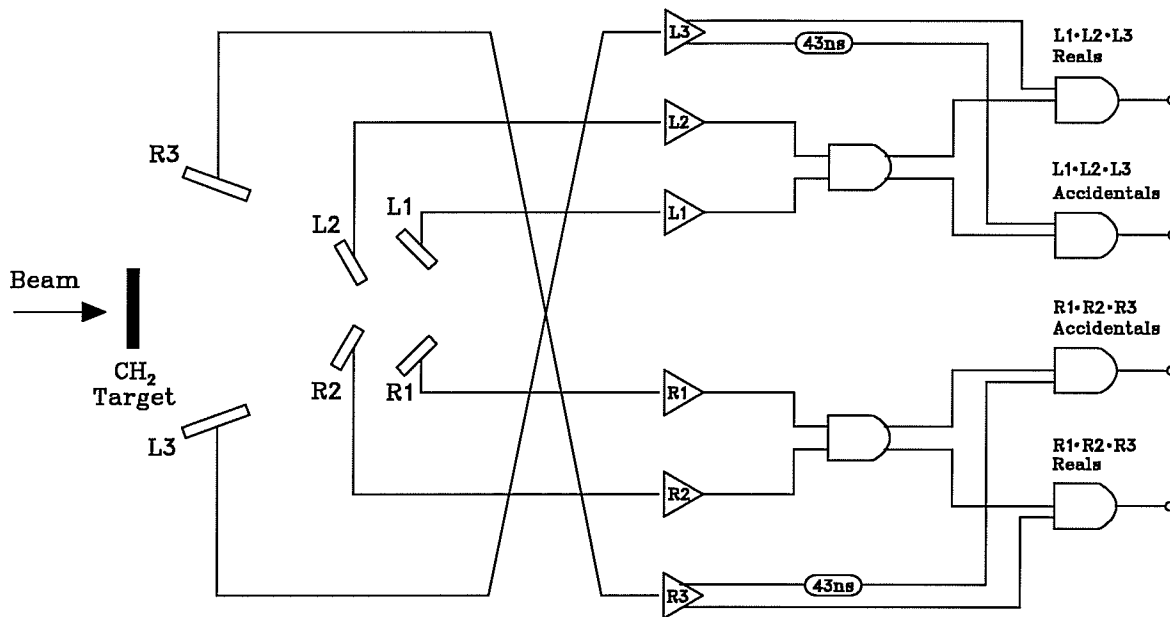


Figure 3.10: *Trigger for IBP. L1, L2, R1 and R2 are scattering counters; L3 and R3 are recoil counters.*

and 89 mm in diameter. Figure 3.11 shows schematically the SEM assembly. The second and fourth plates were split vertically and horizontally, respectively, into two semi-circular halves, separated by a 1 mm gap. These two grounded plates were interleaved by three full circular foils supplied with high voltages (+300 V). The total amount of the energy degrading material in the proton beam was 0.042 mm aluminum for each SEM. The optimum gap width depended on the proton beam profile. It was taken to be 1 mm based upon the beam profile measurements.

Secondary electrons were knocked out of the foils by the proton beam and collected by the plates. A small current was driven by these secondary electrons between the plates, and the signals were collected from each half of the split plates. These signals were proportional to the proton beam current and profile on each half of the split plates. Therefore, the beam charge asymmetries could be calculated from the integrated current to left and right (above and below) of the nominal

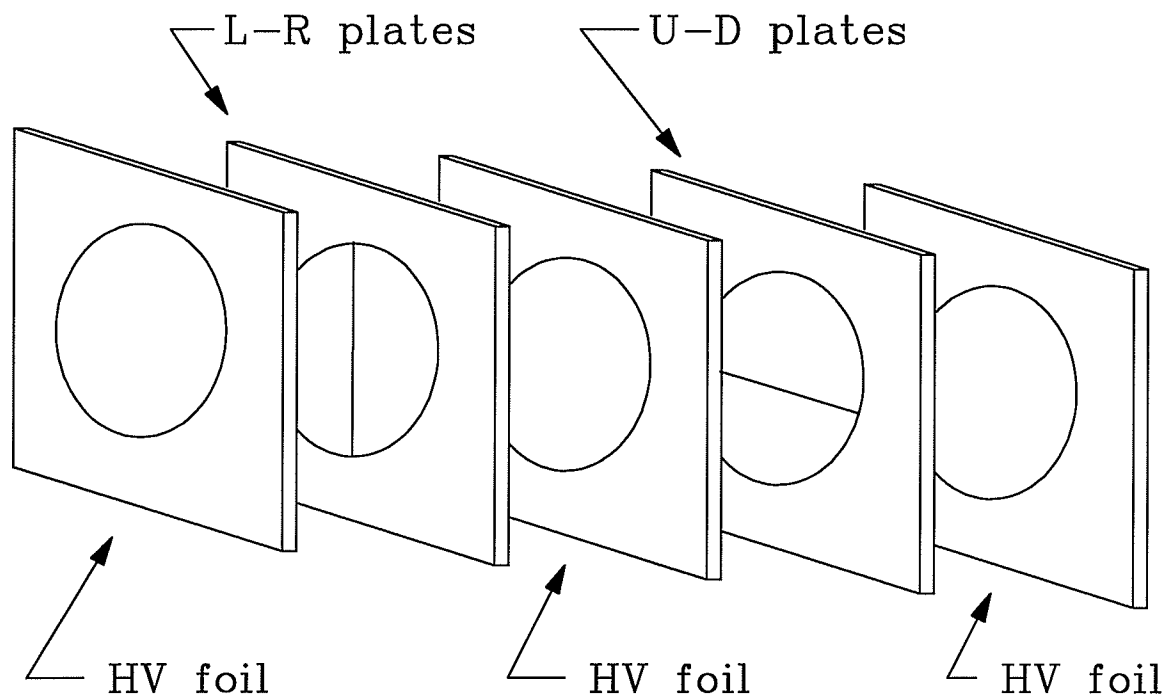


Figure 3.11: *Schematic diagram of the SEM assembly.*

beam axis; so that each SEM gave independent information for the vertical and horizontal beam positions. The integration time was a variable parameter that was matched to the response time of the feedback magnets, the beam intensity, and the time scale of micro-fluctuations in the beam. The output signals from the SEMs were amplified and fed into a dedicated microprocessor system programmed to calculate the appropriate beam transport corrections.

The SEMs were located 0.86 m and 2.18 m upstream of the  $LD_2$  target center and could be positioned remotely within the beam pipe in the left-right and up-down directions with a reproducibility of approximately 0.075 mm. Their vertical and horizontal positions were read out via linear potentiometers. The SEMs were initially set to position the proton beam incident upon the  $LD_2$  target to produce a neutron beam which would be centered on the frozen spin hydrogen target. The

SEM positions were not altered over the duration of the experiment. The proton beam position at the  $LD_2$  target then was stabilized to within 0.05 mm by the two SEMs, through a fast feedback system controlling two horizontal and two vertical steering magnets.

### 3.6 Phase Lock System

Timing with respect to the cyclotron radio-frequency (R.F.) system was needed to monitor the proton beam timing width and to calculate the incident neutron beam energy. The resolution of the timing signals was sensitive to the cyclotron tune-dependent phase shifts between the R.F. and the arrival of each proton beam bunch. In order to prevent shifts in the R.F. phase from degrading the resolution of timing measurements relative to the R.F., a scintillation counter was placed in the  $6^\circ$  port of the neutron collimator at a distance of 5750 mm from the center of the  $LD_2$  target. The port was filled with steel inserts which formed a tapered aperture (with a diameter of 38 mm over the first 990 mm, of 50 mm over the next 1020 mm, and 56 mm over the last 860 mm) in front of a 152 mm long by 75 mm diameter scintillator. The magnetic field of the primary proton beam sweeping magnet and a 44 mm thick brass plug ensured that the scintillation counter would observe only neutral particles from the  $LD_2$  target. A measurement could be made of the arrival time of the beam burst at the  $LD_2$  target with respect to the R.F. phase for rates in excess of 100 kHz in the scintillator. This usually required at least 100 nA incident beam on the  $LD_2$  target or a graphite target. A specially designed electronic module shifted the phase of the R.F. signal such that a constant time difference was maintained between the scintillation counter and the R.F. signal and thus a phase stabilized R.F. timing signal was generated. This signal was used as one of the references to monitor proton beam timing width and

to calculate the neutron beam energy from the  $LD_2$  target to the FST.

### 3.7 Neutron Polarimeter and Profile Monitor

The neutron beam polarization and profiles were monitored by two neutron polarimeters, the NEW and OLD, and a neutron profile monitor. The NEW neutron polarimeter was located at the exit of the collimator, and the OLD was located at 4.07 m downstream from the FST target (Fig. 3.1). The neutron profile monitor was located directly upstream of the OLD neutron polarimeter, 3.65 m downstream of the FST (the distance from the profile monitor scintillator converter to the pivot). Both neutron polarimeters were based on the same principle and had a similar design, consisting of four branches in the horizontal and vertical planes to measure left-right and down-up asymmetries of the recoil protons produced by  $(n, p)$  reactions from a  $CH_2$ /scintillator target.

Figure 3.12 shows schematically the OLD neutron polarimeter and the neutron profile monitor assembly. A 3.2 mm thick veto scintillation sheet (V) was located in front of the polarimeter  $CH_2$  target to accept only neutral particles in the beam, and another 3.2 mm thick trigger scintillator (T) behind the  $CH_2$  target tagged the knock on protons. The target was 5 cm thick, 15 cm wide and 15 cm high. Each polarimeter detection arm was centered at  $30^\circ$  with respect to the polarimeter target center, which was aligned to the neutron beam axis, and consisted of a wedge shaped brass degrader and a scintillator sheet to detect the recoil protons from the polarimeter target. The degrader was used to compensate for the kinematic spread in the energies of the  $(n, p)$  elastic and quasi-elastic protons and to stop low energy protons from quasi-elastic C(n,p) background. The

scintillator, 0.64 cm in thickness, 10 cm by 10 cm in width and height and 50 cm from the target center, spanned a solid angle of 0.040 sr. It was rotated by an angle to make instrumental asymmetries less dependent on the neutron beam position ( as discussed in Section 3.4). The effective analyzing powers of the neutron polarimeters were derived from the measured asymmetries, the measured proton polarization, calibrated magnet settings (see Section 3.8), and the known spin transfer coefficients. A stability and consistency of a few percent (of the value of  $P_n$ ) in the neutron polarization measurement was achieved with both polarimeters.

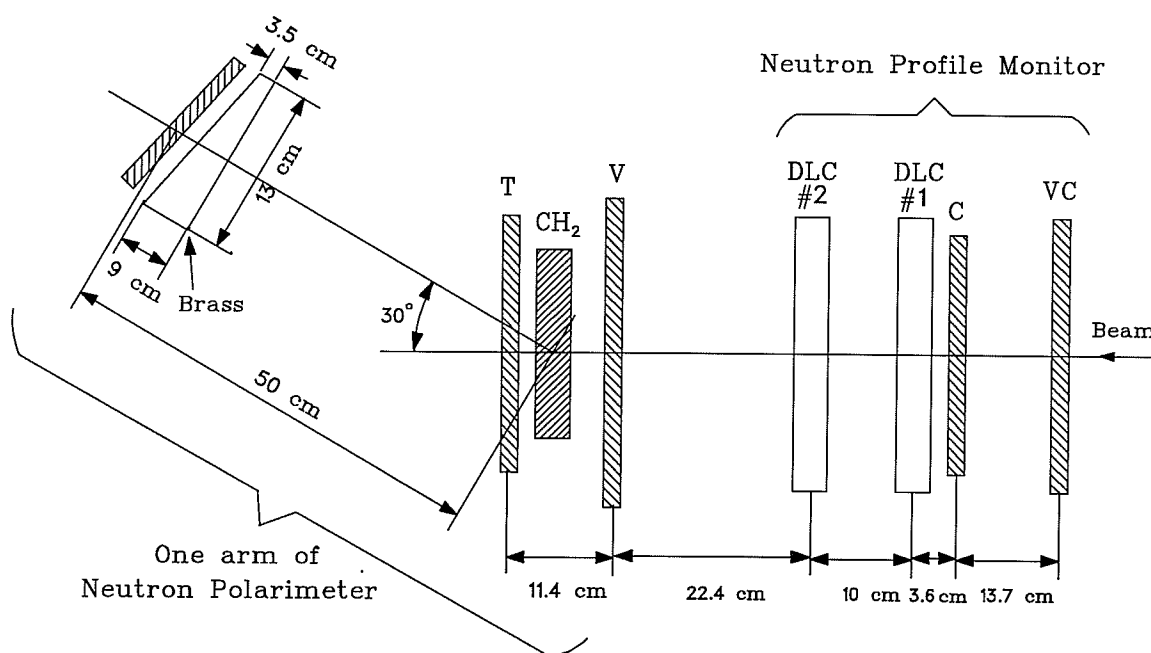


Figure 3.12: Schematic drawing of the neutron profile monitor and polarimeter.

The neutron profile monitor was used to monitor the horizontal and vertical neutron beam intensity distributions and their centroids. It consisted of a scintillation veto counter (VC), a scintillation converter (C), and two wire chambers (#1, #2 DLCs). Charged particles in the beam were vetoed by the veto counter which was 3.2 mm thick and 26 cm in width and height. The converter scintillator,

which was 3.2 mm thick  $\times$  21 cm wide  $\times$  21 cm high, functioned as both the profile monitor target and the trigger counter. Neutrons in the beam were scattered by the converter and recoil protons were tracked by the wire chambers. The wire chambers were of the delay line type and had a dimension of 20.3 cm by 20.3 cm with 2 mm wire spacings both horizontally and vertically. Each chamber had two delay lines, one horizontal and the other vertical. X and Y coordinates of a hit were obtained from the time difference of the two respective ends of each delay line, left-right or top-bottom. The projection of the reconstructed recoil proton tracks to the converter location gave the neutron beam profiles at the profile monitor. All detectors of the profile monitor were aligned to the neutron beam axis. The apparent coordinates obtained from each chamber were calibrated by a plastic cross (with arms about 50 mm thick  $\times$  4 mm wide) located between the veto counter and the trigger counter. The cross, with its center aligned with the beam axis, yielded enhanced narrow peaks in the reconstructed neutron profile distributions. This calibrated the center of the chambers. The neutron profiles were also checked by a steel I-beam aligned to the beam height. Both calibrations gave consistent results (see Chapter 5). The neutron polarimeter and profile monitor information was recorded for off-line analysis.

### 3.8 Spin Precession

To maximize the neutron beam polarization at the FST and cancel systematic errors, the spin polarization directions of the primary proton beam and the secondary neutron beam were rotated by several spin precession magnets along the beam line (Fig. 3.13). The polarized proton beam extracted from the cyclotron was polarized in the normal direction (vertical up, down, or unpolarized as controlled by the OPPIS). To take advantage of the large sideways to sideways

spin transfer coefficient  $r_t$  of the neutron production reaction  $D(\vec{p}, \vec{n})2p$ , three spin precession magnets were required to transform initially transverse vertical proton polarization back to transverse vertical neutron polarization at the FST location.

The spin polarization of the proton beam was rotated to the horizontal transverse (sideways) direction by a 0.42 m long superconducting solenoid (JANIS) capable of reaching an integrated magnetic field strength of 2.2 Tm. The polarized neutrons, produced by the sideways polarized proton beam on the  $LD_2$  target, had a spin polarization in the horizontal transverse (sideways) direction with small components (on the order of a few percent) in the longitudinal and transverse vertical direction due to the parameters  $r'_t$  and  $P$ :

$$P_{n,x'} = r_t \cdot P_p, \quad (3.3)$$

$$P_{n,y} = P, \quad (3.4)$$

$$P_{n,z'} = r'_t \cdot P_p, \quad (3.5)$$

where  $r_t = -0.880 \pm 0.010(stat.) \pm 0.011(syst.)$  at  $9^\circ$  and 363 MeV proton beam energy,  $r'_t = +0.013 \pm 0.010(stat.)$  is the sideways to longitudinal spin transfer parameter [64,65],  $P_{n,i}$  and  $P_p$  are polarizations of the neutrons and the protons, respectively, and  $P \simeq -0.07$  is the polarization production parameter due to the spin-orbit interaction [69,65]. Here, the lower case spin transfer parameters denote parameters for quasi-elastic scattering. For elastic  $np$  scattering,  $R_t = -0.914$  and  $R'_t = -0.017$ [69].

Downstream of the  $LD_2$  target, the neutron spin polarization direction was partly rotated in the horizontal plane by the sweeping magnet 4AB2 located between the  $LD_2$  target and the entrance of the collimator. The 4AB2 fringe field along the neutron beam trajectory was  $0.400 \pm 0.009$  Tm. The neutron beam had

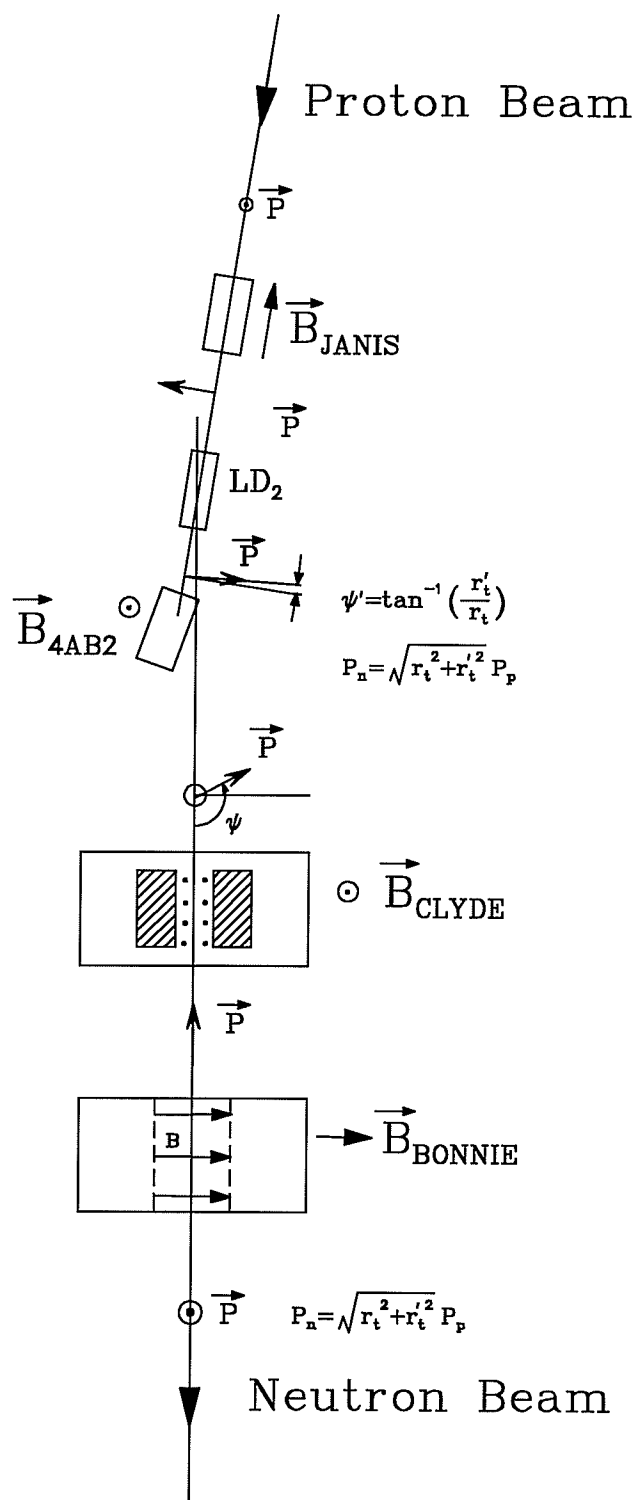


Figure 3.13: Schematic diagram of spin precession along the beam line.

a spin polarization direction of about  $113^\circ$  with respect to the beam direction at the exit of the collimator. The small component of the neutron polarization in the normal direction was unaffected by the 4AB2 vertical field. At the NEW neutron polarimeter location, near the exit of collimator, the neutron polarization was:

$$P_{n,x} = \sqrt{r_t^2 + r_t'^2} \cdot P_p \cdot \cos(180^\circ - \psi) \quad (3.6)$$

$$P_{n,y} = P \quad (3.7)$$

$$P_{n,z} = \sqrt{r_t^2 + r_t'^2} \cdot P_p \cdot \sin\psi \quad (3.8)$$

$$\psi \simeq 113^\circ. \quad (3.9)$$

To rotate the neutron spin polarization to the normal direction, a combination of two dipole magnets (one rotated the polarization around the y-axis and the other rotated the polarization around the x-axis) were used instead of a combination of a solenoid and a dipole magnet (with rotations around the z-axis and the x-axis). This combination was chosen to have the  $P_{n,y}$  (Eq. 3.7) rotated into the longitudinal direction at the FST location after the two rotations. The first dipole magnet (CLYDE), with its magnetic field in the normal direction (vertical up), rotated the neutron spin polarization into the longitudinal direction, i.e., opposite to the direction of travel of the neutrons. An additional function performed by this dipole was to sweep the charged particles, which were produced in the  $LD_2$  target, the neutron collimator and along the neutron flight path, out of the neutron beam. The second dipole magnet (BONNIE) with a field of horizontal transverse direction was used to bring the neutron spin polarization from the longitudinal direction into the normal (transverse vertical) direction. Depending on the direction of the BONNIE field, towards the left (“normal” setting) or right (“reversed” setting) looking downstream along the beam direction, the polarization of the neutrons at

the FST was either parallel or anti-parallel to the initial proton spin direction. In this process, the small vertical component of the neutron polarization at the entrance of BONNIE (produced by the neutron production reaction for both polarized and unpolarized protons) was rotated into the longitudinal direction at the FST target location. Because of parity conservation, this component did not contribute to the scattering observables when the target was unpolarized or polarized vertically. The longitudinal neutron polarization was rotated by the FST holding field (vertical) and a small component of sideways polarization was caused. At the FST location, the neutron polarization was:

$$P_{n,x} = P \sin \phi, \quad (3.10)$$

$$P_{n,y} = \sqrt{r_t^2 + r_t'^2} \cdot P_p, \quad (3.11)$$

$$P_{n,z} = P \cos \phi, \quad (3.12)$$

where  $\phi \sim 2^\circ$  ( $\int \vec{B}_{hf} \cdot d\vec{l} \simeq 0.04 \text{ Tm}$ ) is the angle which the longitudinal neutron polarization was rotated by the FST holding field.

The magnet settings were fully calibrated in several test runs (see appendix B for calibration details). To set and reproduce the magnet settings to the required accuracy, nuclear magnetic resonance (NMR) probes and remote readout systems were used for the dipole magnets (BONNIE, CLYDE and 4AB2) and a current readout system was used for the superconducting solenoid (JANIS). The final settings are shown in table 3.4.

Table 3.4: *Spin precession magnet settings. The errors on the settings were about  $\pm 0.0010$  T for BONNIE, CLYDE and 4AB2 and less than  $\pm 0.1$  A for JANIS*

Magnets	Setting	$\int \vec{B} \cdot d\vec{l}$
BONNIE	1.4353 T	1.7628 Tm
CLYDE	0.9316 T	1.2592 Tm
4AB2	1.1685 T	0.400 Tm
JANIS	68.3 A	1.6980 Tm

### 3.9 Frozen Spin Target

A frozen spin polarized hydrogen target (FST) was built for the CSB experiments. It was based on dynamic nuclear polarization which is shown in Fig. 3.14. The target material, butanol ( $C_4H_{10}O$ ), was doped with a small concentration of an electron donor material, a chromium compound  $[Na((C_2H_5)_2COCO_2)_2CrO]$ , to increase the density of free electrons. In the presence of a high magnetic field (a few Tesla) and low temperature (1 K), the four fold energy-degenerate states were split by the Zeeman effect with larger energy splitting due to the electron spin because its magnetic moment is 600 times larger than the proton magnetic moment. The re-population of the states was introduced by irradiating the target material with microwaves at selected frequencies ( $\nu_+$  or  $\nu_-$  in the figure) which corresponded to the electron and proton spin flip at the same time. When the atoms in the excited states decayed to the lower energy states, nuclear polarization was realized because the electrons of paramagnetic impurities in the butanol, being strongly coupled to the lattice, had a very short spin relaxation time compared to the nuclear spin relaxation time. The polarization could be reversed by changing

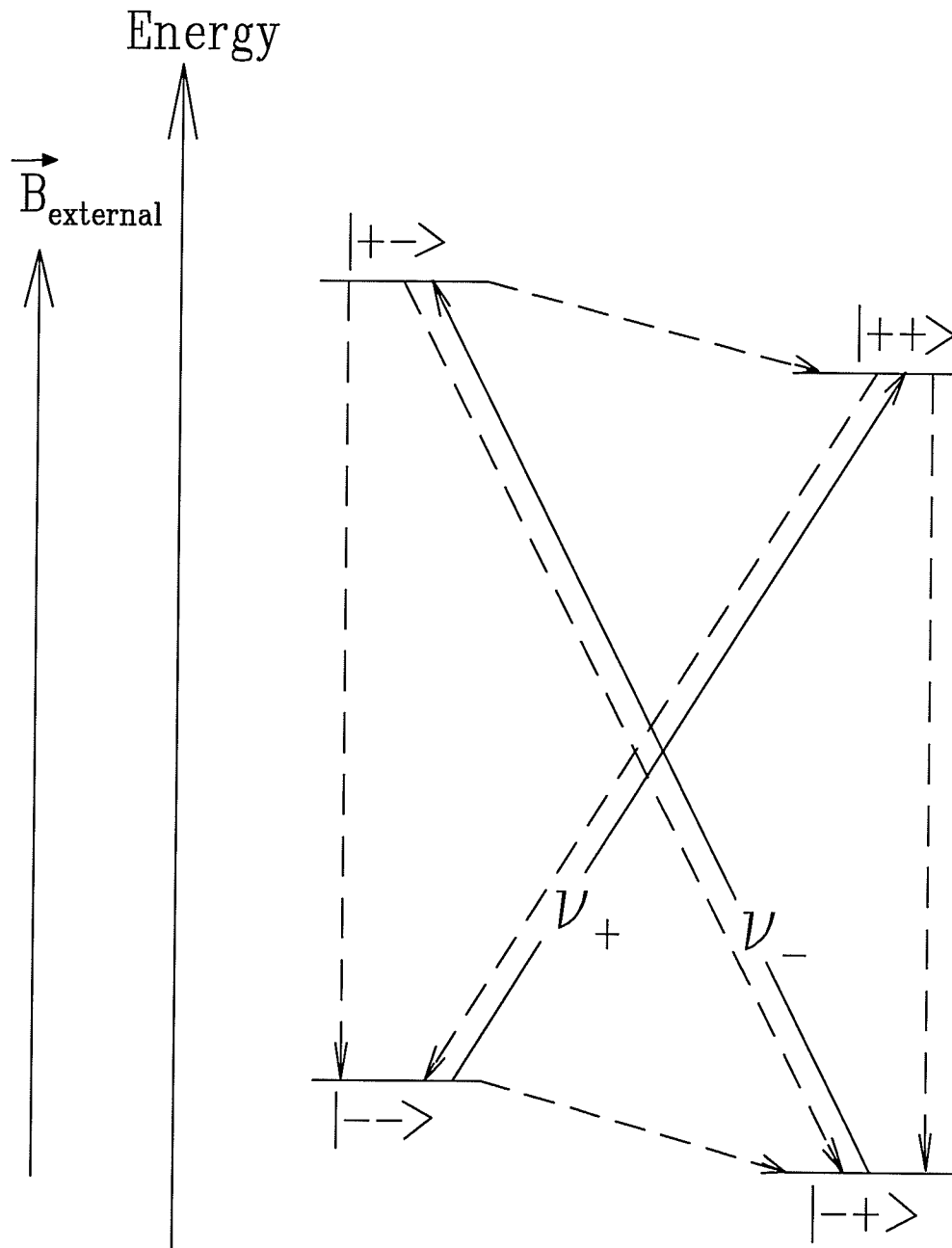


Figure 3.14: *Energy levels of the electron-proton system in presence of a strong magnetic field and re-population of the states by microwave irradiation. Here,  $m_e = \pm 1/2$  and  $m_p = \pm 1/2$  in  $|m_e m_p \rangle$ , are the spin directions of the electrons and protons parallel or anti-parallel to the magnetic field direction, respectively.*

the frequency of the microwaves irradiation (from  $\nu_+$  to  $\nu_-$  or vice versa). After being polarized, this type of target (which was cooled down by a  $^3\text{He}/^4\text{He}$  dilution refrigerator to about 55 mK) operating at very low temperature, allowed the proton polarization to be maintained with a weaker magnetic holding field than other types of polarized targets using butanol as the target material. A small holding field was desired to minimize the bending of the outgoing recoil protons.

The target cell was 3.5 cm long, 2.0 cm wide, and 5.0 cm high and contained  $35 \text{ cm}^3$  of 2-mm-diameter butanol beads immersed in a bath of 94%  $^4\text{He}$  and 6%  $^3\text{He}$  refrigerant (Fig. 3.15). The butanol beads had a packing fraction of 0.59. The volume size and physical position occupied by the butanol beads in the target chamber were determined from X-ray radiographs taken before, during and after each major data-taking period. The neutron beam fully illuminated the entire inner target canister but not the side of the outer 8 cm diameter, 12 cm high flask. Table 3.5 lists the approximate masses and radii of the materials in the FST.

The decay of the polarization of the FST with time can be written as:

$$P = P_0 e^{-\frac{t}{\tau}} \quad (3.13)$$

where  $\tau$  is the decay time of the polarization. Over the operating range of the FST (table 3.6),  $\tau$ , the holding field strength, B, and the target operating temperature, T, had the following relationship [70]:

$$\tau \sim \eta B^4 T^{-6} \quad (3.14)$$

where  $\eta$  is inversely proportional to the concentration of the electron donor. A low holding field is possible if a low temperature is achieved. Significant effort was made to lower the FST operating temperature, and approximately 55 mK was

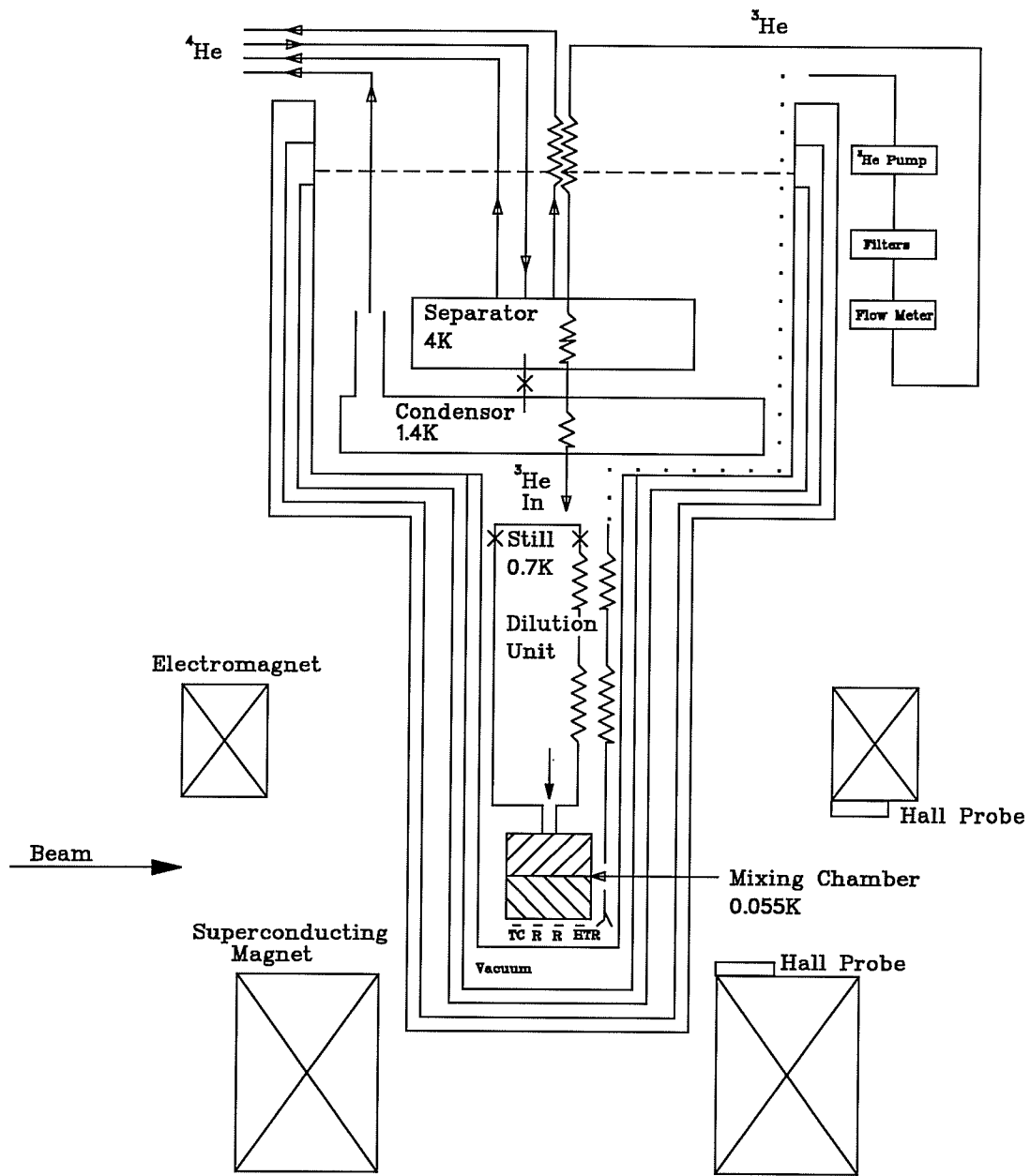


Figure 3.15: Schematic diagram of the FST.

Table 3.5: *FST* material in the particle's paths.

Item	Radius (cm)	Thickness (cm)	Material	Thickness (g/cm <sup>2</sup> )	Cumulative (g/cm <sup>2</sup> )
Butanol	$3.5 \times 2^{(a)}$	$3.5 \times 2$	Target	0.7125	0.7125
Basket	$3.5 \times 2$	0.00508	Cu	0.04552	0.758
LHe Bath	2.22	0.98	LHe	0.1225	0.8805
Target Can	2.22	0.0127	Fe	0.1	0.9805
Shield	2.7	0.00762	Cu	0.068275	1.0503
Shield	3.3	0.00762	Cu	0.068275	1.1187
Shield	4.1	0.00762	Cu	0.068275	1.186942
Super- Insulation	4.1-4.6	0.0144	Mylar	0.0144	1.201335
Outer Can	4.6	0.1	Al	0.27	1.471

(a) The target basket and butanol beads were in rectangle shape. See also Fig. 4.4 (a).

achieved. A holding field of 0.22 T was used during the experiment and a polarization of above 90% and a decay time of greater than 200 hours were attained.

The polarization of the FST was measured by an NMR system after the target was polarized and before it was depolarized. The NMR system was calibrated by the proton polarization at thermal equilibrium (TE). The proton polarization at thermal equilibrium in a static magnetic field can be calculated as:

$$H = -\vec{\mu}_p \cdot \vec{B} = -\gamma \vec{s} \cdot \vec{B} \quad (3.15)$$

$$P_{TE} = \frac{N^+ - N^-}{N^+ + N^-} = \frac{e^{\frac{\gamma B \hbar}{2kT}} - e^{-\frac{\gamma B \hbar}{2kT}}}{e^{\frac{\gamma B \hbar}{2kT}} + e^{-\frac{\gamma B \hbar}{2kT}}} \quad (3.16)$$

where  $H$  is the Hamiltonian of the interaction,  $\mu_p$  is the magnetic moment,  $\gamma$  is the gyromagnetic ratio, and  $s$  is the spin of the proton;  $N^\pm$  are the number of protons with spin parallel or anti-parallel to the magnetic field  $\vec{B}$  direction, and  $T$  is the temperature. The NMR system was calibrated at a temperature of 1.36 K, a magnetic field of 2.51 T and proton polarization of about 0.2%. The whole process and the NMR system were separately calibrated by a  $pp$  elastic scattering experiment to an accuracy of 2.6% where the error was mainly due to reproducibility uncertainties in the NMR measurements [72,73].

An accurate knowledge of the holding field strength and direction along the path of the recoil protons was crucial to understand the systematic errors and the correction for the recoil proton deflection in the holding field. The FST holding field strength was mapped with a Hall probe at a series of radial locations and different heights from the target center to 3 m. Figure 3.16 shows the different components of the field at and around the target as obtained from the field mapping. The field was kept stable and reproducible to within a few tenths of a mT and monitored by two Hall probes, located above and below the FST, during the

Table 3.6: *Typical operating parameters of the FST.*

Polarizing field	2.51 T
Polarizing Temperature	$\sim 1.0$ K
Holding Field	0.22 T
Holding Temperature	55 mK
Polarization	90%
Relaxation Time	200 hours
Target volume	$35 \text{ cm}^3$

data taking. The Hall probe readings were analyzed off-line (see Chapter 5).

Very stringent constraints were placed on the target position (relative to the pivot of the detection system), target holding field symmetry axis, stability, reproducibility, homogeneity and verticality. Their influence on the systematic errors will be discussed in Chapter 6.

### 3.10 Proton Detection System

The recoil protons were detected by two proton time-of-flight (TOF)/range counter telescopes, mirror symmetrically placed with respect to the beam axis. Each telescope included, along the recoil proton tracks, a TOF “start” scintillator (pTOF), four delay line wire chambers (DLCs) for proton track reconstruction, two scintillator E-counters as proton TOF “stop” counters, a wedge shaped brass degrader to stop protons from  $np$  elastic scattering and a veto scintillator to reject high energy background off-line. The degrader was made such that its wedge

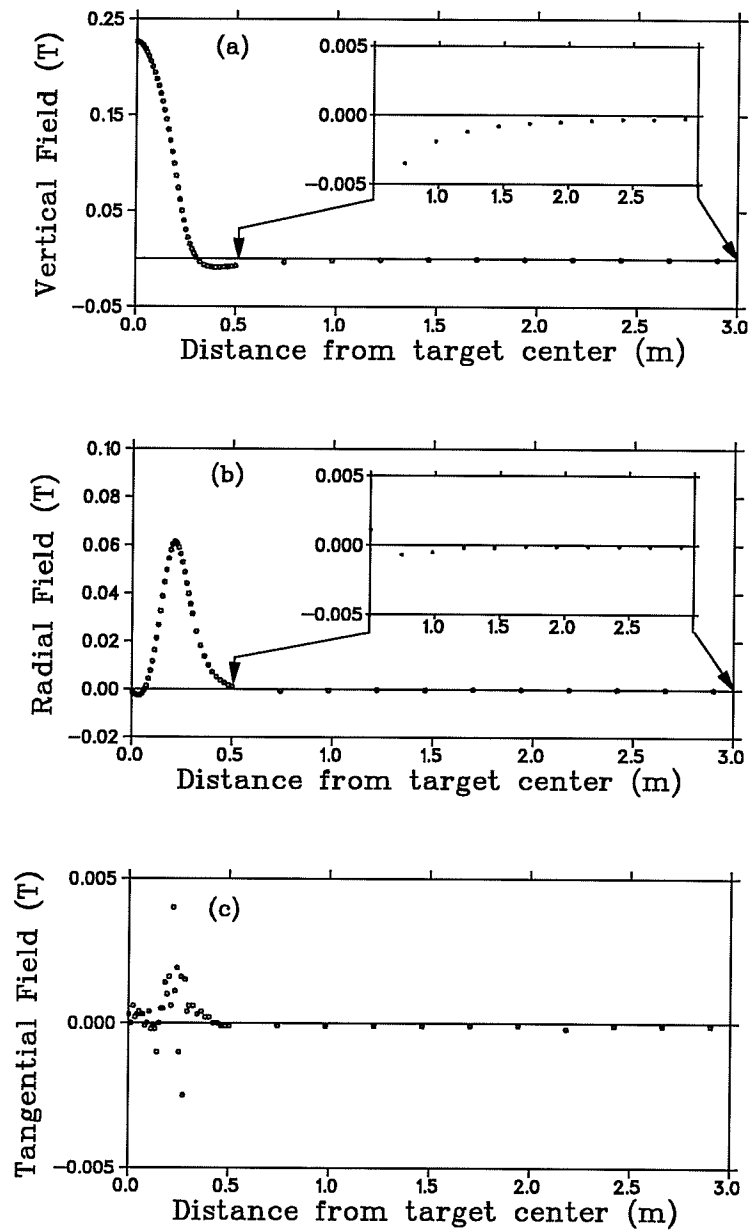


Figure 3.16: *FST* holding field strength around the target from the field mapping.

shape compensated the kinematic spread of the kinetic energies of the recoil protons from elastic scattering. The proton detection systems were supported by aluminium booms centered at  $\pm 53.0^\circ$  in the laboratory frame. Figure 3.17 is a detailed view of the detector system. Table 3.7 gives the radial and angular positions of the proton detection system with respect to the pivot which was also the FST centroid axis, and the neutron beam axis, respectively. The dimensions of various proton detectors is given in table 3.8.

Table 3.7: *Geometric positions of the proton detection system with respect to the pivot (for the radial positions) and the neutron beam axis (for the angular positions) (in mm unless otherwise stated).*

	Logical Left (Physical Right)	Logical Right (Physical Left)
Angle	$-52.96^\circ$	$53.03^\circ$
pTOF	299	298
DLC 1	498.8	499.2
DLC 2	661.8	661.0
DLC 3	1400.5	1401.5
DLC 4	1568.0	1564.5
$E_I$	1718.2	1714.0
$E_{II}$	1871.0	1869.0
Wedge	1950	1950
Veto	2141.8	2144.2

The pTOF with two photomultiplier tubes (PMTs) (top and bottom) and the two E-counters with four PMTs each (two up and two down) defined the trigger of

Table 3.8: Dimensions of the proton detectors (in mm).

Detector	Thickness×Width×Height
PTOF	$1.6 \times 130 \times 152$
DLCs	$(a) \times 580 \times 580$
$E_I$	$6 \times 670 \times 650$
$E_{II}$	$6 \times 670 \times 690$
VETO	$6 \times 670 \times 690$

(a) Thickness equivalent to  $250 \text{ mg/cm}^2$  Al for 50 - 250 MeV protons [76].

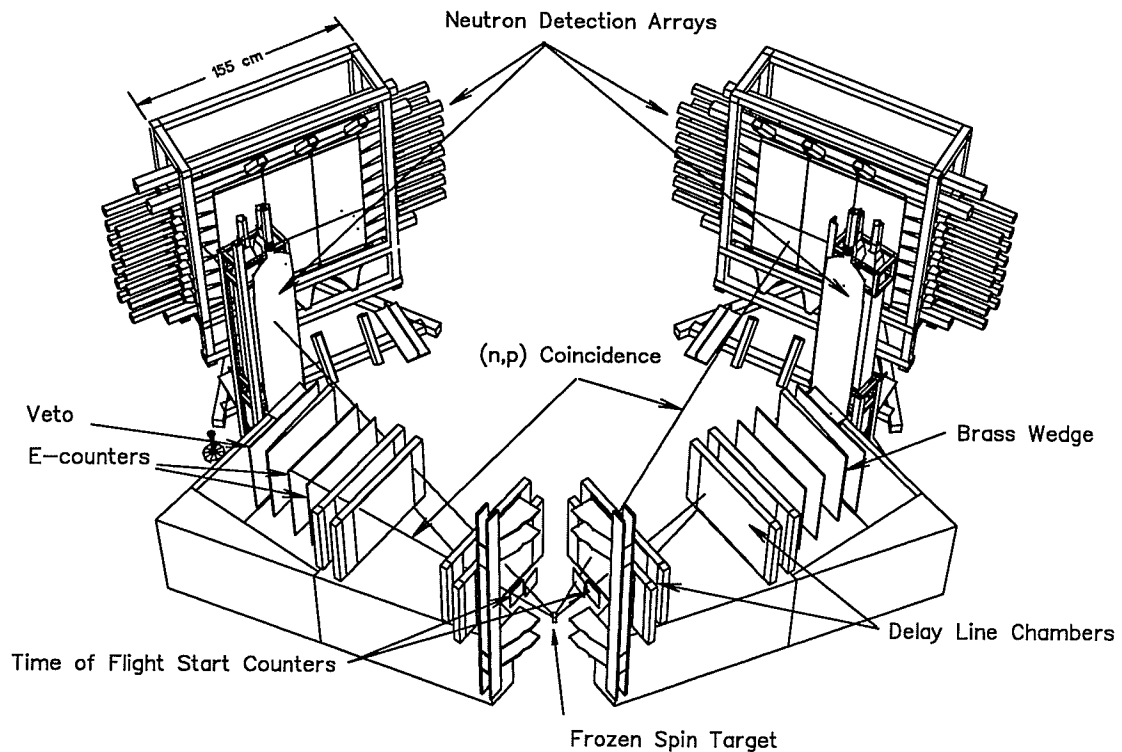


Figure 3.17: A detailed view of the detection system.

the recoil protons and gave the time-of-flight (TOF) for the protons between the pTOF and the E-counters which were separated by about 1.4 - 1.6 m (see table 3.7 for distances). After the calibration and correction for the position dependence of the scintillation light travelling in the E-counters, an energy resolution of about  $\sigma = 8$  MeV in the recoil proton energy measurements or 0.6 ns in their time-of-flight was achieved. The wedge degrader was designed such that the variation in thickness compensated the elastic proton energy variation with its angle. This ensured that no protons from  $np$  elastic scattering could penetrate the degrader and only higher energy charged particles would pass through the degrader, trigger the VETO counter and be rejected.

The DLCs [76] consisted of single anode planes at about +4500 V sandwiched between pairs of planar cathode foils. The cathode foils consisted of 20  $\mu\text{m}$  copper on 25  $\mu\text{m}$  mylar. Both x and y coordinates were determined in each chamber from the centroids of the charge distribution induced on 3.5 mm strips etched on the cathode planes with 0.5 mm spacings. Each anode plane had 291 vertical 20  $\mu\text{m}$  gold-plated tungsten wires, spaced at 2 mm intervals. The gas flow through each chamber was 100  $\text{cm}^3/\text{min}$  and the mixture was prepared by combining 30% isobutane, with 30% of a mixture of 1% freon in argon, and 40% argon bubbled through methylal. The chambers were designed so that the pressure from the gas flow counter-balanced the electrostatic attraction of the anode and cathode planes, thus maintaining a constant 6 mm spacing between them. This ensured that the chamber efficiency remained constant over its active area.

The two delay lines on each chamber were of the solenoid type [77,78] wrapped on flat polyethylene cores. Each was capacitatively coupled to a cathode plane by

pressing the delay line against the cathode strips where they extended outside the chamber frame. The absolute error due to the differential nonlinearity was typically about  $\pm 1$  mm for these delay lines. The on-chamber electronics consisted of pre-amplifier boards mounted at both ends of each delay line. Four inputs were provided on each chamber for pulser injection onto each end of each delay line, with a separation of 552.5 mm ( $\pm 0.7$  mm). These inputs were coupled directly to 1.6 mm wide copper strips mounted on the underside of the cathode planes, which were in turn coupled capacitatively to the cathode foils. Pulser fiducials were crucial for the position calibration of the chambers as well as for providing a check for the time-to-digital conversion gain and the delay line linearity stability. In addition, for mounting and alignment purposes, hardware fiducials, with well defined positions relative to the pulser fiducials, were imbedded in the anode planes. To prevent accidental misalignment, the chambers were bolted firmly to the proton booms.

The DLCs were calibrated for delay line non-linearity (for calibration details see appendix A). The spatial resolution in the horizontal direction was  $\pm 1$  mm limited by the “picket fence” (anode wire image) structure, since most ionizing events result in an avalanche around only a single anode wire, and it is impossible to distinguish on which side of the anode wire the initial ionization occurred. A local resolution of 0.7 mm FWHM was achieved in the vertical coordinate which was not affected by the anode wire spacing. For  $np$  coincidence detection, the DLCs were arranged in two x and y coordinate groups, one set close to the FST and the other set close to the E counters. A charged particle must trigger at least one x and one y coordinate in each group. This arrangement minimized the position error of the track origin after track reconstruction while allowing redundancy so

that the efficiency was high. The front pair, because only a small portion of the chambers was illuminated and the experiment was run at a high beam current (up to  $2.5 \mu\text{A}$ ), were operated at 4450 V high voltage and had an efficiency of around 95% each. The rear pair were operated at 4500 V and had an efficiency of about 98% each. The front pair of the chambers were offset horizontally by 10cm (DLC1) and 16.5 cm (DLC2) towards the beam axis, respectively, to clear the DLC frames from the paths of the scattered neutrons.

### 3.11 Neutron Detection System

The scattered neutrons were detected by two large position-sensitive neutron scintillator detection systems located mirror symmetrically with respect to the beam axis. Each side consisted of a main neutron array and an auxiliary array centered at  $\pm 29.5^\circ$  and  $\pm 40^\circ$  with respect to the beam axis and located 3.96 m and 3.02 m (centers of the detectors) from the center of FST, respectively (Fig. 3.17). Table 3.9 gives the radial position of the neutron detection system, from the pivot, and the detector center angular positions, with respect to the beam axis.

The main neutron detection array consisted of two banks of NE110 scintillator bars, one behind the other, with seven horizontally stacked bars in each bank (Fig. 3.18). Each scintillator bar was 1.05 m long  $\times$  0.15 m high  $\times$  0.15 m thick and was optically isolated one from the other. On each end of each bar there was a light guide terminating in a hybrid Winston cone [79] which accepted light impinging on the inner surfaces of the bars with angles less than about  $15^\circ$  from the axis of the light guide. RCA 8575 or equivalent photomultiplier tubes (PMTs) were used to view the scintillation light and convert to electronic signals. A 6.4 mm thick veto scintillation counter consisting of three vertical pieces of scintillator cov-

Table 3.9: *Geometric positions of the neutron detection system (in mm or otherwise stated; the distances are to the centers of the detectors).*

	Left (Main)	Right (Main)	Left (Aux.)	Right (Aux.)
Angle	29.53°	-29.54°	40.01°	39.98°
nTOF	277	274		
Veto counter	3702	3712	2934	2934
Front bank	3863	3857	3019	3019
Rear bank	4053	4058		
Button counter	4178	4191	3114	3114

ered the upstream side of the arrays to veto charged particles for  $np$  coincidences. The overlap regions of the different pieces of the veto counter gave two well defined horizontal positions to calibrate the neutron position determination using charged particles. Small scintillation “button” counters, with dimensions of 70 mm wide  $\times$  64 mm high  $\times$  7 mm thick, were embedded in a light guide positioned on the downstream side of the main array with each button counter centered at each bar. This provided PMT gain matching and monitoring, as well as neutron position determination calibration, with passing protons. A thin (0.8 mm) scintillator (nTOF), placed close to the FST, provided an additional constraint by requiring that the charged particles penetrating the button counters originated at the target. During data taking, the PMT gains were matched to certain nominal values for the upstream and downstream bars (350 and 500 ADC channels after pedestal subtraction, respectively) by adjusting high voltages on the PMTs a few times every (12 hour) shift. Small differences or drifts in gain matching between high voltage adjustments were recorded and matched by software to better than

1 ADC channel during the off-line analysis.

The neutron horizontal hit position was determined by the time difference of the relative timing signals from both ends of each bar. The full timing width of a bar was determined by “neutron singles” events when the proton coincidence was removed and the neutron bars were fully illuminated. The center of each bar was determined by the button events, which were triggered by charged particles originating from the FST and penetrating the neutron bars as well as the button counters (small offsets were added to account for the known offset of the button counters). A horizontal position resolution of  $\sigma = 16$  mm was achieved by comparing the position difference of the button events observed by the front and rear banks of the neutron arrays. The vertical position was taken to be the middle of a bar and thus had a resolution of  $\pm 75$  mm determined by the height of each bar. The time-of-flight of the neutrons was determined from the arrival times of the neutrons in the neutron arrays (time sum average of the left and right side), the timing signals of the coincident protons in the pTOF scintillator (average of the top and bottom timing signals) and the correction for the protons to travel from the FST center to the pTOFs.

Each auxiliary array consisted of two vertical scintillator bars (BC412), one beside the other, and each bar had an identical geometry and light guide to the scintillator bars in the main array. The auxiliary arrays had their own separate veto and button counters with similar coverage of the arrays to the main arrays.

The detection efficiency of such a neutron detector system was estimated with a Monte Carlo simulation code [80]. A single layer of the neutron scintillation bar

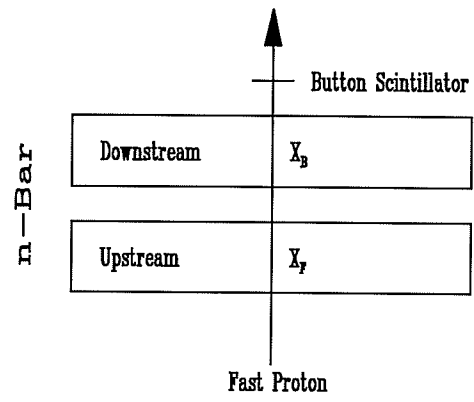
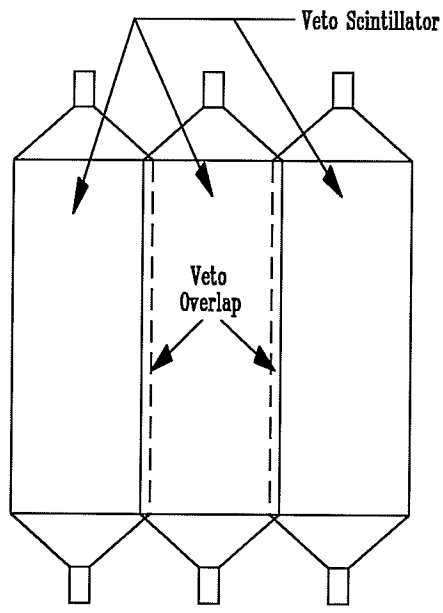
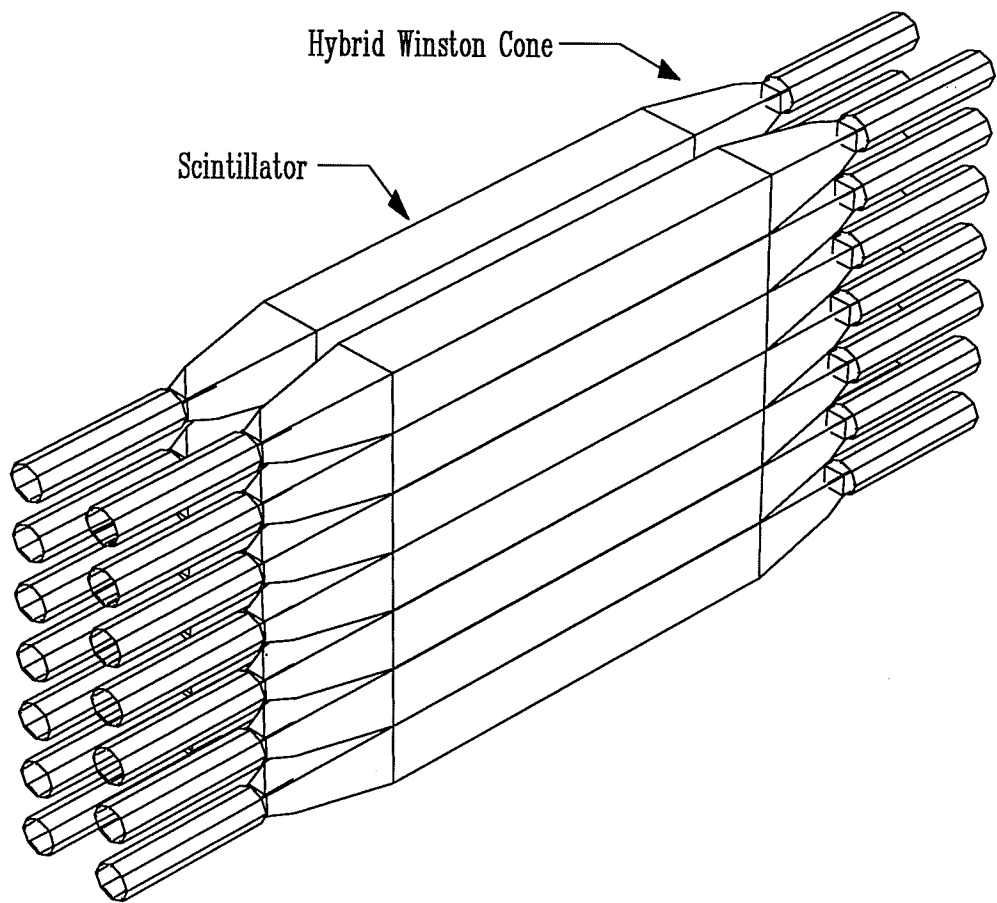


Figure 3.18: *The main neutron detection scintillation array.*

had an efficiency of about 16% and the two banks had an efficiency of about 30% with a reasonable threshold 0.4 - 1.1 MeV electron equivalent (MeVee). The hardware threshold was about 0.4 MeVee and the software thresholds used in data analysis were 0.4 - 1.1 MeVee.

### 3.12 Electronics and Data Acquisition

Simplified electronics block diagrams of the proton and neutron detection system as well as the  $np$  coincidence are shown in Figs. 3.19, 3.20 and 3.21. Each PMT signal was split into two parts, one to constant fraction discriminators (CFDs), which would gate the signal and generate shaped logic signals for the coincidence logic tests, timing and scaler counting, and the other for pulse height information. The timing signals were digitized in LeCroy 2228A (11 bit) time-to-digital converter (TDC) modules which had a conversion of 50 ps per channel for timing signals from the PMTs and 1 ns per channel for the DLCs. The pulse height signals were sent to LeCroy 2249A analog-to-digital converter (ADC) modules for digitizing. A valid recoil proton for a  $np$  coincidence required signals from at least one of the pTOF PMTs (top or bottom), both  $E_I$  and  $E_{II}$  counters (on the same side as the pTOF signal), at least one from the top two PMTs and one from the bottom two PMTs from each E-counter, and no valid signal from the proton veto counter. A proton latch was set if a recoil proton triggered and the proton TDCs were started, the ADCs were gated and the DCR (digital coincidence register) was strobed. A valid neutron required at least one signal from the neutron scintillation bars, and no signals from the neutron veto counters. The number of timing circuits for the neutron arrays was minimized by "daisy chaining" signals from bars 1, 3, 5 and 7 and signals from bars 2, 4 and 6 of a single bank of the scintillator bars. Adjacent bars were not connected so as to avoid confusion when

a single event triggered two bars. A single bank of seven bars was thus served by four timing circuits. Fixed delays were placed in the daisy chains to make each bar distinguishable. If a valid neutron was detected, a neutron latch was set and the neutron TDCs were started, the ADCs were gated and the DCR was strobed. The TDCs, ADCs and DCR were fast cleared by a reset if the proton latch was not set within a certain time window (100 ns) after the neutron latch was set. The button events were defined by requiring valid signals from the nTOFs, the neutron veto counters and the button counters.

When an event was triggered and a LAM ("look at me") was set, the CAMAC modules were read out through the CAMAC highway by a Starburst J-11 residing in the CAMAC system crate. Buffers of data were then passed to a VAX computer for writing to tape and on-line analysis. The readout system was controlled by the TRIUMF VDACS [81] system, running compiled TWOTRAN [82] programs on the J-11. The computer sent a busy signal to inhibit further acquisition of data while the current data were still being transferred. The data stream from the CAMAC crates was divided into seven event types:

- Scaler data (event type 1)
- Neutron profile monitor and polarimeter data (event type 2)
- Left or right  $np$  coincidence or button events (event type 5)
- High voltage data (event type 11)
- FST data (event type 12)
- SEM data (event type 13)
- Magnet's settings information (event type 14)

The left or right events of the  $np$  coincidence or the button events as well as the different spin states of the beam were identified in the DCR unit. The DCR bit map is listed in appendix D.

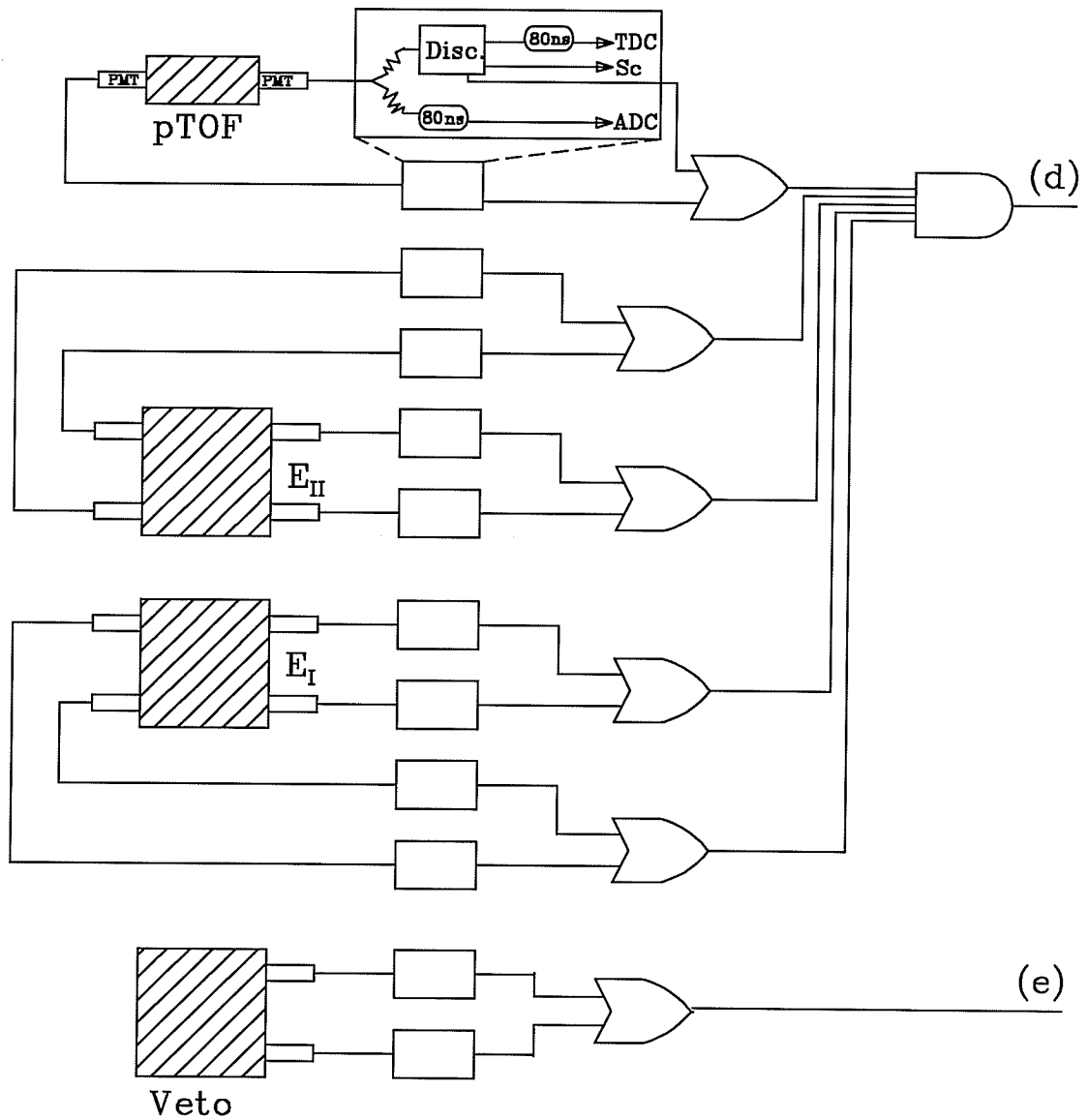


Figure 3.19: *Simplified electronics diagram of the proton detection system.*

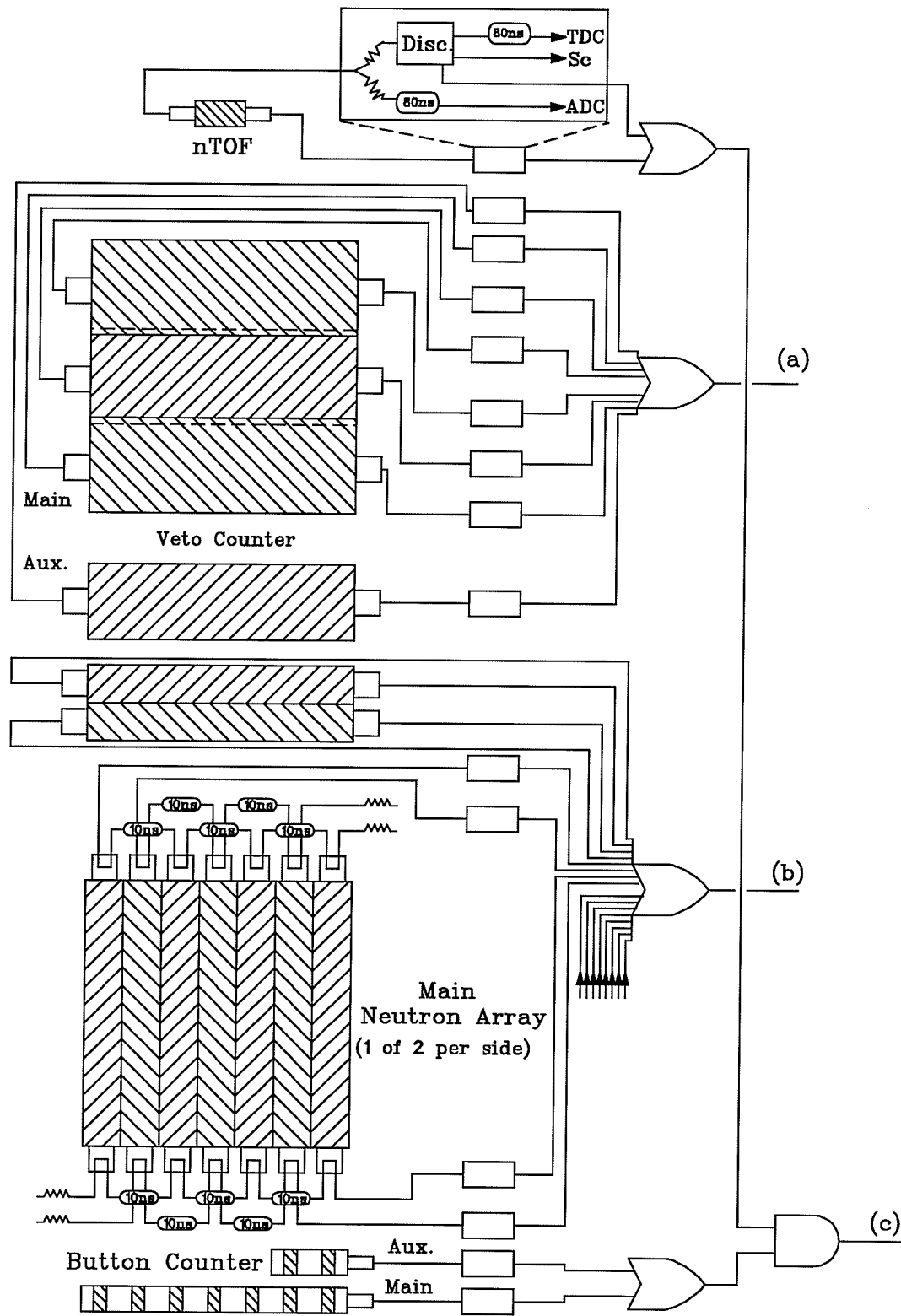


Figure 3.20: Simplified electronics diagram of the neutron detection system.

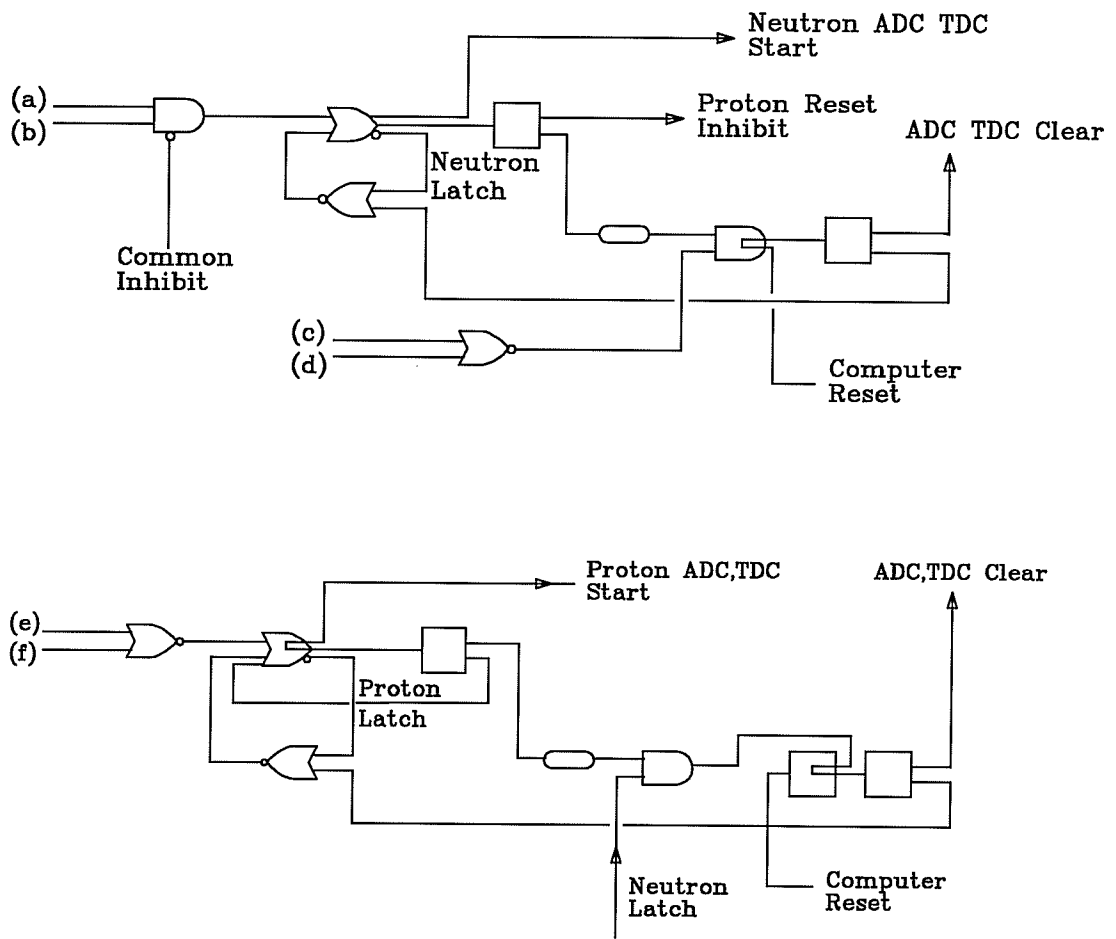


Figure 3.21: *Simplified electronics diagram of the np coincidence.*

### 3.13 Run Procedure

A number of tests and calibrations were conducted for the DLCs, spin precession magnets, and various detectors and monitors. Final data taking took place in three periods, February 1992 (background data only), August 1992 and February 1993, each of which spanned about a month of beam time.

Possible systematic errors could arise from spin correlations, holding field directions and detector efficiency changes with time, or small misalignments of the monitors and detectors (for more details see Chapter 6). To minimize the influence of the systematic errors on the difference of the analyzing powers, besides the use of the mirror symmetric detector setup, polarized beam and target runs were interleaved nominally every (12 hour) shift. The spin polarization direction of the proton beam was frequently flipped at the ion source with random spin flip selection of the "up" or "down" states. The spin polarization and the holding field direction of the FST was reversed once every day and once every two days, respectively. To cancel the possible spin correlations between the longitudinal polarization of the beam (due to the neutron production reaction and inaccurate rotation of the beam polarization) and sideways polarization of the FST (due to misalignment of holding field) the field direction of the last spin rotation magnet (BONNIE) was reversed to have one more set of combinations. Table 3.10 shows a typical 4-day cycle which covered all 16 combinations of different polarized nucleons (n or p), spin directions (up or down), holding field directions (up or down) and last dipole magnet (BONNIE) polarities (normal or reversed).

To study the background contribution due to quasi-elastic scattering of the carbon content of the butanol beads,  $C(n,np)$  data were taken with a dummy target

Table 3.10: *Typical four day cycle run scheme.*

	$P_{Beam}$	$P_{FST}$	Holding Field	BONNIE Polarity
DAY 1	on	off	up	normal
	on	off	up	reversed
	off	up	up	reversed
	off	up	up	normal
DAY 2	on	off	up	normal
	on	off	up	reversed
	off	down	up	reversed
	off	down	up	normal
DAY 3	on	off	down	normal
	on	off	down	reversed
	off	up	down	reversed
	off	up	down	normal
DAY 4	on	off	down	normal
	on	off	down	reversed
	off	down	down	reversed
	off	down	down	normal

which was made of carbon beads replacing the butanol beads such that its density was approximately the same as the butanol target in the absence of hydrogen. The dummy target was operated under the same conditions as the butanol target, the same holding field and temperature, and the same surrounding materials. The dummy target data were taken with the same set of configurations as the butanol data, holding field direction up or down, BONNIE field direction normal or reversed, and polarized beam spin polarization direction up or down. Only polarized beam data were required, since the average of different spin polarization directions would be equivalent to the unpolarized beam provided the amounts of data with spin direction up and down were the same.

# Chapter 4

## Monte Carlo Simulations

### 4.1 Neutron Beam Properties

Understanding the neutron beam properties (intensity, energy and polarization distributions) was important to the experiment. Systematic errors are strongly dependent on these beam properties because these distributions indicate the position and the direction of the incident neutron beam on the FST as well as the uniformity of the energy and polarization distributions over the FST volume. The effective (polarization weighted) average energies of the unpolarized and polarized neutron beam differed by a small amount because the neutron beam energy and polarization distributions were correlated through the production reaction  $D(\vec{p}, \vec{n})2p$ . A detailed study of the neutron energy and polarization distributions and their correlations made it possible to correct for this small difference of the beam energies.

The neutron beam production reaction  $D(\vec{p}, \vec{n})2p$  and the neutron beam collimation were simulated through Monte Carlo calculations in order to explore the neutron beam properties [66]. Particles were tracked from initially polarized (un-

polarized) protons incident on the  $LD_2$  target, producing polarized (unpolarized) neutrons, passing through the  $9^\circ$  port of the collimator to the FST and then to the neutron profile monitor locations. The simulations started with a 369 MeV proton beam incident on the  $LD_2$  target of density  $0.1615 \text{ g/cm}^3$ . The  $D(\vec{p}, \vec{n})2p$  reaction point was randomly selected within the target volume along the central axis at a distance,  $\Delta z$ , from the inner side of the  $LD_2$  target entrance window. The energy loss for protons traveling to the reaction point included two parts, one was due to the target's steel window and the other was in the  $LD_2$  of thickness  $\Delta z$ . The TRIUMF energy loss program LOSSPROG [83] was used to calculate the proton energy loss. The proton energy loss in the target steel entrance window was about 0.09 MeV, and the energy loss (in MeV) of the proton beam in the  $LD_2$  was interpolated as a function of  $\Delta z$  (in cm):

$$\begin{aligned} \Delta E_{pbeam} = & -2.71088 \times 10^{-5} + 0.53163 \times \Delta z + 1.93222 \cdot 10^{-4} \times \Delta z^2 \\ & + 3.45722 \cdot 10^{-7} \times \Delta z^3, \end{aligned} \quad (4.1)$$

for the  $LD_2$  with a density of  $0.1615 \text{ g/cm}^3$ . At the center of the  $(0.217 \pm 0.004)$  m long  $LD_2$  target,  $\Delta z = 0.1085$  m, the proton beam energy was 363.2 MeV. The neutrons were produced at a selected angle ( $\theta_{nbeam}$ ) and energy ( $E_{nbeam}$ ) with a probability weighted by the reaction differential cross-section [64,65]. The angular range of the selected neutrons was from  $8^\circ$  to  $10^\circ$ , which covered the angular acceptance of the entrance aperture of the neutron collimator. The neutron energy ( $E_{nbeam}$ ) and the corresponding  $r_t$  and  $r'_t$  (from which the neutron polarization,  $P_{nbeam}$ , was calculated) were selected followed from the probability distributions of Bugg and Wilkin [64,65] ( where  $r_t$  are the sideways to sideways and  $r'_t$  is the sideways to longitudinal spin transfer parameter, respectively). The parameter  $r'_t$  was small (about 0.015) over the angle and energy range considered here. The “produced” neutrons at the angle  $\theta_{nbeam}$  with energy and polarization,  $E_{nbeam}$  and

$P_{nbeam}$ , were tracked through the collimator and they were saved by the computer program if they could pass the collimator. The collimator geometry as discussed in Section 3.3 and shown in fig 3.6 was used for testing the neutron acceptance as follows:

1. If a neutron cleared the entrance and the exit apertures of the collimator, the neutron was accepted;
2. If a neutron hit the front face of the collimator, the event was rejected;
3. If a neutron cleared the entrance aperture of the collimator but not the exit aperture, the neutron was tracked to the collision point inside the collimator and  $n + Fe$  elastic and inelastic scatterings were considered;
4. If the neutron from (3) cleared the collimator exit aperture after scattering once inside the collimator, it was accepted; otherwise the neutron was rejected.

To track the neutrons of type (3), which entered the collimator and collided with the collimator inner wall, the double differential cross-sections,  $d^2\sigma/d\Omega dE$ , for  $n + Fe$  elastic and inelastic scattering were used. The differential cross-sections were obtained from the Brookhaven National Laboratory nuclear data base [84]. The angles and energies of the scattered neutrons from the collimator wall were selected according to the differential cross-sections. The scattered neutrons were tracked and tested if they cleared the collimator exit aperture. If the neutrons collided with the collimator wall more than once, the events were rejected. Over the small angular range in which neutrons could be accepted, the inelastic scattering differential cross-section is significantly smaller than the elastic scattering cross-section and the elastic scattering cross-section drops sharply when the scattering angle moved away from zero degrees. Determined by the characteristics of

the  $n + Fe$  elastic and inelastic scattering differential cross-sections and the tight geometry of the collimator, simulation results showed that, at the collimator exit, about 99% of the neutrons in the neutron beam had passed through the collimator without a collision, only 1% had undergone a single scattering with the collimator and returned to the beam, and the dominant portion of the scattered and returned neutrons were  $n + Fe$  elastic scattering events. Taking into consideration the dominance of neutrons passing the collimator without scattering and the lack of polarization information, it was assumed that the elastically scattered neutrons had the same polarization as before scattering and that the inelastically scattered neutrons lost all their polarization and became unpolarized. The effect of this assumption on the final results of the polarization distribution was estimated to be negligible by considering other extreme possibilities, i.e., assuming the polarization of both elastically and inelastically scattered neutrons was unchanged or lost totally.

Figures 4.1 (a) and (b) show the simulated horizontal neutron beam profile distributions at the profile monitor location and at the FST location, respectively, while Figs. 4.2 (a) and (b) show the neutron beam energy distribution and the correlation between the neutron beam polarization and energy, respectively. These simulated distributions were compared to the data, and good agreement between the data and the simulations was achieved (for a comparison see Chapter 5). The simulation results showed negligible non-uniformity of the energy and polarization over the FST cross-section (Fig. 4.3). A small non-uniformity of the energy distribution (i.e., within  $\pm 0.1$  MeV) does not cause an error in  $\Delta A$  since it would be the same for both the  $A_n$  and  $A_p$  measurements. Since the beam energy and polarization are correlated for the polarized beam, the effective average beam en-

ergy for a measured zero-crossing angle has to be weighted by the square of the beam polarization. For the unpolarized beam, the average beam energy is the algebraic average of the beam energy distribution. Using the simulation results for the correlation between the neutron beam energy and polarization, the effective neutron beam energy of the polarized and unpolarized beam and their difference were calculated as follows:

$$\overline{E}_{nbeam}^{polarized} = \frac{\sum P_i^2 \cdot E_i \cdot N_i}{\sum P_i^2 \cdot N_i}, \quad (4.2)$$

$$\overline{E}_{nbeam}^{unpolarized} = \frac{\sum E_i \cdot N_i}{\sum N_i}, \quad (4.3)$$

$$\Delta \overline{E} = \overline{E}_{nbeam}^{polarized} - \overline{E}_{nbeam}^{unpolarized} = 0.54 \text{ MeV}. \quad (4.4)$$

The error due to this difference was corrected for in the difference of the zero-crossing angles and the analyzing powers (see Chapter 5). The average of the effective spin transfer parameter,

$$(\sqrt{r_t^2 + r_t'^2})_{avg} = \frac{\sum (\sqrt{r_t^2 + r_t'^2})_i \cdot N_i}{\sum N_i} = -0.854. \quad (4.5)$$

The statistical errors in the Monte Carlo simulation associated with these parameters are negligible.

## 4.2 np Coincidence Events

Monte Carlo simulations for the  $np$  coincidence were essential to the experiment. They were used to optimize the experimental setup and, more importantly, to correct the measured proton kinematical variables to obtain these variables at the scattering vertices. The proton angles and kinetic energies measured from the DLCs and TOF telescopes were different from what they were at the scattering vertices within the FST. This is because the recoil proton tracks were deflected by

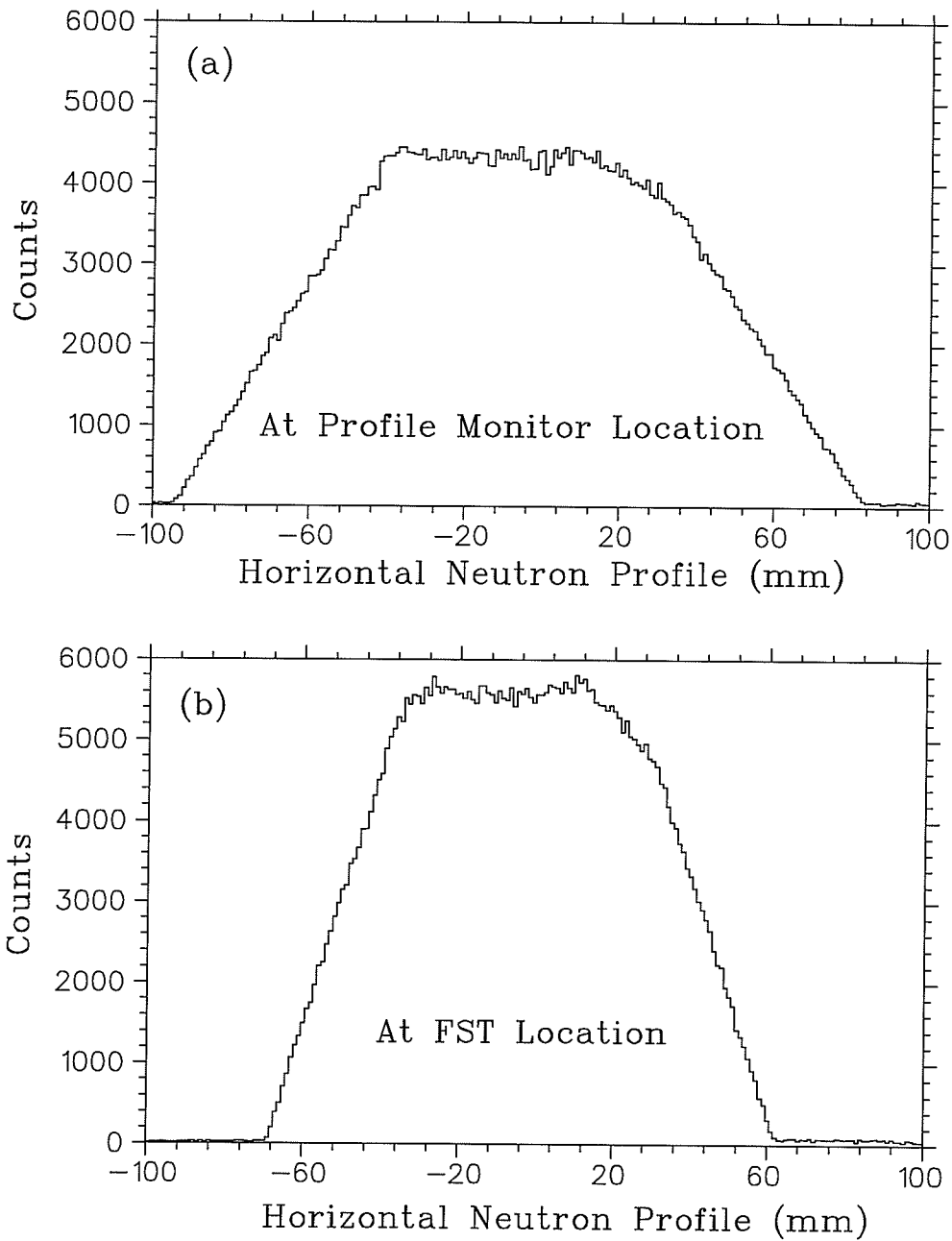


Figure 4.1: *Simulated distributions of the horizontal neutron beam profiles (a) at the profile monitor location; and (b) at the FST location.*

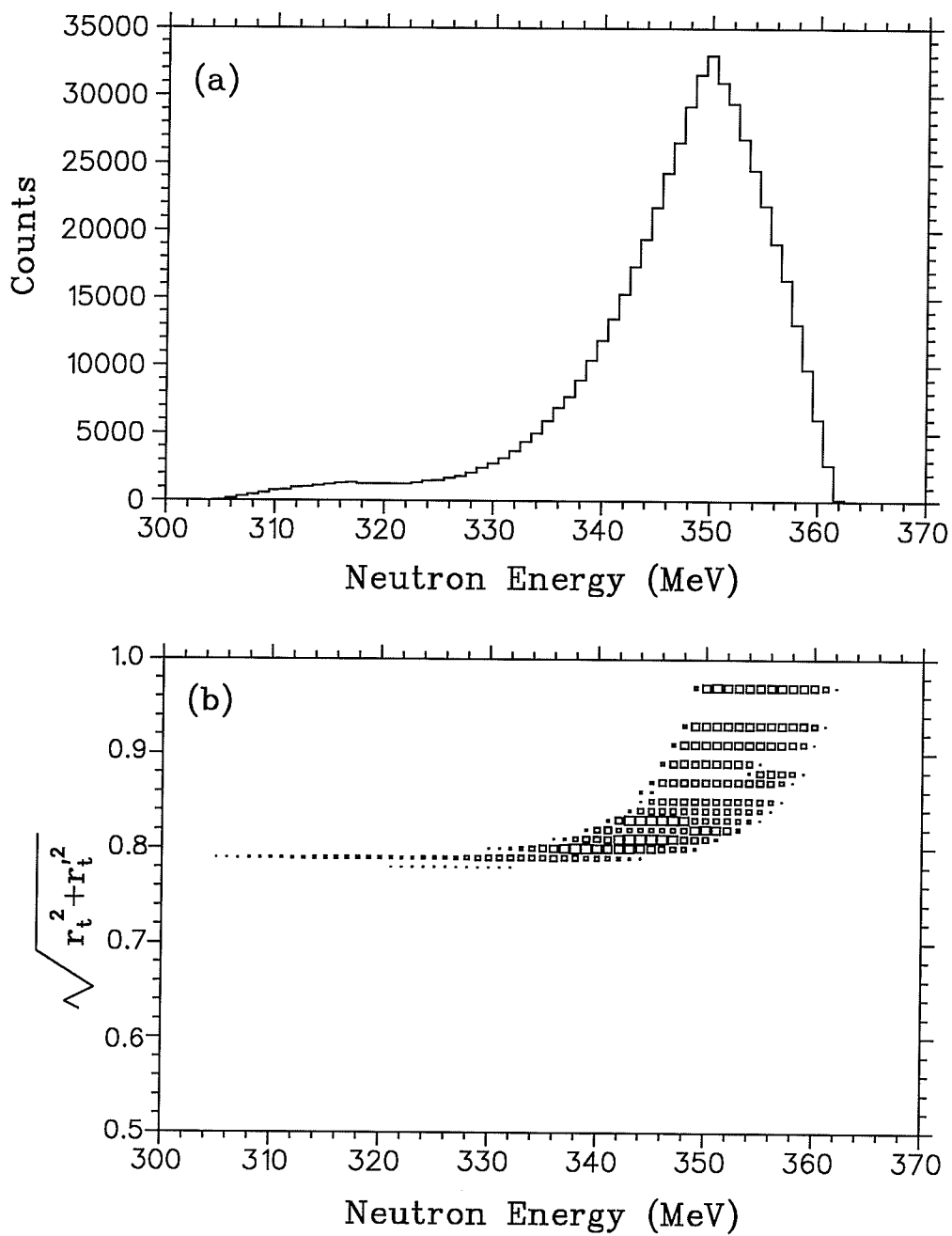


Figure 4.2: (a) simulated neutron beam energy distribution; and (b) the correlation of the neutron beam energy and polarization. The neutron beam polarization, the proton beam polarization and the spin transfer parameters are related by  $P_n = \sqrt{r_t^2 + r_t'^2} \cdot P_p$ .

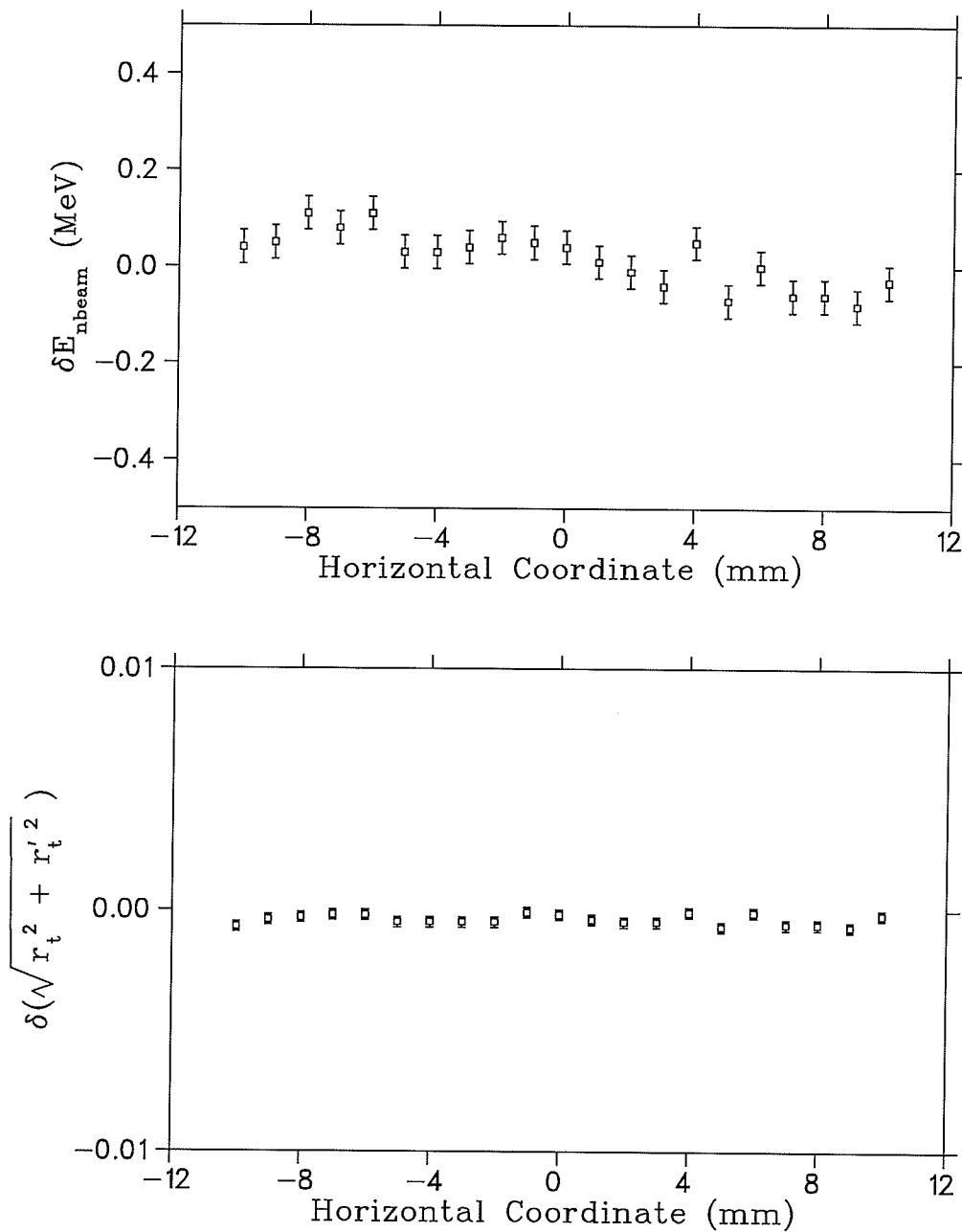


Figure 4.3: (a) a simulated distribution of the variation of the neutron beam energy profile at the FST location; and (b) a simulated distribution of the variation of the neutron beam polarization profile at the FST location.

the FST holding field, and the protons underwent energy loss and multiple scattering within the FST, surrounding materials and the detection system. The proton kinematic variables were required in conjunction with the neutron kinematic variables to distinguish the elastic scattering events from the quasi-elastic background.

The Monte Carlo simulations accounted for all the target and detector geometrical positions, their composition, and the holding field strengths as present during the data taking. The simulations started with a neutron beam along the  $z$  direction with an energy distribution obtained from the neutron beam properties simulations (see previous section). The  $np$  scattering vertices were selected uniformly within the FST volume, and the scattering angles were chosen from the elastic scattering differential cross-sections given by SAID [69]. The neutrons and protons generated were tracked through the target and to the respective detectors where they were “detected”. Fig. 4.4(a) displays a cross-section view of the FST in the  $zx$  plane. The trajectory in the target was broken into small steps (i.e., 2 mm) in which energy loss, multiple scattering and field deflection were calculated. The dots along the trajectory show the interaction points of the protons during their propagation through the target. Following the escape from the target, the calculation proceeded to track the protons in the holding field and in each of the concentric cylindrical obstacles in the target housing. Proton energy loss and multiple scattering was computed for each obstacle. After the outer vacuum can, the protons were tracked through the telescopes. Deflection in the holding field was accounted for to the last DLC; energy loss and multiple scattering were computed in each detector as well as in the air. If the proton reached the  $E_{II}$  counter, the initial and final values of the kinematical variables were logged for later processing (Fig. 4.4(b)). In the calculation of the  $np$  coincidences, the neutrons were tracked

to the neutron arrays. If a track intersected the array, the length of the track within the bank was computed, and a weight approximating the detection probability (efficiency) was used to evaluate the "detection" of the coincident neutron.

The proton deflection in the holding field of the FST was treated using Runge-Kutta solutions of the proton trajectories. Use was made of the routines supplied by Press et al. [85]. The holding field strength obtained from the field mapping was used to calculate the deflection (as shown in Fig. 3.16). Figure 4.5 (a) shows the computed angular deflection experienced by protons travelling through 2 m in the magnetic field.

The energy loss was computed using both Janni's compilations [86] and the TRIUMF energy loss program LOSSPROG [83]. Functions were constructed to interpolate the energy as a function of the range in a given material and vice versa. Figure 4.5 (b) displays the energy loss curve for the protons in the target. The large variation of the energy loss in the target was due to the path length differences of the protons exiting the target.

Multiple scattering was treated using Marion and Zimmerman's [87] energy dependent Gaussian approximation to the theory of Nigam, Sundaresan and Wu (NSW) [88]. The target material was assumed to consist of a compound of 59% butanol and 41% liquid helium by volume. The value  $Z$  for the atomic number was computed from Bragg's rule and was taken as 5.62. The value of the atomic number was then matched so as to reproduce the estimated radiation length of this compound ( $43.8 \text{ g/cm}^2$ ). Calculations were also performed by splitting the FST material into its atomic components; this method did not produce substan-

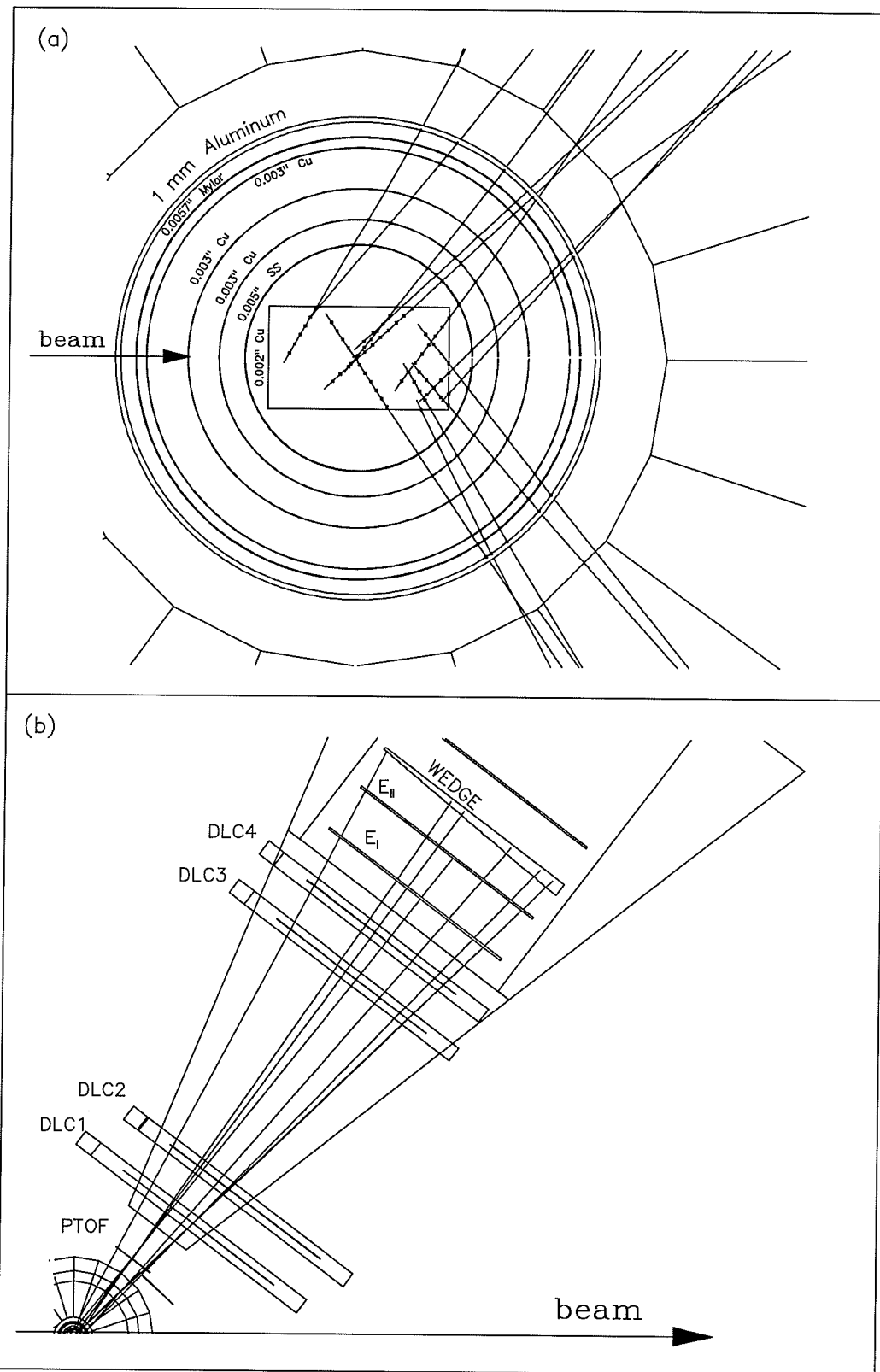


Figure 4.4: (a) cross-section view of the FST; and (b) recoil proton tracking. The tracks are the simulated proton tracks originated from locations inside the target.

tial differences relative to considering the material as possessing a single  $Z$  and  $A$ . Figure 4.5 (c) shows the energy dependence of the angular distribution width (standard deviations) for the target material. The multiple scattering was computed by recomposing the proton's velocity vector in a cone about its initial direction, using a polar angle chosen from the multiple scattering distribution with an appropriate  $\sigma$ , and an azimuthal angle chosen uniformly on  $(0, 2\pi)$ .

For the simulated  $np$  coincidences, with protons and neutrons "detected" in the proton telescopes and the neutron arrays, respectively, histograms were made for their kinematic variables at the scattering vertices and compared to the experimental data. The distributions of these variables are shown in Fig. 4.6. Good agreement was reached between the simulated data and the experimental data after applying corrections for the proton deflection, energy loss and multiple scattering (for a comparison see Chapter 5).

To obtain the proton kinematic variables (angles and kinetic energies) at the scattering vertices, correction functions were required to relate the measured kinematic variables to their values at the vertices:

$$\bar{\theta}_{scattered} = f_1(\theta_m, p_m), \quad (4.6)$$

$$\bar{E}_{scattered} = f_2(\theta_m, p_m), \quad (4.7)$$

where, the subscript "m" denotes the "measured" variables,  $\theta$  and  $p$  stand for the polar angle and momentum, respectively. The correction functions were constructed from the average effect of the proton deflection, energy loss and multiple scattering. These functions were applied to the data on an event-by-event basis. A given measured angle and momentum followed from a distribution of the initial scattering angle and momentum and vice versa. One-to-one correspondence was

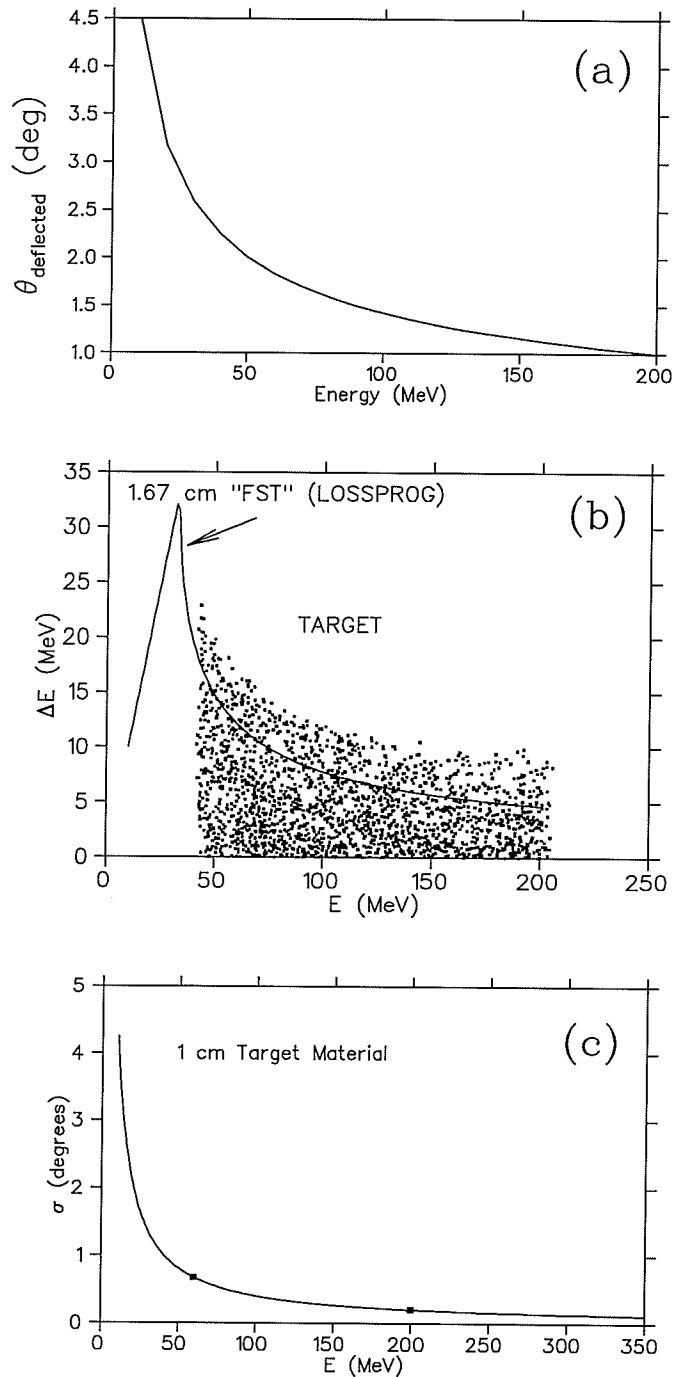


Figure 4.5: (a) holding field deflection; (b) energy loss and (c) the width (standard deviations) of multiple scattering of recoil protons as functions of recoil proton energy; the recoil proton kinetic energy ranges from approximately 50 to 200 MeV as indicated in (c); the scatter plot in (b) shows the different energy losses due to the different scattering points inside the FST volume.

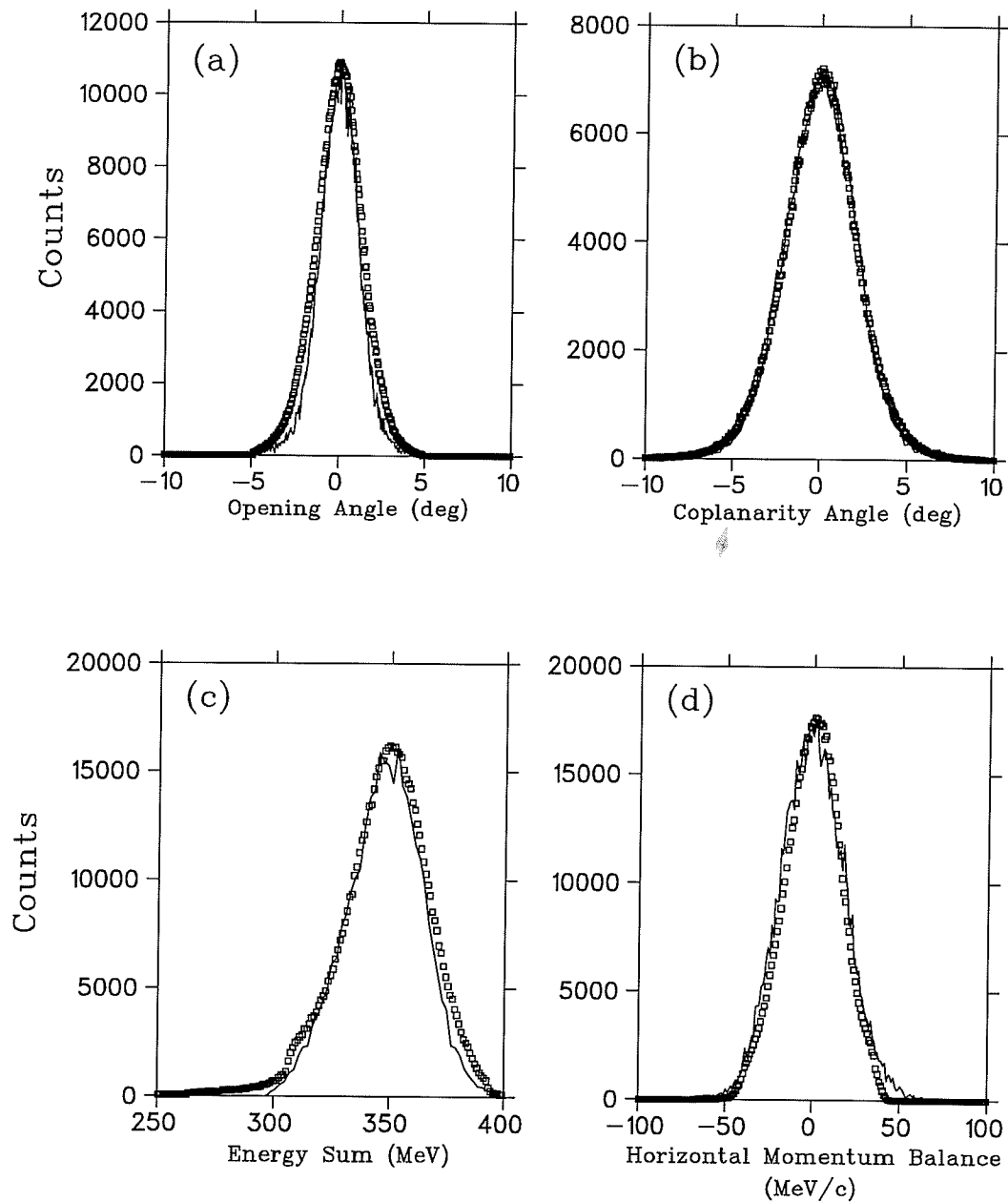


Figure 4.6: *Simulated kinematical variable distributions (connected) and a comparison to the distributions of data (discrete) (a) opening angle (b) coplanarity angle (c) energy sum and (d) horizontal momentum balance. See Chapter 5 for details.*

required from the measured values to the centroids of the corresponding distributions at the initial scattering vertices. The initial and final values of the proton angles and energies of the simulated data were used. The centroids of the distributions of the final states (the simulated “measured” values) were fitted to functions having an one-to-one correspondence to a set of initial values at the scattering points (Fig. 4.7 ). These functions were chosen to have the following forms:

$$\bar{\theta}_{scattered} = f_1(\theta_m, p_m) = \sum_{i=0}^3 \sum_{j=0}^3 A_{ij} \theta_m^i \frac{1}{p_m^j} \quad (4.8)$$

$$\begin{aligned} \bar{E}_{scattered} &= f_2(\theta_m, p_m) \\ &= (p_m^2 + m_p^2)^{1/2} - m_p + C_1 + \\ &\quad \frac{A_1}{\beta_m^2} (B_1 + 2 \ln(\beta_m^2 (\gamma_m^2 - 2))) \left( \frac{1}{\sin(\theta_m/2)} + \frac{E_1}{\sin(\theta_m/2)^2} \right) \end{aligned} \quad (4.9)$$

where the coefficients  $A_{i,j}$ ,  $A_1$ ,  $B_1$ ,  $C_1$ ,  $E_1$  (with proper dimensions) were determined from the fit. The subscript “m” denoted the measured quantity,  $\beta_m$  and  $\gamma_m$  are the usual kinematic variables. These functions were applied to the measured values of the data to obtain the proton kinematic variables at the scattering vertices in the FST (see Chapter 5). The correction on the angles ranged from 1.0° to 1.8°, and the energy correction ranged from 8 MeV to 20 MeV.

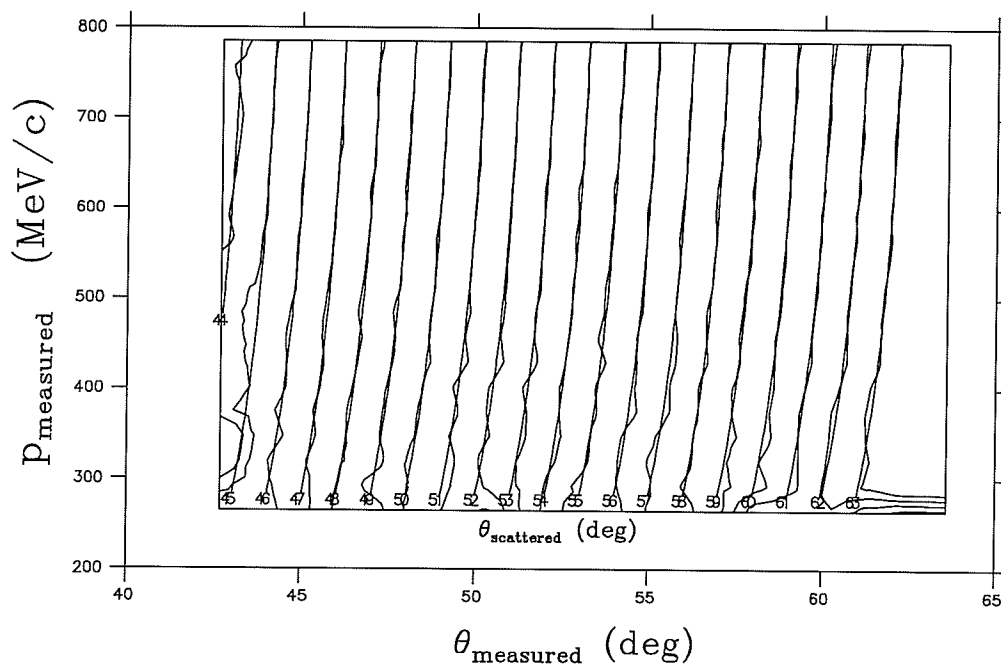


Figure 4.7: *The scattering angles at the vertices versus the measured proton momenta and angles, giving the correspondence of the measured proton variables to their value at the scattering point. The smoother curves in the frame are from a fit to the simulated curves and the scattering angles (in degrees) are also shown in the frame.*

# Chapter 5

## Data Analysis

### 5.1 General Description

As discussed in Chapters 1 and 2, the primary goal of the experiment was to determine the non-zero difference of the  $np$  elastic scattering analyzing powers,  $\Delta A \equiv A_n - A_p$  at the zero-crossing angle where  $\langle A \rangle = 0$ , and the secondary goal was to obtain the shape of the angular distribution of  $\Delta A(\theta)$  in the range covered by the detector system.  $\Delta A$  at the zero-crossing angle was calculated from the experimental measured difference of the zero-crossing angles  $\Delta\theta_0$  and  $\Delta A = -(dA/d\theta) \cdot \Delta\theta_0$  with  $dA/d\theta$  either deduced from phase shift analyses or determined experimentally. The  $\Delta\theta$  and  $\Delta A$  are expected to be small; therefore, the control of systematic errors was crucial to the success of the experiment. The general procedure of the data analysis was as follows:

1. In order to understand the sources of systematic errors, a study was made on a run-by-run basis of all the system parameters recorded during the data taking.

2. Elastic scattering  $np$  events were selected by applying appropriate cuts on the measured or reconstructed kinematic variables of the data.
3. Asymmetry angular distributions were calculated for the selected elastic scattering events, and the zero-crossing angles were obtained from least squares fitting of these angular distributions.
4. Corrections were made for the contributions from quasi-elastic ( $n, np$ ) background and for the effective average neutron beam energy difference between the polarized and unpolarized neutron beams.
5. The slope of the analyzing powers  $dA/d\theta$  was obtained from the FST polarized data using the known value of polarization. The difference of the analyzing powers,  $\Delta A$ , was calculated and the shape of  $\Delta A$  was extracted from the measured asymmetry curves and the average polarizations.
6. Systematic errors were estimated from various limits on the system parameters and tests on the data.

The following sections will describe all aspects of the data analysis listed above except the systematic errors, which will be discussed in detail in Chapter 6. The software used for both on-line as well as off-line analysis was the NOVA data analysis system [89] which is a flexible, general purpose, interactive data analysis program capable of working in the DCL environment of the VAX-VMS system.

## 5.2 System Parameter Analysis

System parameters recorded during the data taking were the proton and neutron beam polarization, proton beam energy, SEM asymmetries,  $LD_2$  target tem-

perature and pressure, proton target (FST) polarizations, holding field strength (Hall probe readings), and neutron beam profiles. Other parameters, such as the FST (target cell) spatial position, were recorded at various times during the data taking periods. Events with charged particles penetrating the neutron button counters (button events) were recorded to calibrate the horizontal positions in the neutron bars and the pulse heights. These parameters would affect the systematic errors in a very direct and dramatic way (see Chapter 6), and they were monitored on-line and kept to specified values within very tight limits. A more detailed analysis of these parameters was carried out off-line to study the sources of systematic errors. The following sections give a summary of the analysis of these parameters and show various results.

### 5.2.1 Proton Beam Energy

The proton beam energy was measured using both the left and right arms of the BEM; the average of the two arms was taken to achieve high statistics and cancel errors due to small offsets in the beam positions relative to the BEM central axis (see Section 3.4). The energy was calculated in the following way:

$$E_{ave}^{L,R} = \frac{\sum N_i E_i}{\sum N_i}, \quad (5.1)$$

$$\bar{E} = \frac{E_{ave}^L + E_{ave}^R}{2}. \quad (5.2)$$

Where  $N_i$  is the number of particles stopping in the  $i$ th scintillator,  $B_i$ , or the Cu downstream of it and  $E_i$  is the average energy of the particles whose last counter triggered is  $B_i$ . The individual  $N_i$ 's were recorded in the scalers, which were read and written to tape once every 30 seconds. The  $E_i$ 's were obtained from a calculation as described in Chapter 3. The average energy of each run, which took on average 1 to 1.5 hours of beam time, was calculated off-line. Figure 5.1(a)

shows the average beam energy of each run analyzed versus run number (run sequence number). A distribution of the average beam energy for every run is shown in Fig. 5.1(b) and yields  $\sigma = 0.038$  MeV. The absolute energy of the proton beam was not calibrated because the experiment only measured the difference of the analyzing powers at a certain fixed energy. This energy only needed to be determined absolutely to about a few MeV (see Chapter 6 for systematic errors associated with this). However, an extremely stable beam energy was crucial since the zero-crossing angles change with the beam energy. A few runs with average energies outside of the window  $\pm 0.05$  MeV were excluded from the analysis. The “absolute” proton beam energy was  $368.3 \pm 1.0$  MeV obtained from the TRIUMF cyclotron operation calibrations [90] of the beam extraction stripping foil radius  $R$  and corresponding energies. The uncertainty here is estimated from the cyclotron operation calibrations and comparisons with various experimental calibrations of the “absolute” beam energies for different experiments at different energies [91,92].

## 5.2.2 Proton Polarization

The proton beam polarization was determined by measuring the asymmetries of the proton beam scattered off the IBP and CSB polarimeter targets. The measured asymmetries were calculated from:

$$\epsilon_y = \frac{(L - L^{acc}) - (R - R^{acc})}{(L - L^{acc}) + (R - R^{acc})} - \epsilon_y^{instr}, \quad (5.3)$$

$$\epsilon_x = \frac{(B - B^{acc}) - (T - T^{acc})}{(B - B^{acc}) + (T - T^{acc})} - \epsilon_x^{instr}, \quad (5.4)$$

where L, R, B, T are the raw counts in the left, right, bottom and top counters of the polarimeters,  $L^{acc}, R^{acc}, B^{acc}, T^{acc}$  are the accidental counts in the respective counters. The instrumental asymmetries of the polarimeters,  $\epsilon_{x,y}^{instr}$  were deter-

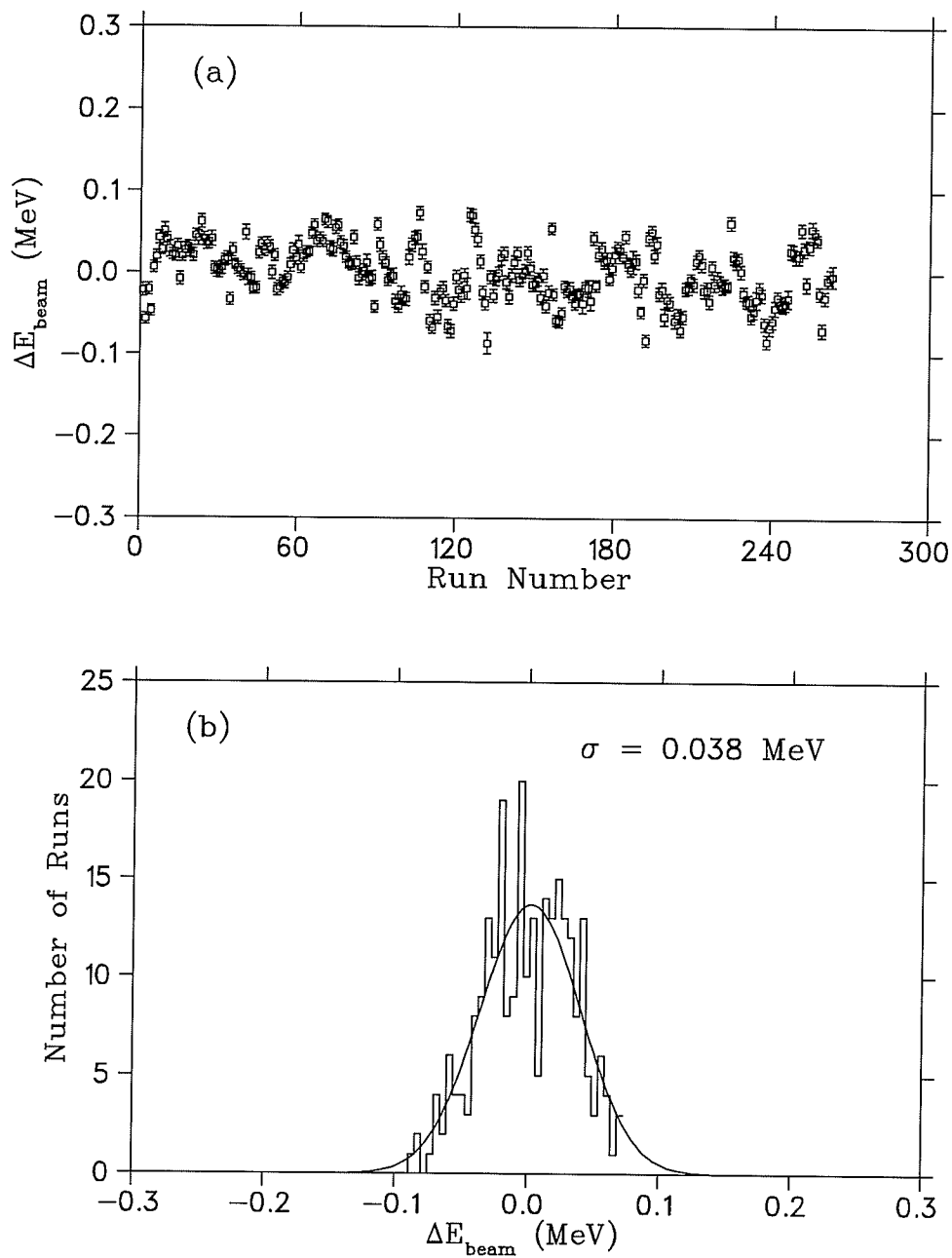


Figure 5.1: Proton beam energy distributions (offset = 366.65 MeV) (a) the average beam energy of each run as a function of time (run sequence); (b) the deviation of the average beam energy is  $\sigma = 0.038$  MeV (all runs are included).

mined from unpolarized beam data.

The measured asymmetry of a given target (Kapton,  $CH_2$  or Parylene) consisted of contributions from both the hydrogen and non-hydrogenous components in the target material. The target material could be described as  $C_xH$ , if the oxygen in the target material was assumed to behave in the same manner as carbon, e.g., the same analyzing power. The measured asymmetry could be expressed as:

$$\epsilon_{C_xH} = \frac{\epsilon_H + r \cdot \epsilon_C}{1 + r}, \quad (5.5)$$

$$\epsilon_{C_xH} \simeq \epsilon_H \left(1 - r + r \cdot \frac{\epsilon_C}{\epsilon_H}\right), \quad (5.6)$$

$$r = \frac{L_{C_xH}^C + R_{C_xH}^C}{L_{C_xH}^H + R_{C_xH}^H}, \quad (5.7)$$

where  $\epsilon_H$  and  $\epsilon_C$  are the asymmetries due to the hydrogen and carbon contents in the target, respectively and  $r$  is the ratio of the number of the observed events originating from hydrogen and carbon.

The polarization of the beam was thus calculated as:

$$P = \frac{\epsilon_H}{A_H^{PSA}} = \frac{\alpha \cdot \epsilon_H}{\alpha \cdot A_H^{PSA}} = \frac{\epsilon_{C_xH}}{A_{eff}}, \quad (5.8)$$

$$A_{eff} = \alpha \cdot A_H^{PSA}, \quad (5.9)$$

$$\alpha = \left(1 - r + r \cdot \frac{\epsilon_C}{\epsilon_H}\right), \quad (5.10)$$

where  $A_H^{PSA}$  is the  $pp$  elastic scattering analyzing power from phase shift analyses (PSA)[69]. An effective analyzing power  $A_{eff}$  was required for each target in order to calculate the polarization directly from the measured asymmetry. The effective analyzing powers were calculated based on the free  $pp$  analyzing power and a correction factor  $\alpha$  to account for the carbon content of the polarimeter targets. The correction factor  $\alpha$  was obtained from several calibration runs taken

during each data taking period with several targets, which had different fractions of non-hydrogenous contents, including very thin carbon targets. The carbon contribution of a  $C_xH$  target could be calculated from the following ratio of the carbon target measurement to the  $C_xH$  target measurement:

$$\frac{L_{C_xH}^C + R_{C_xH}^C}{L_{Carbon}^C + R_{Carbon}^C} = \frac{SEM_{C_xH}}{SEM_C} \times \frac{x \cdot t_{C_xH}}{t_C} \quad (5.11)$$

where  $SEM_i$  are the SEM counts which are proportional to the integrated beam currents with the  $i$ th target; the  $t_i$  are the thicknesses of the targets; and  $x$  the ratio of carbon to hydrogen of a target  $C_xH$ . The typical value of  $\alpha$  for the CSB polarimeter with a Kapton target was 0.98 - 0.99.

After the calibration of the polarimeters, the proton polarization can be calculated from the measured asymmetries and the effective analyzing powers. Figures 5.2(a) and (b) show the proton beam polarization as measured by the CSB polarimeter and the IBP, respectively. The ratio of the two measured polarizations is shown in Fig. 5.2(c). The two measurements agree reasonably well. There are slight differences between the two proton polarization measurements and the ratio varied slightly over the run period (typically one month for each data taking period). The IBP had larger solid angle coverage which caused higher accidental rate and non-negligible variation of the analyzing power over the polarimeter angular range. A thin Parylene target was used to lower the counting rate and hence reduce the accidentals. The residual accidentals were subtracted when the asymmetries were calculated, and the average analyzing power over the angular range after calibration was used to calculate the polarization. The difference between the two polarization measurements was possibly due to the uncertainty of the effective analyzing power over a relatively wider angular range for the IBP (compared to the smaller angular coverage of the CSB polarimeter) and the uncertainty of the

thickness of the very thin parylene target for the IBP. The change of the ratio with time shows the hydrogen loss of the IBP target. The CSB polarimeter was designed specifically for the experiment. It had smaller solid angle, and therefore was capable of handling higher beam current ( $\sim 2 \mu A$ ). Therefore, the proton beam polarization measured by the CSB polarimeter was considered more reliable than that of the IBP. This can be seen from data when the ratios of the measured neutron polarization to the measured proton polarization are formed and the different polarization measurements are cross-checked with each other (see Section 5.2.4 for distributions of the ratios of the measured neutron polarization to the measured proton polarization).

### 5.2.3 $LD_2$ Target

Density fluctuations of the  $LD_2$  target would affect the average energy of the neutron beam, and therefore, the zero-crossing angles. The temperature and the pressure of the target were monitored at regular intervals of at least every 8 hours during the data taking periods. The density of the  $LD_2$  was calculated from the recorded temperature and pressure data. The density fluctuations of the  $LD_2$  target during the data taking were all within  $\delta\rho \leq \pm 0.0005 \text{ g/cm}^3$  as shown in Fig. 5.3(a). The energy loss of the proton beam in the target depends on the target density. The variation of the average energy loss in the target was calculated from the density fluctuations (Fig. 5.3(b)). The errors in the zero-crossing angles due to this effect were estimated with  $d\theta_0/dE = -0.048^\circ/\text{MeV}$  from phase shift analyses, assuming that the average neutron beam energy had the same variation as the average proton beam energy at the center as the  $LD_2$  target (Fig. 5.3(c)).

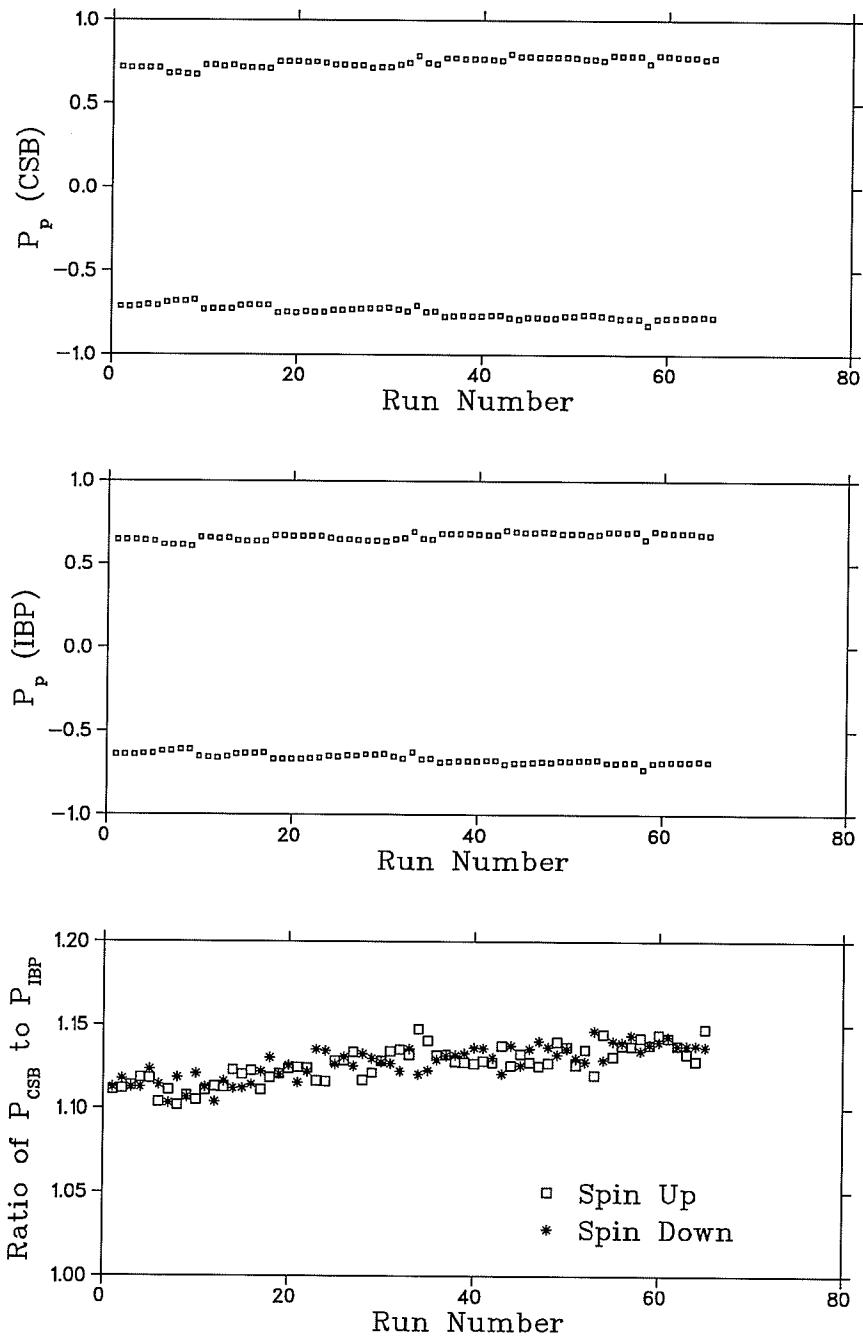


Figure 5.2: (a) and (b) distributions of the proton polarization as measured by the CSB polarimeter and the IBP versus time (run sequence) for February 1993 data taking runs; (c) the ratio of the polarization measured by the two polarimeters showing stability and consistency of the two measurements.

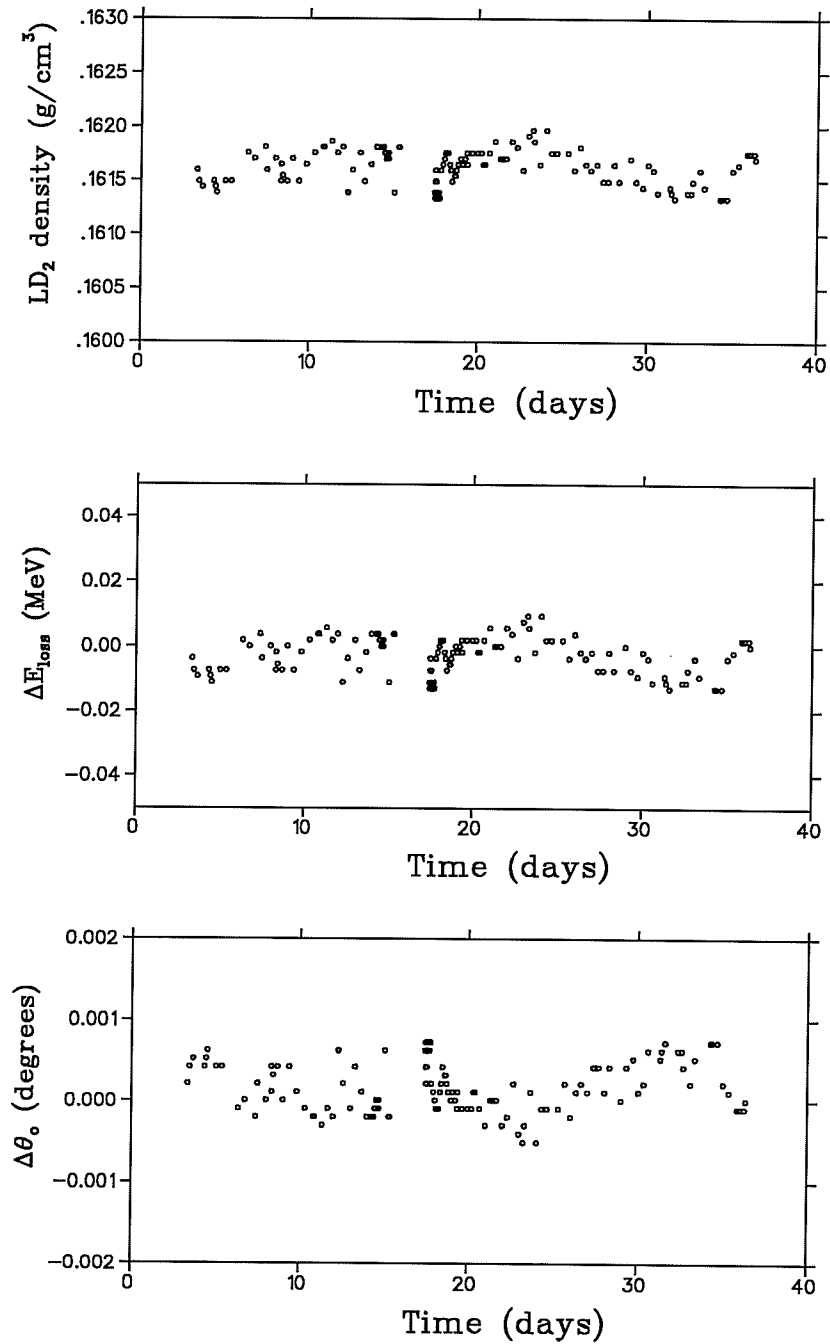


Figure 5.3: (a) the density fluctuation of the LD<sub>2</sub> versus time (February 1993 data taking period); (b) the fluctuation of the average energy loss of the proton beam due to the target density fluctuation; and (c) the predicted changes in the zero-crossing angles due to the fluctuation of the average neutron beam energy.

## 5.2.4 Neutron Beam Polarization

The neutron polarization was measured by the two neutron polarimeters. The four-branch polarimeter measured down-up and left-right asymmetries due to  $P_x$  and  $P_y$  polarization components, but not  $P_z$ , because parity conservation forbids  $P_z$  to contribute to the asymmetries. The polarization could be calculated from the measured asymmetries after correction for the instrumental asymmetry as:

$$\epsilon^{true} = \epsilon^{meas} - \epsilon^{instr}, \quad (5.12)$$

$$P_n = \frac{\epsilon^{true}}{A_{eff}}, \quad (5.13)$$

where  $\epsilon^{meas}$  is the measured asymmetry for a particular spin state,  $\epsilon^{instr}$  is the instrumental asymmetry as measured by the unpolarized beam (or the unpolarized cycle of the polarized beam) and  $\epsilon^{true}$  is the corrected asymmetry.  $A_{eff}$  is the effective analyzing power for a particular plane of the polarimeter in question. Due to the relatively poor knowledge of the analyzing power  $A_n$  of the polarimeters and due to the carbon contribution to the asymmetry,  $A_{eff}^{OLD,NEW}$  of both polarimeters were calibrated using the expected neutron polarization deduced from the measured proton polarization, the known spin transfer parameters and the spin rotation angles (see Section 3.8). Therefore, only the relative stability of the ratio,  $P_n/P_p$ , with the calibrated analyzing powers, was used to cross-check other measurements.

At the OLD neutron polarimeter location, the neutron spin polarization had a major component  $P_y$ , which was responsible for the measured left-right asymmetry:

$$P_{n,y}^{OLD} = \sqrt{r_t^2 + r_t'^2} \cdot P_p. \quad (5.14)$$

The neutrons also had a small polarization component  $P_{n,z}$  due to the param-

eter P, but it did not contribute to the asymmetries. The FST holding field rotated the  $P_{n,z}$  by a small amount (about  $4^\circ$ ,  $\int \vec{B}_{hf} \cdot d\vec{l} \simeq 2 \times 0.04 \text{ Tm}$ ) to  $P_{n,x} \simeq P \sin 4^\circ \simeq 0.0049$ . This component of neutron polarization caused a small down-up asymmetry. The calibrated effective analyzing power for the OLD neutron polarimeter was  $A_{eff}^{OLD} = 0.18 \pm 0.01$  with  $(\sqrt{r_t^2 + r_t'^2})_{avg} = -0.854 \pm 0.015$  [64,65,66]. As expected, only a few percent asymmetry was observed in the down-up scattering. At the NEW neutron polarimeter location, the neutrons had polarization components:

$$P_{n,x} = \sqrt{r_t^2 + r_t'^2} \cdot P_p \cdot \sin\psi, \quad (5.15)$$

$$P_{n,y} = P, \quad (5.16)$$

$$P_{n,z} = \sqrt{r_t^2 + r_t'^2} \cdot P_p \cdot \cos\psi, \quad (5.17)$$

$$\psi \simeq 113^\circ (\pm 2^\circ), \quad (5.18)$$

where, the angle  $\psi$  is as shown in Fig. 3.13, and the uncertainty of  $\psi$  is estimated from the calibration of the spin precession magnets (see Chapter 3 and Appendix B) and a calculation of  $\int \vec{B} \cdot d\vec{l}$  along the path of the neutron beam. The effective analyzing power of the NEW neutron polarimeter was  $A_{eff}^{NEW} = 0.20 \pm 0.01$ . At this location, a sizable down-up asymmetry was expected for a polarized beam and a small vertical asymmetry was also observed corresponding to the induced polarization from the reaction  $D(\vec{p}, \vec{n})2p$ . Figures. 5.4(a)-(d) show the various ratios of the measured neutron polarization to the measured proton polarization.

### 5.2.5 Neutron Beam Profile

The neutron beam profile monitor information was processed on-line to help re-tune the neutron beam (if necessary) to center it on the FST at the beginning

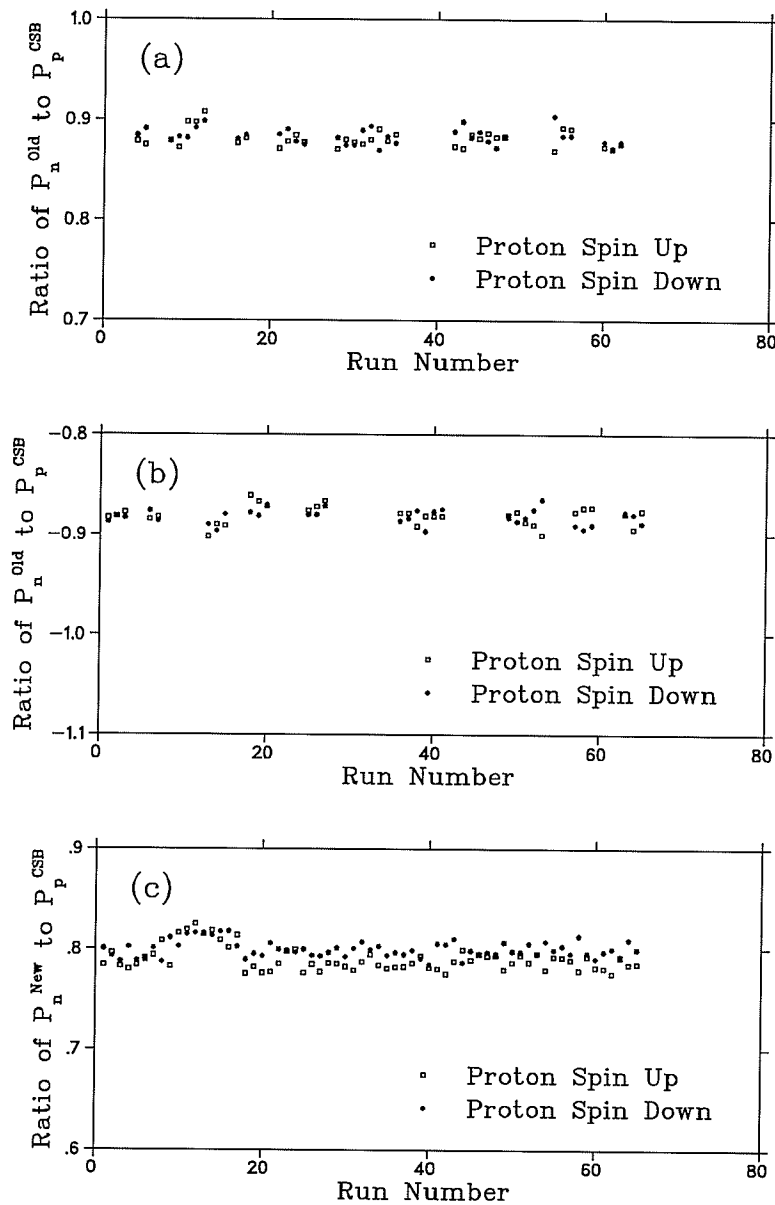


Figure 5.4: (a) and (b) the ratio of the neutron beam normal direction polarization as measured by the old neutron polarimeter for BONNIE field “Normal” and “Reversed” directions, respectively, to the proton beam polarization as measured by the CSB polarimeter; (c) the ratio of the neutron beam sideways polarization as measured by the new neutron polarimeter to the proton beam polarization; the distributions show the stability and consistency of the two neutron polarimeters and the CSB polarimeter (February 1993 data taking runs).

of each (12 hour) shift, and was monitored throughout data taking to ensure no accidental shift of the neutron beam profile occurred. The timing and pulse height signals from the neutron beam profile monitor and polarimeters were recorded as a separate event type and were processed in more detail off-line. The neutron beam profile distributions were compared to the Monte Carlo simulations (as described in Chapter 4). The neutron beam profile centroids in x and y were analyzed on a run-by-run basis to ensure that there were no systematic shifts in the profile centroids (by more than 1 mm).

To obtain the neutron profile, recoil proton tracks from the profile monitor target (converter) were reconstructed from their coordinates in the profile monitor delay line wire chambers and projected to the converter location:

$$x_c = C \cdot (x_2 - x_1), \quad y_c = C \cdot (y_2 - y_1), \quad (5.19)$$

$$x_1 = x_1^{raw} + x_1^{const}, \quad y_1 = y_1^{raw} + y_1^{const}, \quad (5.20)$$

$$x_2 = x_2^{raw} + x_2^{const}, \quad y_2 = y_2^{raw} + y_2^{const}, \quad (5.21)$$

where  $(x_c, y_c)$ ,  $(x_1, y_1)$ ,  $(x_2, y_2)$  are coordinates at the converter, and the front and rear chambers, respectively (see Fig. 3.12).  $C$  is a constant giving the projection back to the converter location and is determined by the profile monitor geometry. The constants  $(x_1^{const}, y_1^{const})$ ,  $(x_2^{const}, y_2^{const})$  were determined by the chamber calibrations. A plastic cross, which had its center aligned to the beam axis and two arms aligned to the x and y axes, respectively, was used to calibrate the observed centroids of the chambers and the profile (Figs. 5.5(a)-(c)). This calibration of the centroids was checked by a steel I-beam which was aligned to the beam height (top surface) and the horizontal center (Fig. 5.5(d)). Figures 5.6(a)-(d) show the vertical and horizontal neutron beam profile at the location of the profile monitor and a comparison with the Monte Carlo simulations as shown in Chapter 4. It

was noticed that the horizontal neutron beam profile was displaced towards the right (negative x direction) by about 8 mm. Monte Carlo simulations showed that this displacement was due to a misplacement of the  $LD_2$  target cell by about 6 mm downstream along the proton beam axis. The actual physical location of the  $LD_2$  cell was surveyed and confirmed to be displaced downstream along the proton beam axis by  $6.2 \pm 3.9$  mm. At the FST location, the horizontal beam profile had a "flat" top region (above 90% intensity) of approximately 80 mm wide which was wide enough to cover the whole FST width, even with the beam displacement, and small enough to cause negligible illumination of surrounding materials. This displacement did cause a small error in the beam direction (8 mm/12.85 m), but it was a constant error throughout the experiment and caused a negligible error in the zero-crossing angle difference (see Chapter 6 for details in systematic errors). The vertical beam profile had a "flat" top (above 90% intensity) about 55 mm at the FST location which was sufficient to cover the whole target cell containing the beads, but small enough to cause negligible illumination of the surrounding materials, and therefore, to minimize the background.

### 5.2.6 SEM Asymmetry and Beam Position Stability

The SEM left-right (horizontal) and bottom-top (vertical) asymmetries were calculated from their integrated current signals every 5 seconds. The analog asymmetry signals were sent to the feedback system and after digitization were recorded on tape. The SEM asymmetries were calibrated with respect to beam position offsets by steering the beam away from the established center position by a known amount. The beam position was determined by a beam profile wire monitor. This calibration gave an estimate of the SEM asymmetry with about 0.15 correspond-

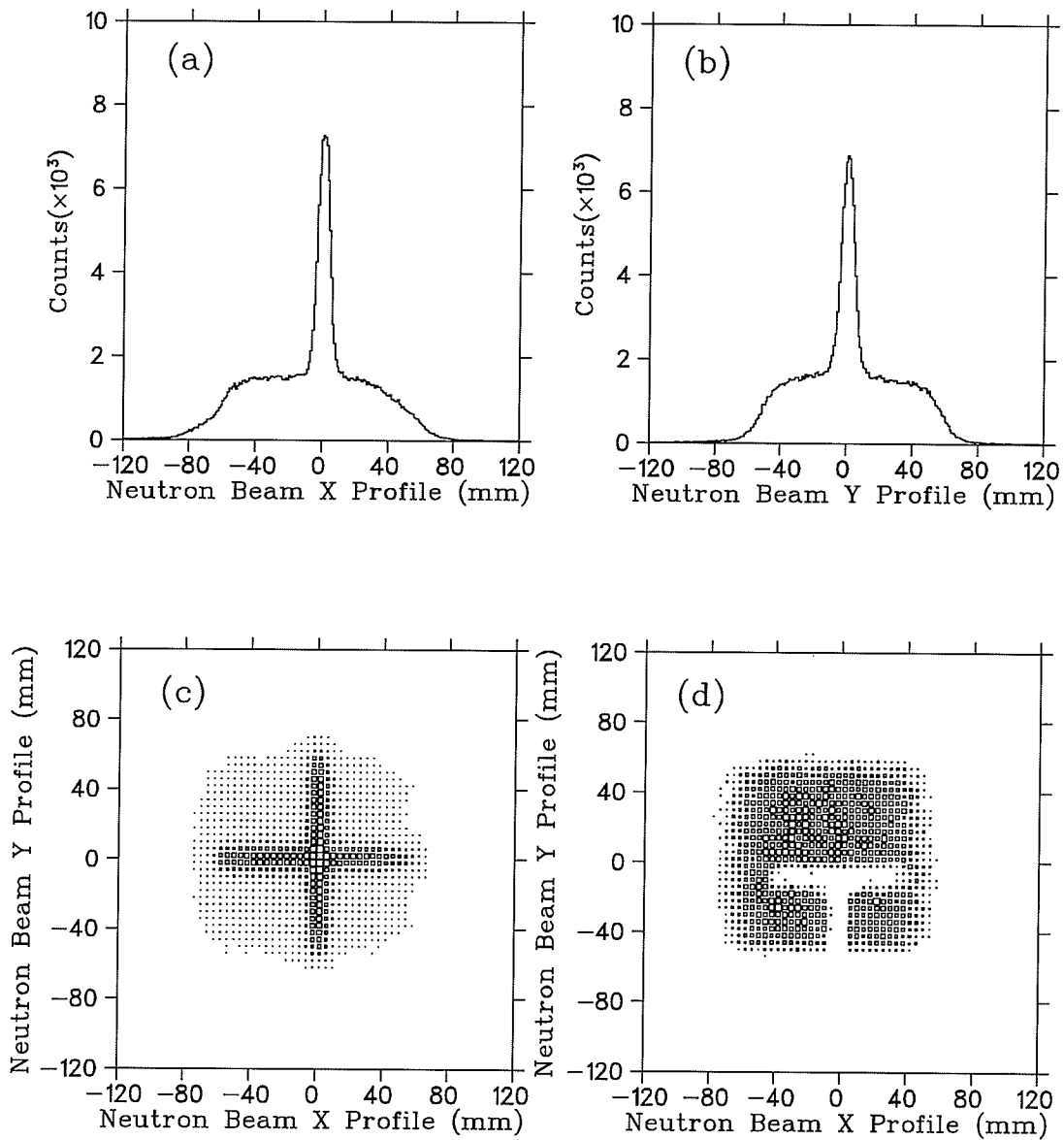


Figure 5.5: (a)- (c) the neutron beam profile with a plastic cross centered along the beam axis to calibrate the profile monitor chambers. and (d) the calibration checked by a steel I-beam with top surface aligned at the beam height and centered in the horizontal direction.

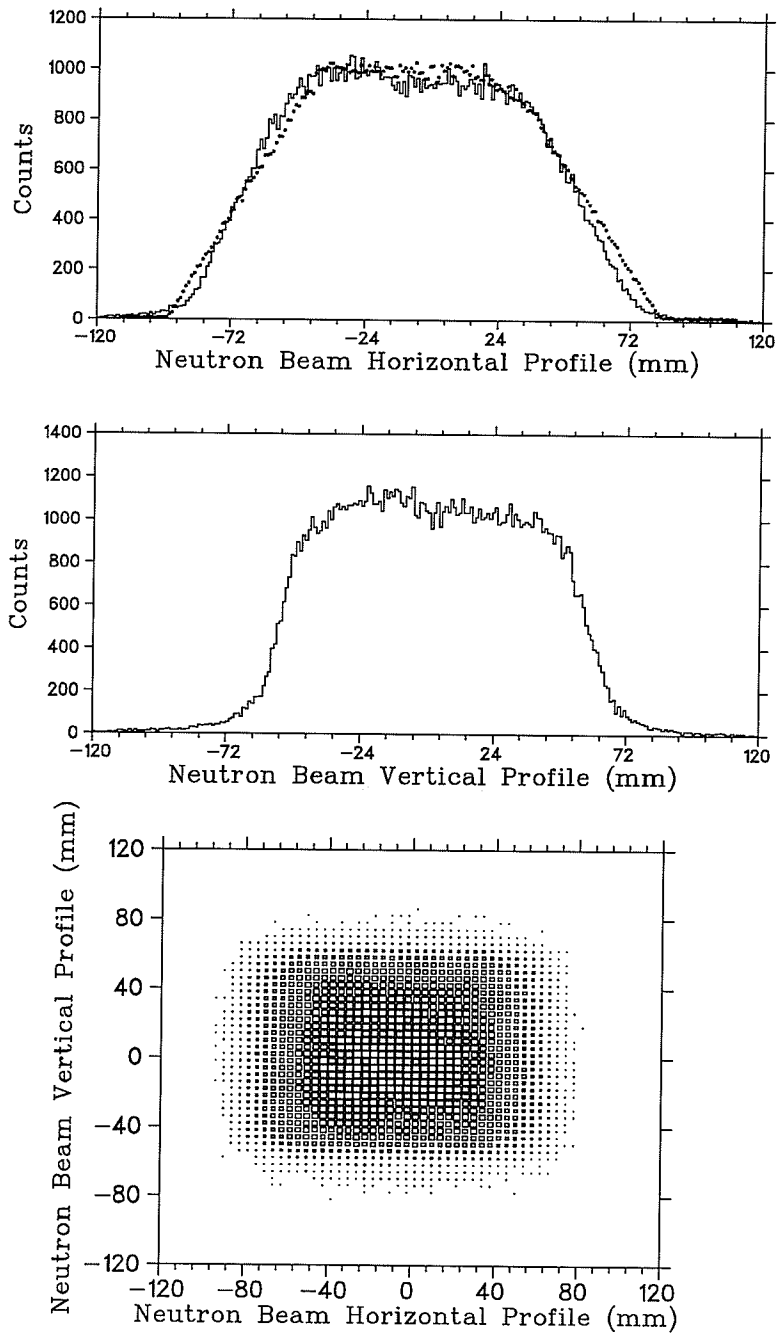


Figure 5.6: (a) horizontal neutron beam profile at the profile monitor location compared to a Monte Carlo simulation, the connected curve represents the data and the discrete curve the simulations; (b) vertical neutron beam profile; (c) neutron beam intensity distribution in the  $x$ - $y$  plane.

ing to a beam centroid offset of  $\sim 1$  mm. Figures. 5.7 (a) and (b) show the vertical and horizontal SEM asymmetries as measured by the first and second SEMs as a function of run number. A beam position stability of better than 0.03 mm was achieved. This implied the stability of the proton beam direction better than  $\pm 0.002^\circ$ .

### 5.2.7 FST Holding Field, Polarization and Position

The FST holding field strength was kept stable and monitored by two Hall probes located one above and one below the target cell. The Hall probe readings were recorded on tape and analyzed off-line. The calibration constants of the Hall probes with zero holding field were obtained before and after every FST polarized shift. The measured holding field strength (Fig. 5.8) showed that a stability and reproducibility of  $\pm 0.3$  mT (the average of the two Hall probe readings) was achieved after the calibration constants were subtracted.

The FST polarization was measured at the beginning ( $P(t_1)$ ) and at the end ( $P(t_2)$ ) of each polarized target shift with a calibrated NMR system. An exponential function was used to interpolate the average polarization for each run:

$$P(t) = P(0) \cdot e^{-\frac{t}{\tau}}, \quad (5.22)$$

$$\tau = \frac{t_2 - t_1}{\ln(P(t_1)/P(t_2))} \quad (5.23)$$

The NMR system was calibrated several times before, between and after each data taking period as described in Chapter 3. Four thermal equilibrium (TE) calibrations were performed during the February, 1993 data taking period. The largest difference in different NMR calibrations was 0.59%. This included the accuracy of

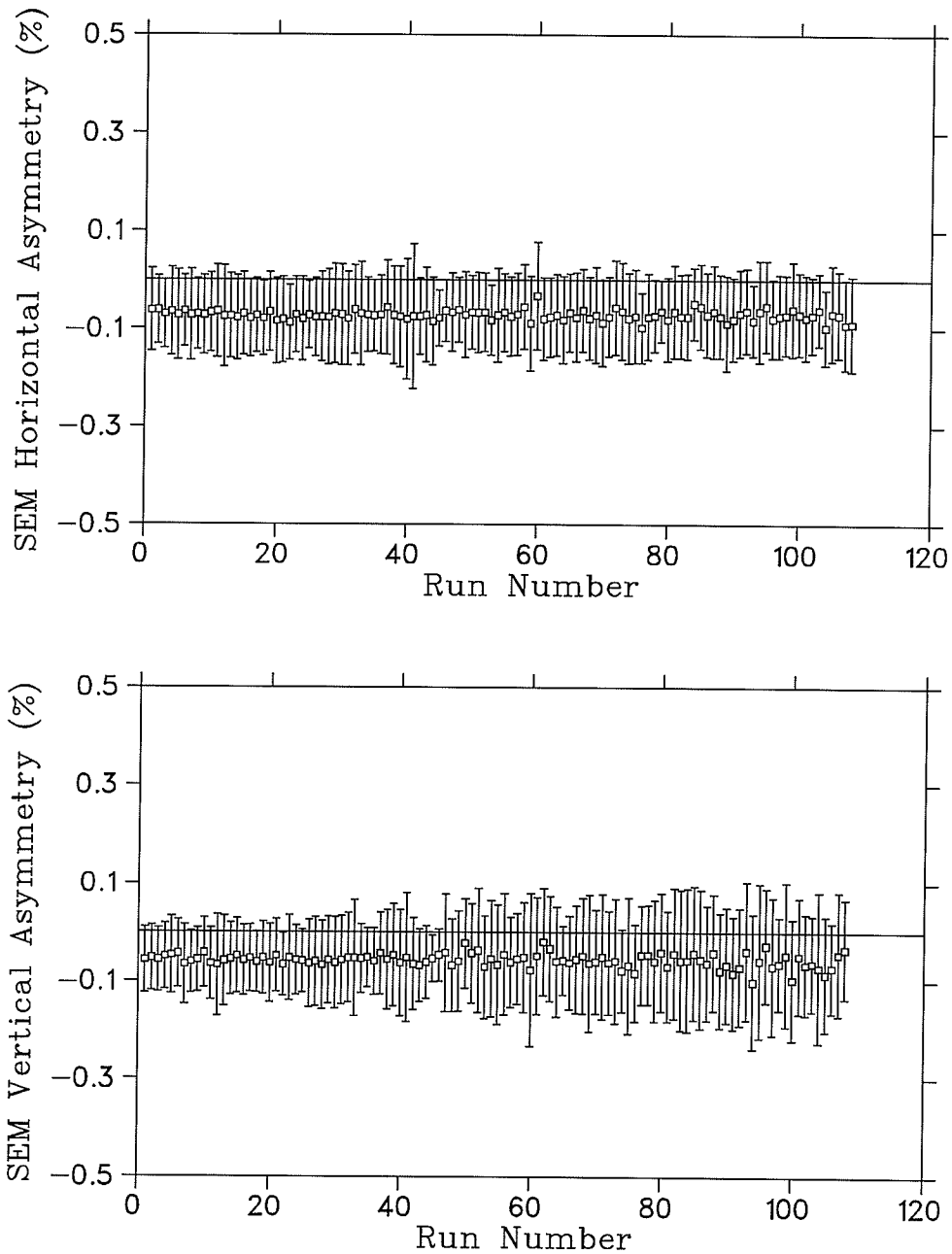


Figure 5.7: (a) and (b) the SEM horizontal and vertical asymmetries, respectively, versus run sequence number (February 1993 data taking runs). Each data point represents the centroid and  $\sigma$  of the variation of SEM asymmetries over a run period. The consistent small negative values of the centroids are due to the granularity of the digitizing in the controlling system.

a germanium thermometer which was calibrated with a  $^3\text{He}$  vapour pressure thermometer and showed the calibration temperature to be  $1.36 \pm 0.01$  K. An error of 2% was estimated for polarizations measured during the February 1993 data taking period. This estimate was based on a comparison to the earlier calibration of the NMR system in an *pp* elastic scattering experiment to an accuracy of 2.6% where the error was dominated by the reproducibility of the NMR value ( $\pm 2\%$ ). Since there was only one TE calibration of the NMR system performed during the August 1992 data taking period, the overall FST polarization measured in the current experiment was estimated to be known to better than  $\pm 3\%$ . Polarizations as high as 85% - 90% and decay times of greater than 200 hours were achieved. The average FST polarization of the February 1993 data was 85.6%, which was used to determine the slope of the analyzing power  $dA_p/d\theta$  (see Section 5.7). The average FST polarization of all the polarized target data was 73.2%.

The dimensions and the positions of the FST beads were surveyed during and after each data taking period by X-ray radiography. The measured offsets (table 5.1) of the FST beads and container from the target central position were taken into account in the subsequent data analysis.

### 5.2.8 Neutron Detector Position and Gain Calibration

Charged particles penetrating the small "button" counters behind the neutron arrays were recorded as "button" events (for a diagram of the neutron detector arrays see Fig. 3.18). The button events were analyzed on a run-by-run basis to calibrate the neutron timing and photonmultiplier tube (PMT) gain shifts.

The time difference between both ends of each bar for "button" events gave

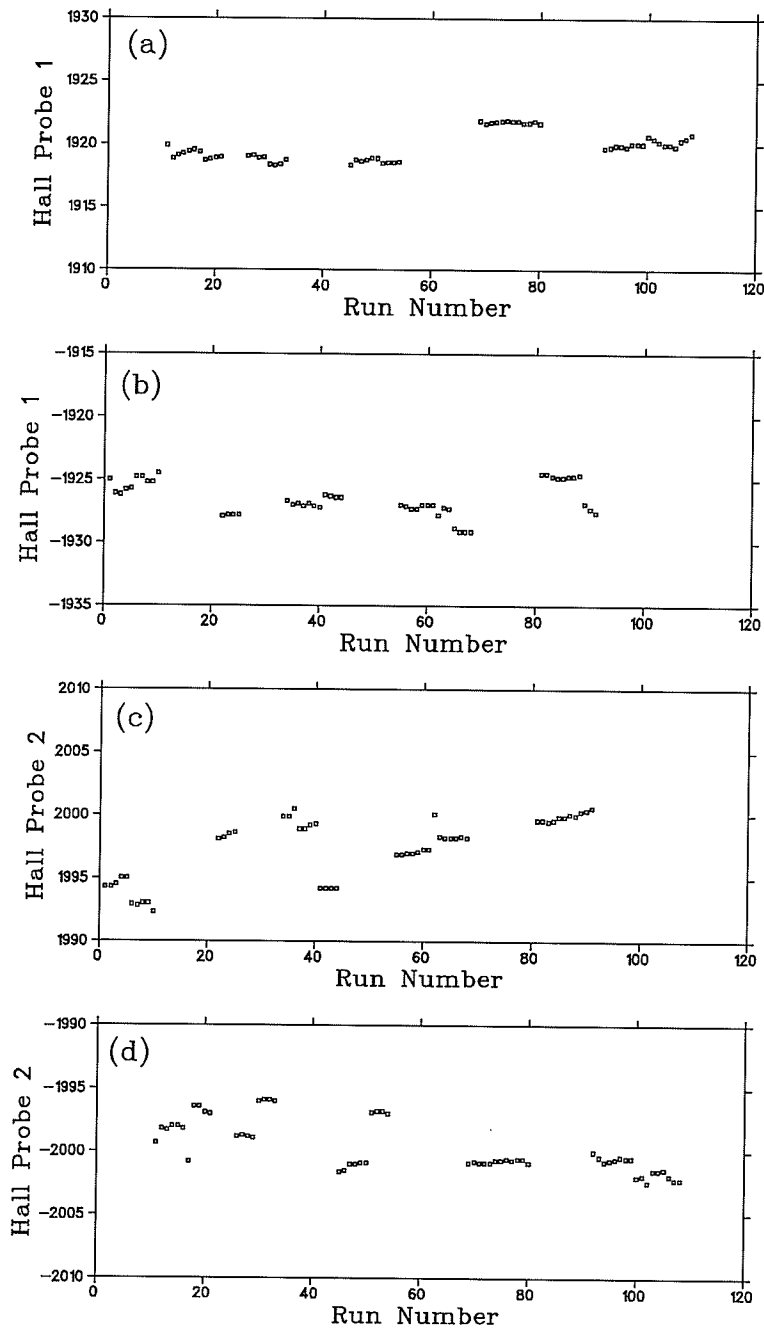


Figure 5.8: *Hall probe readings showing the stability of the FST holding field; (a) and (b) are Hall probe 1 readings for the holding field directions up and down, respectively; (c) and (d) are Hall probe 2 readings for the holding field directions up and down, respectively (February 1993 data taking runs).*

Table 5.1: *FST position offsets ( in mm). The uncertainty of the position determination from X-ray radiography was about  $\pm 1.0$  mm or better.*

Date	x	y	z
19 August 1992	-1.0	2.0	-2.0
2 September 1992	-0.5	-1.0	-1.5
4 February 1993	1.0	-1.3	-1.5
17 February 1993	1.3	-1.3	-0.5
3 March 1993	1.5	-2.3	-1.5

a calibration of the horizontal positions in the neutron bars (see next section for neutron bar position determination). A position resolution of  $\sigma = 16$  mm was determined from the observed position differences of the button events in the front and rear banks of the bars (Fig. 5.9).

The kinematically (by angle and energy) well-defined charged particles corresponding to the button events deposited a fixed amount of energy each scintillator bar, and therefore they could be used to calibrate the pulse height of each PMT. During the data taking, high voltages on the PMTs were adjusted to match the gains; this was done by matching the centroids of the ADC distributions of the button events. The nominal centroids after pedestal subtraction were 350, 500, and 500 ADC channels for the front, rear and “new” bars, respectively. Small differences in the pulse heights (typically around  $\pm 10$  ADC channels) between high voltage adjustments were recorded during the data taking. A pulse height (ADC) re-scaling was performed during the off-line analysis based on the centroids of the button event ADC distributions. The various centroids were matched to better

than 1 ADC channel (Fig. 5.10).

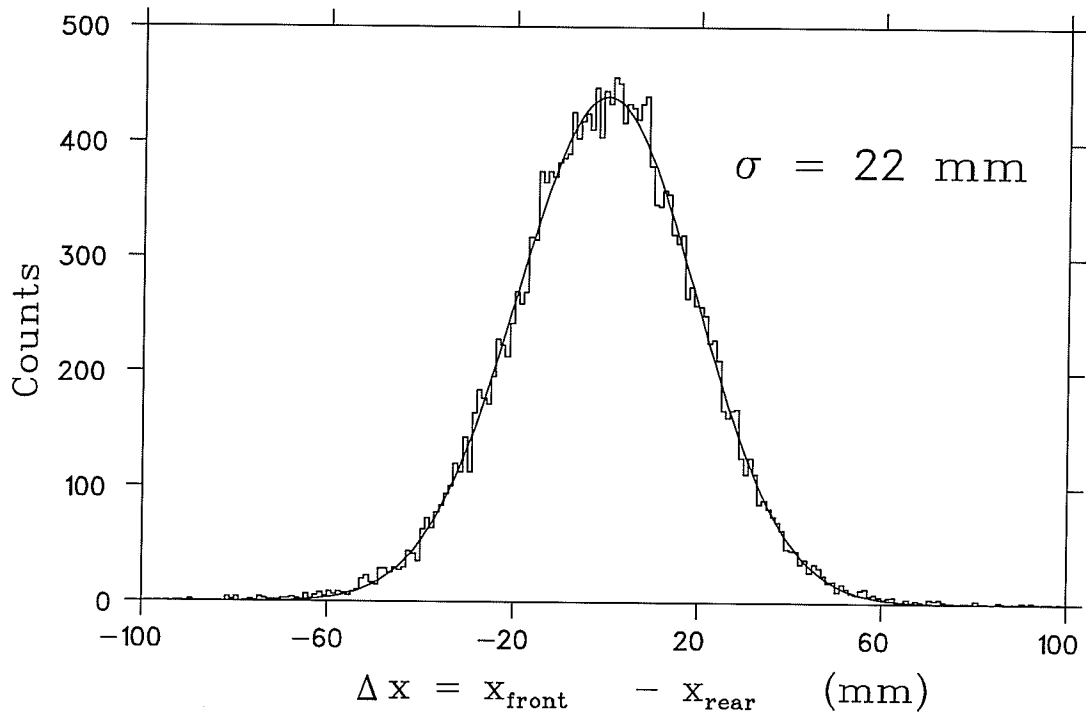


Figure 5.9: *The difference of the measured horizontal positions of the button events in the front and rear banks of the neutron bars.*

## 5.3 Selection of Elastic Scattering $np$ Events

### 5.3.1 Proton Track Reconstruction

The recoil proton tracks were reconstructed from their signatures in the delay line wire chambers, i.e., the “true” horizontal and vertical coordinates  $x$  and  $y$  in mm of a hit in any of the eight DLCs (see Fig. 3.1 and 3.18). To determine the “true” coordinates in the DLCs, geometrical and measured pulser positions were used as reference points. Pulser events were analyzed on a run-by-run basis. From the raw TDC values from the top (T), bottom (B), left (L), and right (R)

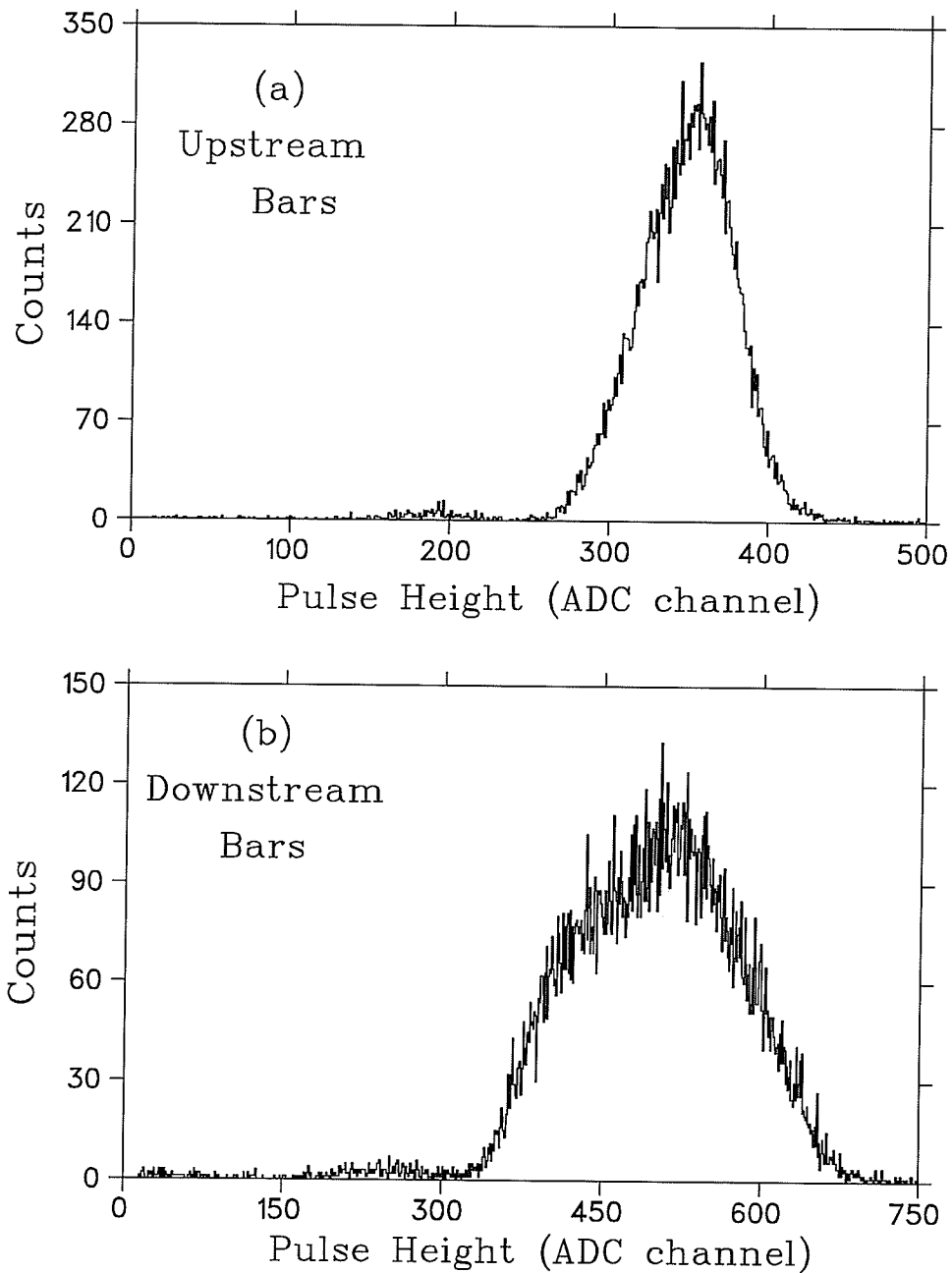


Figure 5.10: (a) and (b) typical scaled pulse height distributions of the button events in the front and rear bars, respectively. The centroids of the distributions were scaled to  $350 \pm 1$  and  $500 \pm 1$  ADC channels, respectively. The wider distribution in (b) than the one in (a) is because charged particles interacted with the up-stream bars (e.g., energy loss and multiple scattering) before they reached the downstream bars.

discriminators of each chamber, the time difference between the respective ends gave the pulser positions in TDC channels ( 1 TDC channel = 0.5 ns ). Special care was taken to observe any unexpected large changes in the apparent pulser positions as well as in the width of the pulser peaks. Figure 5.11 (a) shows a time difference spectrum of the pulser events. The typical widths of the pulser peaks were  $\sigma = 0.5 - 1.0$  ns which gave an error of the mean of 0.005 - 0.010 ns for a typical run. The separation of two pulser peaks in terms of the delay line time difference was about 1550 ns. The physical separation of the pulser positions was  $552.5 \pm 0.7$  mm [76].

In the horizontal direction, the “picket fence” structure of the anode wire image was used to determine the absolute positions and separations of the two pulsers when the DLCs were fully illuminated and all the “pickets” (291) and pulser peaks were observed (Fig. 5.11 (b)). This gave somewhat more accurate pulser positions than the blueprint specifications,  $552.5 \pm 0.7$  mm (for details see Appendix A). Table 5.2 lists the horizontal pulser separations as determined from the DLC calibrations. For the vertical direction, a pulser separation of 552.5 mm from the design note [76] was used in the analysis. The physical separation of the pulser locations (in mm) and the observed separation in time difference (in ns), gave the time-to-distance conversion factors, which were used to calculate the spatial coordinates:

$$\frac{dx}{dt} = \frac{\Delta x}{\Delta t_x} = \frac{\Delta x_{pulser}}{t_{R,P} - t_{L,P}}, \quad (5.24)$$

$$\frac{dy}{dt} = \frac{\Delta y}{\Delta t_y} = \frac{552.5 \text{ mm}}{t_{B,P} - t_{T,P}}, \quad (5.25)$$

where  $t_{i,P}$  refer to the TDC values of the pulser events at the respective ends.

The apparent position of a hit was calculated from the time difference of the

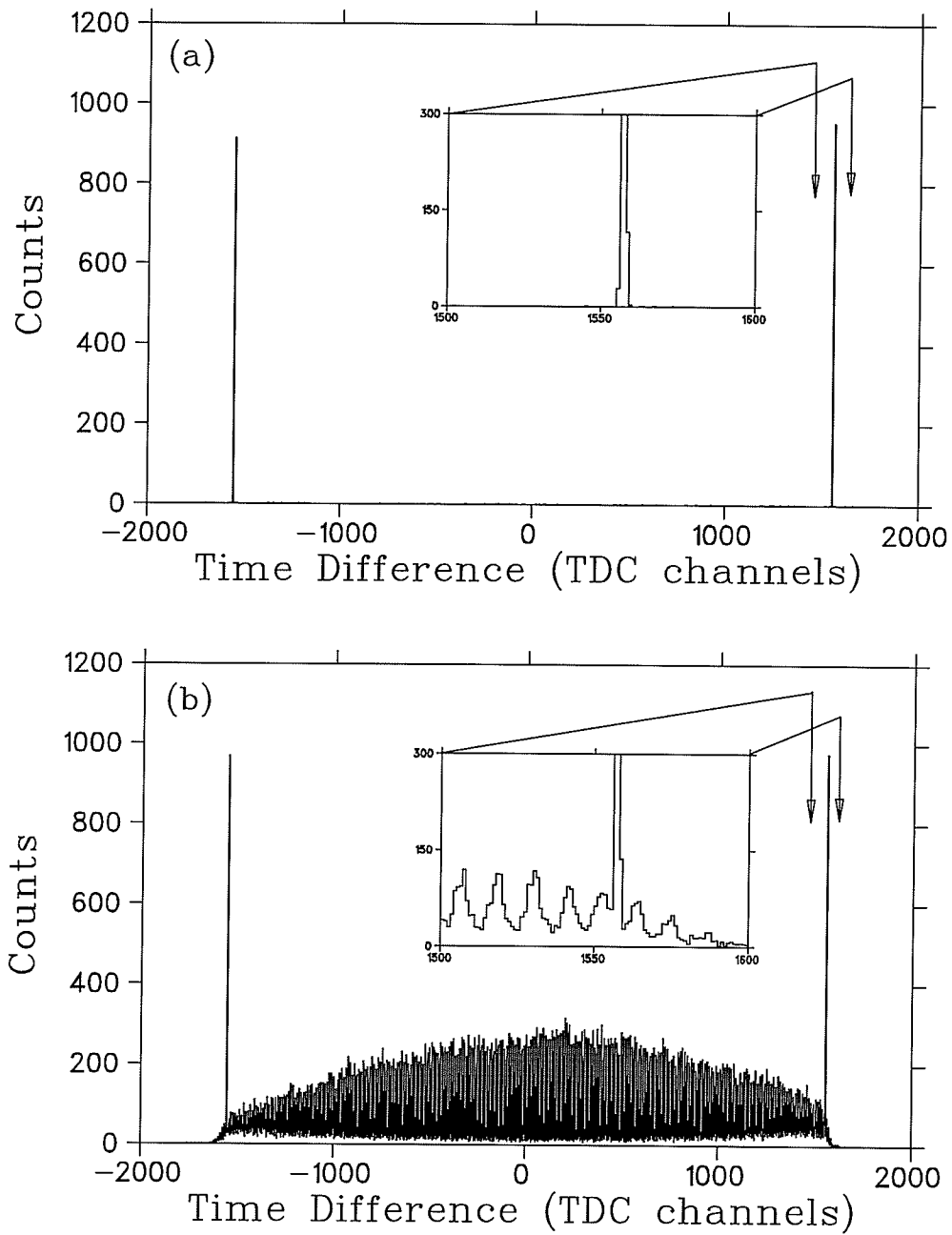


Figure 5.11: (a) *time difference spectrum of the pulser events in the DLCs; and* (b) *relative positions of the pulser peaks and the picket fence structure which gave the pulser locations and separations better than the design note [76] specifications.*

Table 5.2: *Horizontal pulser positions as determined from the DLC calibrations. The statistical uncertainties of the determined pulser separations are estimated to be better than 0.05 mm.*

DLC	Separation (mm)
L1	553.06
L2	550.88
L3	550.97
L4	552.91
R1	551.20
R2	551.59
R3	551.95
R4	552.80

timing signals from the opposite ends of each delay line (left-right and top-bottom, respectively),

$$x_A = (t_{R,A} - t_{L,A}) \cdot \frac{dx}{dt} \text{ (mm)}, \quad (5.26)$$

$$y_A = (t_{B,A} - t_{T,A}) \cdot \frac{dy}{dt} \text{ (mm)}. \quad (5.27)$$

To calculate the “true” horizontal coordinates and correct for non-linearities, calibration tables generated from the DLC calibration data were used (see Appendix A for DLC calibrations). For the horizontal coordinates, the measured positions were rounded off to the nearest wire positions in the calibration table and returned as “true” coordinates of the hits. The “true” vertical coordinates were calculated simply by adding position dependent corrections  $\Delta y_A$  from the calibration table to the “measured” vertical coordinates.

$$x_A^{true} = IWIRE(x_A) \times 2 + OFF_x, \quad (5.28)$$

$$y_A^{true} = y_A + \Delta y_A + OFF_y, \quad (5.29)$$

where the offsets  $OFF(x)$  and  $OFF(y)$  corrected for any “absolute” offsets and possible misalignment of the chambers. They were free parameters and were adjusted when proton tracks were reconstructed.

The proton tracks were reconstructed from least squares fitting of the “hit” points to a straight line, and the deviation (residual) of each coordinate was calculated, i.e., the difference between the measured coordinate and the expected position from the fit. At least one pair of good coordinates (x and y) from each group of chambers (front or rear) was required to reconstruct the proton track. For an event with an overdetermined track, i.e., more than 2 sets of good coordinates obtained, a loose cut of  $\Delta^2 = \Sigma(x_r - x_o)^2 / (N - 4) \leq 40 \text{ mm}^2$  was applied. Here  $x_r$  and  $x_o$  are the observed and reconstructed coordinates, respectively, and

$(N - 4)$  is the number of coordinates used ( $N$ ) in the track reconstruction minus the minimum four coordinates necessary to reconstruct a track. This loose cut rejected about 3% of the total events and only eliminated events with large multiple scattering in individual DLCs or multiple hits in the chambers (singles or accidentals). Figure 5.12 shows the proton track residual distributions, which is the difference between the observed proton coordinates and the reconstructed (from the proton track) coordinates at each DLC.

The proton vertices were reconstructed by projecting the reconstructed tracks to the  $y$ - $z$  plane ( $x=0$ ) at the center of the FST. The free parameters,  $OFF_{x,y}$  (Eqs. 5.29 and 5.30), were used to center the distribution of the residual of each coordinate and to center the proton vertices. They were adjusted using data with the FST holding field turned off, because the holding field deflected the proton tracks and shifted the reconstructed proton vertices differently depending on the holding field direction. Figure 5.13 shows a schematic diagram of the proton track deflection and reconstruction. A shift of a few mm in the  $z$  vertices was observed when the holding field changed direction. Therefore, only a loose cut was applied to the reconstructed vertices as shown in the Fig. 5.14. The offset parameter ( $OFF$ ) of each plane ( $x$  and  $y$ ) of each chamber arose from the misalignment of the DLCs either internally or externally. These misalignments were typically around 1 mm. Plots of the reconstructed proton vertices and the residual distributions in the  $x$  and  $y$  planes are shown in Figs. 5.14 and 5.12.

Proton polar and azimuthal angles ( $\theta_p$  and  $\phi_p$ ) were calculated for the reconstructed tracks. However, due to the holding field deflection and multiple scattering, the measured proton polar angle was not the same as the polar angle

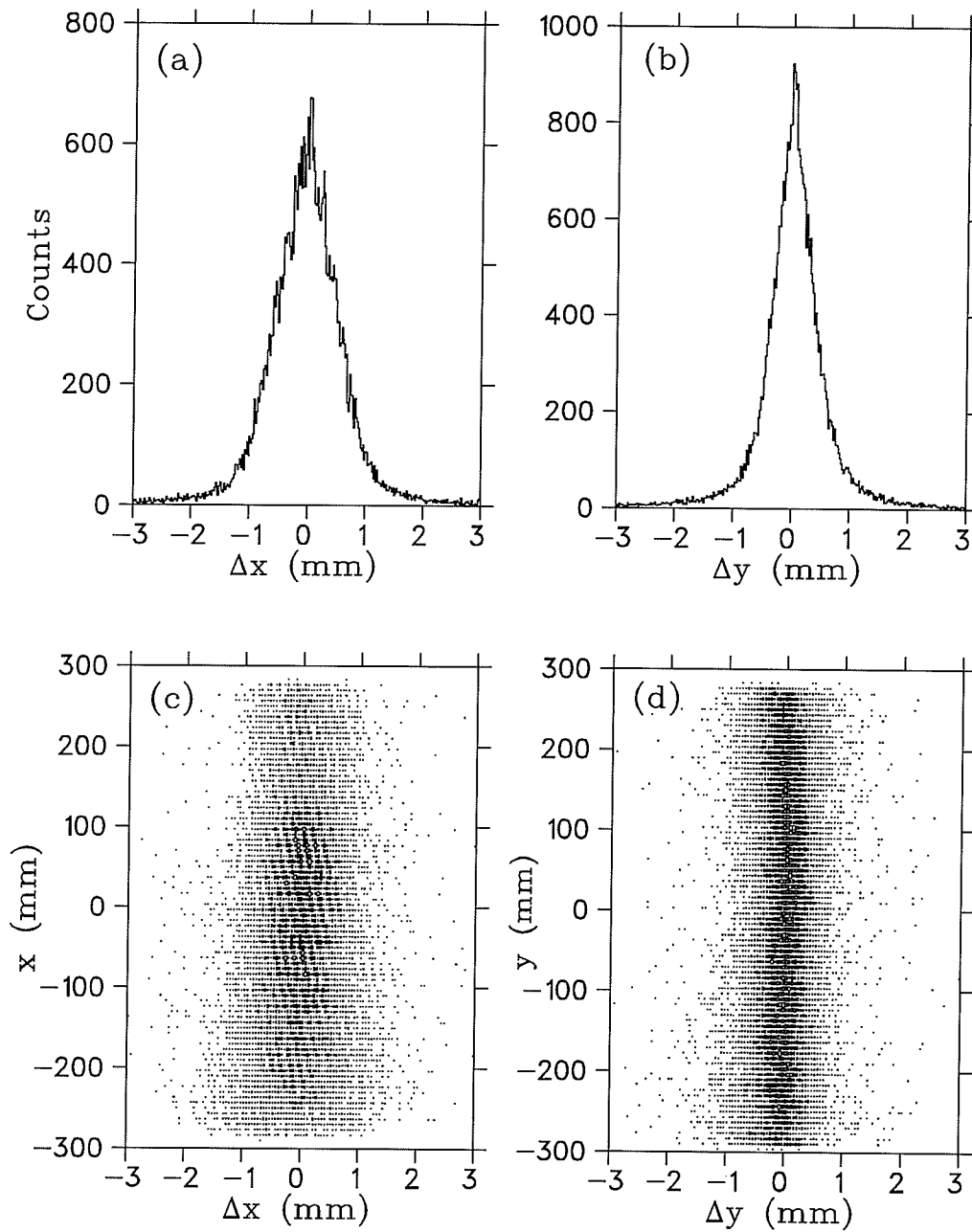


Figure 5.12: Proton track residual distributions (the difference between the observed and reconstructed coordinates), (a) horizontal coordinate residual ( $\sigma = 0.6$  mm); (b) vertical residual ( $\sigma = 0.4$  mm); and (c) and (d) residual as a function of the chamber coordinate indicating the chambers were well calibrated for non-linearities.

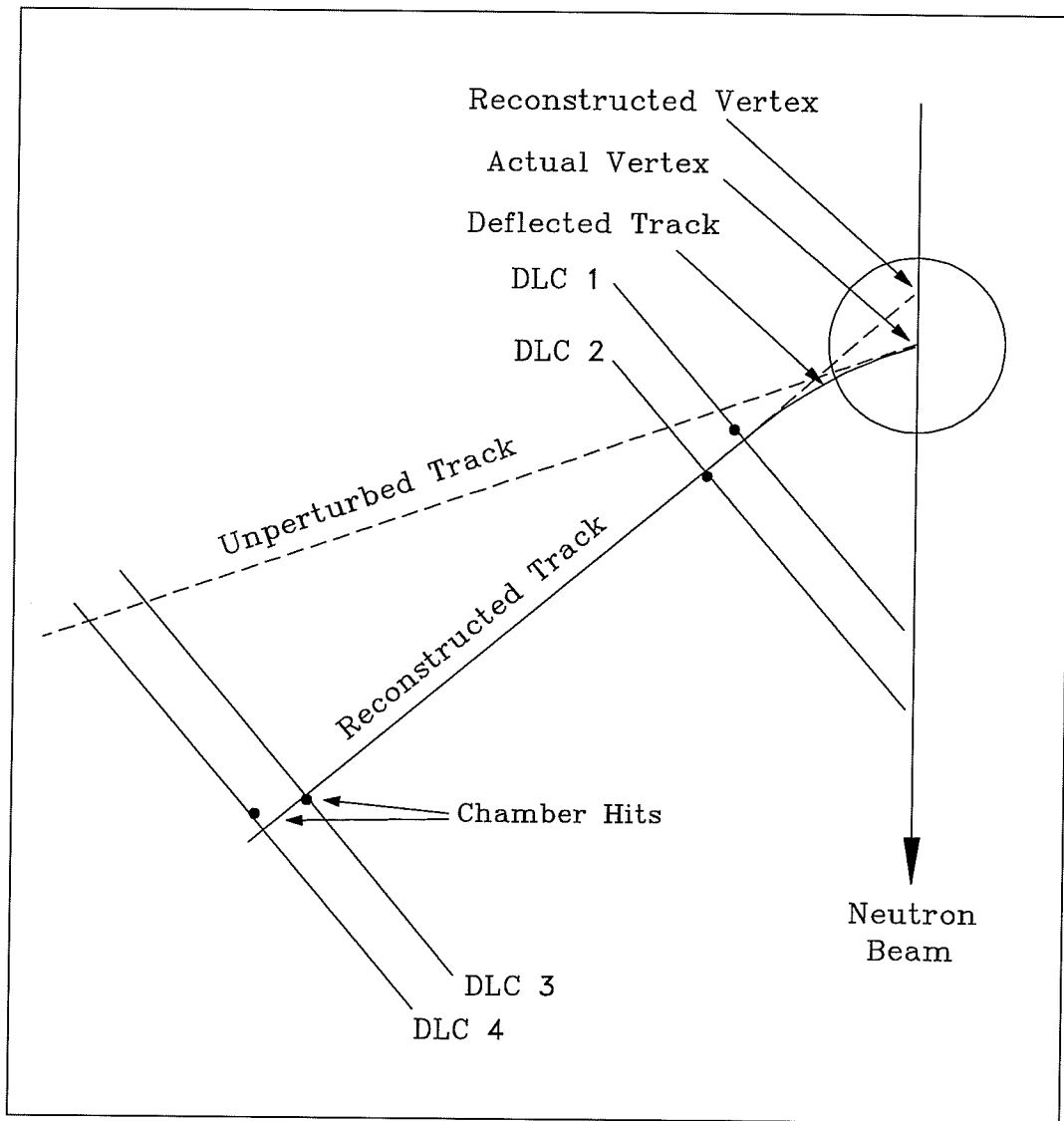


Figure 5.13: *Schematic diagram of the proton track deflection in the holding field and the reconstructed proton track and vertices from the measured coordinates.*

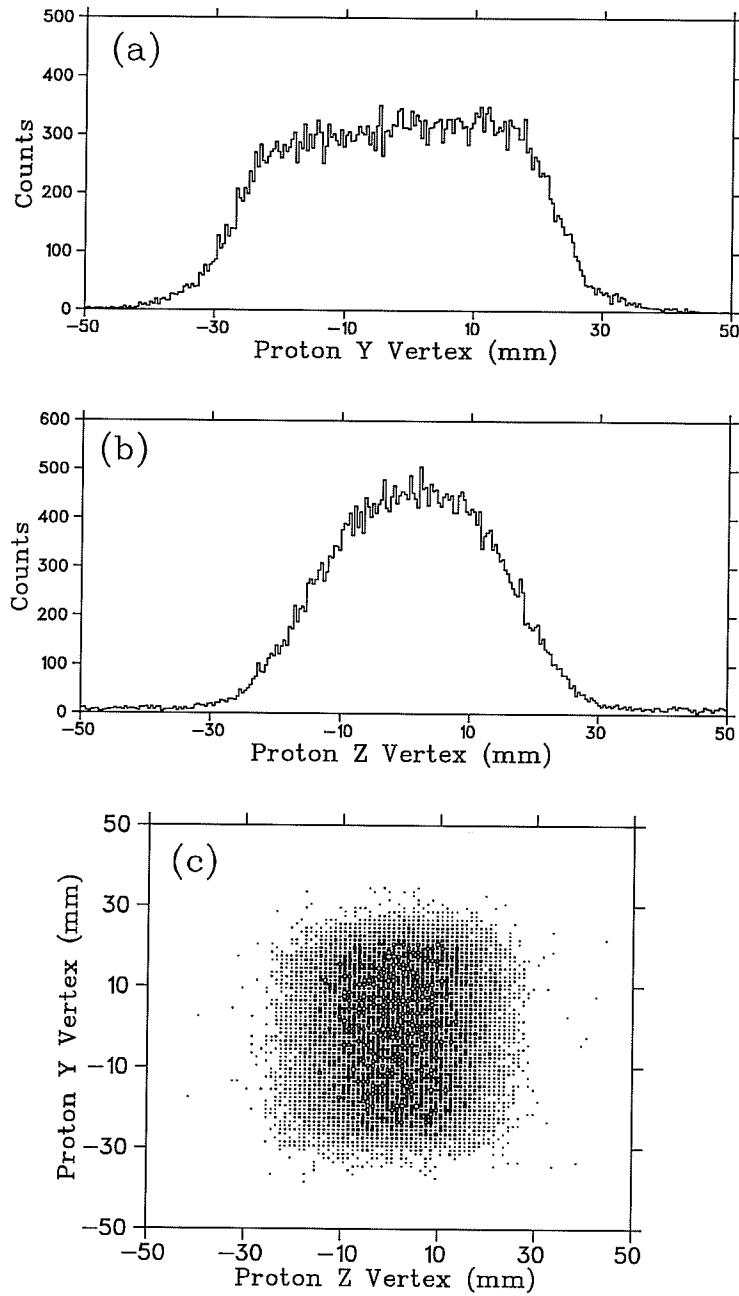


Figure 5.14: Distributions of the reconstructed proton vertices, (a)  $y$  vertex, (b)  $z$  vertex, and (c) the proton vertex in the  $y$ - $z$  plane at the FST location.

at the scattering point inside the FST. The correction generated by Monte Carlo simulations as described in Chapter 4 (Eq. 4.9) was used, and the measured proton polar angle was corrected as an average effect (1.2-1.8 degrees) on an event-by-event basis. Figure 5.15 shows the corrected proton polar and azimuthal angle distributions.

The DLC efficiencies were monitored on-line and re-evaluated during the off-line analysis. Each front chamber had an individual efficiency of about 95% and each rear chamber about 98% at a proton beam current of about  $2 \mu A$ . Some runs were rejected when the efficiency changed by more than a few percent. The front chamber efficiencies were lower due to their proximity to the target and because only a small portion of each chamber was illuminated. Since each group contained two chambers and the minimum good coordinates were one x and one y, the combined efficiencies of each group were 99.75% and 99.96% for the front and rear pairs, respectively.

### 5.3.2 Proton Time-Of-Flight and Kinetic Energy

The recoil proton time-of-flight (TOF) was measured between the proton TOF "start" scintillation counter (pTOF) and two TOF "stop" scintillation E-counters (E1 and E2) (see Fig. 3.1 and 3.17). Timing (TDC) signals were required from both of the pTOF PMTs (top and bottom); the time average of the top and bottom TDCs was used as the proton TOF start signal. Each E-counter was subdivided into 5 sections of a  $18 \times 28$  grid (Fig. 5.16). Three, or all four, timing signals from a total of 4 PMTs of each E-counter were required depending on the section in which a hit occurred. In the center region (region 5 in Fig. 5.16), valid timing signals from all four PMTs were required to be present, and the time av-

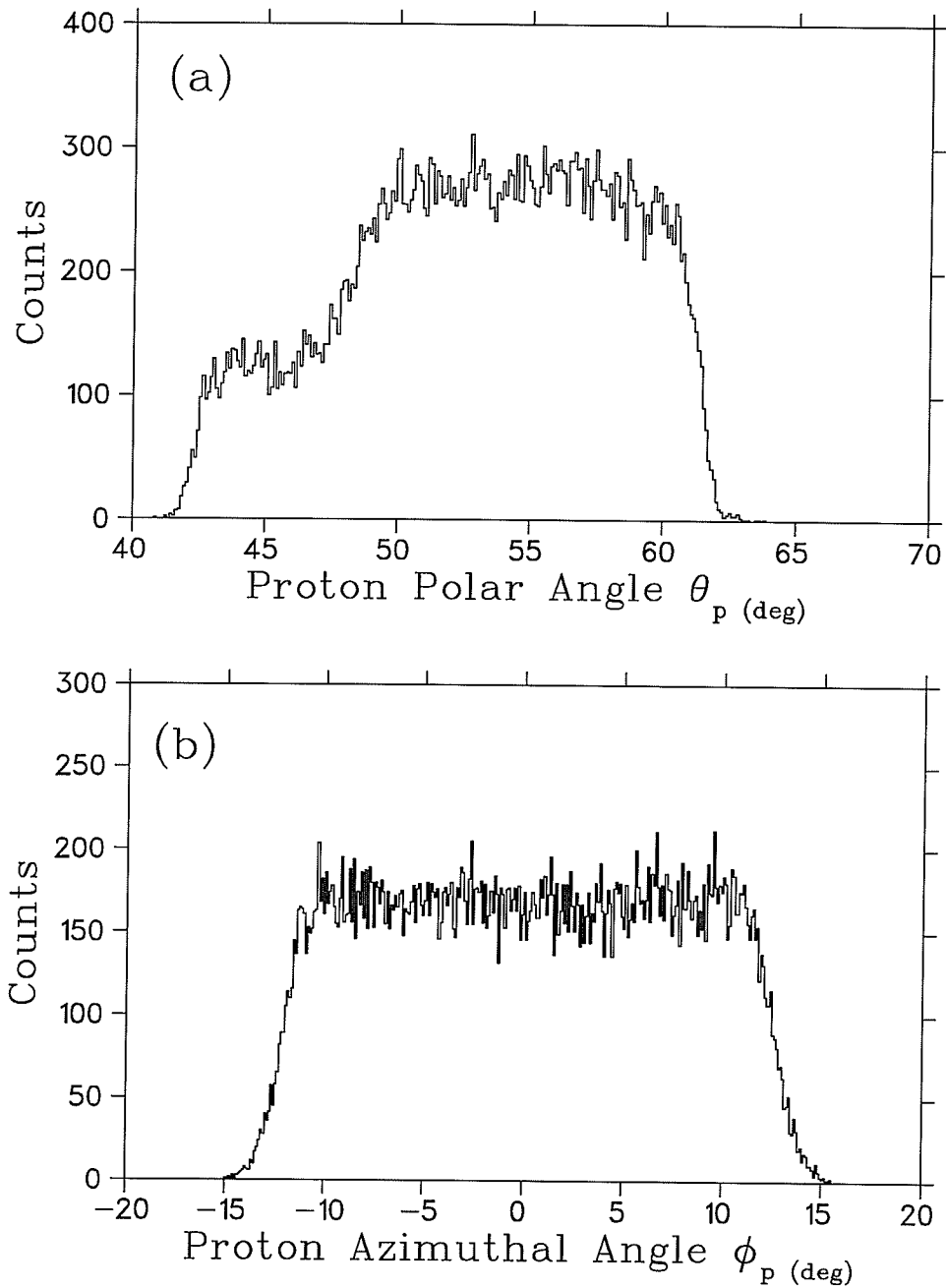


Figure 5.15: (a) proton polar angle  $\theta_p$  distribution and (b) azimuthal angle  $\phi_p$  distribution in laboratory system. The "shoulder" in the  $\theta_p$  distribution is due to the coincident neutrons detected in the "New" neutron bars which had a single layer of scintillator bars and had therefore lower detection efficiency than the main arrays.

erage of all four was used. In the other four regions only three favorable timing signals were required, and the time average of the three PMTs timing signals was used to calculate the stop time (e.g., in region 1, only valid timing signals from PMT1, PMT3 and PMT4 were required). This was because in the regions 1, 2, 3 and 4, one of the PMTs accepted light mainly from reflections in the scintillator and these reflections would degrade the timing resolution. It was determined that the average time of the opposite three PMTs which viewed direct light would give better timing resolution. Since the average absolute time of 3 or 4 TDCs was position dependent (due to the time differences for light travelling within the scintillator to the PMTs), a correction table which was a 18 by 28 matrix corresponding to the 18 by 28 grids of each E counter was used to correct for this effect. The size of a grid was chosen so that the intrinsic time spread for light to cross the grid much smaller than the resolution of the detection system. The correction constants for adjacent grids within the same section were different with each other by a few TDC channels (50 ps /per TDC channel). The correction tables were created from the E-counter calibrations in the initial phase of the data analysis.

The proton path lengths from the pTOF counters to the hit points at both E-counters were calculated using the reconstructed tracks and the projected coordinates of the tracks at these detector locations. The proton kinetic energy ( $E_p$ ) was calculated from the known path length and TOF. This calculated energy represented the average energy of the proton from the pTOF counter to the E-counters. In order to deduce the proton energy at the scattering point in the FST, another correction function from the Monte Carlo simulations (as described in Chapter 4, Eq. 4.10) was used. This function corrected for proton energy loss and multiple scattering effects along its path. This correction was an average effect,

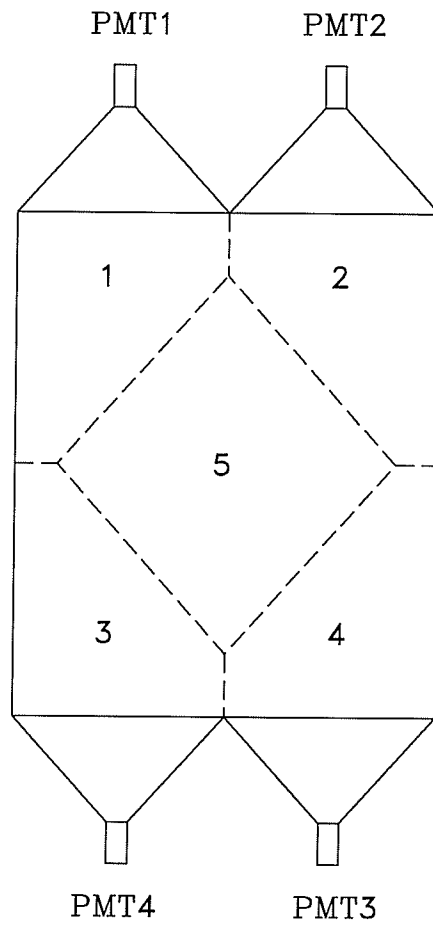


Figure 5.16: *Schematic diagram showing the division of the E-counters into five areas for timing calculations.*

but again the proton energy was corrected on an event-by-event basis. Figure 5.17 shows the proton kinetic energy distribution,  $E_p$ , and the difference,  $\Delta E_p$ , of the measured and kinematically expected proton energy at the given corrected proton polar angle. An average resolution of 9 MeV was obtained in  $\Delta E_p$  after the E-counter calibrations.

### 5.3.3 Neutron Position and Angle

The hit positions in the neutron bars were calculated from the time difference of the timing signals (TDC) from the opposite ends of each bar. To determine the neutron bar time width, neutron singles data, which did not require the coincident protons to be present, were used. Taking the FWHM of the time difference distributions of the neutron singles data, the time width was determined to be  $260 \pm 2$  TDC channels (or  $13.0 \pm 0.1$  ns). The button events were used to determine the center of the neutron bars in time differences (as described in Section 5.2.8). The veto overlap events, with charged particles penetrating the overlapping regions of the veto scintillators (see Chapter 3 for detector details) and the neutron array scintillator bars, were used to calculate the separation of the observed veto overlap regions and to compare with the physical known separations ( $363 \pm 2$  mm). Figure 5.18 (a), (b) and (c) show time difference spectra for neutron singles, button and veto overlap events.

The horizontal coordinate of a neutron intersecting the main neutron array was determined by the time difference of timing signals (TDC) from both ends (left and right) of each bar, and by the time width and centroid of the bar determined from the neutron singles and the button events, respectively (as described

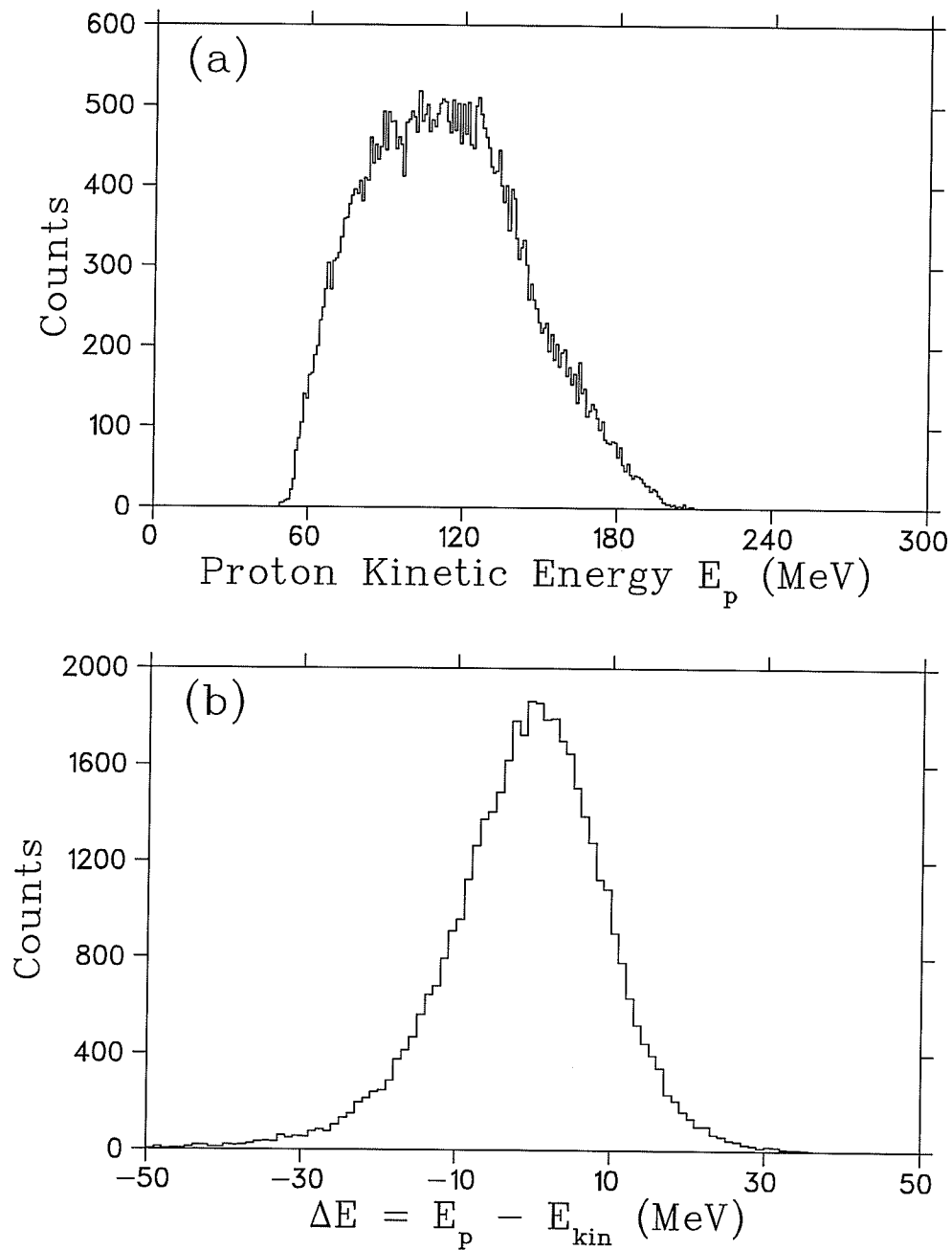


Figure 5.17: (a) a distribution of the corrected proton kinetic energy and (b) a distribution ( $\sigma \simeq 9.0$  MeV) of the difference between the measured proton kinetic energy and the kinematically expected proton energy from the measured proton angle.

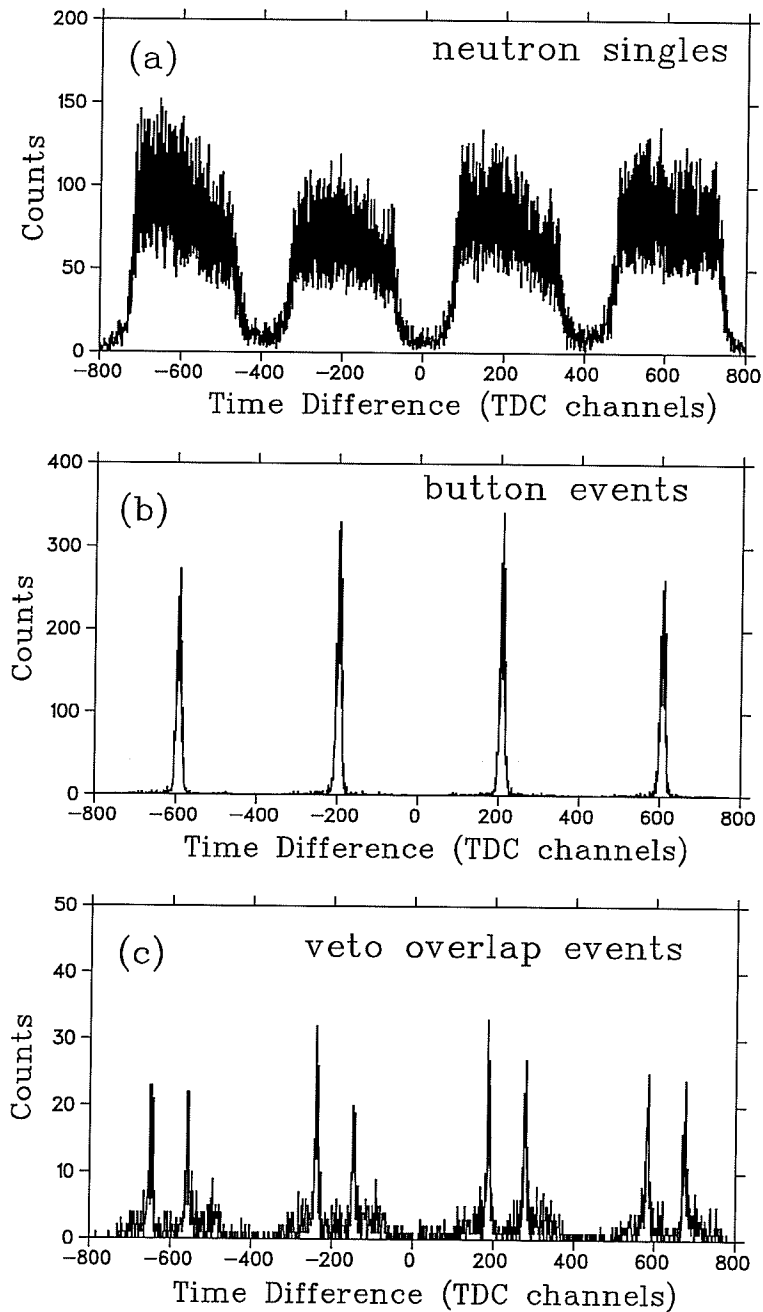


Figure 5.18: *Time difference spectra of (a) the neutron singles (b) button events and (c) veto overlap events to determine the neutron bar time width and centroid (in TDC channels) and to check the position determination. Here, the time differences are of four scintillator bars (bar 1, 3, 5, 7) which were “daisy chained” (see Chapter 3 for details).*

above). The vertical coordinate was chosen as the middle of the bar that was hit, and a spatial resolution of 75 mm was determined by the total bar width of 150 mm. An event that fired more than one bar (multiple hit) was treated according to which bars were hit. If two adjacent bars were hit, the averages of vertical and horizontal positions in the two bars were taken; if the hits were in the same bank but not adjacent, the event was rejected; if a multiple hit was such that it was detected in both the front and rear banks, only coordinates in the front bars were taken.

The scattered neutron 'tracks' were determined by two points; one was the hit point at the neutron detection array, and the other was the assumed scattering point in the target.

The neutrons detected in the auxiliary neutron bars were analyzed in a similar way to those in the main array. Since the auxiliary neutron bars were set up vertically, the time difference between the top and bottom PMTs gave the vertical coordinate, and the horizontal coordinate was taken as the cross-section weighted bar center position. The distance between the neutron arrays and the FST was determined from the geometric centroid of each bank of the arrays with a small offset to account for the scattering probability of neutrons in a scintillator bar.

The neutron positions at the scattering points in the target were assumed to be along the central vertical axis ( $x = 0, z = 0$ ) with  $y$  coordinates determined by the proton vertices. A neutron "track" was determined by the two points defined above, and the neutron polar and azimuthal angles ( $\theta_n$  and  $\phi_n$ ) were calculated. Figure 5.19 shows the distributions of  $\theta_n$  and  $\phi_n$ .

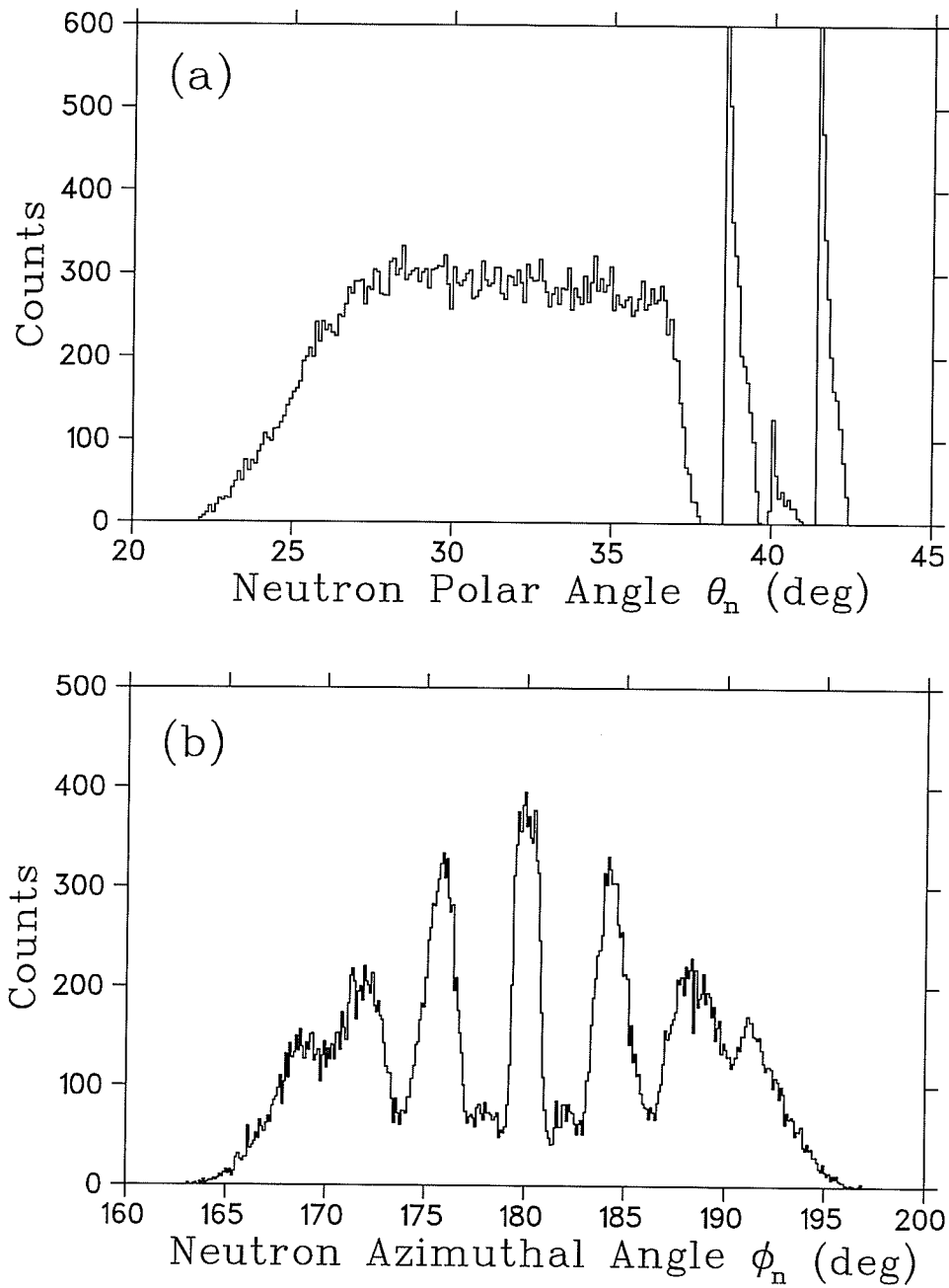


Figure 5.19: *Distributions of polar (a) and azimuthal (b) angles of the scattered neutrons; the three “spikes” in (a) are due to the auxiliary bars which were set up vertically and therefore had a horizontal resolution of half of the bar width 75 mm, the middle “spike” corresponds to the events detected in both auxiliary bars; the “picket” structure in (b) is due to the main neutron array scintillator bars which had a vertical resolution of half of the bar height of 75 mm.*

### 5.3.4 Neutron Time-of-Flight (TOF) and Kinetic Energy

The neutron kinetic energy was calculated from its TOF and flight distance. The proton arrival time at the pTOF was used as the neutron TOF “start” and the neutron arrival time at the neutron array was used as the neutron TOF “stop”. The neutron arrival time at the array was taken as the time average of the two ends of the scintillator bar. The neutron TOF was calculated from the time difference between the ‘start’ and ‘stop’ timing signals, and a timing correction for the coincident proton travelling from the FST to the pTOF was included. The neutron flight distance was calculated from its coordinates at the neutron array and the assumed scattering position. The neutron kinetic energy,  $E_n$ , was then obtained from its given flight length and TOF. The difference between the measured kinetic energy and the kinematically expected kinetic energy at the observed neutron angle,  $\Delta E_n$ , was also calculated (Fig. 5.20). An average resolution of  $\sigma = 13.0$  MeV was achieved in  $\Delta E_n$ .

### 5.3.5 Neutron Bar Gain Renormalization

The neutron bar pulse height signals (in ADC channels) after pedestal subtraction were renormalized with reference to the pulse height of the “simultaneous” button events (passing protons) as follows:

$$ADC_n^{adjusted} = ADC_n^{measured} \times \frac{ADC_{button}^{nominal}}{ADC_{button}^{measured}}, \quad (5.30)$$

where  $ADC_i$  are the neutron bar pulse height signals in ADC channels after subtraction of pedestals. Figure 5.21 shows a typical normalized neutron bar pulse height spectrum. The hardware discrimination threshold was in a region where the pulse height distribution was rising rapidly. A typical software threshold of 20

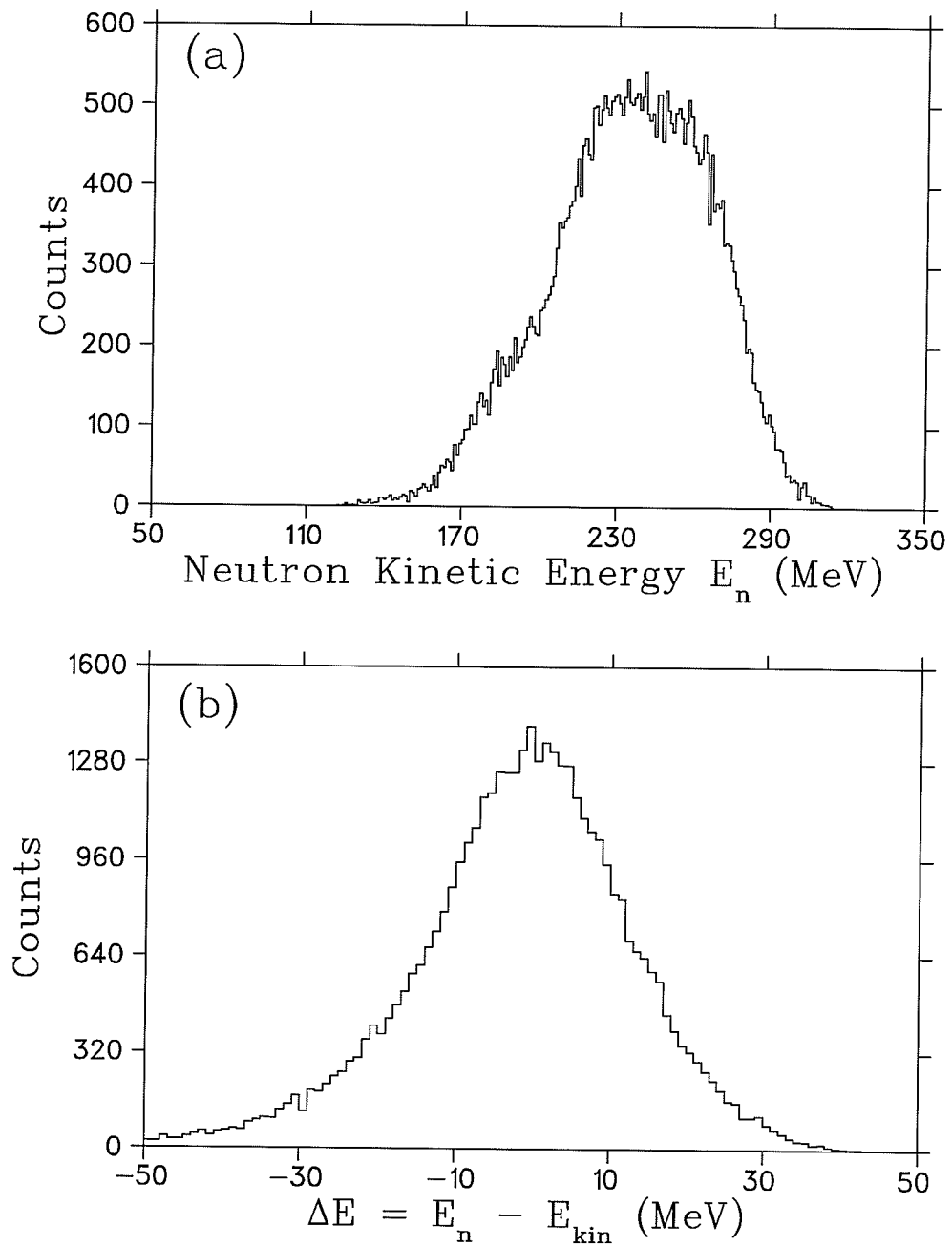


Figure 5.20: (a) the measured neutron kinetic energy and (b) a distribution ( $\sigma \simeq 13.0$  MeV) of the difference of the measured neutron kinetic energy and the kinematically expected neutron kinetic energy at the measured neutron angle.

ADC channels (about 1 MeV electron equivalent) on the neutron bar pulse height was applied to the data. In order to check for possible systematic errors associated with gain changes and the hardware thresholds, software thresholds were varied from 15, 20 to 25 ADC channels. Their influence on the zero-crossing angles will be discussed in Chapter 6.

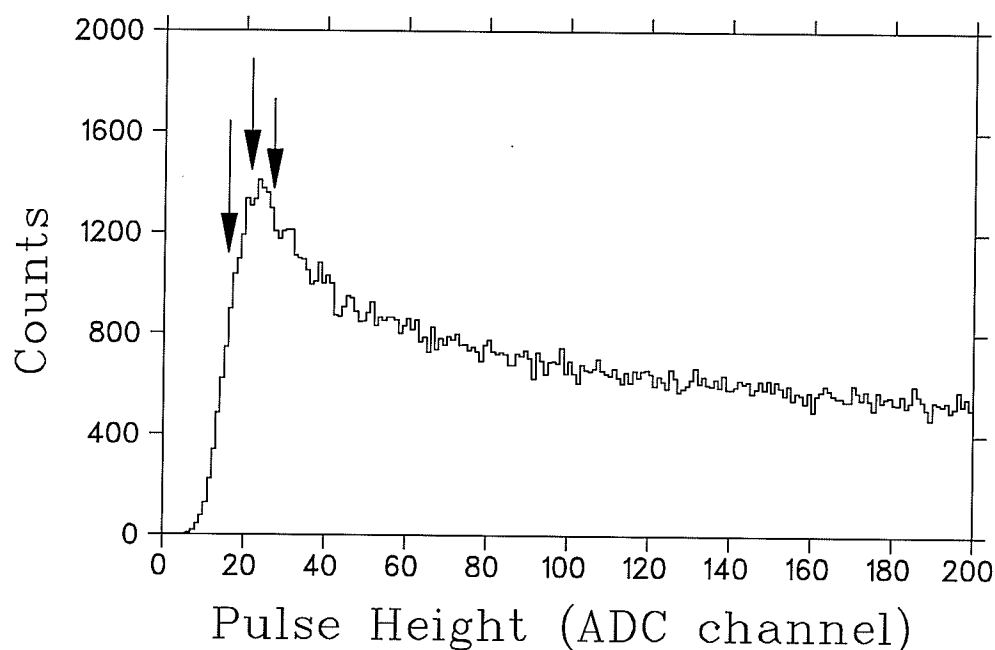


Figure 5.21: *A distribution of the neutron scintillator bar pulse height after pedestal subtraction and pulse height renormalization. Arrows show the channel positions where the various cuts were applied (15, 20 and 25 ADC channels).*

### 5.3.6 Kinematical Observables and Data Constraints

The experiment determined neutron and proton polar and azimuthal angles,  $(\theta_n, \phi_n, \theta_p, \phi_p)$ , momenta,  $(p_n, p_p)$ , and kinetic energies,  $(E_n, E_p)$ , to distinguish elastic scattering events from inelastic background. Energy and momentum con-

ervation require:

$$E_i = E_n + E_p, \quad (5.31)$$

$$\vec{p}_i = \vec{p}_n + \vec{p}_p, \quad (5.32)$$

where  $E$  is kinetic energy, subscripts  $i$ ,  $n$  and  $p$  denote initial particle (neutron beam), scattered neutron and recoil proton, respectively, and  $p$  is momentum. For two-body scattering (known particle masses) at a known energy, one azimuthal angle and any other, independent kinematical parameter determine an  $np$  elastic scattering event. Determination of more parameters permits rejection of  $(n, np)$  background. The overdetermined kinematic observables were combined into four variables for chi-squares tests for  $np$  elastic scattering events. These variables were the following (in laboratory system):

### (1) Opening angle

Opening angle was defined as:

$$\theta_{open} = \theta_n + \theta_p - \theta_{kin}, \quad (5.33)$$

where  $\theta_{kin}$  is the kinematically expected opening angle,  $\theta_{kin} = (\theta_n + \theta_p)_{kin}$ , at the nominal neutron beam energy 347 MeV.  $\theta_{kin}$  is a function of  $\theta_n$  and the incident neutron beam energy (347 MeV) according to energy and momentum conservation and was approximated by a polynomial:

$$\begin{aligned} \theta_{kin} = & 85.608 - 8.00063 \times 10^{-2} \cdot (\theta_n - 29.5) + 2.90074 \times 10^{-3} \cdot (\theta_n - 29.5)^2 \\ & + 5.44775 \times 10^{-6} \cdot (\theta_n - 29.5)^3, \end{aligned} \quad (5.34)$$

with  $\theta_n$  in degrees and  $\theta_{kin}$  in degrees.

## (2) Coplanarity angle

Coplanarity angle was defined as:

$$\phi_{coplan} = \phi_n - \phi_p - 180^\circ. \quad (5.35)$$

Vertical (perpendicular to scattering plane) momentum conservation requires

$$\phi_{coplan} = 0.$$

## (3) Kinetic energy sum

The kinetic energy sum was defined as:

$$E_{sum} = E_n + E_p. \quad (5.36)$$

Energy conservation determines  $E_{sum}$  to be the same as the incident particle (beam) kinetic energy.

## (4) Horizontal momentum sum

Horizontal momentum was defined as:

$$\Delta p_x = p_{n,x} + p_{p,x}, \quad (5.37)$$

where  $p_{n,x}$  and  $p_{p,x}$  are the  $x$  components (see Fig. 3.2) of the scattered neutron and recoil proton momenta, and they were calculated as,

$$p_{n,x} = p_n \sin \theta_n \cos \phi_n, \quad (5.38)$$

$$p_{p,x} = p_p \sin \theta_p \cos \phi_p. \quad (5.39)$$

Horizontal momentum conservation requires  $\Delta p_x = 0$  since the initial particle momentum was along the  $z$  axis.

The momentum dependent chi-squares of these four variables were calculated for every event:

$$\chi_i^2 = (x_i - x_i^0)^2 / \sigma_i(p)^2, \quad (5.40)$$

where  $\sigma_i(p)$  is the momentum dependent  $\sigma$  of the distribution of each variable determined from the data,  $x_i$  is one of the kinematic variables as measured, and  $x_i^0$  is the nominal centroid of the variable. Figure 5.22(a) shows how the  $\sigma(p)$  of the opening angle distribution was obtained and (b) shows the difference of the weighted and non-weighted  $\sigma$ 's. Different chi-squares tests were applied to the data. These tests were either the individual chi-squares  $\chi_i^2 \leq 9, 7.5, 5$  or the sum of the chi-squares of the four different variables  $\chi_{sum}^2 = \Sigma \chi_i^2 \leq 20, 15, 10$  (Fig. 5.23). Figure 5.24 shows the distributions for the kinematic variables before and after the cuts.

## 5.4 Asymmetries and Zero-Crossing angles

For the  $np$  coincident events passing the software cuts, scattering asymmetries were calculated. In order to cancel systematic errors to second order, an "overlap" method was used, and a combination was made of different spin states (up or down) and physical orientations (left or right event). A total of eight asymmetries were calculated for beam or target polarized, holding field up or down, BONNIE magnet field direction normal or reversed, using the following equations:

$$\epsilon = \frac{r - 1}{r + 1}, \quad (5.41)$$

$$r = \left[ \frac{N_L^+ N_R^-}{N_L^- N_R^+} \right]^{\frac{1}{2}}, \quad (5.42)$$

where the superscripts indicate the spin polarization directions. Figure 5.25 shows a sample distribution of the scattering asymmetries versus the scattering angles

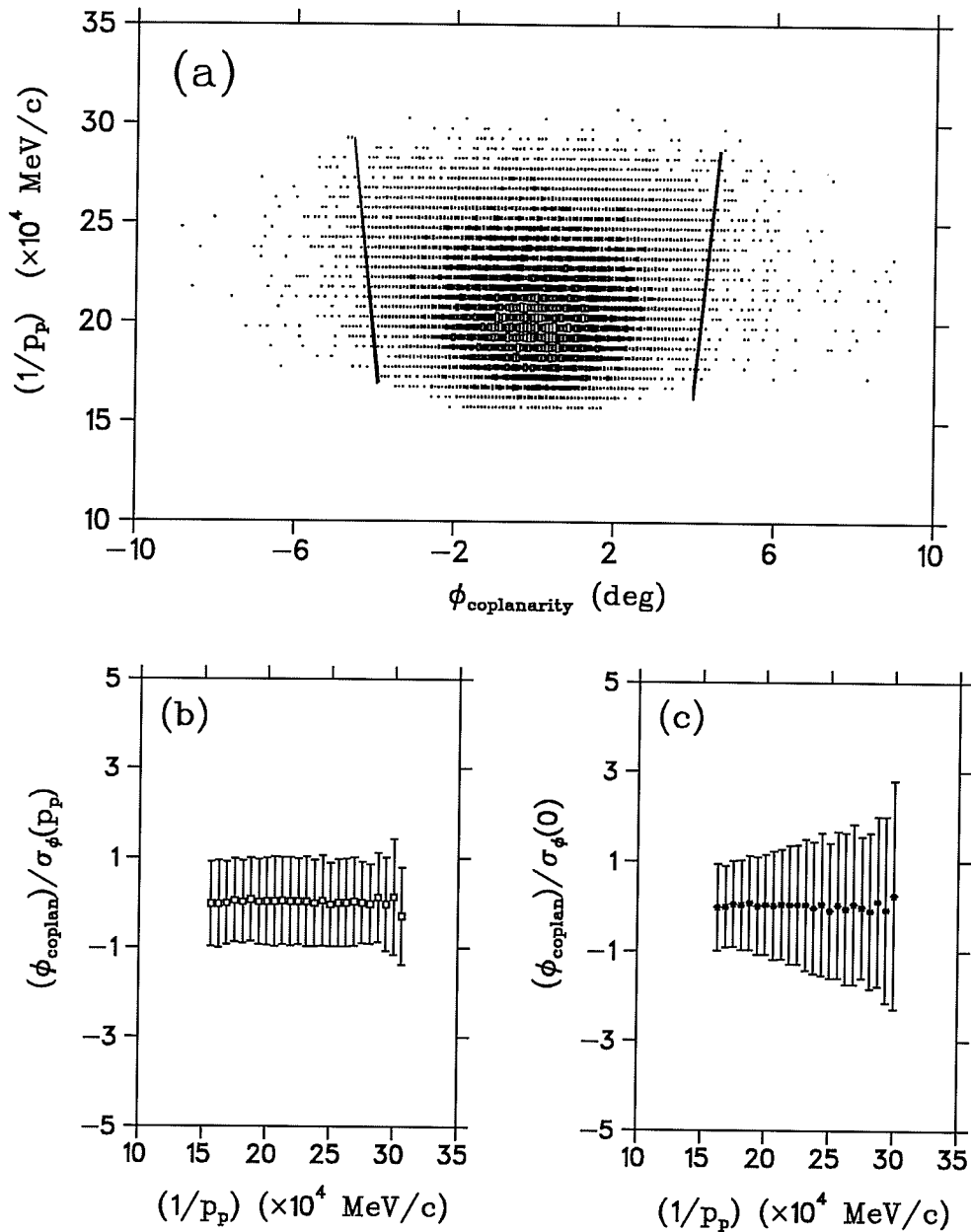


Figure 5.22: (a) a distribution of the coplanarity angle versus the inverse of the corrected proton momentum (the effects of the physical processes involved, e.g., multiple scattering and energy loss, are proportional to the inverse of the momentum), (b) and (c) the coplanarity angle distribution centroids and sigmas (momentum weighted or non-weighted, respectively) dependence on the proton momentum.

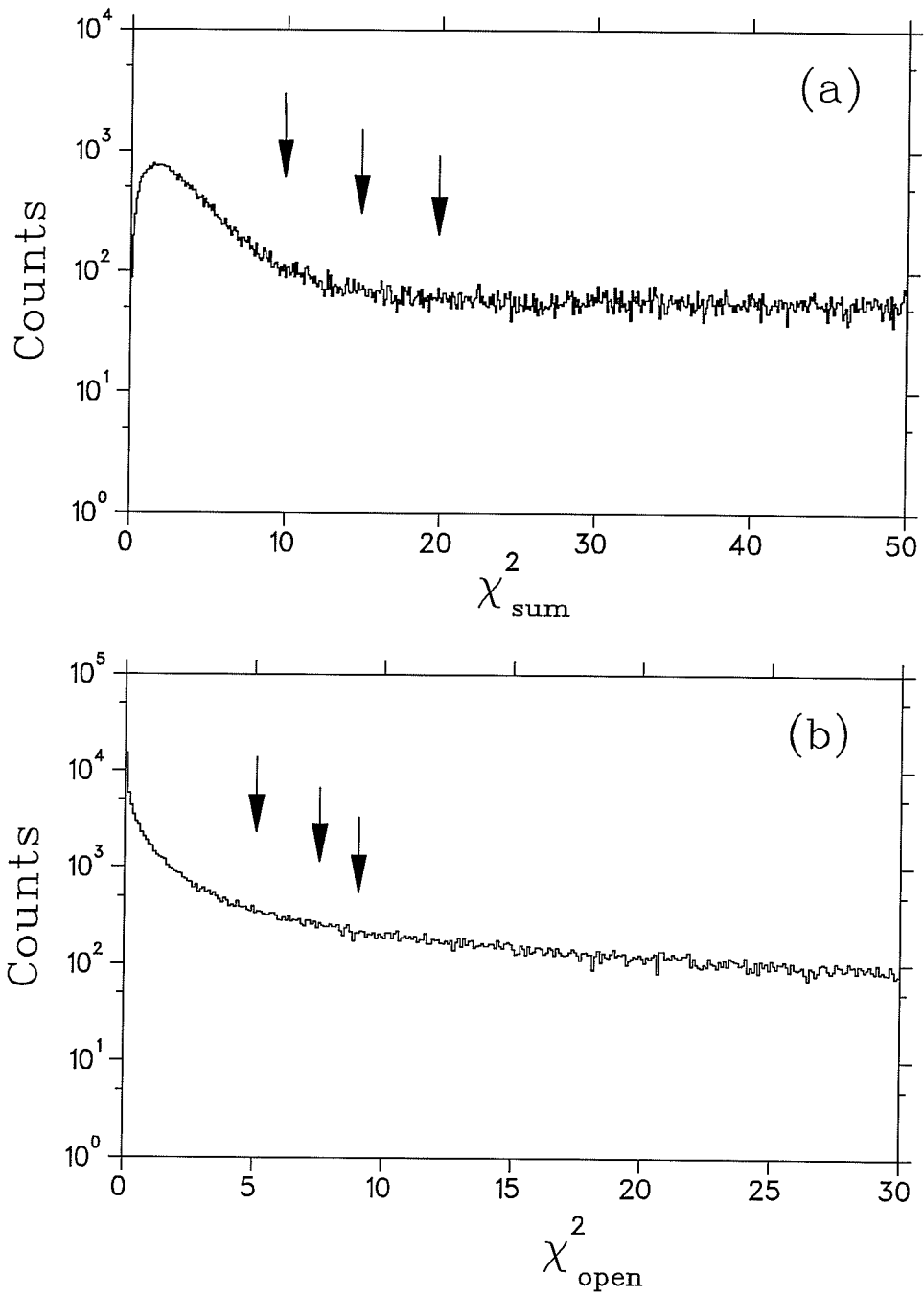


Figure 5.23:  $\chi_{sum}^2$  and  $\chi_i^2$  distributions. Arrows indicate the cuts applied. (a)  $\chi_{sum}^2 \leq 10, 15$  and  $20$  (b) opening angle  $\chi^2 \leq 5, 7.5$  and  $9$ .

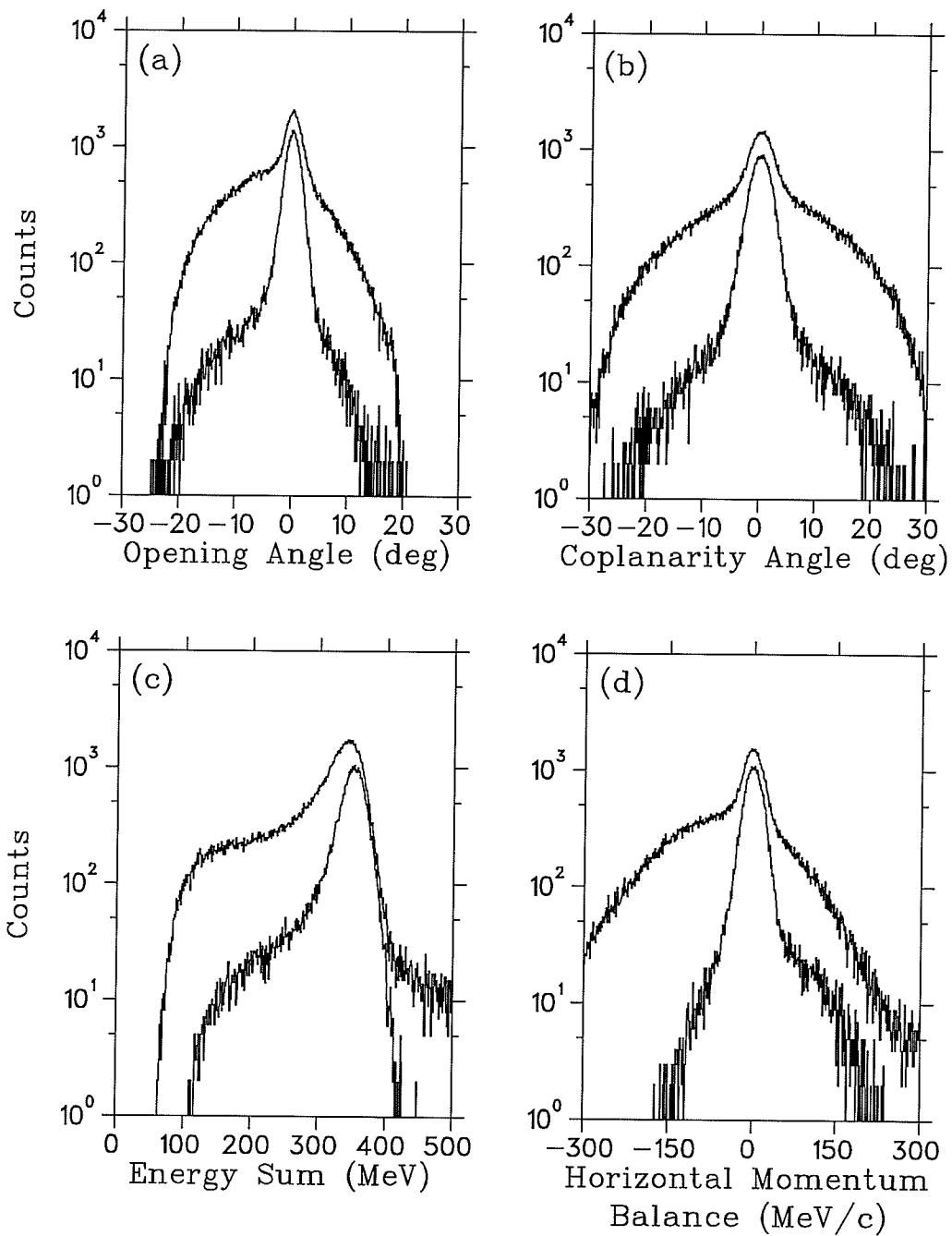


Figure 5.24: Distributions of (a) opening angle ( $\sigma \simeq 1.3^\circ$ ), (b) coplanarity angle ( $\sigma \simeq 1.9^\circ$ ), (c) kinetic energy sum ( $\sigma \simeq 17.0 \text{ MeV}$ ), and (d) horizontal momentum balance ( $\sigma \simeq 16.8 \text{ MeV}/c$ ) before (upper curves) and after (lower curves) the cuts.

in the center of mass (c.m.) system as determined from the proton angle. A least squares fitting routine was used to obtain the zero-crossing angles and slopes. Since the zero-crossing angles from the fits were slightly dependent on the functions chosen to accommodate the shape (quadratic term) of the analyzing power angular distribution, the variation of the shape (cubic term) over the angular range, and the weight by the polarization, asymmetries were fitted to the function:

$$\epsilon = c_0 \cdot [(\theta - \theta_0) + c_1(\theta - \theta_0)^2 + c_2(\theta - \theta_0)^3], \quad (5.43)$$

where  $\theta_0$  is the zero-crossing angle as determined from the measured asymmetry,  $c_0$  is the slope of the asymmetry at the zero-crossing angle and is proportional to the slope of analyzing power and the reciprocal value of the corresponding beam or target polarization. That is,

$$c_0 = \left. \frac{d\epsilon}{d\theta} \right|_{\theta_0} = P \cdot \frac{dA}{d\theta}. \quad (5.44)$$

An average of the extracted zero-crossing angles as obtained from the above fitting process applied to different holding field (up or down) and BONNIE field directions (normal or reversed) is shown in table 5.3. Both polarized target ( $A_p$ ) and polarized beam ( $A_n$ ) measurements are given in the table. The non-zero difference of the zero-crossing angles for  $A_n$  and  $A_p$  is due to charge symmetry breaking (table 5.4).

## 5.5 Neutron Beam Energy

The neutron beam energy was determined in two ways: one was the sum of the scattered neutron and recoil proton kinetic energies, the other was from the TOF of the neutrons from the  $LD_2$  target to the FST. The energy sum has been shown in Fig. 5.24. To calculate the TOF of the neutrons from the  $LD_2$  target to the FST, the r.f. phase stabilized timing signals were used as the relative timing for

Table 5.3: Zero-crossing angles of  $A_n$  and  $A_p$  before the corrections.

Cuts	February 1993		August 1992	
	$\theta_{cm}(A_n = 0)$	$\theta_{cm}(A_p = 0)$	$\theta_{cm}(A_n = 0)$	$\theta_{cm}(A_p = 0)$
$ADC \geq 20.$				
$\chi_{sum}^2 \leq 10$	$72.931^\circ \pm 0.056^\circ$	$72.477^\circ \pm 0.051^\circ$	$72.802^\circ \pm 0.059^\circ$	$72.399^\circ \pm 0.055^\circ$
$\chi_{sum}^2 \leq 15$	$72.961^\circ \pm 0.053^\circ$	$72.626^\circ \pm 0.051^\circ$	$72.906^\circ \pm 0.056^\circ$	$72.531^\circ \pm 0.053^\circ$
$\chi_{sum}^2 \leq 20$	$73.016^\circ \pm 0.052^\circ$	$72.652^\circ \pm 0.051^\circ$	$72.982^\circ \pm 0.055^\circ$	$72.614^\circ \pm 0.054^\circ$
$\chi_i^2 \leq 5$	$72.884^\circ \pm 0.058^\circ$	$72.324^\circ \pm 0.053^\circ$	$72.816^\circ \pm 0.061^\circ$	$72.312^\circ \pm 0.056^\circ$
$\chi_i^2 \leq 7.5$	$72.923^\circ \pm 0.054^\circ$	$72.504^\circ \pm 0.051^\circ$	$72.851^\circ \pm 0.057^\circ$	$72.439^\circ \pm 0.054^\circ$
$\chi_i^2 \leq 9$	$72.937^\circ \pm 0.053^\circ$	$72.539^\circ \pm 0.051^\circ$	$72.897^\circ \pm 0.056^\circ$	$72.487^\circ \pm 0.054^\circ$

Table 5.4: Difference of the zero-crossing angles before the corrections.

Cuts	February 1993	August 1992	All data
$ADC \geq 20.$	$\Delta\theta_{cm}$	$\Delta\theta_{cm}$	$\Delta\theta_{cm}$
$\chi_{sum}^2 \leq 10$	$0.454^\circ \pm 0.076^\circ$	$0.403^\circ \pm 0.081^\circ$	$0.428^\circ \pm 0.056^\circ$
$\chi_{sum}^2 \leq 15$	$0.335^\circ \pm 0.074^\circ$	$0.375^\circ \pm 0.077^\circ$	$0.355^\circ \pm 0.053^\circ$
$\chi_{sum}^2 \leq 20$	$0.364^\circ \pm 0.073^\circ$	$0.368^\circ \pm 0.077^\circ$	$0.366^\circ \pm 0.053^\circ$
$\chi_i^2 \leq 5$	$0.560^\circ \pm 0.079^\circ$	$0.504^\circ \pm 0.083^\circ$	$0.532^\circ \pm 0.057^\circ$
$\chi_i^2 \leq 7.5$	$0.419^\circ \pm 0.074^\circ$	$0.412^\circ \pm 0.078^\circ$	$0.415^\circ \pm 0.054^\circ$
$\chi_i^2 \leq 9$	$0.398^\circ \pm 0.074^\circ$	$0.410^\circ \pm 0.078^\circ$	$0.404^\circ \pm 0.054^\circ$

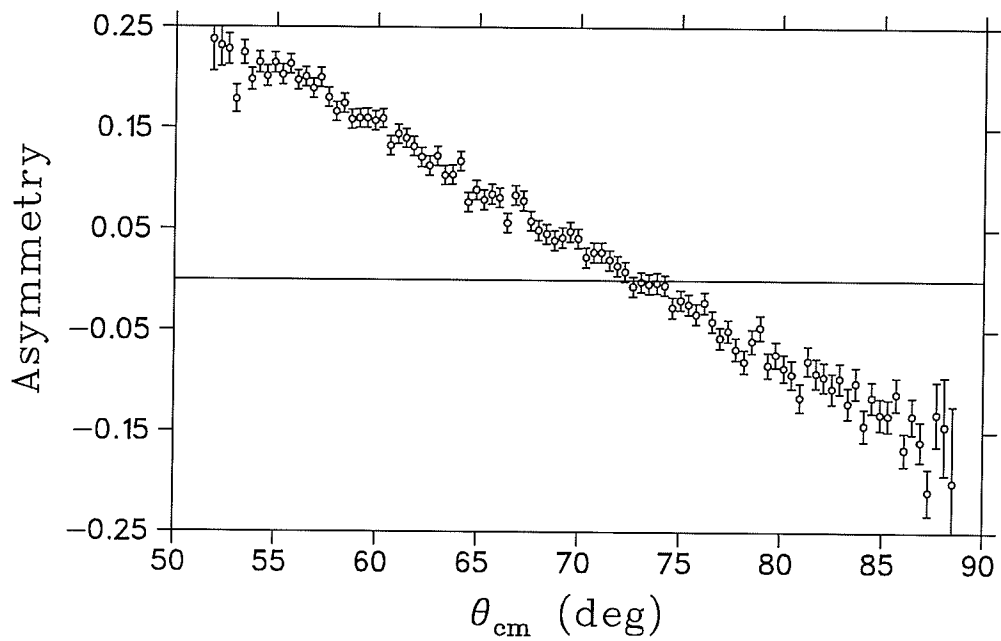


Figure 5.25: A sample asymmetry distribution of polarized FST data (from February 1993 runs, data with the holding field direction up and the Bonnie field direction “Normal”).

the neutron beam TOF “start”, and the timing signals from the pTOF triggered by the recoil proton were used as the “stop”. A timing correction was made for the recoil proton from the presumed scattering point to the pTOF location; this was calculated from the measured recoil proton TOF. The neutron beam flight distance from the  $LD_2$  target to the FST was 12.85 m. The neutron beam kinetic energy was calculated from the TOF and the flight distance. (see Fig. 5.26(a)). Compared to the energy sum determination, a better energy resolution was achieved due to the use of the phase restricted beam tune in the cyclotron (see Chapter 3). A comparison was made between the Monte Carlo simulated neutron beam energy (as described in Chapter 4) and the experimentally measured neutron beam energy after folding the experimental resolution represented by a Gaussian distribution to the simulated distribution (also shown in Fig. 5.26 (a) ). The neutron beam energy determined by the two methods is plotted in Fig. 5.26 (b). Around the peak region (at the nominal beam energy), the correlation of the results is not obvious because the resolutions of the two measurements were broader than the true beam energy spread. The correlation becomes clearer in the low energy tail of the beam because the resolutions of the energy measurements were superior for the slower particles to travel the given flight distance.

## 5.6 Background and Other Corrections

### 5.6.1 Background Correction

Background data obtained with the dummy target (as described in Section 3.13) were analyzed in the same fashion as the FST data. Identical sets of cuts were applied. Figure 5.27 shows the opening angle and coplanarity angle spectra for the background data. Clearly, hydrogen peaks are also present. They were due

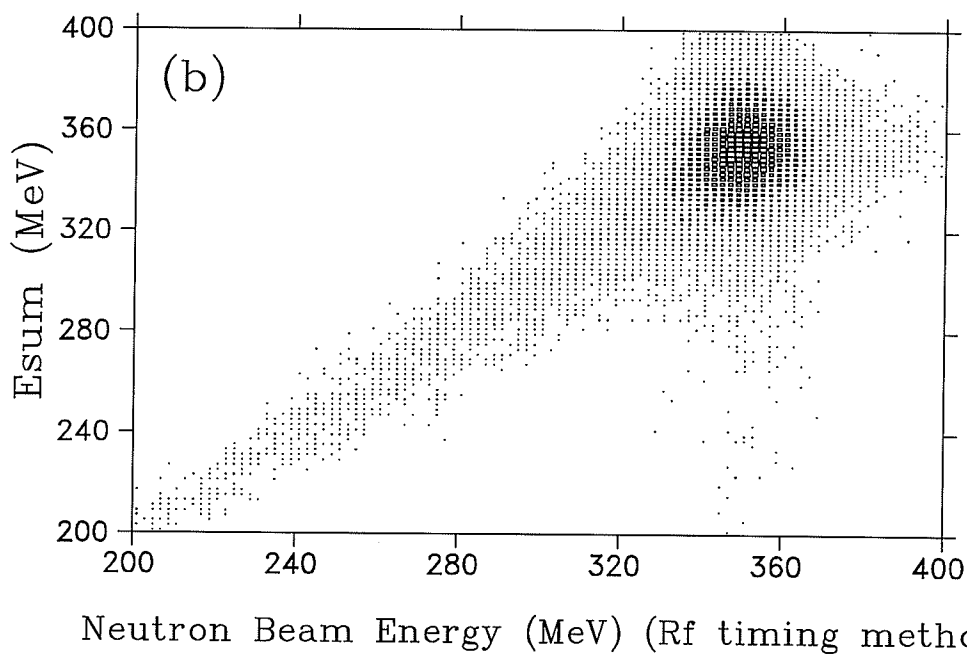
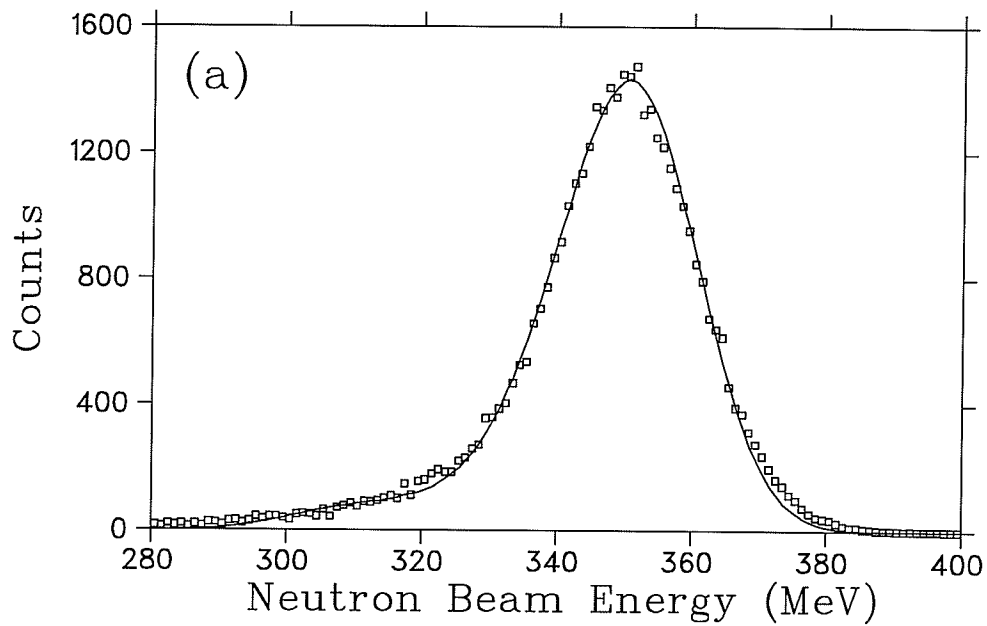


Figure 5.26: (a) distribution of the neutron beam energy determined with the r.f. timing signals (discrete curve) and comparison to the simulated neutron beam energy after considering the measurement resolution represented by a Gaussian distribution (connected). (b) the correlation between the two determinations of the neutron beam energy, with the r.f. timing signals or from the energy sum.

to a hydrogen-containing resistor at the bottom of the FST and super-insulation material around the target. To estimate the “true” carbon content, three different ways of implementing cuts in the off-line analysis were used:

1. A cut on the  $y$  vertex reduced the hydrogen contribution from the resistor but did not affect the hydrogen contribution from the super-insulation material;
2. Cuts of  $1 \leq \chi_i^2 \leq 7.5$  removed both the hydrogen peak and the carbon contribution underneath it as seen in the opening angle distribution. A correction factor was calculated to compensate for the carbon contribution underneath the hydrogen peak. There were uncertainties in estimating the carbon contribution within the  $\chi_i^2 \leq 1$  window and the hydrogen contamination to the data inside  $7.5 > \chi_i^2 > 1$  (i.e., due to multiple scattering);
3. Through a combination of the FST data and the carbon data, the background contribution was estimated. The FST data after cuts were used to estimate the hydrogen contribution to the background data by subtracting the hydrogen peak in the background data with scaled “clean” FST data.

For those results involving individual  $\chi_i^2$  cuts, the carbon contribution to the FST data was obtained by normalizing the tails of the opening angle and coplanarity distributions of the background data to the FST data (Fig. 5.28). Similar results were obtained for the background contribution to the FST data from the methods (2) and (3) above. An estimate of 25% uncertainty on the determination of the background contribution was assumed, which includes uncertainties in normalization, hydrogen contamination elimination from the background data and

different analysis procedures (as described above). The yields from the carbon data were used to evaluate the analyzing powers of  $(n, np)$  background with the given cuts. For this purpose, only method (3) was used, because it gave the largest “net” carbon yield. The asymmetry distribution of the carbon data was calculated in the same manner as the FST data, and the same fitting function and fitting procedure were used to determine the analyzing power of the background at the  $A_n$  zero-crossing angle. For those results involving  $\chi_{sum}^2$  cuts, the carbon contributions and the analyzing powers for the different cuts were estimated by comparing the yields and scaling to the results of the individual  $\chi_i^2$  cuts. Table 5.5 shows the ratios of the background contribution to the FST data and the analyzing powers for the different  $\chi^2$  tests.

Table 5.5: *Ratios [background/(total - background)] and analyzing powers of the background contribution.*

Cuts	$\chi_i^2 \leq 9$	$\chi_i^2 \leq 7.5$	$\chi_i^2 \leq 5$	$\chi_{sum}^2 \leq 20$	$\chi_{sum}^2 \leq 15$	$\chi_{sum}^2 \leq 10$
ratio(%)	$5.2 \pm 1.3$	$4.1 \pm 1.0$	$2.3 \pm 0.6$	$6.0 \pm 1.5$	$5.2 \pm 1.3$	$3.2 \pm 0.8$
$A_b (10^{-3})$	$-1 \pm 5$	$-4 \pm 7$	$-5 \pm 9$	$-2 \pm 5$	$-3 \pm 6$	$-4 \pm 7$

The free  $np$  analyzing power, the measured analyzing power with background and the analyzing power of the background have the following relationship:

$$A_{true} = \frac{A_{measured} - rA_{background}}{1 - r}, \quad (5.45)$$

where  $r$  is the ratio of background contribution to elastic scattering contribution. The carbon contribution affects the zero-crossing angle of the analyzing power with

the beam polarized ( $A_n$ ) but not the zero-crossing angle of the analyzing power with the target polarized ( $A_p$ ) ( an unpolarized beam on carbon does not produce a scattering asymmetry). Thus, a correction for the carbon contribution was only applied to the zero-crossing angle of the polarized beam data. However, the slopes of the measured asymmetries for both polarized beam and polarized target were affected by the carbon contribution. For the polarized target data, the background diluted the slope of the asymmetry. This was taken into consideration when the slope of  $A_p$  was evaluated (see Section 5.7) Corrections for the zero-crossing angles of  $A_n$  calculated with different cuts were made. The corrected  $A_n$  zero-crossing angles were compared to the results from a bin-by-bin subtraction of the carbon data from the FST (butanol) data. These two procedures of corrections gave consistent results.

### 5.6.2 Neutron Beam Energy Difference Correction

The average neutron beam energies of the polarized and unpolarized beams differed by a small amount due to the correlation between the beam energy and the polarization in the  $D(\vec{p}, \vec{n})2p$  reaction (see Section 4.1). For the polarized and unpolarized beam, the average neutron beam energy was calculated from:

$$\bar{E}^{polarized} = \frac{\sum P_i^2 \cdot N_i \cdot E_i}{\sum P_i^2 \cdot N_i} \quad \text{and} \quad (5.46)$$

$$\bar{E}^{unpolarized} = \frac{\sum E_i \cdot N_i}{\sum N_i}, \quad (5.47)$$

respectively. The difference of the beam energies was found to be:

$$\Delta \bar{E} = \bar{E}^{polarized} - \bar{E}^{unpolarized} = 0.54 \text{ MeV}, \quad (5.48)$$

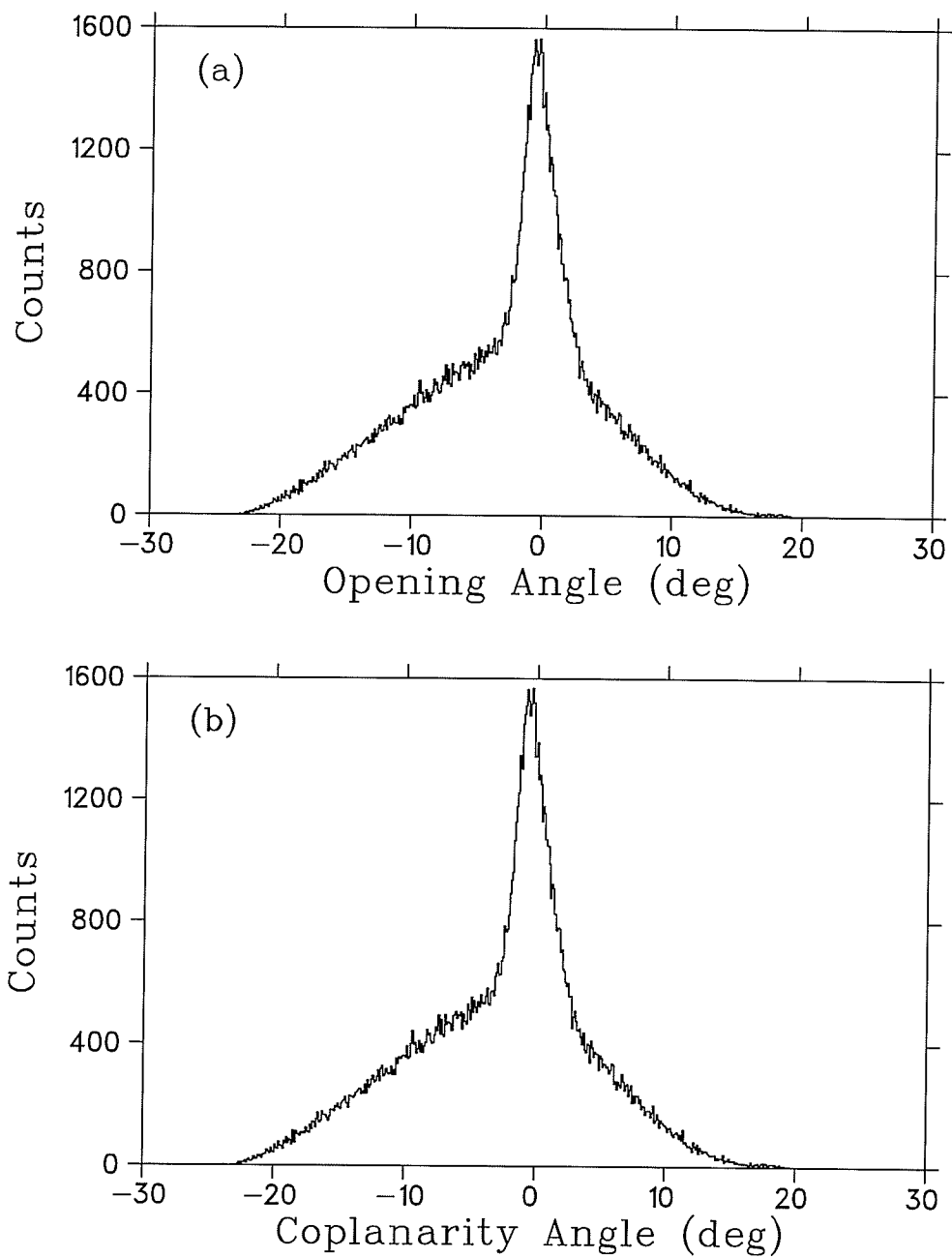


Figure 5.27: *Opening angle (a) and coplanarity angle (b) distributions of the back-ground data. The elastic scattering peaks are due to hydrogen contaminants in the dummy target.*

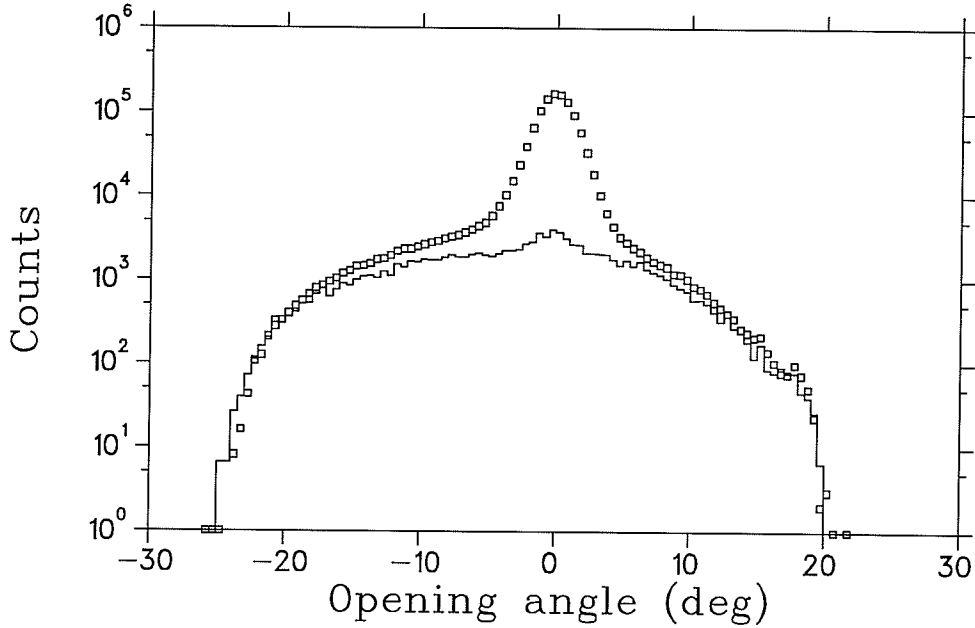


Figure 5.28: *Opening angle distribution of the carbon data (bottom) and the FST data (top) for normalizing the tails and estimating the carbon contribution to the FST data.*

based on Monte Carlo simulations. The variation of the zero-crossing angle with respect to the beam energy was taken from phase shift analyses [69] to be:

$$d\theta_0/dE_{nbeam} \simeq -4.75 \times 10^{-2} \text{ deg/MeV}. \quad (5.49)$$

The 0.54 MeV difference of beam energy will give a difference in zero-crossing angles of +0.026 degree ( or  $\delta A = +3 \times 10^{-3}$ ) which was used as a correction to the data. The uncertainty associated with this correction is discussed in Chapter 6.

## 5.7 Slope of the Analyzing Powers

To interpret the finite difference of the zero-crossing angles in terms of the difference of the analyzing powers, the slope of the analyzing powers at the zero-

crossing angle ( $dA/d\theta$ ) was required. In principle, this parameter could be obtained from phase shift analyses [69]. Unfortunately the phase shift analysis results for this parameter over the last few years and from different calculations have about 10% discrepancies. The experiment determined the parameter  $dA/d\theta$  to 4% accuracy from the polarized target measurement as shown in the following discussion.

For the polarized target measurement ( $A_p$ ) where the FST polarization was known to better than  $\pm 2\%$  as discussed in Section 5.2.7, the slope of the analyzing power was determined experimentally as follows:

$$\frac{dA}{d\theta} = \frac{1}{P_{FST}} \cdot \frac{d\epsilon_p}{d\theta}, \quad (5.50)$$

where  $P_{FST}$  is the average polarization of the FST and  $d\epsilon_p/d\theta$  is the measured slope of the asymmetry. Only a subset of the data was required to achieve a 1% statistical uncertainty in  $d\epsilon_p/d\theta$ . This subset was taken from those runs with high polarizations (85.6%) and long decay times (over 200 hours). The quasi-elastic background did not affect the zero-crossing angle determination of the polarized target data, but it diluted the slope of the measured asymmetry. A correction was included in the measured asymmetry slope:

$$\frac{dA_p}{d\theta} = \frac{1}{P_{FST}} \cdot \frac{1}{1-r} \cdot \frac{d\epsilon_p}{d\theta}, \quad (5.51)$$

where  $r$  is the ratio of the background contribution to elastic scattering. The slope of the analyzing power was determined, from the known FST polarization and the slope of the asymmetry, to be

$$\frac{dA_p}{d\theta} = (1.35 \pm 0.05) \times 10^{-2} \text{ deg}^{-1}, \quad (5.52)$$

where the error is dominated by the uncertainty of the absolute value of the FST

polarization, systematic errors from different  $\chi^2$  cuts and the uncertainty of the correction for the background contribution (dilution).

## 5.8 Shape of “ $\Delta A(\theta)$ ”

The angular distribution of the difference of the analyzing powers is important because it is sensitive to the different contributions of the meson exchanges, in particular the  $\rho^0 - \omega$  mixing contribution. However, as discussed in Chapter 2, it is very difficult to extract the angular distribution. Since the zero-crossing angles of  $\Delta A(\theta)$  as calculated by theoretical predictions are not very well determined, and the experimental systematic errors around the predicted zero-crossing angles of  $\Delta A$  were not negligible, extraction of only the shape of  $\Delta A(\theta)$  was attempted. As discussed in Chapter 2, the shape of  $\Delta A(\theta)$  can be determined up to an uncertainty of  $c$  weighted by the analyzing power:

$$\text{“}\Delta A_{\text{expt}}\text{”} = \Delta A_{\text{true}} + c \cdot A(\theta), \quad (5.53)$$

where  $c$  is directly related to the uncertainty of  $P_n/P_p$ . “ $\Delta A_{\text{expt}}$ ” was obtained from the measured asymmetries, the average neutron beam polarization ( $61.2 \pm 1.8$ )% and the average FST polarization ( $73.2 \pm 2.2$ )%. Here, an error in the neutron beam polarization was estimated to be  $\pm 3\%$  which is the quadrature sum of the estimated  $\pm 2\%$  uncertainty of the proton beam polarization (the effective  $pp$  analyzing power of the CSB polarimeter) and  $\pm 2\%$  uncertainty of the average of  $\sqrt{r_t^2 + r_t'^2}$ . To compare with theoretical predictions,  $\Delta A_{\text{true}}$  was taken to be the predicted theoretical distribution and the constant  $c$  was adjusted until the  $\chi^2$  between the theoretical prediction and the measured distribution was minimized. A ten-point distribution of the shape of  $\Delta A$  was obtained following this procedure (see Chapter 7 for results).

# Chapter 6

## Systematic Errors

### 6.1 Introduction

As discussed in the previous chapters, the goal of the experiment was to determine the difference of the analyzing powers,  $\Delta A \equiv A_n - A_p$ , from the difference of the zero-crossing angles,  $\Delta\theta_o \equiv \theta_n - \theta_p$ .  $\Delta A$  was expected to be small, on the order of at most one percent, and control of the systematic errors was critical to the success of the experiment. The experiment was conducted such that all systematic errors except those correlated with spin reversals or due to background were cancelled to at least second order in the difference of the zero-crossing angles (to first order in the individual zero-crossing angles,  $\theta_n$  or  $\theta_p$ ). This was achieved by a mirror symmetric detection system, identical beam and target properties (except polarization) for the  $A_n$  and  $A_p$  measurements and interleaving of these two measurements, and frequent flipping of the holding field direction, polarization direction and the last spin precession magnet (BONNIE) field direction. Various estimates of the systematic errors were made with assumed system parameters. Based on these estimates, very stringent limits were applied to the system parameters during the experiment in order to constrain the individual systematic error

contributions to  $\Delta A$  to below  $10^{-4}$ . This chapter will summarize the estimates and the limits of the major systematic errors (Section 6.2) and the various tests applied to the data to study the systematic errors (Section 6.3).

Three types of systematic errors are discussed here, these are (a) fixed errors (these did not change during the course of the experiment), (b) errors correlated with polarization direction reversals; (c) errors randomly varying during the experiment. Because of the design of the experiment, most fixed errors were cancelled in  $\Delta\theta_o$  or  $\Delta A$  if these errors affected  $A_n$  and  $A_p$  in the same way, since if:

$$\delta A_n = \delta A_p, \quad (6.1)$$

$$\text{then } \delta(\Delta A) = 0. \quad (6.2)$$

Therefore, the fixed errors of most concern were those which affected  $A_n$  and  $A_p$  differently, thus introducing errors to  $\Delta A$ , since if:

$$\delta A_n \neq 0, \text{ and/or, } \delta A_p \neq 0, \quad (6.3)$$

$$\text{then } \delta A_n \neq \delta A_p, \quad (6.4)$$

$$\text{and } \delta(\Delta A) \neq 0. \quad (6.5)$$

The errors that were correlated with beam or target polarization direction reversals would only affect the polarized beam data ( $A_n$ ) or polarized target data ( $A_p$ ), respectively. It should be noted that these errors are of obscure origin and their existence is based PURELY on ASSUMPTIONS, e.g., there is no apparent reason why a neutron detector should change gain or detection efficiency when the spin is flipped. However, errors of this type could arise if there was a long term drift of a parameter, so that for a pair of spin up and spin down runs, the average value of the parameter which was drifting was different for spin up and down. These

errors would affect  $\Delta A$ . The random errors would affect  $A_n$  and  $A_p$  as well as  $\Delta A$ .

The notation used in the following sections is discussed here. The observed count rates in the left and right side neutron detection apparatus (left and right events, respectively as defined in Chapter 3) can be written as:

$$L^+ \propto \sigma_L^+ \epsilon_L^+ (1 + P^+ A_L^+), \quad (6.6)$$

$$R^+ \propto \sigma_R^+ \epsilon_R^+ (1 - P^+ A_R^+), \quad (6.7)$$

$$L^- \propto \sigma_L^- \epsilon_L^- (1 - P^- A_L^-), \quad (6.8)$$

$$R^- \propto \sigma_R^- \epsilon_R^- (1 + P^- A_R^-). \quad (6.9)$$

Here “ $\pm$ ” superscripts represent the direction of the target or beam polarization for measurements of  $A_p$  and  $A_n$ ; “L,R” subscripts are for the left or right events;  $\sigma_{L,R}^\pm$  are the differential cross-sections involving unpolarized nucleons;  $\epsilon_{L,R}^\pm$  are the detection efficiencies (dictated by the neutron detection efficiency since the proton detection efficiency was above 99.7% as discussed in Chapter 3); P is the polarization of the nucleons; and A is the analyzing power. It is assumed that the quantities,  $\sigma_{L,R}^\pm$ ,  $\epsilon_{L,R}^\pm$ ,  $P^\pm$  and  $A_{L,R}^\pm$ , may change from one detector to the other and/or from spin polarization direction up to down.

The asymmetries and analyzing powers were determined from the data as follows:

$$\epsilon = \frac{r-1}{r+1} + \text{error terms}, \quad (6.10)$$

$$A = \frac{1}{P} \cdot \frac{r-1}{r+1} + \text{error terms}, \quad (6.11)$$

$$\begin{aligned} \text{with } r^2 &= \frac{L^+ R^-}{L^- R^+} \\ &= \frac{\sigma_L^+ \sigma_R^- \epsilon_L^+ \epsilon_R^- (1 + P^+ A_L^+) (1 + P^- A_R^-)}{\sigma_L^- \sigma_R^+ \epsilon_L^- \epsilon_R^+ (1 - P^- A_L^-) (1 - P^+ A_R^+)}. \end{aligned} \quad (6.12)$$

Here, the error terms are very small, particularly in the angular range around  $A \simeq 0$ . In the complete absence of any experimental errors and with identical detection system, (6.12) reduces to:

$$r_o^2 = \left( \frac{1 + PA}{1 - PA} \right)^2. \quad (6.13)$$

The following parameters,  $s_{L,R}^\pm$ ,  $\delta\epsilon_{L,R}^\pm$ ,  $a_{L,R}^\pm$  and  $\alpha$ , are introduced into the differential cross-sections, detection efficiencies, analyzing powers and polarizations to study the variation of these quantities and their effects on the systematic errors.

(1) The unpolarized differential cross-section, as a function of angle, is assumed to differ from its nominal value due to slight geometric or other imperfections as:

$$\sigma_{L,R}^\pm = \sigma(1 + s_{L,R}^\pm). \quad (6.14)$$

To first order in  $s$ ,

$$r^2 = \frac{(1 + s_L^+)(1 + s_R^-)}{(1 + s_R^+)(1 + s_L^-)} \cdot r_o^2, \quad (6.15)$$

$$r \simeq \left( 1 + \frac{s_L^+}{2} - \frac{s_R^+}{2} - \frac{s_L^-}{2} + \frac{s_R^-}{2} \right) \cdot r_o,$$

$$\delta A = \frac{1}{P} \frac{2}{(r+1)^2} \delta r \simeq \frac{1}{2P} \delta r, \quad (r \simeq 1),$$

$$\delta A \simeq \frac{1}{4P} (s_L^+ - s_R^+ - s_L^- + s_R^-), \quad (r_o \simeq 1). \quad (6.16)$$

(2) The detection probability is assumed to change as:

$$\epsilon_{L,R}^\pm = \epsilon(1 + \delta\epsilon_{L,R}^\pm). \quad (6.17)$$

The result is analogous to the expression for a differential cross-section change:

$$\delta A \simeq \frac{1}{4P} (\delta\epsilon_L^+ - \delta\epsilon_R^+ - \delta\epsilon_L^- + \delta\epsilon_R^-), \quad (r_o \simeq 1). \quad (6.18)$$

(3) The observed analyzing power variation is expressed as:

$$A_{L,R}^\pm = A + a_{L,R}^\pm. \quad (6.19)$$

Substituting into (6.12), this equation becomes:

$$\begin{aligned}
 r^2 &= \frac{1 + P(A + a_L^+)}{1 - P(A + a_R^+)} \cdot \frac{1 + P(A + a_R^-)}{1 - P(A + a_L^-)}, \\
 r^2 &\simeq r_o^2 [1 + P(a_L^+ + a_R^+ + a_L^- + a_R^-) \\
 &\quad - P^2 A(a_L^+ - a_R^+ - a_L^- + a_R^-) + O(a^2)], \tag{6.20}
 \end{aligned}$$

$$\delta A \simeq \frac{1}{4} [a_L^+ + a_R^+ + a_L^- + a_R^- - PA(a_L^+ - a_R^+ - a_L^- + a_R^-)]. \tag{6.21}$$

This first-order formula should be sufficiently accurate, provided that  $(a_{L,R}^\pm)^2 \leq 10^{-4}$ .

(4) The magnitude of the polarization changes between up and down states as:

$$|P^\pm| = |P| \pm \alpha. \tag{6.22}$$

Substituting into (6.12), one obtains,

$$\begin{aligned}
 r^2 &= \frac{1 + (P + \alpha)A}{1 - (P + \alpha)A} \cdot \frac{1 + (P - \alpha)A}{1 - (P - \alpha)A} \\
 &\simeq r_o^2 [1 + 4PA^3\alpha^2 + 8\alpha^2 P^3 A^5 + O(\alpha^4 A^5)], \tag{6.23}
 \end{aligned}$$

$$\delta A \simeq \alpha^2 A^3 + 2\alpha^2 P^2 A^5, \quad (r_o \simeq r \simeq 1). \tag{6.24}$$

The effect of the polarization changes on the analyzing powers is normally very small, e.g., for  $\alpha = \pm 5\%$ , at the zero-crossing angle,  $\delta A = 0$ ; and for  $A = 0.2$ ,  $\delta A = 2 \times 10^{-5}$ . Therefore, most discussions of the beam and target properties in the following sections do not consider the polarization changes unless explicitly stated.

The equations (6.16), (6.18), (6.21) and (6.24) will be used throughout the next section where various systematic errors are discussed. The phase shift analysis results from SAID [69] are used when such parameters are required.

## 6.2 Sources of Systematic Errors

### 6.2.1 Proton Beam Energy, Position and Direction at the $LD_2$ Target

#### (1) Proton Beam Energy

The zero-crossing angles are dependent on the neutron beam energy. Any change in the proton beam energy will cause a change in the neutron beam energy, and thus cause a change in the analyzing powers as well as the zero-crossing angles.

##### (a) Fixed energy difference:

A fixed energy difference (for all runs) with respect to the nominal value was not important. The absolute knowledge of the proton beam energy only needed to be known to a few MeV as long as it was much smaller than the neutron beam energy spread (about 11 MeV FWHM), since only the difference of the analyzing powers at a certain (fixed) nominal energy was a concern to the experiment. However, an energy change between the  $A_n$  and  $A_p$  measurements would introduce an error in  $\Delta A$ :

$$\delta A = \frac{dA}{d\theta} \delta\theta = \frac{dA}{d\theta_o} \frac{\partial\theta_o}{\partial E_{nbeam}} \cdot \frac{\partial E_{nbeam}}{\partial E_{pbeam}} \cdot \delta E_{pbeam}. \quad (6.25)$$

Here,  $\theta_o$  is the zero-crossing angle;  $E_{nbeam}$  and  $E_{pbeam}$  are the neutron and proton beam energies, respectively. Taking  $dA/d\theta_o = -1.35 \times 10^{-2}$  /deg (c.m.),  $\partial\theta_o/\partial E_{nbeam} = -0.048$  deg/MeV (c.m.), and  $\partial E_{nbeam}/\partial E_{pbeam} \simeq 1.0$ , for  $\delta(\Delta A) \leq 10^{-4}$ ,  $\delta E_{pbeam}$  should be kept within 0.154 MeV between the  $A_n$  and  $A_p$  measurements.

##### (b) Spin-correlated energy difference:

To consider the effects of beam energy changes when the spin was flipped (either for the polarized beam or polarized target phases of the experiment), one may make the following assumptions:

$$\begin{aligned} s_L^+ &= s_R^+ = s^+, & s_L^- &= s_R^- = s^-, \\ a_L^+ &= a_R^+ = a^+, & a_L^- &= a_R^- = a^-, \\ P^+ &= P^- = P. \end{aligned} \quad (6.26)$$

Substituting into (6.16), (6.18), (6.21) and (6.24), the only non-vanishing term is:

$$\delta A_{measured} \simeq \frac{1}{2}(a^+ + a^-). \quad (6.27)$$

$a^\pm$  can be expanded and substituted into (6.27):

$$a^\pm = \pm \frac{\partial A}{\partial \theta_o} \cdot \frac{\partial \theta_o}{\partial E_{nbeam}} \cdot \frac{\partial E_{nbeam}}{\partial E_{pbeam}} \cdot \delta E_{pbeam}; \quad (6.28)$$

consequently,  $a^+$  and  $a^-$  cancel to first order:

$$\delta A_{measured} = 0 + O\left(\frac{\partial^2 A}{\partial E_{nbeam}^2} \delta E_{nbeam}^2\right). \quad (6.29)$$

Such an error would not contribute to the error in  $A_n$ ,  $A_p$  or  $\Delta A$  at  $10^{-5}$  level.

(c) Random changes in the beam energy:

A randomly changing beam energy would give:

$$\delta A_{measured} \simeq \frac{\sigma_a}{\sqrt{2}}. \quad (6.30)$$

Here  $\sigma_a$  is the width (standard deviation) of the random variation of the analyzing power due to the beam energy variation. The condition  $\sigma_{E_{pbeam}} \leq 0.22$  MeV would satisfy  $\delta A \leq 10^{-4}$ . This applies to both  $A_n$  and  $A_p$ . For  $\Delta A = A_n - A_p$  to be measured to  $\pm 10^{-4}$ , the statistical error on keeping the beam energy stable should be reduced by a factor of  $\sqrt{2}$  to 0.15 MeV.

During the experiment, the proton beam energy was kept the same with a standard deviation  $\sigma = 0.038$  MeV (see Chapter 5), and the error in  $\Delta A$  due to this effect is less than  $10^{-4}$ .

## (2) Proton Beam Position at the $LD_2$ Target

A change of the proton beam spot position would alter the angle of the neutron beam on the FST and also produce a small change in the neutron beam energy. Asymmetries were not affected by minor drifts of the proton beam in the vertical direction since they would produce the same effects on the left-right and spin up-down events. However, deviations in the horizontal position were directly related to the polar scattering angles of elastic np pairs and therefore to the observed asymmetries.

(a) Fixed beam position error:

The FST was positioned 12.85 m from the center of the  $LD_2$  target. A change in the x position alters the angle of the neutron beam incident on the FST by  $\delta\theta = 4.4 \times 10^{-3}$  deg/mm. Since this  $\delta\theta$  is very small in the expansion of the differential cross-sections and the analyzing powers, only the first order terms need to be considered:

$$\begin{aligned} s_L^+ &= s_L^-, & s_R^+ &= s_R^-, \\ a_L^+ &= a_L^- = \frac{\partial A}{\partial \theta} \delta\theta, & a_R^+ &= a_R^- = -\frac{\partial A}{\partial \theta} \delta\theta, \\ P^+ &= P^- = P. \end{aligned} \tag{6.31}$$

Substituting into (6.16), (6.18), (6.21) and (6.24), all first order terms in the equations cancel:

$$\delta A_{measured} \simeq 0 + O\left(\frac{\partial^2 A}{\partial \theta^2} \delta\theta^2\right). \tag{6.32}$$

A constant error in the incident neutron beam direction due to an error in the proton beam position at the  $LD_2$  target contributes neither to  $A_n$  nor to  $A_p$ .

(b) Spin-correlated changes in the beam position:

If the change in the beam spot on the  $LD_2$  target was correlated with the polarization direction:

$$\begin{aligned} s_L^\dagger &= -s_R^\dagger = -s_L^- = s_R^- = s, \\ a_L^\dagger &= -a_R^\dagger = -a_L^- = a_R^- = a, \\ P^+ &= P^- = P. \end{aligned} \quad (6.33)$$

Substituting into (6.16), (6.18), (6.21) and (6.24), one obtains:

$$\delta A_{measured} \simeq \frac{s}{P} - PAa. \quad (6.34)$$

At  $A = 0$ ,

$$\delta A_{measured} \simeq \frac{s}{P} \simeq \frac{1}{P\sigma} \cdot \frac{\partial\sigma}{\partial\theta} \delta\theta, \quad (6.35)$$

where  $\sigma \simeq 6.1$  mb/sr (lab) and  $\partial\sigma/\partial\theta \simeq -0.36$  mb/sr·deg (lab) at the zero-crossing angle (at  $34.2^\circ$  lab or  $73.0^\circ$  c.m.) and  $P = 0.7$ . For  $\delta A \leq 10^{-4}$ ,  $\delta\theta$  should be  $\leq 1.2 \times 10^{-3}$  deg. or  $\delta x \leq 0.27$  mm. As  $A_p$  was not affected by deviations in the proton beam position correlated with beam polarization direction reversals, it follows that  $\delta A_p = 0$ . Therefore,  $\delta\Delta A = \delta A_n \leq 10^{-4}$  for  $\delta\theta \leq 1.2 \times 10^{-3}$  deg. or  $\delta x \leq 0.27$  mm. This value is likely an over-estimation of the error, as the neutron collimator defined the acceptance region for neutrons originating in the  $LD_2$  target.

(c) Random changes in the beam position:

For a random horizontal displacement of the proton beam on the  $LD_2$  target  $\delta x$ :

$$s_L^\dagger = -s_R^\dagger = s^+, \quad s_L^- = -s_R^- = s^-,$$

$$\begin{aligned}
a_L^\dagger &= -a_R^\dagger = a^+, & a_L^- &= -a_R^- = a^-, \\
P^+ &= P^- = P.
\end{aligned}
\tag{6.36}$$

Substituting into (6.16), (6.18), (6.21) and (6.24), one obtains:

$$\delta A_{measured} \simeq \frac{s^+ - s^-}{2P} \simeq \frac{1}{\sqrt{2}P\sigma} \cdot \frac{\partial\sigma}{\partial\theta} \delta\theta.
\tag{6.37}$$

For  $\delta A_{measured} \leq 10^{-4}$ , one should have  $\sigma_x \leq 0.38$  mm.

(d) Position-correlated beam energy changes:

Changes in the proton beam spot position on the  $LD_2$  target can also cause changes in the neutron beam energy. The neutron collimator axis intersected the center of the  $LD_2$  target at an angle of  $9^\circ$  relative to the proton beam axis. The intersection of the proton beam with the  $LD_2$  target, seen from the position of the FST, depended on the precise position of the proton beam. The average length, for the proton beam passing through the  $LD_2$  target, would depend on where the collimator axis intersected the proton beam. Protons of 369 MeV lose approximately 0.05 MeV/mm in the  $LD_2$ . The analyzing power zero-crossing angles change as a function of the neutron beam energy as  $\partial\theta_0/\partial E = -0.048^\circ/\text{MeV}$  (c.m.). Therefore, a change in the proton beam horizontal (x) position on the  $LD_2$  by 1.0 mm will cause a change to the average path length of those protons (which produced the neutron beam) by 6.3 mm, thereby changing the average neutron beam energy by 0.315 MeV. This would result in a change in the zero-crossing angle of  $1.5 \times 10^{-2}$  deg. or, equivalently, a change in the analyzing power at the zero-crossing angle of  $2.0 \times 10^{-4}$ . To keep  $\delta A \leq 10^{-4}$ , the proton beam horizontal (x) position at the  $LD_2$  target had to be kept to within  $\pm 0.5$  mm.

The proton beam position at the  $LD_2$  target was stabilized to within 0.03 mm during the experiment (see Chapter 5). The error of  $\Delta A$  due to the proton

beam position was therefore kept well below the  $10^{-4}$  level.

### (3) Proton Beam Direction

Changes in the direction of the proton beam on the  $LD_2$  target effectively alter the angle between the proton beam axis and the collimator, and therefore alter the energy of the outgoing neutron beam, and lead to errors in  $A$  and  $\Delta A$ :

$$\delta A \simeq \frac{\partial A}{\partial \theta_o} \cdot \frac{\partial \theta_o}{\partial E_{nbeam}} \cdot \frac{\partial E_{nbeam}}{\partial \theta_{pbeam}} \delta \theta_{pbeam}. \quad (6.38)$$

At  $E_{pbeam} = 369$  MeV,  $\partial E_{nbeam} / \partial \theta_{pbeam} = -2.4$  MeV/deg (lab),

$\partial \theta_o / \partial E_{nbeam} = -0.024^\circ / \text{MeV}$  (lab), and  $\partial A / \partial \theta_o = -0.027 / \text{deg}$  (lab) at  $A = 0$ .

These values result in  $\partial A / \partial \theta_{pbeam} = 1.6 \times 10^{-3} / \text{deg}$  at the nominal zero-crossing angle.

(a) Fixed errors in the proton beam direction:

A fixed error in the proton beam direction would affect both the  $A_n$  and  $A_p$  measurements in the same way and have no effect on  $\Delta A$ .

(b) Spin-correlated changes in the beam direction:

A modulation of the beam direction on the  $LD_2$  target of  $|\theta^+ - \theta^-| = 0.1^\circ$  correlated with the primary beam polarization direction would result in a systematic deviation of  $\delta \Delta A = \delta A_n = 1.6 \times 10^{-4}$ .

(c) Random changes in the beam direction:

A randomly varying error in the proton beam direction of  $\sigma_\theta = 0.1^\circ / \sqrt{2}$  would cause a deviation in  $\delta \Delta A = 1.6 \times 10^{-4}$ .

In the experiment, the direction of the proton beam was estimated to be stable to  $\pm 0.005^\circ$  as given by the SEM data, and therefore the resultant error in  $\Delta A$  was  $\leq 10^{-5}$ .

## 6.2.2 Neutron Beam Energy Stability

The analyzing powers and the zero-crossing angles change with the incident neutron beam energy. At  $E_{nbeam} = 347$  MeV, and  $\theta_o = 34.2^\circ$  (lab),  $\partial A / \partial \theta_o = -0.027$  deg $^{-1}$  (lab) and  $\partial \theta_o / \partial E_{nbeam} = -0.024$  deg/MeV (lab). Absolute knowledge of the beam energy was unimportant to a few MeV as long as it did not change between data taking runs. The neutron beam energy was influenced not only by the proton beam properties but also by the  $LD_2$  target density. The fluctuations in the  $LD_2$  density will cause the average neutron beam energy to fluctuate, therefore causing an error in the zero-crossing angles. To achieve  $\delta A \leq 10^{-4}$ , the  $LD_2$  density should be kept constant within  $\pm 0.009$  g/cm $^3$ . The  $LD_2$  target density was found to be stable to  $\pm 0.0005$  g/cm $^{-3}$  during the data taking (see Section 5.2.3).

## 6.2.3 FST Parameters

### (1) Holding Field Strength

Small changes in the magnitude of the holding field strength would cause changes in the deflection of the recoil proton trajectories. The holding field deflected np elastic proton trajectories at the large angle limit of the detection system by  $\sim 1.8^\circ$  and at the small angle limit of the detection system by  $\sim 1.2^\circ$ . The FST holding field at the center of the FST was 0.22 T and the  $\int \vec{B} \cdot d\vec{l}$  seen by a proton

originating in the center of the target was about 0.04 Tm.

(a) Fixed error in the holding field strength:

A fixed error in the holding field setting would have the effect of rotating the proton angle scale, causing an error of  $\delta\theta$  on one side and of  $-\delta\theta$  on the other side of the beam axis. The error due to this can be expressed as:

$$\begin{aligned} s_L^+ &= s_L^-, & s_R^+ &= s_R^-, \\ a_L^+ &= a_L^-, & a_R^+ &= a_R^-, \\ P^+ &= P^-. \end{aligned} \quad (6.39)$$

From equations (6.16), (6.18), (6.21) and (6.24), this gives:

$$\delta A_{measured} \simeq \frac{a_L + a_R}{2}. \quad (6.40)$$

Expanding  $a_L$  and  $a_R$  in terms of  $\delta\theta$ ,

$$\begin{aligned} a_L &= \frac{\partial A}{\partial \theta} \delta\theta + \frac{1}{2} \frac{\partial^2 A}{\partial \theta^2} \delta\theta^2 + \dots, \\ a_R &= -\frac{\partial A}{\partial \theta} \delta\theta + \frac{1}{2} \frac{\partial^2 A}{\partial \theta^2} \delta\theta^2 + \dots. \end{aligned} \quad (6.41)$$

With first order terms cancelling, equation (6.40) becomes,

$$\delta A_{measured} \simeq \frac{1}{2} \frac{\partial^2 A}{\partial \theta^2} \delta\theta^2, \quad (6.42)$$

where  $\partial^2 A / \partial \theta^2 \simeq 7.64 \times 10^{-4} \text{ deg}^{-2} \text{ (lab)}$ . For  $\delta A \simeq 10^{-4}$ , one has  $\delta\theta_0 \leq 0.5^\circ$  which is about 1/3 of the average total deflection angle  $1.5^\circ$ . Therefore, any reasonable deviation in the holding field strength not correlated with polarization direction changes would cause  $\delta(\Delta A) \ll 10^{-4}$ .

(b) Spin-correlated changes in the holding field strength:

If the holding field deviations were directly correlated with the target polarization

direction, then:

$$\begin{aligned}
s_L^+ &= -s_R^+ = -s_L^- = s_R^- = s \quad (\text{to first order in } \delta\theta), \\
a_L^+ &= -a_R^+ = -a_L^- = a_R^- = a, \\
P^+ &= P^-.
\end{aligned} \tag{6.43}$$

Then, the non-vanishing terms are:

$$\delta A_{measured} \simeq \frac{s}{P} - PAa, \tag{6.44}$$

$$s \simeq \frac{1}{\sigma} \frac{\partial \sigma}{\partial \theta} \cdot \delta\theta - PA \frac{\partial A}{\partial \theta} \cdot \delta\theta. \tag{6.45}$$

At  $A = 0$ ,  $\theta = 34.2^\circ$  lab and  $E_n = 347$  MeV,  $\sigma = 6.1$  mb/sr (lab), and  $((1/\sigma) \cdot \partial\sigma/\partial\theta) = -0.059$  deg $^{-1}$  (lab). For  $\delta A \simeq 10^{-4}$  and  $P = 0.8$ ,  $\delta\theta$  should be  $1.3 \times 10^{-3}$  deg (lab). At  $\theta_p = 53^\circ$ ,  $p_p = 476$  MeV/c, and  $\partial\theta_p/\partial B_{hf} \simeq 5.0 \times 10^{-2}$  deg/mT. Therefore, to keep  $\delta(\Delta A) \leq 10^{-4}$ , the holding field should be kept stable to within  $B \simeq 0.26$  mT. At  $A \neq 0$ , since the term  $PA(\partial A/\partial\theta) \ll (1/\sigma)(\partial\sigma/\partial\theta)$ , the result is the same as at  $A = 0$ . There is no good reason why the holding field strength would have changed with FST polarization direction reversals.

(c) Random changes in the holding field strength:

If the error in the holding field strength was random,

$$\begin{aligned}
s_L^+ &= -s_R^+ = s^+, & s_L^- &= -s_R^- = s^-, \\
a_L^+ &= -a_R^+ = a^+, & a_L^- &= -a_R^- = a^-, \\
P^+ &= P^-.
\end{aligned} \tag{6.46}$$

Substituting into equations (6.16), (6.18), (6.21) and (6.24), the non-vanishing terms are:

$$\delta A_{measured} \simeq \frac{(s^+ - s^-)}{2P} - PA \frac{a^+ - a^-}{2}. \tag{6.47}$$

At  $A = 0$ ,  $\sigma_A \simeq \sigma_s/\sqrt{2P}$ , and the requirement that  $\sigma_A \leq 10^{-4}$  gives  $\sigma_{hf} \leq 0.37$  mT, corresponding to  $\sigma_\theta \leq 1.8 \times 10^{-3}$  deg., where  $\sigma_i$  are standard deviations of respective distributions of the random variation of the variables.

The holding field strength as read by the Hall probes was stable to better than  $\pm 0.3$  mT during data taking, implying  $\delta(\Delta A) \leq 7 \times 10^{-5}$ .

## (2) Relative Position of Target and Holding Field to the Symmetry Axis

Deviations in the target cell position and/or the holding field with respect to the symmetry axis (the nominal pivot axis of the detection system) caused shifts between the actual scattering angles and those measured by the deflected proton tracks. The main contribution to the resultant angular deviations was the different  $\int \vec{B} \cdot d\vec{l}$  which protons experienced due to the shift in the holding field. As such, shifts in the target position had an effect similar to shifts in the holding field.

A lateral displacement of the target or the holding field by  $\delta x$  would cause the line integral of the field,  $\int \vec{B} \cdot d\vec{l}$ , seen by the recoil protons to be increased on one side and decreased on the other side of the beam axis. The protons detected at a nominal angle  $\theta$  on either side of the beam were actually emitted at a slightly larger or smaller angle depending on the holding field direction and the direction of the displacement. If the holding field direction was vertically up and the displacement was towards the left by  $\delta x$ , recoil protons were deflected to the right and those on the physical right side experienced less magnetic field than those on the physical left side. If the protons were detected at an angle  $\theta$  in both the physical left and right side detectors, the left side protons originated from  $\theta + \Delta\theta + \delta\theta$  and the right side protons originated from  $\theta - \Delta\theta + \delta\theta$ , where  $\Delta\theta$  is the nominal

deflection angle due to the holding field (if there was no error in the holding field) and  $\delta\theta$  is the error in the deflection angle due to the displacement. Both the left and right proton angles would be shifted by the same amount  $\delta\theta$  with the same sign due to the holding field displacement.

A vertical displacement  $\delta y$  of the target would change the magnetic field through which the recoil protons passed; the line integral of the field changing by  $(\frac{\partial}{\partial y} \int \vec{B} \cdot d\vec{l})\delta y$ , would cause a rotation of the angle scale. Its effect would be similar to an error in the holding field strength.

A longitudinal displacement  $\delta z$  would have a similar effect to a displacement  $\delta y$ . The recoil protons would experience a different holding field,  $\delta(\int \vec{B} \cdot d\vec{l})$ , dependent on the direction of the shift (in the upstream or downstream directions).

The position of the target cell was determined to within  $\pm 1.0$  mm from X-ray photographs of the FST taken at least once per data taking period. The holding field spatial distribution was obtained from field mapping done twice during the course of the experiment.

(a) Fixed error in the FST position:

Assume the target shifted to one side by  $\delta x$ . Protons to one side would pass on average through a larger  $\int \vec{B} \cdot d\vec{l}$  and be bent through a larger angle, and those to the other side would pass through a smaller  $\int \vec{B} \cdot d\vec{l}$  and be deflected by a smaller angle. The errors can be written as:

$$s_L^+ = s_L^- = s_R^+ = s_R^- = s,$$

$$\begin{aligned}
a_L^{\dagger} &= a_L^{-} = a_R^{\dagger} = a_R^{-} = a, \\
P^+ &= P^- = P.
\end{aligned}
\tag{6.48}$$

Substituting into equations (6.16), (6.18), (6.21) and (6.24), the non-vanishing terms are:

$$\delta A_{measured} \simeq a. \tag{6.49}$$

The parameter  $a$  can be estimated from:

$$a = \frac{\partial A}{\partial \theta} \frac{\partial \theta}{\partial x} \delta x. \tag{6.50}$$

For a fixed  $\delta x$ , holding field  $B_o$  and recoil protons at an angle  $\theta$  and deflected by  $\Delta\theta$ , the change of  $\Delta\theta$ ,  $\delta\theta$ , in deflection by the field due to the displacement is:

$$\begin{aligned}
\delta\theta &\simeq \frac{0.3}{pc} B_o \sin\theta \times \frac{180}{\pi} \delta x, \quad \text{or} \\
\frac{\partial\theta}{\partial x} &\simeq \frac{0.3}{pc} B_o \sin\theta \times \frac{180}{\pi},
\end{aligned}
\tag{6.51}$$

where 0.3 is a constant with proper dimension for protons (with charge  $e$ ),  $pc$  is the momentum in MeV,  $\delta\theta$  in deg.,  $B_o$  in T and  $\delta x$  in mm;  $pc \simeq 476$  MeV at  $\theta_p = 53^\circ$  and  $B_o = 0.22$  T at the center of the FST. The change in the magnetic field deflection can be determined to find that  $\partial\theta/\partial x \simeq 6 \times 10^{-3}$  deg/mm at  $\theta_p = 53^\circ$  and with  $\partial A/\partial\theta \simeq -0.027$  deg $^{-1}$ , to be given by  $\delta A \simeq 1.6 \times 10^{-4} \delta x$ . Therefore,  $\delta x$  should be kept less than 0.6 mm. Note that these errors are the same for the  $A_n$  and  $A_p$  measurements, and the estimates represent an upper limit.

For a fixed vertical displacement  $\delta y$ ,  $\int \vec{B} \cdot d\vec{l}$  changes by the same amount for protons scattered to the left and to the right and gives a result similar to that for a fixed error in the setting of the holding field:

$$\delta A_{measured} \simeq \frac{1}{2} \left( \frac{\partial^2 A}{\partial \theta^2} \right) \delta \theta^2. \tag{6.52}$$

For  $\delta A \simeq 10^{-4}$ ,  $\delta\theta \simeq 0.5^\circ$  gives  $\delta \int \vec{B} \cdot d\vec{l}$  of  $\leq 0.013$  Tm which is about 30% of the total  $\int \vec{B} \cdot d\vec{l}$  of about 0.04 Tm. The allowable  $\delta y$  depends on the uniformity of the holding field.

For a longitudinal displacement  $\delta z$ , the effect is similar to a vertical displacement. In order to keep  $\delta\theta$  within 0.5 deg., the allowable displacement depends on the holding field distribution.

Both fixed vertical and longitudinal displacements were not very critical to the experiment, giving for a substantial displacement from the nominal position (i.e., a few mm), the errors in  $\delta A$  as well as  $\delta(\Delta A)$  below the  $10^{-4}$  level.

(b) Spin-correlated changes in the FST position:

If  $\delta x$  changed sign with polarization direction reversals:

$$\begin{aligned} s_L^+ &= -s_L^- = s_R^+ = -s_R^- = s, \\ a_L^+ &= a_R^+ = a^+, \quad a_L^- = a_R^- = a^-, \\ P^+ &= P^- = P. \end{aligned} \tag{6.53}$$

Then the non-vanishing error term is:

$$\delta A_{measured} \simeq \frac{a^+ + a^-}{2}. \tag{6.54}$$

$$\frac{a^+ + a^-}{2} \simeq \frac{1}{2} \left( \frac{\partial A}{\partial \theta} \frac{\partial \theta}{\partial x} \delta x^+ + \frac{\partial A}{\partial \theta} \frac{\partial \theta}{\partial x} \delta x^- \right) + \frac{1}{2} \left( \frac{\partial^2 A}{\partial \theta^2} \right) \left( \frac{\partial \theta}{\partial x} \delta x \right)^2, \tag{6.55}$$

where  $\partial^2 A / \partial \theta^2 = 7.6 \times 10^{-4}$  deg<sup>2</sup> (lab) and  $\partial \theta / \partial x \simeq 6 \times 10^{-3}$  deg/mm is given by Eq. (6.51). This effect is very small and is not critical. The target lateral displacement should be kept within a reasonable range (i.e., a few mm).

A  $\delta y$  displacement changing with polarization direction gives:

$$\begin{aligned} s_L^+ &= -s_R^+ = -s_L^- = -s_R^- = s, \\ a_L^+ &= -a_R^+ = -a_L^- = a_R^- = a, \\ P^+ &= P^- = P, \end{aligned} \quad (6.56)$$

and

$$\delta A_{measured} \simeq \frac{s}{P}. \quad (6.57)$$

Analogous to an error in the holding field strength (b), this requires  $\delta\theta \leq 1.3 \times 10^{-3}$  deg. for  $\delta(\Delta A) \leq 10^{-4}$ . Since

$$\delta\theta = \frac{\Delta\theta}{\int \vec{B} \cdot d\vec{l}} \cdot \left( \frac{\partial}{\partial y} \int \vec{B} \cdot d\vec{l} \right) \cdot \delta y, \quad (6.58)$$

where  $\Delta\theta \simeq 1.5^\circ$  is the average deflection angle, one finds that to keep  $\delta A \simeq 10^{-4}$ ,  $\delta y$  should be kept 1 mm and  $\partial(\int \vec{B} \cdot d\vec{l})/\partial y \leq 0.035$  Tm/mm.

For a longitudinal displacement correlated with polarization direction changes, the effect is similar to a holding field strength error correlated with polarization direction changes.  $\delta z$  can be estimated as follows:

$$\frac{\delta\theta}{\Delta\theta} = \frac{\delta(\int \vec{B} \cdot d\vec{l})}{\int \vec{B} \cdot d\vec{l}}, \quad (6.59)$$

where  $\Delta\theta$  and  $\delta\theta$  are the proton bending angle and the error in the bending angle, respectively. To keep  $\delta A \leq 10^{-4}$ ,  $\delta\theta$  should be  $\leq 1.3 \times 10^{-3}$  degrees. At  $\theta = 53^\circ$ ,  $\Delta\theta \simeq 1.5^\circ$  and for a longitudinal displacement,  $\delta(\int \vec{B} \cdot d\vec{l}) = B_o \cdot \delta z \cos\theta$ . Substituting into the above equation,  $\delta z$  should be kept within 0.26 mm. Again, there is no reason why a longitudinal displacement could occur when the FST polarization direction was reversed.

(c) Random changes in the FST position:

For a random  $\delta x$ :

$$\begin{aligned} s_L^+ &= s_R^+ = s^+, & s_L^- &= s_R^- = s^-, \\ a_L^+ &= a_R^+ = a^+, & a_L^- &= a_R^- = a^-, \\ P^+ &= P^- = P, \end{aligned} \tag{6.60}$$

and

$$\delta A_{measured} = \frac{a^+ + a^-}{2} = \frac{1}{\sqrt{2}} \sigma_A, \tag{6.61}$$

$$\begin{aligned} \sigma_A &\simeq \frac{\partial a}{\partial x} \sigma_x, & (6.62) \\ \frac{\partial a}{\partial x} &\simeq \frac{\partial A}{\partial \theta_o} \frac{\partial \theta_o}{\partial x} \simeq -0.027 \times 6 \times 10^{-3} \text{ mm}^{-1} \\ &= -1.6 \times 10^{-4} \text{ mm}^{-1}. \end{aligned}$$

For  $\delta A = 10^{-4}$ ,  $\sigma_x \leq 0.9$  mm. Note that the sign of  $\partial a/\partial x$  can be reversed by reversing the holding field, and therefore these errors were cancelled when data with different holding field directions were combined.

For a random vertical displacement, to keep  $\delta A \leq 10^{-4}$ ,  $\delta y$  should be kept within 1 mm. Similarly, random longitudinal displacements should be kept to less than 0.37 mm.

### (3) Relative Orientation of Holding Field and Target Symmetry Axes

The following errors cancel if the neutron beam and the holding field were symmetric about the target median plane. If the holding field was relatively uniform in the vertical direction at the position of the target, the main effects of a tilt of the holding field axis with respect to the target vertical axis would have been to displace the axis of the field from the source of protons and to modify the

$\int \vec{B} \cdot d\vec{l}$  along the proton path. The effect was zero to first order at the center of the target. The vertical component of the holding field changes with the tilt of the field. It is the same effect as a change in the holding field strength. The following estimates are for a point 20 mm above the median plane of the target. For a tilt angle of  $1.0^\circ$ , the change in the vertical holding field strength is  $B_o(1 - \cos 1.0^\circ) = 0.033$  mT, which is not significant.

(a) Fixed errors in the holding field direction:

For a fixed tilt of  $\delta\phi$ , i.e., to the right, the  $\int \vec{B} \cdot d\vec{l}$  for protons emitted to the left would decrease by  $\sim B_o \cdot 20 \tan \delta\phi \cdot \sin\theta$  at a point 20 mm above the median plane of the target and would increase by the same amount for protons emitted to the right (approximately a path length change of  $(20 \tan \delta\phi \cdot \sin\theta)$  in the field of  $B_o$ ). The effect would be the same as for a fixed displacement  $\delta x$  of the holding field with respect to the target, where  $\delta x = 20 \tan \delta\phi$ . For  $\delta A = 10^{-4}$ ,  $\delta x$  should be  $\leq 1$  mm, giving  $\delta\phi \leq 2.8^\circ$ . For a fixed  $\delta\phi$  to the downstream (or upstream), the effect was as for a fixed  $\delta l$  of the holding field, where  $\delta l = 20 \tan \delta\phi$ . As has been shown earlier for a fixed displacement, a fixed tilt is not critical.

(b) Spin-correlated changes in the holding field direction:

A  $\delta\phi$  to the right (or left) correlated with polarization direction has the same effect as a correlated displacement  $\delta x$  of the holding field, where  $\delta x \simeq 20 \tan \delta\phi$ . Following the same evaluation of  $\delta x$ , for  $\delta A \leq 10^{-4}$ ,  $\delta\phi \leq 2.8^\circ$ . If a displacement  $\delta\phi$  to the downstream direction was correlated with spin, the effect is the same as for a  $\delta l$ , where  $\delta l = 20 \tan \delta\phi$ . For  $\delta A = 10^{-4}$ ,  $\delta l \leq 0.26$  mm and  $\delta\phi \leq 0.74^\circ$ .

(c) Random changes in the holding field direction:

A random  $\delta\phi$  to the right corresponds to a random  $\delta x = 20\tan\delta\phi$ ,  $\delta x \leq 1.0$  mm (corresponding to  $\delta A \leq 10^{-4}$ ), giving  $\delta\phi \leq 3.1^\circ$ . A random  $\delta\phi$  downstream corresponds to a random  $\delta l = 20\tan\delta\phi$ ,  $\delta l \leq 0.37$  mm, giving  $\delta\phi \leq 1.0^\circ$ .

The angle  $\delta\phi$  was kept to within  $0.5^\circ$  during the experiment, implying  $\delta(\Delta A) \leq 5 \times 10^{-5}$ .

## 6.2.4 Beam or Target Polarization

### (1) Inequality of Up and Down Polarizations

If the beam or target polarization differed in magnitude between up and down states as  $P^\pm = P \pm \alpha$ , then from equation (6.24),  $\delta A_{n,p} = A^3\alpha^2 + 2P^2A^5\alpha^2$ . At  $A = 0$ ,  $\delta A_{n,p} = 0$  and therefore  $\delta(\Delta A) = 0$ . At the limits of the detection apparatus, the analyzing powers approach a value of  $A=0.2$ . Taking the difference in up and down beam or target polarization states as large as 0.1 (that is,  $\alpha = 0.05$ ),  $\delta(\Delta A) = \delta A_{n,p} = 2 \times 10^{-5}$ , which is negligible.

### (2) Incorrect Spin Precession of the Polarized Beam

Any residual proton polarization perpendicular to the horizontal plane remaining after the proton spin precession (by JANIS) could only result in a contribution to the neutron polarization also perpendicular to the horizontal plane. Such a neutron polarization component, which was rotated into the beam axis by the dipole magnet BONNIE, could not in itself result in a false asymmetry. However, an error in the proton spin precession leaving a residual vertical component coupled with an error in the neutron spin precession could cause an error in the measured asymmetry. Assuming an error in both the proton and neutron spin precession of  $\psi_p = 5^\circ$  and  $\psi_n = 5^\circ$ , there would exist an additional vertical

component to the neutron polarization at the FST which would change sign with proton beam polarization ( $P_p$ ) direction reversals as:

$$\Delta P_n^\pm = \frac{(P \pm D_t P_p \sin \psi_p)}{(1 \pm A P_p \sin \psi_p)} \sin \psi_n. \quad (6.63)$$

The Wolfenstein polarization transfer parameter  $D_t$  equals  $+0.231$ , and the polarization, equal to the analyzing power, is given by  $P \equiv A \sim -0.07$ . The resultant extra component to the neutron vertical polarization is exceedingly small ( $< 1\%$ ). It has been shown earlier that a difference in the up and down polarizations contributes nothing (at  $A = 0$ ) or very little ( $2 \times 10^{-5}$ , away from the zero-crossing angle) to a false asymmetry if  $|P^+ - P^-| < 0.1$ .

### (3) Residual Neutron Polarization at the Polarized FST

Spurious neutron polarization of the “unpolarized” neutron beam could correlate with the FST polarization. The major neutron polarization component at the FST location for an “unpolarized” beam was:

$$|P_{n,z}| \simeq 0.07, \quad (6.64)$$

as discussed in Chapter 3. There could be a small component of  $P_{n,y}$  due to an error in the spin precession (the BONNIE setting):

$$P_{n,y} \simeq P_{n,z} \sin \psi_n, \quad (6.65)$$

where  $\psi_n = 5^\circ$  is the assumed error in the spin precession.  $P_{n,z}$  was rotated in the horizontal plane by the FST holding field, and a component  $P_{n,x}$  arose:

$$P_{n,x} \simeq P_{n,z} \sin \psi_{hf}, \quad (6.66)$$

where  $\psi_{hf}$  is the rotation angle of the neutron polarization in the horizontal plane due to the FST holding field. Spin correlation parameters (Fig. 6.1),  $C_{yy}$ ,  $C_{zx}$ ,  $C_{xz}$

and  $C_{xx}$ , as well as  $A_n$  could contribute to a false asymmetry. The unwanted neutron polarization component  $P_{n,z}$  changes sign when the BONNIE field is reversed as does  $P_{n,x}$ . The following estimates of the systematic errors represent the upper limits. These errors were partially cancelled when the BONNIE field was reversed.

(1) Consider the parameters  $A_n$  and  $C_{yy}$ . The polarized target state ( $A_p$  measurement) left and right count rates would ( after dropping common factors ) be proportional to:

$$\begin{aligned}
 L^+ &\propto (1 + P_{n,y}A_n + P_{p,y}A_p + P_{n,y}P_{p,y}C_{yy}) , \\
 R^+ &\propto (1 - P_{n,y}A_n - P_{p,y}A_p + P_{n,y}P_{p,y}C_{yy}) , \\
 L^- &\propto (1 + P_{n,y}A_n - P_{p,y}A_p - P_{n,y}P_{p,y}C_{yy}) , \\
 R^- &\propto (1 - P_{n,y}A_n + P_{p,y}A_p - P_{n,y}P_{p,y}C_{yy}) .
 \end{aligned} \tag{6.67}$$

The spin correlation parameter  $C_{yy}$  does not change sign on the left and right sides of the beam axis (i.e., it does not in itself cause a left-right asymmetry).

(a) Fixed neutron beam polarization ( $P_{n,y}$ ) at the polarized FST:

The effects of a fixed  $P_{n,y}$  can be seen by defining errors in the analyzing power:

$$\begin{aligned}
 a_L^+ &= P_{n,y} \left( \frac{A_n}{P_{p,y}} + C_{yy} \right) , \\
 a_R^+ &= P_{n,y} \left( \frac{A_n}{P_{p,y}} - C_{yy} \right) , \\
 a_L^- &= P_{n,y} \left( -\frac{A_n}{P_{p,y}} + C_{yy} \right) , \\
 a_R^- &= P_{n,y} \left( -\frac{A_n}{P_{p,y}} - C_{yy} \right) .
 \end{aligned} \tag{6.68}$$

Adopting the usual notation of (6.21),

$$\delta A = 0 + O(a^2) . \tag{6.69}$$

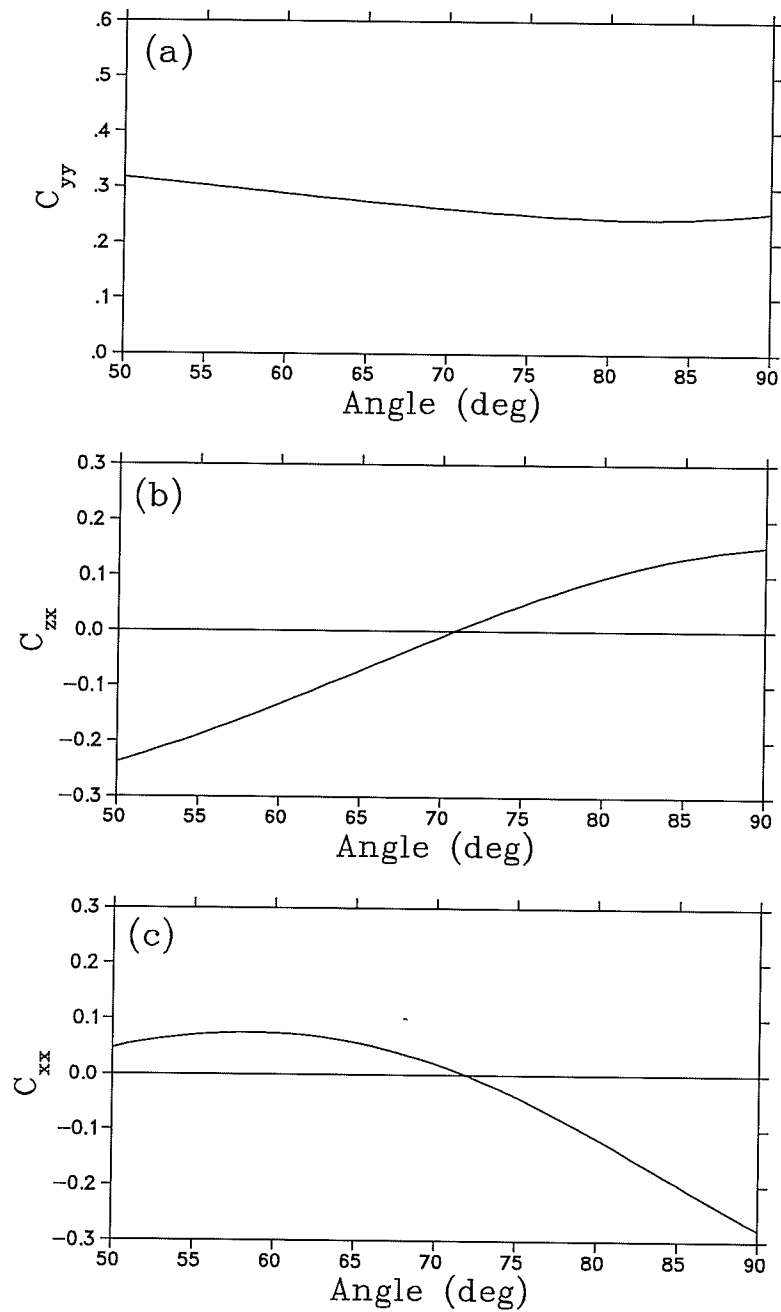


Figure 6.1: *Angular distributions (c.m.) of spin correlation parameters for  $np$  elastic scattering at 347 MeV (a)  $C_{yy}$ , (b)  $C_{zx}$ , and (c)  $C_{xx}$  obtained from phase shift analyses [69].*

This effect cancels out at least to second order and therefore contributes neither to  $\delta A$  nor to  $\delta(\Delta A)$  both at  $A = 0$  and away from  $A = 0$  at the level  $\ll 10^{-5}$ .

(b) Spin-correlated neutron beam polarization ( $P_{n,y}$ ) at the polarized FST:

If one made the assumption that  $P_{n,y}$  changed sign with spin flip at the polarized FST,

$$\begin{aligned} a_L^{\dagger} &= P_{n,y} \left( \frac{A_n}{P_{p,y}} + C_{yy} \right), \\ a_R^{\dagger} &= P_{n,y} \left( \frac{A_n}{P_{p,y}} - C_{yy} \right), \\ a_L^{\bar{}} &= -P_{n,y} \left( -\frac{A_n}{P_{p,y}} + C_{yy} \right), \\ a_R^{\bar{}} &= -P_{n,y} \left( -\frac{A_n}{P_{p,y}} - C_{yy} \right), \end{aligned} \quad (6.70)$$

$$\text{and hence } \delta A \simeq \frac{P_{n,y}}{P_{p,y}} \cdot A_n - P_{n,y} P_{p,y} A_p C_{yy}. \quad (6.71)$$

The spin correlation parameter  $C_{yy}$  is equal to 0.255 ( $E_n = 347$  MeV,  $34.2^\circ$  lab). Assuming  $A_n = 10^{-3}$  at  $A_p = 0$ , one finds  $\delta A_p \ll 10^{-4}$ . Since there was no similar effect on the  $A_n$  measurement, this results in the systematic error  $\delta(\Delta A) \ll 10^{-4}$ . At  $A = 0.2$ ,  $\delta A = 1.0 \times 10^{-3}$ . However, for any BONNIE field setting,  $P_{n,y}$  does not change sign with FST polarization direction change. Therefore, this correlation is unlikely to have occurred in the data.

(c) Random changes in the neutron beam polarization ( $P_{n,y}$ ) at the polarized FST:

If  $P_{n,y}$  varied randomly,

$$\begin{aligned} a_L^{\dagger} &= P_{n,y}^+ \left( \frac{A_n}{P_{p,y}} + C_{yy} \right), \\ a_R^{\dagger} &= P_{n,y}^+ \left( \frac{A_n}{P_{p,y}} - C_{yy} \right), \\ a_L^{\bar{}} &= P_{n,y}^+ \left( -\frac{A_n}{P_{p,y}} + C_{yy} \right), \end{aligned}$$

$$a_{\bar{R}} = P_{n,y}^+ \left( -\frac{A_n}{P_{p,y}} - C_{yy} \right), \quad (6.72)$$

$$\delta A \simeq \frac{P_{n,y}^+ - P_{n,y}^-}{2} \cdot \left( \frac{A_n}{P_{p,y}} - P_{p,y} A_p C_{yy} \right), \quad (6.73)$$

$$\sigma_A \simeq \frac{1}{\sqrt{2}} \cdot \left( \frac{A_n}{P_{p,y}} - P_{p,y} A_p C_{yy} \right) \sigma_{P_n}, \quad (6.74)$$

where  $\sigma_i$  are the standard deviations of the random variations of the variables "i". To keep  $\sigma_{A_p} = 10^{-4}$ , standard deviation of the neutron beam polarization  $\sigma_{P_n}$  should be less than 0.11 if  $A_n = 10^{-3}$  at the angle where  $A_p = 0$ , or given  $\sigma_{P_n} \leq 0.0052$ ,  $\delta A_p$  and  $\delta(\Delta A) \ll 10^{-4}$ . Away from the zero crossing angle, e.g., at  $A = 0.2$ ,  $\sigma_{A_p} = 0.14\sigma_{P_n}$ , the standard deviation of the analyzing power  $\sigma_{A_p} = 1.4 \times 10^{-4}$  for  $\sigma_{P_n} = 10^{-3}$ .

(2) The residual longitudinal neutron beam polarization could have been correlated with a lateral FST polarization component by the parameter  $C_{zx}$  when FST was polarized. The lateral FST polarization could have been due to the non-vertical holding field (i.e., tilt towards the left by  $1.0^\circ$ ). The counts to the left and right detectors with the FST polarized up or down can be expressed as:

$$\begin{aligned} L^+ &\propto (1 + P_{p,y} A_p + P_{n,z} P_{p,x} C_{zx}), \\ R^+ &\propto (1 - P_{p,y} A_p - P_{n,z} P_{p,x} C_{zx}), \\ L^- &\propto (1 - P_{p,y} A_p - P_{n,z} P_{p,x} C_{zx}), \\ R^- &\propto (1 + P_{p,y} A_p + P_{n,z} P_{p,x} C_{zx}). \end{aligned} \quad (6.75)$$

(a) Fixed errors in  $P_{p,x}$  and  $P_{n,z}$ :

For a fixed  $P_{p,x}$  and  $P_{n,z}$ , the effects could be expressed again in the errors of the analyzing power:

$$a_L^+ = a_L^- = a_R^+ = a_R^- = \frac{1}{P_{p,y}} P_{n,z} P_{p,x} C_{zx}. \quad (6.76)$$

Using equation (6.21),

$$\delta A = \frac{1}{P_{p,y}} P_{n,z} P_{p,x} C_{zx} = P_{n,z} C_{zx} \tan \phi , \quad (6.77)$$

where  $\phi$  is the tilt angle of the holding field setting and assumed to be  $\leq 1.0^\circ$ . With  $C_{zx} = 0.025$  at 347 MeV and  $73^\circ$  c.m.,  $\delta A \simeq 2.6 \times 10^{-5}$ . Away from  $A = 0$ , at  $A = 0.2$  or  $\theta_{cm} = 55^\circ$ ,  $C_{zx} \simeq -0.12$ ,  $\delta A \simeq 1.5 \times 10^{-4}$ . These errors were partially cancelled when the BONNIE field direction was reversed.

(b) Spin-correlated errors in  $P_{p,x}$  and  $P_{n,z}$ :

If  $\phi$  or  $P_{n,z}$  were spin dependent,

$$\begin{aligned} a_L^+ &= -a_R^+ = a^+ = P_{n,z} C_{zx} \tan \phi , \\ a_L^- &= -a_R^- = a^- = -P_{n,z} C_{zx} \tan \phi . \end{aligned} \quad (6.78)$$

Substituting into equation (6.21),

$$\begin{aligned} \delta A = P A \cdot P_{n,z} \tan \phi C_{zx} &= 0 && \text{at } A = 0 \\ &\leq 2 \times 10^{-5} && A = 0.2 . \end{aligned} \quad (6.79)$$

(c) Random changes in  $P_{p,x}$  and  $P_{n,z}$ :

For random  $\phi$  and  $P_{n,z}$ , at  $A = 0$ ,  $\delta A \ll 10^{-5}$ . Away from  $A = 0$ ,  $\delta A \leq 10^{-4}$ . However, both at  $A = 0$  and away from  $A = 0$ , these errors would be partially cancelled when the BONNIE field direction was reversed.

(3) Other spin correlation parameters,  $C_{xz}$  and  $C_{xx}$ , could have contributed to the systematic errors in  $\delta(\Delta A)$ . In considering the effects of  $C_{xz}$ , a comparison to the  $C_{zx}$  contribution can be made since  $C_{xz} = C_{zx}$  (charge symmetry!). Here,  $P_{n,x} \leq 0.07 P_{n,z}$  (the holding field rotates the residual neutron polarization  $P_{n,z}$  by  $4^\circ$  and  $\sin 4^\circ = 0.07$ ) and  $P_{p,x} = P_{p,y} \sin \phi$ ,  $P_{n,x} P_{p,z} \leq P_{n,z} P_{p,x}$ , for an assumed

1.0° tilt of the holding field (either towards the x or z axes),  $C_{xz}$  contributes at least a factor of 14 less than the contribution of  $C_{zx}$ .  $C_{xx}$  has similar shape and magnitude to  $C_{zx}$  (see Fig. 6.1) and couples to  $P_{n,x}$  and  $P_{p,x}$ . Following the same argument as used for  $C_{xz}$ ,  $C_{xx}$  contributes at least a factor of 2 less than  $C_{zx}$  does.

Thus, with the use of the two dipole magnets to precess the neutron spin to the vertical direction, and the reversal of the BONNIE field direction, the spin correlation parameters as well as the analyzing power  $A_n$  did not cause non-negligible errors to  $\Delta A$ ; at  $A = 0$ ,  $\delta(\Delta A) \leq 10^{-5}$  and away from the zero-crossing angle,  $\delta(\Delta A) \leq 10^{-4}$ .

### 6.2.5 Misalignment of Apparatus

Since the experiment used a mirror symmetric detection system, a small misalignment of the detectors would cause errors in  $A_n$  and  $A_p$ , but the effect on  $\Delta A$  would be cancelled to first order if the misalignment was the same for the two measurements. If the apparatus was misaligned with respect to a nominal angle  $\theta$  by:

$$\begin{aligned}\theta_L &= \theta + \psi_L, \\ \theta_R &= \theta + \psi_R,\end{aligned}\tag{6.80}$$

where  $\psi_{L,R}$  are the errors in the left and right angles, respectively. Then the errors due to the misalignment would have been:

$$\begin{aligned}s_L^\pm &= \frac{1}{\sigma}(\psi_L\sigma' + \psi_L^2\sigma''/2), \\ s_R^\pm &= \frac{1}{\sigma}(\psi_R\sigma' + \psi_R^2\sigma''/2), \\ a_L^\pm &= \psi_L A' + \psi_L^2 A''/2,\end{aligned}$$

$$\begin{aligned}
a_R^\pm &= \psi_R A' + \psi_R^2 A''/2, \\
P^+ &= P^- = P.
\end{aligned}
\tag{6.81}$$

Substituting into equations (6.16), (6.18), (6.21) and (6.24), the non-vanishing terms are:

$$\delta A = \frac{1}{2}[(\psi_L + \psi_R) \cdot A' + (\psi_L^2 + \psi_R^2) \cdot \frac{A''}{2}].
\tag{6.82}$$

Assuming the errors were random,

$$\delta A = \frac{\psi}{\sqrt{2}} \cdot A' + \psi^2 \cdot \frac{A''}{2}.
\tag{6.83}$$

To keep  $\delta A \simeq 10^{-4}$  (the analyzing power),  $\psi$  should be kept within  $0.01^\circ$ . The error in  $\delta(\Delta A)$  is cancelled at least to second order. If second order terms were considered, then with  $|A''| < 3 \times 10^{-3} \text{ deg}^{-2}$  and  $\delta(\Delta A) \ll 10^{-4}$ , throughout the angular range for a misalignment of  $0.1^\circ$ . The proton and neutron detection systems were located to an accuracy of better than  $\pm 0.03^\circ$  and  $\pm 0.05^\circ$  (absolute angle scale), respectively, during the experiment, hence,  $\delta(\Delta A) \ll 10^{-4}$  due to this effect.

## 6.2.6 Multiple Scattering

Multiple scattering smeared the angles of the recoil protons emerging from the target. Assuming that the multiple scattering had a Gaussian distribution, the effective differential cross-section given by:

$$\bar{\sigma}(\theta) = \frac{1}{\delta_0 \sqrt{\pi}} \int \sigma(\theta + \delta) e^{-\delta^2/\delta_0^2} d\delta.
\tag{6.84}$$

The parameter  $\delta_0$  was related to the magnitude of multiple scattering by  $\delta_0 = \sqrt{2} \sigma_{rms}$ .  $\sigma(\theta)$  and  $A(\theta)$  could be expanded as a function of  $\theta$  as,

$$\sigma(\theta + \delta) = \sigma(\theta) + \sigma'(\theta) \cdot \delta + \frac{1}{2} \sigma''(\theta) \cdot \delta^2 + \dots.
\tag{6.85}$$

Substituting into Eq. (6.84) and integrating, the effective differential cross-section is given by:

$$\bar{\sigma}(\theta) = \sigma(\theta) + \sigma''(\theta) \frac{\delta_o^2}{4} + \dots O(\delta_o^4). \quad (6.86)$$

The unsmeared differential cross-section for polarized beam is  $\sigma_{L,R} = \sigma(1 \pm PA)$ , the plus sign being for scattering to the left, and the minus for scattering to the right, hence:

$$\frac{d^2\sigma_{L,R}}{d\theta^2} = \sigma''(1 \pm PA) \pm 2P\sigma'A' \pm P\sigma A'', \quad (6.87)$$

$$\bar{\sigma}_{L,R} = \sigma(1 \pm PA) + [\sigma''(1 \pm PA) \pm 2P\sigma'A' \pm P\sigma A''] \frac{\delta_o^2}{4} + \dots O(\delta_o^4). \quad (6.88)$$

For spin up and down states the count rates are:

$$\begin{aligned} L^+ &\propto \sigma(1 + PA) + [\sigma''(1 + PA) + 2P\sigma'A' + P\sigma A''] \frac{\delta_o^2}{4} + \dots O(\delta_o^4), \\ R^+ &\propto \sigma(1 - PA) + [\sigma''(1 - PA) - 2P\sigma'A' - P\sigma A''] \frac{\delta_o^2}{4} + \dots O(\delta_o^4), \\ L^- &\propto \sigma(1 - PA) + [\sigma''(1 - PA) - 2P\sigma'A' - P\sigma A''] \frac{\delta_o^2}{4} + \dots O(\delta_o^4), \\ R^- &\propto \sigma(1 + PA) + [\sigma''(1 + PA) + 2P\sigma'A' + P\sigma A''] \frac{\delta_o^2}{4} + \dots O(\delta_o^4). \end{aligned} \quad (6.89)$$

Absorbing the multiple scattering terms in the analyzing power errors,

$$\begin{aligned} a_L^+ &= \left[ \frac{\sigma''}{\sigma} \frac{(1 + PA)}{P} + \frac{2\sigma'A'}{\sigma} + A'' \right] \frac{\delta_o^2}{4}, \\ a_R^+ &= \left[ -\frac{\sigma''}{\sigma} \frac{(1 - PA)}{P} + \frac{2\sigma'A'}{\sigma} + A'' \right] \frac{\delta_o^2}{4}, \\ a_L^- &= \left[ -\frac{\sigma''}{\sigma} \frac{(1 - PA)}{P} + \frac{2\sigma'A'}{\sigma} + A'' \right] \frac{\delta_o^2}{4}, \\ a_R^- &= \left[ \frac{\sigma''}{\sigma} \frac{(1 + PA)}{P} + \frac{2\sigma'A'}{\sigma} + A'' \right] \frac{\delta_o^2}{4}. \end{aligned} \quad (6.90)$$

Inserting the above results into the expression (6.21), one obtains

$$\delta A_{measured} \simeq \left[ \frac{\sigma''}{\sigma} A + \frac{2\sigma'A'}{\sigma} + A'' \right] \frac{\delta_o^2}{4}. \quad (6.91)$$

Near the zero-crossing angle,  $A' = -0.027 \text{ deg}^{-1}$ ,  $|A''| < 7.6 \times 10^{-4} \text{ deg}^{-2}$ ,  $\sigma = 6.1 \text{ mb/sr (lab)}$ , and  $\sigma' = -0.36 \text{ mb/sr} \cdot \text{deg (lab)}$ . Assuming  $\delta_0 = 1.0 \text{ deg} (= \sqrt{2}\sigma_{rms})$  and substituting these parameters into (6.91), one obtains  $\delta A = 7 \times 10^{-4}$  when  $A=0$ . Since  $\delta A_n = \delta A_p$ ,  $\delta(\Delta A) = 0$ , and the above estimate should be regarded as an upper limit.

### 6.2.7 Neutron Detection Efficiency Stability

The neutron detection efficiency depended on the hardware and software thresholds and the photomultiplier gains. A higher threshold on the neutron detectors effectively discriminated against a percentage of otherwise detectable  $np$  pairs.

(a) Fixed errors in the neutron detection efficiency:

If the efficiency of a left and right neutron bar increased or decreased by a fixed specific percentage  $\delta\epsilon$ , it had no effect on  $\delta A$  (6.18).

(b) Spin-correlated efficiency changes:

If the error in efficiency is assumed to be correlated with polarization direction,

$$\delta\epsilon_L^+ - \delta\epsilon_R^+ = \delta\epsilon_R^- - \delta\epsilon_L^- = 2\delta\epsilon, \quad (6.92)$$

then using (6.18),

$$\delta A_{measured} \simeq \frac{\delta\epsilon}{P}. \quad (6.93)$$

This could only have happened for the polarized target runs, since the polarization direction reversal of the target was far less often than the polarization direction reversal of the beam. For  $P = 0.8$  and keeping  $\delta A \leq 10^{-4}$ , the efficiency change,  $\epsilon$ , should be kept under  $8 \times 10^{-5}$ .

(c) Random changes in the efficiency:

If the efficiency changed randomly as the experiment progressed:

$$\sigma_A \simeq \frac{\sigma_\epsilon}{\sqrt{2}\sqrt{NP}}, \quad (6.94)$$

where  $N = 8$  is the number of discriminators on each main neutron detector array. For  $P = 0.8$  and keeping  $\delta A \leq 10^{-4}$ , the efficiency change,  $\epsilon$ , should be kept under  $3.2 \times 10^{-4}$ .

The neutron detection efficiency could change due to the photomultiplier gain shifts. Estimates of  $\delta\epsilon$  could be made based on results from the experiment. The experiment had neutron software cuts at roughly 1.1 MeV electron equivalent (MeVee). At this energy, the neutron bar efficiency changes with respect to the energy threshold by  $-0.017/\text{MeV}$ . The absolute efficiency of the neutron bars for the experiment was about 30%. To keep  $\delta A < 10^{-4}$ , changes in efficiency should be kept within  $\pm 3.2 \times 10^{-4}$ . Therefore the software cuts at 1.1 MeVee must not change by more than 0.019 MeVee, or 1.7%. Since changes in software threshold were directly proportional to photomultiplier gains, an equivalent condition to the stability of thresholds to  $\pm 1.7\%$  was that photomultiplier gains should also be kept to within  $\pm 1.7\%$ . This was achieved by matching the gain by software with the button event ADC signals. The gain was matched to better than 1 ADC channel out of 350, 500 and 500 ADC channels for the front, rear and vertical bars, respectively. This is much better than 1.7% as required. These particular ADC values were chosen to keep the ratio of the ADC values to be the same as the ratio of the energies deposited in the respective bars by charged particles.

## 6.2.8 Background

### (1) Polarized Neutron Beam

Let  $f$  be the fraction of target nuclei which could cause quasifree scattering of differential cross-section  $\sigma_b$ . If the analyzing power for the background was  $a_b$ , the total count rates for a polarized neutron beam run were:

$$\begin{aligned}
 L^+ &\propto \sigma(1 + PA) + f\sigma_b(1 + Pa_b) , \\
 R^+ &\propto \sigma(1 - PA) + f\sigma_b(1 - Pa_b) , \\
 L^- &\propto \sigma(1 - PA) + f\sigma_b(1 - Pa_b) , \\
 R^- &\propto \sigma(1 + PA) + f\sigma_b(1 + Pa_b) .
 \end{aligned} \tag{6.95}$$

Adopting the notation (6.19), the effect of the background can be simulated by errors in the  $np$  analyzing power:

$$\begin{aligned}
 a_L^+ &= \frac{f\sigma_b}{P\sigma}(1 + Pa_b) , \\
 a_R^+ &= -\frac{f\sigma_b}{P\sigma}(1 - Pa_b) , \\
 a_L^- &= -\frac{f\sigma_b}{P\sigma}(1 - Pa_b) , \\
 a_R^- &= \frac{f\sigma_b}{P\sigma}(1 + Pa_b) .
 \end{aligned} \tag{6.96}$$

Then, substituting the above to equation (6.21):

$$\delta A_n \simeq \frac{f\sigma_b}{\sigma} \cdot a_b . \tag{6.97}$$

(a) Fixed ratio of the background contribution:

For a constant background, to keep the effects on  $\delta A$  due to the background to be within  $\pm 10^{-4}$ , the ratio of background counts to real  $np$  elastic counts multiplied by the background asymmetry must be kept within  $\pm 10^{-4}$ . An upper limit on the uncertainty in the ratio of background to real  $np$  elastic events would be  $\approx 1\%$ . If

the  $^{12}\text{C}(n, np)^{11}\text{B}$  background analyzing power is estimated to be within  $\pm 0.010$ , inserting these values into equation (6.97) results in  $\delta A_n \simeq 10^{-4}$ .

(b) Spin-correlated changes in the ratio of the background contribution:

If the intensity  $f$  of the background were spin dependent:

$$\delta A_{measured} \simeq a_b \frac{\sigma_b}{\sigma} \cdot \frac{(f^+ + f^-)}{2} . \quad (6.98)$$

(c) Random changes in the ratio of the background contribution:

If the intensity  $f$  of the background varied randomly:

$$\delta A_{measured} \simeq a_b \frac{\sigma_b}{\sigma} \cdot \frac{\sigma_f}{\sqrt{2}} . \quad (6.99)$$

There are no reasons why situations (b) and (c) should have occurred. However, a similar effect could arise when the background was corrected for the data.

For uncertainties of both the ratio and the analyzing power of the background contribution less than  $\pm 0.01$ , the error contribution due to the background would be below the  $10^{-4}$  level.

## (2) Polarized Proton Target

A background merely served to lessen the asymmetry since the contents of the target other than  $^1\text{H}$  could not have been polarized. However, the effect of the background in the polarized target runs was to dilute the asymmetry. The count rates were:

$$\begin{aligned} L^+ &\propto \sigma(1 + PA) + f\sigma_b , \\ R^+ &\propto \sigma(1 - PA) + f\sigma_b , \\ L^- &\propto \sigma(1 - PA) + f\sigma_b , \\ R^- &\propto \sigma(1 + PA) + f\sigma_b . \end{aligned} \quad (6.100)$$

Using the notation of equation (6.19),

$$a_L^\dagger = -a_R^\dagger = -a_L^- = a_R^- = \frac{f}{P} \cdot \frac{\sigma_b}{\sigma} . \quad (6.101)$$

(a) Fixed ratio of the background contribution:

For fixed background,

$$\delta A_{measured} \simeq A \cdot \frac{\sigma_b}{\sigma} f = A \cdot r , \quad (6.102)$$

where  $r$  is the ratio of the background contribution to the foreground in the yields.  $\delta A_{measured} = 0$  at  $A = 0$ , and away from  $A = 0$ ,  $A_H = A_{CH}/(1-r)$  and  $\delta A \simeq A \cdot \delta r$  (where  $\delta r$  is the uncertainty of  $r$  in the correction for the background).

(b) Spin-correlated changes in the ratio of the background contribution:

If  $f$  depended on spin,  $\delta A_{measured} \simeq 0$  at  $A = 0$ .

(c) Random changes in the ratio of the background contribution:

For a random  $f$ ,  $\sigma_A = 0$  at  $A = 0$ .

The background did not cause an error in  $A_p$  at the zero-crossing angle and caused an error proportional to  $A$  away from the zero-crossing angle.

A summary of these estimates of the systematic errors as discussed above is listed in table 6.1.

Table 6.1: Summary of the estimates of the systematic errors in the difference of the analyzing powers from the system parameters.

Sources of Systematic errors	Assumed Parameters	Contribution to $\delta(\Delta A)$	Experimental Parameters	$\delta(\Delta A)$
Proton beam energy shift	$\delta E = 0.1$ MeV	$7 \times 10^{-5}$	0.038 MeV	$3 \times 10^{-5}$
Proton beam spot shift at $LD_2$ target	$ x^+ - x^-  = 0.5$ mm	$2 \times 10^{-4}$	0.03 mm	$1 \times 10^{-5}$
Proton beam angle modulation	$ \theta^+ - \theta^-  = 0.1^\circ$	$1.6 \times 10^{-4}$	$0.005^\circ$	$1 \times 10^{-5}$
$LD_2$ density stability	$\delta\rho = 0.01$ g/cm $^{-3}$	$1.1 \times 10^{-4}$	$0.0005$ g/cm $^{-3}$	$< 10^{-5}$
Irreproducibility of holding field (HF)	$\sigma_{hf} = 0.25$ mT	$6 \times 10^{-5}$	$< 0.3$ mT	$< 7 \times 10^{-5}$
$\Delta r$ of FST wrt HF	$\Delta r = 1$ mm	$5 \times 10^{-5}$	0.5 mm	$3 \times 10^{-5}$
Inequality of up/down polarization	$ P^+ - P^-  = 0.1$	0 at A=0 $2 \times 10^{-5}$ at A=0.2	$< 0.05$	0 $\leq 10^{-5}$
$P_{pbeam}$ precession	$\delta\psi_p = 5^\circ$	$\ll 10^{-4}$	$\sim 3^\circ$	$\ll 10^{-4}$
$P_{nbeam}$ precession	$\delta\psi_n = 5^\circ$	$\ll 10^{-4}$	$\sim 3^\circ$	$\ll 10^{-4}$
HF tilt	$\phi = 1^\circ$	$\leq 1 \times 10^{-4}$	$< 0.5^\circ$	$< 5 \times 10^{-5}$
Residual $P_n$ on polarized FST	$ P_n  \simeq 0.07$ $\psi = 5^\circ, \phi = 1^\circ$	$\leq 10^{-5}$ at A = 0 $\leq 10^{-4}$ at A = 0.2	$\psi \sim 3^\circ,$ $\phi = 0.5^\circ$	$< 10^{-5}$ $< 10^{-4}$
Misalignment of detectors	$ \theta_L - \theta_R  = 0.1^\circ$	$\ll 10^{-4}$	$0.03^\circ$	$\ll 10^{-4}$
Multiple scattering in FST	$\theta_{rms} = 0.7^\circ$	$\delta(\Delta A) \ll 10^{-5}$	$< 0.7^\circ$	$\ll 10^{-5}$
Neutron detector instability	1% gain shift	$6 \times 10^{-5}$	$\leq 0.3\%$	$\leq 2 \times 10^{-5}$
Background	1%, $ A_b  = 0.01$	$1 \times 10^{-4}$	1%, $(-4 \pm 7) \times 10^{-3}$	$2.8 \times 10^{-4}$

## 6.3 Tests of Systematic Errors in The Data Analysis

Various tests were applied to the data to test for systematic errors. These tests included different  $\chi^2$  cuts, different neutron bar software thresholds, and fitting the asymmetry curves for different angular ranges. The following sections give a summary of the results of these tests as well as other contributions to systematic errors including the background and effective neutron beam energy difference corrections. The mean and the error of the results with different cuts were calculated as:

$$\overline{\Delta\theta_o} = \frac{\Sigma\theta_{o,i}}{N} \quad (6.103)$$

$$\delta(\Delta\theta_o) = \frac{\sqrt{\Sigma(\Delta\theta_{o,i} - \overline{\Delta\theta_o})^2}}{\sqrt{N-1}}, \quad (6.104)$$

where N is the number of cuts applied.

### 6.3.1 Different $\chi^2$ Tests

After applying the corrections for the background and the effective average neutron beam energy difference to the data, the results of the zero-crossing angles and their differences with different  $\chi^2$  cuts are shown in table 6.2 and table 6.3.

It was noticed that the results with  $\chi^2 \leq 5$  were almost two standard deviations away from the other results and showed bias in the data. This was primarily caused by the two ends of the detection angular range. At large recoil proton angles (small neutron angles), the large multiple scattering and the holding field deflection of the low energy protons caused the standard deviations ( $\sigma$ 's) of the kinematic variable distributions increase significantly, and only partial distribu-

Table 6.2: Zero-crossing angles of  $A_n$  and  $A_p$  after the corrections.

Cuts	February 1993		August 1992	
	$\theta_{cm}(A_n = 0)$	$\theta_{cm}(A_p = 0)$	$\theta_{cm}(A_n = 0)$	$\theta_{cm}(A_p = 0)$
$ADC \geq 20$	$72.967^\circ \pm 0.056^\circ$	$72.477^\circ \pm 0.051^\circ$	$72.838^\circ \pm 0.059^\circ$	$72.399^\circ \pm 0.055^\circ$
$\chi_{sum}^2 \leq 10$	$72.967^\circ \pm 0.056^\circ$	$72.477^\circ \pm 0.051^\circ$	$72.838^\circ \pm 0.059^\circ$	$72.399^\circ \pm 0.055^\circ$
$\chi_{sum}^2 \leq 15$	$72.999^\circ \pm 0.053^\circ$	$72.626^\circ \pm 0.051^\circ$	$72.944^\circ \pm 0.056^\circ$	$72.531^\circ \pm 0.053^\circ$
$\chi_{sum}^2 \leq 20$	$73.051^\circ \pm 0.052^\circ$	$72.652^\circ \pm 0.051^\circ$	$73.017^\circ \pm 0.055^\circ$	$72.614^\circ \pm 0.054^\circ$
$\chi_i^2 \leq 5$	$72.919^\circ \pm 0.058^\circ$	$72.324^\circ \pm 0.053^\circ$	$72.851^\circ \pm 0.061^\circ$	$72.312^\circ \pm 0.056^\circ$
$\chi_i^2 \leq 7.5$	$72.961^\circ \pm 0.054^\circ$	$72.504^\circ \pm 0.051^\circ$	$72.888^\circ \pm 0.057^\circ$	$72.439^\circ \pm 0.054^\circ$
$\chi_i^2 \leq 9$	$72.967^\circ \pm 0.053^\circ$	$72.539^\circ \pm 0.051^\circ$	$72.927^\circ \pm 0.056^\circ$	$72.487^\circ \pm 0.054^\circ$

Table 6.3: Difference of the zero-crossing angles after the corrections.

Cuts	February 1993	August 1992	Total
$ADC \geq 20$	$\Delta\theta_{cm}$	$\Delta\theta_{cm}$	$\Delta\theta_{cm}$
$\chi_{sum}^2 \leq 10$	$0.490^\circ \pm 0.076^\circ$	$0.439^\circ \pm 0.081^\circ$	$0.464^\circ \pm 0.056^\circ$
$\chi_{sum}^2 \leq 15$	$0.373^\circ \pm 0.074^\circ$	$0.413^\circ \pm 0.077^\circ$	$0.393^\circ \pm 0.053^\circ$
$\chi_{sum}^2 \leq 20$	$0.399^\circ \pm 0.073^\circ$	$0.403^\circ \pm 0.077^\circ$	$0.401^\circ \pm 0.053^\circ$
$\chi_i^2 \leq 5$	$0.595^\circ \pm 0.079^\circ$	$0.539^\circ \pm 0.083^\circ$	$0.567^\circ \pm 0.057^\circ$
$\chi_i^2 \leq 7.5$	$0.457^\circ \pm 0.074^\circ$	$0.450^\circ \pm 0.078^\circ$	$0.453^\circ \pm 0.054^\circ$
$\chi_i^2 \leq 9$	$0.428^\circ \pm 0.074^\circ$	$0.440^\circ \pm 0.078^\circ$	$0.434^\circ \pm 0.054^\circ$

tions were observed due to the physical cutoff in the detector geometry. These effects caused large uncertainties in the  $\sigma$ 's determined from the data, which in turn were used to calculate the  $\chi^2$  for the events, and, therefore, errors in the  $\chi^2$  calculations were introduced. The angular range corresponding to the large neutron angles (small proton angles) was covered by the "new" neutron bars. The "new" neutron bars were set up vertically and therefore had different angular resolution compared to the main neutron arrays. Since the "new" neutron bars had only very limited angular coverage on one side (determined by the coincident proton geometrical acceptance and the holding field distortion), only part of the error distributions were observed, and therefore the experimentally determined  $\sigma$  and  $\chi^2$  had larger uncertainties. These uncertainties (at both large and small angles) caused bias of the data when tight cuts were applied. Comparing the individual  $\chi_i^2$  cuts to the  $\chi_{sum}^2$  cuts, similar statistically significant samples can be selected when matched values are chosen. However, when the individual  $\chi_i^2$  cuts are applied, they strictly require each individual variable to be within the statistical ranges. The  $\chi_{sum}^2$  cuts, on the other hand, only require the combination of the four variables to be within the the statistical range. Therefore, the  $\chi_{sum}^2$  cuts do not have the same strict conditions as the individual  $\chi_i^2$  cuts even though they can both give the same statistical significance. The  $\chi_{sum}^2$  cuts were considered to be superior to the individual  $\chi^2$  cuts given the uncertainties of the  $\sigma$ 's as discussed above. The results of  $\chi^2 \leq 5$  were excluded from the calculation of the final results and systematic errors. The systematic error as indicated by the different  $\chi^2$  cuts is:

$$\delta(\Delta\theta_o) = \pm 0.031^\circ .$$

### 6.3.2 Different Neutron Bar Software Thresholds

As discussed in the last section, neutron detection efficiency could change with different hardware and software thresholds. After hardware (online during data taking) and then software (in the data analysis) gain matching of the neutron bar ADC signals, different software thresholds were applied to the data to study the systematic errors associated with the neutron bar efficiency. The results of the zero-crossing angle differences are listed in table 6.4. The systematic error limit from the different software thresholds is:

$$\delta(\Delta\theta_o) = \pm 0.028^\circ .$$

Table 6.4: *Dependence of the difference in the zero-crossing angles on the neutron bar software threshold.*

Cuts	FEB93	AUG92	Total
$\chi_{sum}^2 \leq 10, \text{Nbar ADC} \geq 0$	$0.432^\circ \pm 0.075^\circ$	$0.413^\circ \pm 0.078^\circ$	$0.423^\circ \pm 0.054^\circ$
$\chi_{sum}^2 \leq 10, \text{Nbar ADC} \geq 15$	$0.440^\circ \pm 0.076^\circ$	$0.422^\circ \pm 0.080^\circ$	$0.431^\circ \pm 0.055^\circ$
$\chi_{sum}^2 \leq 10, \text{Nbar ADC} \geq 20$	$0.490^\circ \pm 0.076^\circ$	$0.439^\circ \pm 0.081^\circ$	$0.464^\circ \pm 0.056^\circ$
$\chi_{sum}^2 \leq 10, \text{Nbar ADC} \geq 25$	$0.516^\circ \pm 0.076^\circ$	$0.458^\circ \pm 0.081^\circ$	$0.487^\circ \pm 0.056^\circ$
$\chi_i^2 \leq 7.5, \text{Nbar ADC} \geq 15$	$0.403^\circ \pm 0.074^\circ$	$0.432^\circ \pm 0.078^\circ$	$0.418^\circ \pm 0.054^\circ$
$\chi_i^2 \leq 7.5, \text{Nbar ADC} \geq 20$	$0.457^\circ \pm 0.074^\circ$	$0.450^\circ \pm 0.078^\circ$	$0.454^\circ \pm 0.054^\circ$
$\chi_i^2 \leq 7.5, \text{Nbar ADC} \geq 25$	$0.483^\circ \pm 0.075^\circ$	$0.477^\circ \pm 0.080^\circ$	$0.480^\circ \pm 0.055^\circ$

### 6.3.3 Different Angular Range Fits

Systematic errors were also studied by fitting the data with different angular ranges. The zero-crossing angle differences from the different angular range are listed in table 6.5. The systematic error indicated from this test is:

$$\delta(\Delta\theta_o) = \pm 0.019^\circ .$$

Table 6.5: *Difference of the zero-crossing angles for different angle ranges.*

Cuts	FEB93	AUG92	Total
$\chi_{sum}^2 \leq 10, 53.4^\circ \leq \theta \leq 86.9^\circ$	$0.490^\circ \pm 0.076^\circ$	$0.439^\circ \pm 0.081^\circ$	$0.464^\circ \pm 0.056^\circ$
$\chi_{sum}^2 \leq 10, 55.3^\circ \leq \theta \leq 84.9^\circ$	$0.475^\circ \pm 0.079^\circ$	$0.443^\circ \pm 0.085^\circ$	$0.459^\circ \pm 0.058^\circ$
$\chi_{sum}^2 \leq 10, 57.3^\circ \leq \theta \leq 82.9^\circ$	$0.403^\circ \pm 0.083^\circ$	$0.417^\circ \pm 0.090^\circ$	$0.410^\circ \pm 0.061^\circ$
$\chi_i^2 \leq 7.5, 53.4^\circ \leq \theta \leq 86.9^\circ$	$0.457^\circ \pm 0.074^\circ$	$0.450^\circ \pm 0.078^\circ$	$0.454^\circ \pm 0.054^\circ$
$\chi_i^2 \leq 7.5, 55.3^\circ \leq \theta \leq 84.9^\circ$	$0.447^\circ \pm 0.078^\circ$	$0.434^\circ \pm 0.084^\circ$	$0.441^\circ \pm 0.057^\circ$
$\chi_i^2 \leq 7.5, 57.3^\circ \leq \theta \leq 82.9^\circ$	$0.411^\circ \pm 0.083^\circ$	$0.474^\circ \pm 0.088^\circ$	$0.443^\circ \pm 0.060^\circ$

### 6.3.4 Background

The error due to the background contribution was estimated from table 5.5. There were two possible sources of errors associated with background contribution; one was the error in determining the ratio of the background contribution to the elastic scattering events after the cuts, and the other source was the uncertainty of the background analyzing power which is in table 5.5. The uncertainty in determining the ratio of the background contribution to the elastic scattering events was estimated by assuming that the errors in the ratio determination of the

background contribution were 25% of the percentage determined (i.e., assuming 1% uncertainty out of a 4% background contribution). Combining these two factors, it was determined that the systematic errors associated with the background subtraction and correction are:

$$\delta(\Delta\theta_o) = \pm 0.021^\circ \quad \text{or} \quad \delta(\Delta A) = 2.8 \times 10^{-4} .$$

### 6.3.5 Average Neutron Beam Energy Difference

The effective average beam energy difference for the polarized and unpolarized neutron beam was corrected with the result from Monte Carlo simulations as discussed in Chapter 4. The systematic errors associated with this were estimated by assuming that the correction was accurate to about 20% (upper limit) of the total difference  $\Delta E = 0.54$  MeV,  $\delta(\Delta E) = 0.11$  MeV. Therefore, the systematic errors on the zero-crossing angle difference and the difference of the analyzing powers are:

$$\delta(\Delta\theta_o) = \pm 0.005^\circ \quad \text{or} \quad \delta(\Delta A) = 0.7 \times 10^{-4} .$$

A summary of the different contributions to the systematic errors as discussed above is listed in table 6.6.

Table 6.6: *Summary of the systematic errors in the difference of the zero-crossing angles.*

Item	$\delta(\Delta\theta_0)$
Different Cuts	0.031°
Background	0.021°
Nbar ADC cuts	0.028°
Different Fits	0.019°
$E_{nbeam}$ Correction	0.005°

# Chapter 7

## Results and Discussions

Charge symmetry breaking effects have been measured with high precision in  $np$  elastic scattering at 347 MeV. The experiment presented here measured the difference of the zero-crossing angles  $\Delta\theta_o \equiv \theta_{cm}(A_n = 0) - \theta_{cm}(A_p = 0)$ . The difference of the analyzing powers at the zero-crossing angle, where  $\langle A(\theta) \rangle = 0$ , is obtained from  $\Delta\theta_o$  by multiplying by the experimentally determined slope of the analyzing power,  $dA/d\theta_{cm}$ . The shape of  $\Delta A(\theta)$  is also extracted. The following are the results from the experiment:

- (1) The difference of the center-of-mass zero-crossing angles of the analyzing powers:

$$\begin{aligned}\Delta\theta_o &\equiv \theta_{cm}(A_n=0) - \theta_{cm}(A_p=0) \\ &= 0.438^\circ \pm 0.054^\circ (stat.) \pm 0.051^\circ (syst.),\end{aligned}$$

based on fits of the measured asymmetry angular distributions over the angle range  $53.4^\circ \leq \theta_{cm} \leq 86.9^\circ$  in the center-of-mass system. Above, the first error is the statistical error and the second error is the systematic error which is obtained as the quadrature sum of the different contributions (as discussed in chapter 6).

(2) The slope of the analyzing power  $A_p$  at the center-of-mass zero-crossing angle:

$$\frac{dA_p}{d\theta_{cm}} = (-1.35 \pm 0.05) \times 10^{-2} \text{ deg}^{-1},$$

based on the least-squares fits of the asymmetry curves and the average proton target (FST) polarization. The error here is dominated by the uncertainty in the FST polarization and the estimated systematic errors from different cuts and the background subtraction.

(3) Using the slope of the analyzing power  $A_p$  given above and assuming  $d\langle A(\theta_o) \rangle / d\theta_{cm} = dA_p / d\theta_{cm}$ , the difference of the analyzing powers at the zero-crossing angle, where  $\langle A(\theta) \rangle = 0$ , is obtained:

$$\begin{aligned} \Delta A &= -\frac{d\langle A \rangle}{d\theta_{cm}} \cdot \Delta\theta_o \\ &= [ 59 \pm 7(\text{stat.}) \pm 7(\text{syst.}) \pm 2(\text{syst.}) ] \times 10^{-4}; \end{aligned}$$

here the first error is the statistical error, the second error is the systematic error and the third error is an additional systematic error due to the uncertainty in the slope parameter  $dA/d\theta_{cm}$ .

(4) The shape of the  $\Delta A(\theta)$  is shown in Fig. 7.1. A  $\chi^2 = 18.7$  for a total of 10 points is obtained from fitting the experimental  $\Delta A(\theta)$  to the theoretical predictions of Iqbal and Niskanen [23,24] by adjusting the value of  $c = \delta(\Delta P / \langle P \rangle)$  (see equation 5.53). The constant  $c$ , so determined, equals  $-0.030 \pm 0.015$ . This value of  $c$  is well within the range of uncertainty of  $\delta(\Delta P / \langle P \rangle)$  (about  $\pm 4.2\%$ ) which follows from  $\bar{P}_n = 61.2\% \pm 1.8\%$  and  $\bar{P}_p = 73.2\% \pm 2.2\%$  or  $\langle P \rangle \equiv (\bar{P}_n + \bar{P}_p)/2 = 67.2\% \pm 1.4\%$  and  $\Delta P \equiv \bar{P}_n - \bar{P}_p = -12.0\% \pm 2.8\%$ .

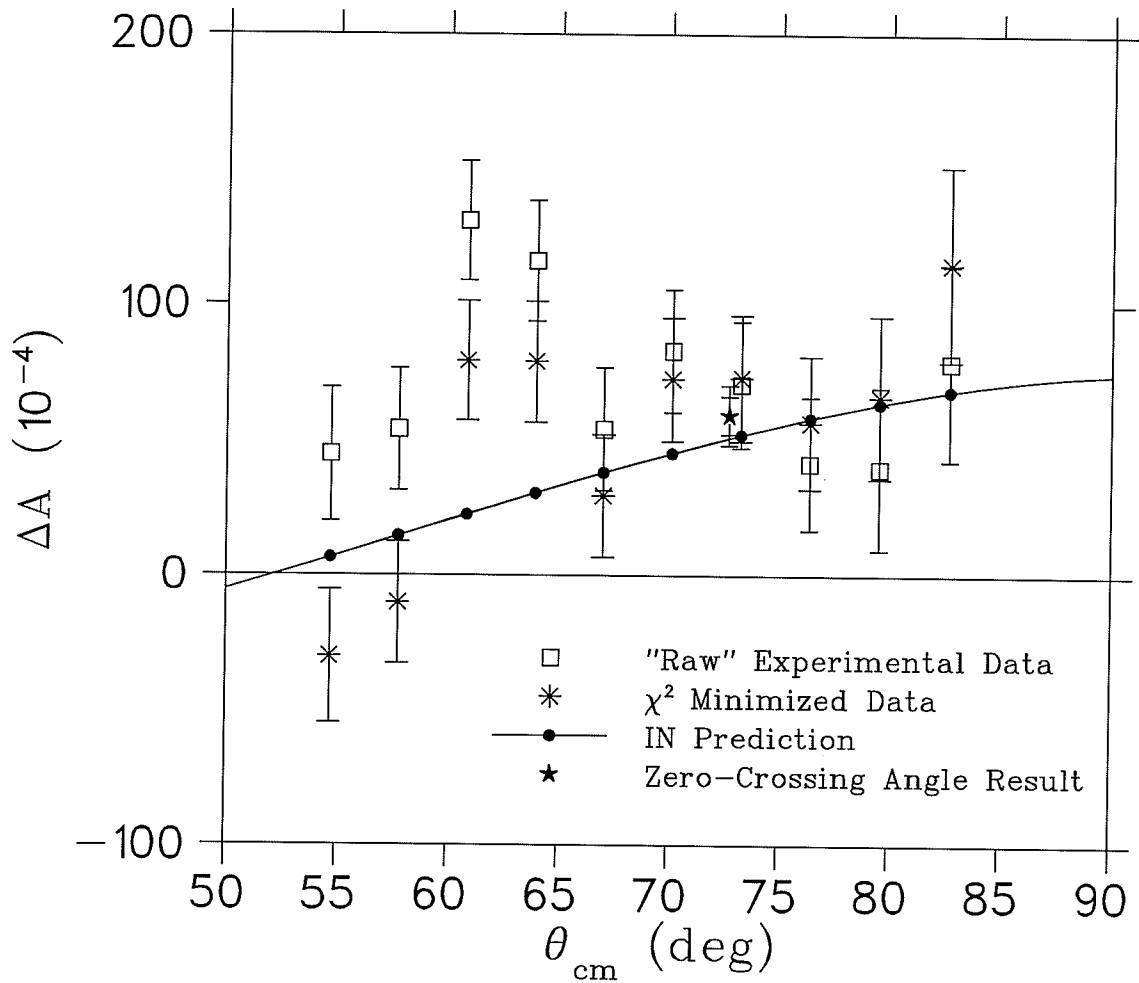


Figure 7.1: *The shape of the  $\Delta A$ . The connected points are from Iqbal and Niskanen's predictions [24]. The discrete "square" points are from the experiment ("raw" data) and the discrete "asterisk" points are obtained from the  $\chi^2$  minimization between the experimental data and theoretical predictions by varying  $c$  of equation (5.53). The error bars on the experimental data shown in the figure are statistical errors only. The "star" point is the experimental result at the zero-crossing angle; the inner error bar is the statistical error and the outer error bar is the quadrature sum of the systematic and statistical errors.*

(5) The zero-crossing angles of the analyzing powers and the analyzing power angular distributions at 347 MeV. These experimental results are of very high precision and are presented in Appendix C. They improve on the  $np$  phase shift analyses as well as the knowledge of the NN interaction.

The non-zero difference of the analyzing powers measured in the present experiment shows clear evidence of charge symmetry breaking and represents the largest effect (6 standard deviations from zero) among the available experimental results on charge symmetry breaking in  $np$  elastic scattering. The results of the experiment, the difference of the analyzing powers ( $\Delta A(\theta_o)$ ) and the shape of the  $\Delta A(\theta)$  in the angular range  $53.4^\circ \leq \theta_{cm} \leq 84.2^\circ$ , agree well with the theoretical predictions of Iqbal and Niskanen [23,24] and Holzenkamp, Holinde and Thomas [27] (only  $\Delta A(\theta_o)$  is compared, the shape of the  $\Delta A(\theta)$  is not available) which are based on meson exchange nucleon-nucleon potential models. At 347 MeV, the photon exchange and the one pion exchange contributions together account for most of the analyzing power difference at the zero-crossing angle. The result of  $\Delta A$  at the zero-crossing angle differs from the electromagnetic contribution alone by four standard deviations, and therefore shows clear evidence of a strong interaction contribution to CSB. The  $\rho^\circ - \omega$  mixing contribution crosses zero at the vicinity of the zero-crossing angles of the analyzing powers,  $A_n$  and  $A_p$ , and therefore its contribution is small. However, the angular distribution of  $\Delta A(\theta)$  depends on the  $\rho^\circ - \omega$  mixing contribution. Therefore, an accurate determination of the angular distribution of  $\Delta A(\theta)$  gives information on the interesting  $\rho^\circ - \omega$  mixing contribution which is of short range and is related to the up-down quark masses difference [5,17]. In the present experiment, the determination of the shape of  $\Delta A(\theta)$  is limited by the larger systematic errors away from the zero-

crossing angles and the inadequate knowledge of the absolute values of the beam and target polarizations. The other contributions to  $\Delta A(\theta)$ , which come from one  $\rho$  exchange,  $2\pi$  exchange and indirect quark effects, are small; the contribution from  $\gamma - \pi$  exchange has not yet been calculated but is estimated to be small [5].

To date, charge symmetry breaking has been studied in  $np$  elastic scattering at three different energies: at 477 MeV at TRIUMF [8], at 183 MeV at IUCF [21], and, in the present experiment, at 347 MeV at TRIUMF. These high precision experiments have established CSB in the NN interaction in an unambiguous way. Quantitative comparisons between the experimental data and theoretical predictions have been made. The triptych in Fig. 7.2 shows the existing experimental results in a comparison to the theoretical predictions by Iqbal and Niskanen [23,24] (IN) and Holzenkamp, Holinde and Thomas [27] (HHT). The results show that the effective parameterization of the nucleon-nucleon potential in terms of meson exchanges gives quantitatively satisfactory predictions of experiment. It is quite apparent that non-electromagnetic contributions have to be included in the theoretical predictions in order to agree with experiment. The contribution due to the neutron-proton mass difference affecting one-pion exchange has been clearly observed in both of the TRIUMF experiments. This second TRIUMF CSB experiment has more than three times higher precision than the first experiment. It shows more convincingly the quantitative agreement with the theoretical predictions including the one-pion exchange contribution (an approximately four standard deviation effect). The theoretical predictions with on-shell  $\rho^0 - \omega$  mixing agree with all current available experimental results in this class of CSB, in particular, the on-shell  $\rho^0 - \omega$  mixing contribution has to be included to interpret the IUCF experimental results (about a two standard deviation effect). The contro-

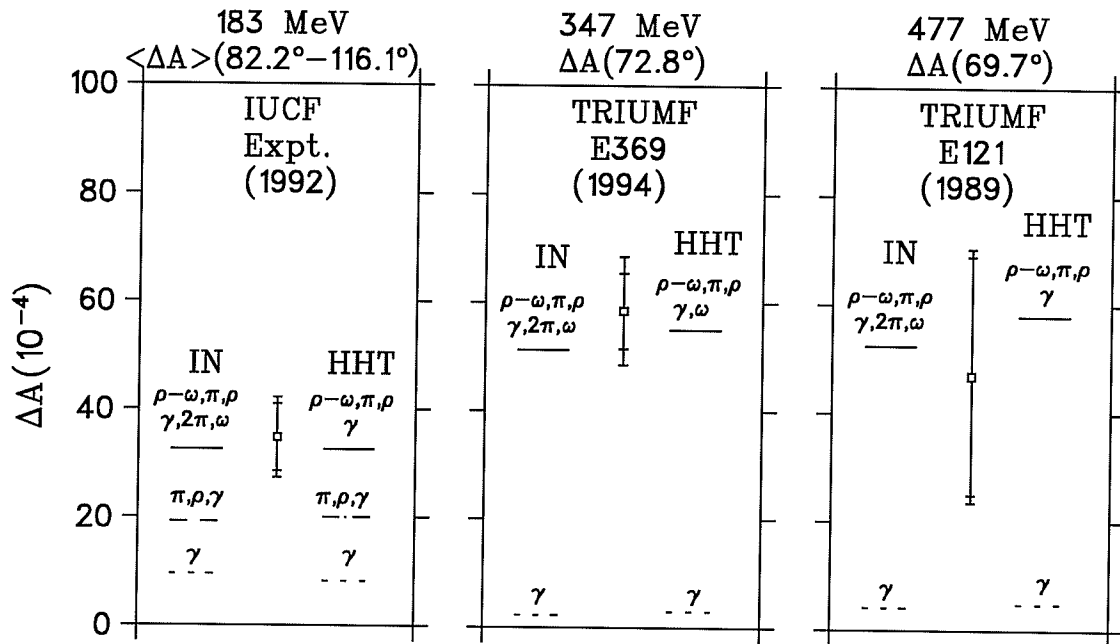


Figure 7.2: Summary of currently available experimental results on CSB in  $np$  elastic scattering compared to the theoretical predictions by Iqbal and Niskanen [24] (IN) and Holzenkamp, Holinde and Thomas [27] (HHT). The inner (smaller) error bars on the data points represent the statistical errors alone and the outer (larger) error bars represent the quadrature sum of the systematic and statistical errors. The horizontal lines are the various summed contributions obtained by IN and HHT.

versy regarding the  $\rho^0 - \omega$  mixing (the off-shell effect) remains to be settled. The argument of the off-shell effect needs experimental support.

In order to untangle the different contributions to  $\Delta A$  and test the role of  $\rho^0 - \omega$  mixing, it is necessary to perform even higher precision experiments, measuring not only the difference of the analyzing powers at the zero-crossing angle but also the angular distribution of  $\Delta A(\theta)$  over a wide angular and energy range. Accurate determination of the angular distribution of  $\Delta A(\theta)$  with an absolute scale requires precise knowledge of the polarization of beam and target and control of systematic errors away from the zero-crossing angles. An optimum experimental energy should be sought to enhance the  $\rho^0 - \omega$  contribution both to  $\Delta A$  at the zero-crossing angle as well as to the angular distribution of  $\Delta A(\theta)$ . Other classes of CSB experiments can also provide information on the  $\rho^0 - \omega$  mixing contribution. The  $\rho^0 - \omega$  mixing contribution is believed to account for most of the NN singlet scattering length difference [11,12]. The ongoing TRIUMF experiment to measure  $a_{nn}$  [13] will hopefully shed light on the controversy of  $\rho^0 - \omega$  mixing. The off-shell effect in meson mixing has also been investigated for the case of  $\pi - \eta$  mixing; a similar effect as for  $\rho^0 - \omega$  mixing was suggested [48,49]. Another TRIUMF CSB experiment which will measure the forward-backward asymmetry in the reaction  $np \rightarrow d\pi^0$  is a sensitive test of the  $\pi - \eta$  mixing contribution, and therefore could provide information on the on-shell versus off-shell treatments of  $\pi - \eta$  meson mixing [47].

Further theoretical investigations of CSB are required to solve the  $\rho^0 - \omega$  mixing controversy (on-mass-shell or off-mass-shell treatments), to evaluate the  $\pi - \gamma$  exchange contribution, and to interpret in detail the current available ex-

perimental results. The current theoretical evaluations of off-shell effects in meson mixing have been criticized primarily for their theoretical imperfections, model dependence and lack of underpinning experimental support [6,24]. If off-shell effects are significant, the current excellent agreement between the theoretical predictions and the experimental results would be no longer valid, and therefore other contributions must be sought. Further detailed studies of CSB in different systems could provide more information on the underlying quark structure of the nucleon, and therefore help to form a direct bridge between phenomenological NN potential models represented by the meson exchange theory and the fundamental theory of QCD describing the strong interaction.

# Bibliography

- [1] E. Segre, *Nuclei and Particles* (W.A. Benjamin, Inc., 1977)
- [2] E.M. Henley, in *Isospin in Nuclear Physics*, ed. D.H. Wilkinson (North-Holland, Amsterdam, 1969) p. 15
- [3] L. Heller, *Rev. Mod. Phys.* **39**, 584 (1967)
- [4] E.M. Henley and G.A. Miller, in *Mesons in Nuclei*, ed. M. Rho and D.H. Wilkinson (North-Holland, Amsterdam, 1979) p. 407
- [5] G.A. Miller, B.M.K. Nefkens and I. Slaus, *Phys. Rep.* **194**, 1 (1990)
- [6] G.A. Miller and W.T.H. van Oers, in *Symmetries and Fundamental Interactions in Nuclei*, ed. W.C. Haxton and E.M. Henley (World Scientific, Singapore), in press
- [7] R. Tkachuk, L.G. Greeniaus and W.T.H. van Oers, *TRIUMF Experiment 369 Proposal*, (1985)
- [8] R. Abegg et al., *Phys. Rev. D* **39**, 2464 (1989)
- [9] L.G. Greeniaus and W.T.H. van Oers, *TRIUMF Experiment 369 Proposal update*, (1989)
- [10] O. Dumbrajs et al., *Nucl. Phys. B* **216**, 277 (1983)

- [11] S.A. Coon and R.C. Barrett, Phys. Rev. C **36**, 2189 (1987)
- [12] P.G. Blunden and M.J. Iqbal, Phys. Lett. **198**, 14 (1987)
- [13] M. A. Kovash, TRIUMF Experiment 661 proposal, (1993)
- [14] K. Okamoto, Phys. Lett. **11**, 150 (1964)
- [15] J.A. Nolen, Jr. and J.P. Schiffer, Ann. Rev. Nucl. Sci. **19**, 471 (1969)
- [16] E.M. Henley and G. Krein, Phys. Rev. Lett. **62**, 2586 (1989)
- [17] G.A. Miller, Nucl. Phys. **A518**, 345 (1990)
- [18] L. Wolfenstein, Ann. Rev. Nucl. Sci. **6**, 43 (1956)
- [19] R. Abegg et al., Phys. Rev. Lett. **56**, 2571 (1986)
- [20] L.D. Knutson et al., Phys. Rev. Lett. **66**, 1410 (1991)
- [21] S.E. Vigdor et al., Phys. Rev. C **46**, 410 (1992)
- [22] S.E. Vigdor, private communication ( The value of  $\Delta A$  changed by about 4% due to a new calibration of the neutron beam polarization and consequent renormalization of the result)
- [23] M.J. Iqbal and J.A. Niskanen, Phys. Rev. C **38**, 2259 (1988)
- [24] M.J. Iqbal and J.A. Niskanen, private communication (1994)
- [25] A.G. Williams, A.W. Thomas and G.A. Miller, Phys. Rev. C **36**, 1956 (1987)
- [26] G.A. Miller, A.W. Thomas and A.G. Williams, Phys. Rev. Lett. **56**, 2567 (1987)

- [27] B.H. Holzenkamp, K. Holinde and A.W. Thomas, Phys. Lett. B **195**, 121 (1987)
- [28] L. Ge and J.P. Svenne, Phys. Rev. C **33**, 417 (1986); erratum C **34**, 756 (1987)
- [29] J.A. Niskanen and S.E. Vigdor, Phys. Rev. C **45**, 3021 (1992)
- [30] G.A. Miller, Phys. Rev. C **39**, 1563 (1989)
- [31] T. Goldman, J.A. Henderson, and A.W. Thomas, Few Body System **12**, 123 (1992)
- [32] J. Bystricky, F. Lehar and P. Winternitz, J. Physique **39**, 1 (1978)
- [33] P. LaFrance and P. Winternitz, J. Physique **41**, 1391 (1980)
- [34] A. Gersten, Phys. Rev. C **24**, 2174 (1981)
- [35] C.Y. Cheung, E.M. Henley and G.A. Miller, Nucl. Phys. **A348**, 365 (1980)
- [36] L.M. Barkov et al., Nucl. Phys. **B256**, 365 (1985)
- [37] T. Hatsuda et al., Phys. Rev. C **49**, 452 (1994)
- [38] G. Krein, A.W. Thomas and A.G. Williams, Phys. Lett. B **317**, 293 (1993)
- [39] J. Piekarewicz and A.G. Williams, Phys. Rev. C **47**, R2462 (1993)
- [40] M.J. Iqbal and J.A. Niskanen, Phys. Lett. B **322**, 7 (1994)
- [41] K. Saito and A.W. Thomas, Phys. Lett. B **335**, 17 (1994)
- [42] K.L. Mitchell et al., Phys. Lett. B **335**, 282 (1994)
- [43] H.B. O'Connell et al., Phys. Lett. B **336**, 1 (1994)

- [44] J.A. Niskanen, M. Sebestyén and A.W. Thomas, Phys. Rev. C **38**, 838 (1988)
- [45] S.S. Wilson et al., Nucl. Phys. **B33**, 253 (1971)
- [46] C.L. Hollas et al., Phys. Rev. C. **24**, 1561 (1981)
- [47] A.K. Opper and E. Korkmaz, TRIUMF Experiment 704 proposal, (1993)
- [48] K. Maltman, Phys. Lett. B **313**, 203 (1993)
- [49] K. Maltman and T. Goldman, Nucl. Phys. **A572**, 682 (1994)
- [50] J. Piekarewicz, Phys. Rev. C **48**, 1555 (1993)
- [51] G.R. Smith et al., Phys. Rev. C **38**, 240 (1988)
- [52] B. Brinkmüller et al., Phys. Rev. C **44**, 2031 (1991)
- [53] L. Goldzahl et al., Nucl. Phys. **A533**, 675 (1991)
- [54] C.R. Howell et al., Phys. Rev. C **48**, 2855 (1993)
- [55] R.E.J. Florizone et al., Phys. Rev. Lett. **72**, 3476 (1994)
- [56] A.R. Bodmer and Q.N. Usmani, Phys. Rev. C **31**, 1400 (1985)
- [57] Polarization Phenomena in Nuclear Reactions, ed. by H.H. Barschall and W. Haeberli (The University of Wisconsin Press, Madison, 1970)
- [58] R. Abegg et al., Nucl. Instr. and Meth. **A234**, 11 (1985)
- [59] R. Abegg et al., Nucl. Instr. and Meth. **A234**, 20 (1985)
- [60] A.N. Zelenskii et al., Nucl. Instr. and Meth. **A334**, 285 (1993)
- [61] L.W. Anderson, Nucl. Instr. and Meth. **167**, 363 (1979)

- [62] P.G. Sona, *Energia Nucl.* **14**, 295 (1967)
- [63] W.D. Ramsay et al., *Nucl. Instr. and Meth.* **A327**, 265 (1993)
- [64] D.V. Bugg and C. Wilkin, *Nucl. Phys.* **A467**, 575 (1993)
- [65] D.V. Bugg, private communication
- [66] L. Gan et al., in preparation
- [67] R. Abegg and R. Schubank, TRIUMF Internal Report, TRI-DN-87-17, 1987, unpublished
- [68] L.G. Greeniaus and J. Soukup, TRIUMF Internal Report, TRI-DN-81-1, 1981, unpublished
- [69] R.A. Arndt, Interactive dial-in program SAID, 1993
- [70] P.P.J. Delheij, D.C. Healey, and G.D. Wait, *Nucl. Instr. and Meth.* **A264**, 186 (1988)
- [71] R. Abegg et al., *Nucl. Instr. and Meth.* **A254**, 469 (1987)
- [72] R. Abegg et al., *Nucl. Instr. and Meth.* **A306**, 432 (1991)
- [73] K. Chantziantoniou, M.Sc. thesis, University of Manitoba (1989), unpublished.
- [74] R. Abegg et al., *Phys. Rev. C* **38**, 2173 (1988)
- [75] D. Bandyopadhyay et al., *Phys. Rev. C* **40**, 2684 (1989)
- [76] P. Poffenberger, TRIUMF Internal Report, TRI-DN-84-30, 1984, unpublished
- [77] R. Grove et al., *Nucl. Instr. and Meth.* **99**, 381 (1972)

- [78] R. Grove, V. Perez-Mendez and J. Sperinde, Nucl. Instr. and Meth. **106**, 407 (1973)
- [79] W.T. Welford and R. Winston, The Optics of Non-Imaging Concentrators - Light and Solar Energy (Academic Press, New York, 1978)
- [80] R.A. Cecil, B.D. Anderson and R. Madey, Nucl. Instr. and Meth. **161**, 439 (1979)
- [81] G.A. Ludgate, The VADACS Data Acquisition and Analysis System, 1988, unpublished
- [82] TRIUMF Data Acquisition Software Group, TWOTRAN Reference Manual, 1988, unpublished
- [83] L.G. Greeniaus, TRIUMF Interactive Energy Loss Computer Program, 1991, unpublished
- [84] S. Pearlstein, Astrophysical J. **346**, 1049 (1989)
- [85] W.H. Press et al, "Numerical Recipes", Cambridge University Press (1986)
- [86] J.F. Janni, Atomic Data and Nuclear Data Tables, **27**, 147 (1982)
- [87] J.B. Marion and B.A. Zimmerman, Nucl. Instr. and Meth., **51**, 93 (1967)
- [88] B.P. Nigam, M.K. Sundaresan and Ta-You Wu, Phys. Rev. **115**, 491 (1959)
- [89] P.W. Green, Introduction to the NOVA data analysis system, 1991, unpublished
- [90] TRIUMF cyclotron operation manual, unpublished.
- [91] D.A. Hutcheon et al., Nucl. Phys. **A535**, 618 (1991)

[92] C.A. Davis et al., in preparation

# Appendix A

## Delay Line Multiwire Chamber Calibrations

To calculate the proton positions ( $x$  and  $y$ ) in the DLCs, as discussed in Chapter 5, time differences of the timing signals from the opposite ends were taken, and a time to distance conversion was obtained from the known physical pulser separations and their time differences. Since the relations between the delay times and the lengths of the delay lines were not perfectly linear, a calibration of the DLCs was needed in order to achieve higher position resolution. To calibrate the spatial linearity of the DLCs, recoil protons were used to form the characteristic “picket fence” image of the anode wires. The picket fence image corresponded to an intrinsic resolution of  $\pm 1$  mm for the direction perpendicular to the anode wires since most ionizing events resulted in an avalanche around only a single anode wire, with the impossibility of distinguishing on which side of the anode wire the initial ionization occurred. Each group of four chambers (one on each side, physical left or right) was placed as close together and as far away from the target along the proton boom as possible, thus allowing for full and simultaneous illumination of all the chambers by the recoil protons.

The individual vertical anode wires were easily distinguishable in the horizontal time difference spectra, while the absolute spatial position of each anode wire was known. A calibration table relating the centroid of each picket in TDC channels to the absolute spatial position of the wire was constructed.

The vertical delay time difference spectra had no characteristic structure. Their calibration was achieved by rotating the first and the third chambers of each group by  $90^\circ$  about the proton detection telescope axis, thus putting the picket fence coordinate in the vertical direction for half of chambers (as shown in Fig. A.1). The picket fence structure and ray tracing through the appropriate pair of chambers was used to calibrate the vertical delay lines of the second pair of chambers. Again, a calibration table was constructed. A local resolution of 0.7 mm FWHM was achieved in the vertical direction.

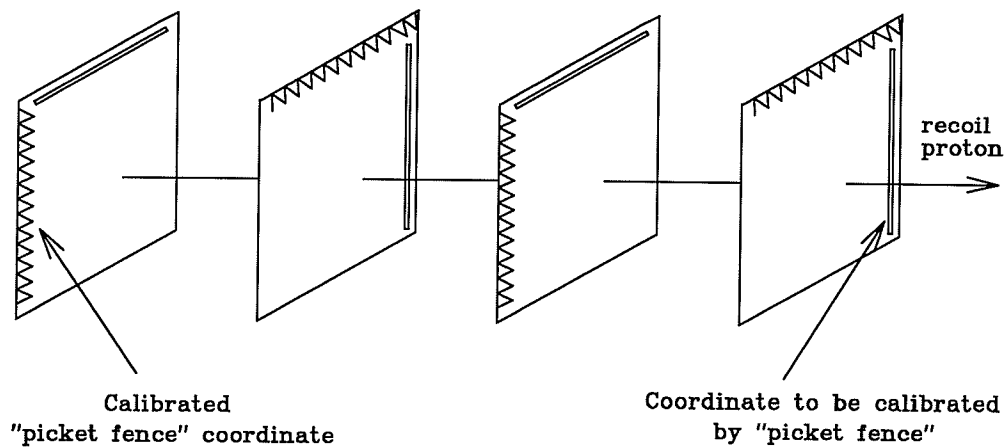


Figure A.1: *DLCs in calibration mode. They were moved as close together and as far away from the FST as possible along the boom and the first and third DLCs rotated by 90 degree to calibrate the non-picket fence side with the picket fence.*

The non-linearity of a delay line would change if the pressure on the delay line changes or if it is physically moved inside the chamber (with respect to the cathode strips). A few of the DLCs (no more than two at a time) had to be cleaned or repaired between the different data taking periods because some DLCs had “dirty” wires or broken windows. The non-linearity of the DLCs changed after the necessary servicing and a new calibration table was required. To re-calibrate those DLCs, proton singles events, which did not require coincident neutrons to be present, were used to “fully” illuminate the DLCs at their data taking locations (see Chapter 3 and Chapter 5). This procedure was followed since the front pairs were only partially illuminated by  $np$  elastic scattering events. Three other chambers with no changes on the same side or at least one from each pair (front and rear) were used to re-calibrate the refurbished chamber. Reconstructed proton tracks were used to re-calibrate the DLC following the same procedure used in the original calibration mode. Here, no rotation of the chambers was needed because the other chambers had been calibrated to the “picket fence” resolution ( $\pm 1$  mm) or better ( $\pm 0.7$  mm for “non-picket fence” direction).

# Appendix B

## Spin Precession Magnets

### Calibration

The precession magnet settings were fully calibrated in several test runs. The calibrations of all three spin precession magnets (JANIS, CLYDE and BONNIE) were made by varying the appropriate magnetic field strength and determining the zero-crossing of both the left-right and down-up asymmetries at the neutron polarimeters. Precession curves of the neutron polarimeter asymmetries normalized by the incident proton polarimeter asymmetries versus the magnet excitations, were fit to a function of the form:

$$F(x) = \alpha \cos \frac{\pi(x + \gamma)}{2(\beta + \gamma)} \quad (\text{B.1})$$

with  $\alpha, \beta, \gamma$  as free parameters. The quantity  $\beta$  corresponded to the zero-crossing and therefore was the required field strength for the precession magnet. The offset angle  $\gamma$  (in units of kG) indicated the initial orientation of the polarization in the plane of precession. Figure B.1 shows the spin polarization components in different directions and after each of the spin precession magnets or the  $LD_2$  target, (a) JANIS, (b) the  $LD_2$  target, (c) CLYDE, and (d) BONNIE when the magnets

were properly calibrated and all the magnets were turned on.

To calibrate JANIS, BONNIE was turned off and CLYDE was set to the nominal (calculated) value. The left-right asymmetries in the OLD neutron polarimeter as a function of the JANIS excitation current were measured. Using this configuration (see figure B.1) the OLD neutron polarimeter should have only measured a small vertical component of polarization due to the parameter  $P \simeq -0.07$  with JANIS calibrated properly. Therefore, the zero-crossing in the left-right asymmetry corresponded to the desired value with a small error due to the parameter  $P \simeq -0.07$ . This error can be corrected with unpolarized beam data. Figure B.2(a) shows the precession curve of JANIS with BONNIE off and CLYDE at its nominal setting. The left-right asymmetries in both NEW and OLD neutron polarimeters were measured; small improper settings of CLYDE (field vertical) did not affect the zero-crossing of the JANIS asymmetry curve.

To calibrate CLYDE, BONNIE was turned off and JANIS was set for a  $90^\circ$  rotation (rotation of the proton polarization from transverse vertical to transverse horizontal) after the above calibration. The down-up asymmetry of the OLD neutron polarimeter was measured as a function of the CLYDE excitation current. When CLYDE was properly calibrated and set, the polarization should be rotated into the longitudinal direction with a small vertical polarization component, but no horizontal transverse direction polarization component as shown in Fig. B.1 before the BONNIE magnet (d). Figure B.2 (b) shows the precession curve of CLYDE with BONNIE off and JANIS set for a  $90^\circ$  rotation. The zero-crossing of the down-up asymmetry corresponded to the desired maximum longitudinal polarization. The small vertical polarization did not affect the result (down-up

asymmetry).

The BONNIE magnet was calibrated both by the zero-crossing of the precession curve with CLYDE at its nominal setting and JANIS off and by the plateau of the precession curve with all magnets on. When JANIS was off, the neutron polarization between the  $LD_2$  target and BONNIE should have only a vertical component due to the Wolfenstein polarization parameter  $D_t$  and parameter  $P$ . The vertical field of CLYDE did not affect the vertical polarization. The vertical polarization was rotated by the BONNIE field from the vertical direction to the longitudinal direction; therefore, a 90 degree rotation would correspond to zero left-right asymmetry in the OLD neutron polarimeter. However, both  $D_t$  and  $P$  are rather small ( $D_t = +0.231$  and  $P = -0.07$ ) requiring long data taking times to obtain the required statistics. Therefore, the BONNIE magnet was also calibrated with both JANIS and CLYDE at their calibrated settings. When JANIS and CLYDE were both turned on, a 90 degree rotation of polarization by BONNIE would correspond to the maximum left-right asymmetry in the OLD neutron polarimeter with a small error due to the parameter  $P$  (causing a small vertical component of vertical polarization before the BONNIE magnet). Therefore, the plateau of the precession curve would correspond to the desired setting (a 90 degree rotation) of the BONNIE magnet. Figure B.2 (c) shows the precession curve of BONNIE with all magnets on. In this case, a plateau in left-right asymmetry of the OLD neutron polarimeter corresponded to the maximum vertical polarization.

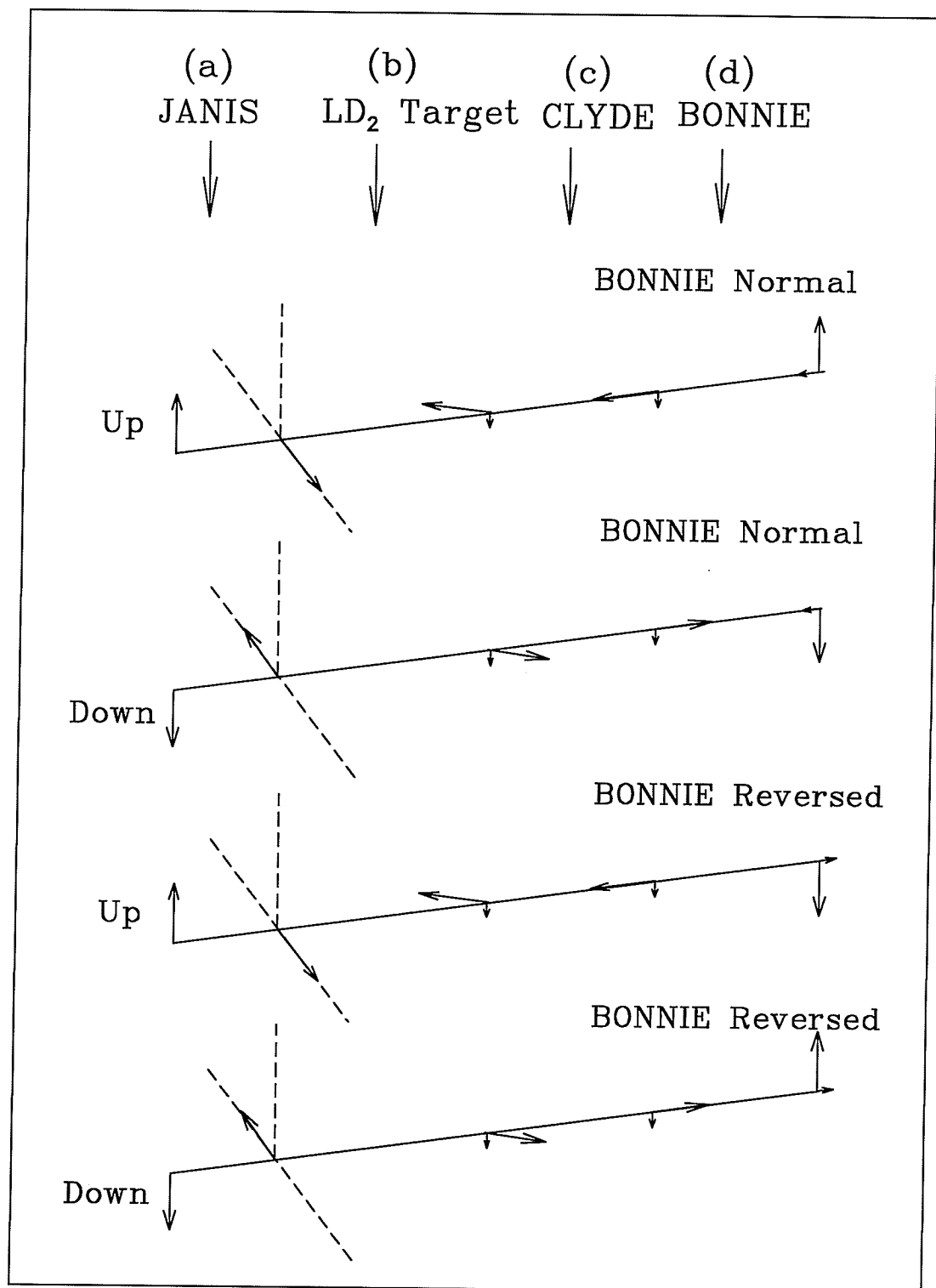


Figure B.1: Schematic diagram of the rotations and directions of the polarization at various locations (a) JANIS, (b) the LD<sub>2</sub> target, (c) CLYDE, and (d) BONNIE.

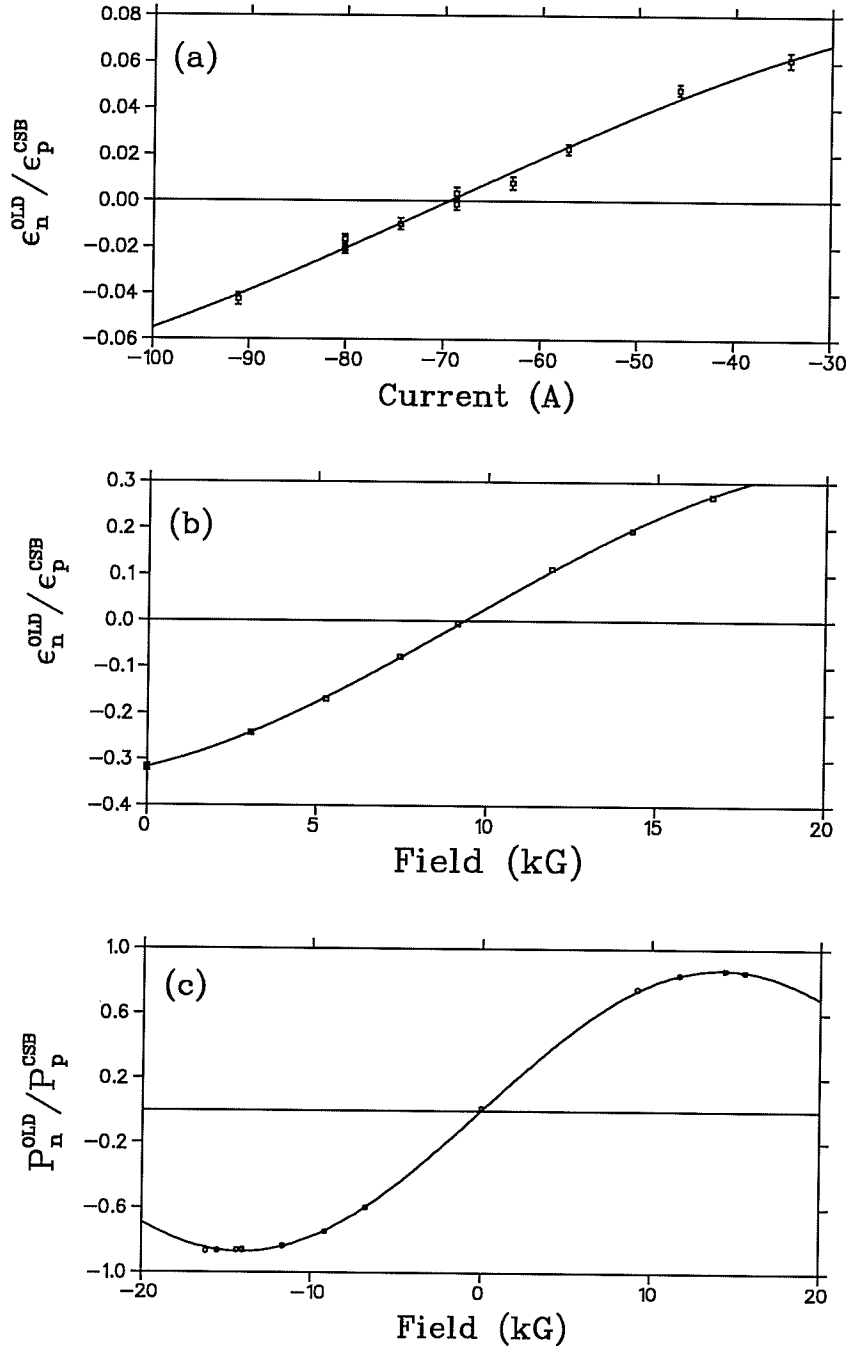


Figure B.2: *Precession curves of the precession magnets; (a) JANIS (b) CLYDE (d) BONNIE.*

# Appendix C

## Analyzing Power Angular Distributions and Zero-crossing Angles

The average of the center-of-mass zero-crossing angles of the analyzing powers at 347 MeV has been measured with very high precision:

$$\begin{aligned}\bar{\theta}_{cm} &= \frac{\theta_{cm}(A_n=0) + \theta_{cm}(A_p=0)}{2} \\ &= 72.74^\circ \pm 0.03^\circ(\text{stat.}) \pm 0.14^\circ(\text{syst.})\end{aligned}$$

where the first error is the statistical error and the second is the systematic error, which is based on estimates of various uncertainties including the detector locations ( $\delta\theta_{cm} = \pm 0.05^\circ$ ), corrections for the holding field deflection ( $\delta\theta_{cm} = \pm 0.10^\circ$ ), the uncertainty of the absolute proton beam energy ( $\delta\theta_{cm} = \pm 0.05^\circ$ ), and various tests of the systematic errors ( $\delta\theta_{cm} = \pm 0.07^\circ$ ). With the experimentally determined difference of the zero-crossing angles (as presented in Chapter 7):

$$\begin{aligned}\Delta\theta_o &\equiv \theta_{cm}(A_n=0) - \theta_{cm}(A_p=0) \\ &= 0.438^\circ \pm 0.054^\circ(\text{stat.}) \pm 0.051^\circ(\text{syst.}),\end{aligned}$$

the zero-crossing angles  $\theta_{cm}(A_n=0)$  and  $\theta_{cm}(A_p=0)$  can be determined with high precision.

The experiment has also determined the analyzing power angular distributions  $A_n$  and  $A_p$  and the average zero-crossing angles of the analyzing powers with very high accuracy at 347 MeV. Table C.1 shows the angular distributions of  $A_n$  and  $A_p$  in about  $2^\circ$  center-of-mass angular bins. Each data point has a systematic error of about 0.0020, which is an estimate based on the systematic errors of the “absolute” zero-crossing angles. A scale error of 3.0% for the polarized beam data  $A_n$  and 3.0% for the polarized target data  $A_p$  has been assigned to each data point to account for the uncertainty of the respective polarization determination.

The experimentally determined slope of the analyzing power, the zero-crossing angle and angular distributions of the analyzing powers can be used to enlarge the phase shift analysis data base, and help to constrain phase shift analysis results. This also improves on the understanding of the nucleon-nucleon interaction. It has been demonstrated that finite differences of the zero-crossing angles due to CSB are consistently present at different energies. In order to achieve higher accuracy predictions (better than  $\sim \pm 0.2^\circ$ ) in phase shift analyses, it is necessary to separate  $A_n$  and  $A_p$  in the data base.

Table C.1: *The analyzing powers,  $A_p$  and  $A_n$ , at 347 MeV. Each data point has a systematic error of about 0.0020 and scale errors of 3.0% on the value of  $A_p$  and 3.0% on the value of  $A_n$ , respectively.*

ANGLE (deg.) (c.m.)	$A_p$	$A_n$
86.11	$-0.1643 \pm 0.0036$	$-0.1507 \pm 0.0038$
84.11	$-0.1442 \pm 0.0032$	$-0.1317 \pm 0.0035$
82.13	$-0.1181 \pm 0.0030$	$-0.1104 \pm 0.0033$
80.15	$-0.0967 \pm 0.0027$	$-0.0937 \pm 0.0029$
78.17	$-0.0715 \pm 0.0023$	$-0.0639 \pm 0.0025$
76.20	$-0.0486 \pm 0.0021$	$-0.0444 \pm 0.0022$
74.24	$-0.0233 \pm 0.0020$	$-0.0164 \pm 0.0022$
72.28	$-0.0004 \pm 0.0020$	$0.0092 \pm 0.0021$
70.33	$0.0291 \pm 0.0020$	$0.0323 \pm 0.0021$
68.38	$0.0550 \pm 0.0019$	$0.0642 \pm 0.0021$
66.44	$0.0871 \pm 0.0019$	$0.0896 \pm 0.0021$
64.50	$0.1088 \pm 0.0019$	$0.1186 \pm 0.0021$
62.57	$0.1376 \pm 0.0019$	$0.1493 \pm 0.0021$
60.65	$0.1655 \pm 0.0019$	$0.1759 \pm 0.0020$
58.73	$0.1934 \pm 0.0019$	$0.1975 \pm 0.0021$
56.81	$0.2207 \pm 0.0019$	$0.2248 \pm 0.0021$
54.90	$0.2436 \pm 0.0020$	$0.2434 \pm 0.0022$
53.56	$0.2450 \pm 0.0037$	$0.2544 \pm 0.0039$

# Appendix D

## Event Structure

The data stream from the CAMAC crates was divided into seven event types:

- Scalar data (event type 1)
- Neutron profile monitor and polarimeter data (event type 2)
- Left or right np coincidence or button events (event type 5)
- High voltage data (event type 11)
- FST data (event type 12)
- SEM data (event type 13)
- Magnets settings information (event type 14)

The left or right events of the np coincidence or the button events as well as the different spin states of the beam were identified in the DCR unit. The DCR bit map is also listed in table D.1.

Table D.1: *DCR bit map.*

Bit	First np DCR (LEFTDCR)	Bit	Second np DCR (RIGHTDCR)
0	L n Trigger	0	R n Trigger
1	L Button Old	1	R Button Old
2	L Button New	2	R Button New
3	L Veto Overlap	3	R Veto Overlap
4	L p Trigger	4	R p Trigger
5	Pulser In	5	Acc Pulser
6	L Pulser	6	R Pulser
7	Up.(Busy)	7	p Singles Enable Switch
8	Down.(Busy)	8	n Singles Enable Switch
9	Off.(Busy)	9	n Veto Enable Switch
10	Busy	10	Profile Enable Switch
11	Gold Box Phase Locked	11	Polarimeter Enable Switch
12		12	
13		13	
14		14	
15		15	